

Interactions of Grid-Forming Converters for  
Windfarm Applications

PhD Thesis

Callum Henderson

Power Electronics, Drives and Energy Conversion Group

Electronic and Electrical Engineering

University of Strathclyde, Glasgow

May 18, 2023

This thesis is the result of the author's original research. It has been composed by the author and has not been previously submitted for examination which has led to the award of a degree.

The copyright of this thesis belongs to the author under the terms of the United Kingdom Copyright Acts as qualified by University of Strathclyde Regulation 3.50. Due acknowledgement must always be made of the use of any material contained in, or derived from, this thesis.

# Abstract

The electricity network is undergoing a paradigm shift due to the strive for cleaner generation and enhanced electrification of heat, transport and industry. Due to the removal of synchronous generation and the increased penetration of inverter-based resources numerous issues have been highlighted. The reduction of system inertia, frequency response, lower fault current provision and apparent decline in system strength are all leading to reduced frequency, voltage and harmonic stability on the network. To remedy this, converters are being designed with enhanced grid services to replicate the useful behaviour lost with the removal of synchronous generation. Conventional grid-following structures are being augmented with enhanced power and voltage control loops and grid-forming converters have been suggested as a promising source of inertia, frequency response and system strength. However, with the inclusion of these structures the way the network interacts is fundamentally changing and new analysis techniques are required to properly represent the system. The structures are capable of deployment into any inverter-based resource however this work takes a main focus on wind energy which is the fastest growing renewable energy source at present with a high volume of capacity already installed. Additionally, wind farms are often located far from shore leading to long transmission lines, high impedances and weak networks. This makes them an ideal case for testing the interactions of grid following and forming converters. This thesis explores different methods of analysing the interactions in wind parks via the system impedances. The mathematical implications of the system admittance when including converter control action are explored. This analysis is used to justify the use of multiple-input multiple-output models for study over simpler Single-Input Single-Output models. The interactions between single and

multiple turbine systems are then explored using impedance-based stability techniques where a new method of analysing the system is proposed capable of dealing with issues of previous techniques and allowing the system to be studied from different points of view. The interactions of different grid-following and grid-forming structures are explored with the robustness of each combination explored. Following this the link between system strength and stability is explored where a novel method of determining system strength is proposed (known as GSIM) incorporating converter control action and decoupling system strength from fault current provision. This method is used to investigate the useful or detrimental behaviour of each control topology towards system strength. Finally, all analyses are combined to analyse a full wind farm including multiple turbines capable of operating under different control structures. This allows the work to answer the important question, what is the appropriate balance of grid forming to grid following in a wind park and what system components affect this. Moreover, the optimal location to place grid-forming turbines is explored in terms of providing system strength and stability.

# Contents

<b>Abstract</b>	<b>ii</b>
<b>List of Figures</b>	<b>viii</b>
<b>List of Tables</b>	<b>xiii</b>
<b>List of Abbreviations</b>	<b>xv</b>
<b>List of Symbols</b>	<b>xix</b>
<b>Acknowledgements</b>	<b>xxvii</b>
<b>1 Introduction</b>	<b>1</b>
1.1 Challenges of a Converter Dominated Network . . . . .	2
1.1.1 Inertia and Frequency Stability . . . . .	3
1.1.2 System Strength and Voltage Stability . . . . .	6
1.1.3 Disturbance Ride-Through and Protection System Impact . . . . .	8
1.1.4 Adverse System Interaction and Accurate Simulation Models . . . . .	9
1.2 The Role of Wind Energy in Achieving Net-Zero . . . . .	10
1.2.1 Enhanced Grid Services from Wind Farms . . . . .	10
1.3 Objectives and Summary of Work . . . . .	14
1.4 Scientific Contributions . . . . .	16
1.5 List of Publications . . . . .	17
<b>2 Converter Modelling</b>	<b>20</b>
2.1 Introduction . . . . .	20

## Contents

2.2	Grid-connected Converter Control . . . . .	20
2.2.1	Grid-following converters . . . . .	21
2.2.2	Grid-forming converters . . . . .	22
2.2.3	Grid-supporting converters . . . . .	25
2.3	Converter Modelling . . . . .	26
2.3.1	Grid-Following Control Topology . . . . .	27
2.3.2	Synchronisation . . . . .	27
2.3.3	Inner Loop Control . . . . .	28
2.3.4	Outer Loop Control . . . . .	31
2.4	Grid-Forming Control Topology . . . . .	33
2.4.1	Grid-Forming Droop Control . . . . .	34
2.4.2	Virtual Synchronous Machine . . . . .	35
2.5	Behind and Beyond the Grid-Side Converter . . . . .	41
2.5.1	Permanent Magnet Synchronous Generator . . . . .	42
2.5.2	Two-mass drive-train . . . . .	43
2.5.3	Machine Side Control . . . . .	43
2.5.4	DC Link . . . . .	44
2.6	Further Network Components . . . . .	45
2.7	Small-Signal Modelling . . . . .	46
2.7.1	Power Calculation . . . . .	47
2.7.2	PLL . . . . .	48
2.7.3	Park Transforms . . . . .	48
2.7.4	Negative Sequence Transformation . . . . .	48
2.7.5	Negative Sequence PLL . . . . .	49
2.7.6	Negative Sequence Park Transform . . . . .	49
2.7.7	Negative Sequence Notch Filters . . . . .	50
2.7.8	Negative Sequence Current Control . . . . .	50
2.7.9	Negative Sequence Voltage FeedForwards . . . . .	51
2.7.10	Grid-forming Park Transform . . . . .	51
2.7.11	DC Link . . . . .	52

2.7.12	Hardware Implications . . . . .	52
<b>3</b>	<b>Equivalent Converter Output Impedance</b>	<b>54</b>
3.1	Introduction . . . . .	54
3.2	SISO vs MIMO . . . . .	55
3.3	Admittance Formulation . . . . .	57
3.4	Comparison and Verification of Controller Admittance . . . . .	58
3.4.1	PVCC . . . . .	59
3.4.2	PVCCI . . . . .	59
3.4.3	PVCCD . . . . .	60
3.4.4	GFMD . . . . .	61
3.4.5	VSMCC . . . . .	62
3.4.6	VSM . . . . .	62
3.5	Diagonal Dominance in MIMO Systems . . . . .	63
3.6	Measuring Diagonal Dominance . . . . .	66
3.7	The effect of Diagonal Dominance on SISO Stability Analysis . . . . .	70
3.7.1	Traditional SISO Gain Margin . . . . .	70
3.7.2	Traditional SISO Phase Margin . . . . .	73
3.8	Disk Margins for Robust MIMO Stability Analysis . . . . .	76
<b>4</b>	<b>Impedance-Based Stability</b>	<b>83</b>
4.1	Introduction . . . . .	83
4.2	Single Converter Systems . . . . .	84
4.3	MIMO Stability Analysis . . . . .	88
4.3.1	Generalised Nyquist Criterion . . . . .	88
4.3.2	Generalised Bode Criterion . . . . .	90
4.3.3	Eigenvalue Analysis . . . . .	91
4.3.4	Comparison of Stability Techniques . . . . .	92
4.3.5	Applications of MIMO Techniques . . . . .	94
4.4	Multi-Converter System . . . . .	95
4.5	MIMO Multi-Converter System . . . . .	97

## Contents

4.6	Multi-Converter Case Studies . . . . .	99
4.6.1	Converter Common Mode . . . . .	101
4.6.2	Converter 1 Differential Mode . . . . .	104
4.6.3	Converter 2 Differential Mode . . . . .	108
<b>5</b>	<b>Screening Stability Issues</b>	<b>114</b>
5.1	Short-Circuit Ratio and Weak Networks . . . . .	116
5.2	Alternative Definitions . . . . .	119
5.2.1	Composite Short Circuit Ratio . . . . .	119
5.2.2	Weighted Short Circuit Ratio . . . . .	119
5.2.3	Short Circuit Ratio with Interaction Factors . . . . .	120
5.2.4	Equivalent Circuit Short Circuit Ratio . . . . .	120
5.2.5	Drawbacks of Present Methods . . . . .	121
5.3	Grid Strength Impedance Metric . . . . .	122
5.3.1	Defining GSIM . . . . .	122
5.3.2	Exploring the Properties of GSIM . . . . .	124
5.4	Validation . . . . .	133
5.4.1	Stability Analysis . . . . .	133
5.4.2	Voltage Disturbances . . . . .	135
5.4.3	Power Flow . . . . .	136
5.5	Case Studies . . . . .	139
5.5.1	Fundamental Frequency . . . . .	139
5.5.2	GSIM Across the Frequency Range . . . . .	146
<b>6</b>	<b>System Interactions of Windfarms</b>	<b>158</b>
6.1	Mechanical Interactions . . . . .	160
6.1.1	Recommendations Considering Mechanical Effects . . . . .	166
6.2	Adverse System Interactions in Windfarms . . . . .	168
6.2.1	Line Analysis . . . . .	170
6.2.2	Array Analysis . . . . .	179
<b>7</b>	<b>Conclusion</b>	<b>188</b>



Contents

<b>Bibliography</b>	<b>192</b>
<b>A Converter Parameters</b>	<b>213</b>
<b>B Chapter 3 Figures</b>	<b>216</b>
<b>C Chapter 4 Figures</b>	<b>218</b>
<b>D Chapter 5 Figures</b>	<b>220</b>
<b>E Wind Farm Parameters</b>	<b>222</b>

# List of Figures

2.1	GFL Control Diagram . . . . .	28
2.2	GFL Control Diagram with NSC . . . . .	30
2.3	Droop Control Outer Loop Diagram . . . . .	32
2.4	Inertia Emulation Control Outer Loop Diagram . . . . .	33
2.5	Grid-forming Droop Control Diagram . . . . .	35
2.6	Simplified VSM Structure with Current Control . . . . .	37
2.7	Synchronous Machine Closed Loop Function . . . . .	38
2.8	Virtual Synchronous Machine Closed Loop Function . . . . .	39
2.9	VSM Structure . . . . .	40
2.10	Simplified Type-4 Turbine Diagram . . . . .	42
2.11	Generator Control Structure . . . . .	44
2.12	General Linearised Small-signal Model of GFL Controllers . . . . .	46
2.13	General Linearised Small-signal Model of GFM Controllers . . . . .	47
3.1	PVCC Admittance Model Verification . . . . .	59
3.2	PVCCI Admittance Model Verification . . . . .	60
3.3	PVCCD Admittance Model Verification . . . . .	61
3.4	GFMD Admittance Model Verification . . . . .	61
3.5	VSMCC Admittance Model Verification . . . . .	62
3.6	VSM Admittance Model Verification . . . . .	63
3.7	Current Control Equivalent Converter Admittance in the SRF . . . . .	64
3.8	Current Control Equivalent Converter Admittance in the Sequence Frame . . . . .	66

List of Figures

3.9	Validation of Negative Sequence Controllers in the Sequence Frame (solid blue: Time domain frequency sweep)(Dashed orange: Small-signal admittance) . . . . .	67
3.10	Current Control Equivalent Converter Admittance in the Sequence Frame	68
3.11	Current Control Equivalent Converter Admittance in the Sequence Frame	69
3.12	Comparison of SISO gain margins for CC (a) SRF (b) sequence frame .	71
3.13	Application of SISO dq and pn phase margins to (a) CC + PLL (b) CC +VC (c) CC + PC (d) CC + NSC (e) Full Control . . . . .	72
3.14	Application of SISO dq and pn phase margins to (a) CC (b) CC +PLL (c) CC + VC (d) CC + PC 1st Loci (e) CC + PC 2nd Loci (f) CC + NSC 1st Loci (g) CC + NSC 2nd Loci (h) Full . . . . .	75
3.15	Comparison of LAT and ML disk margins for CC system . . . . .	79
3.16	Comparison of LAT and ML disk margins for (a) CC + PLL (b) CC + VC (c) CC + PC 1st loci (d) CC + PC 2nd loci (e) CC + NSC (f) Full Control . . . . .	80
3.17	Comparison of Diagonal Dominance of Controllers for Varying Operating Point at SCR = 2 . . . . .	82
4.1	Source and Load Subsystem Representation . . . . .	85
4.2	Multi-converter system diagram . . . . .	93
4.3	Multi-converter system diagram . . . . .	97
4.4	Norton Equivalent Circuit for Multi-converter system . . . . .	98
4.5	Robustness Measure for Common Mode Converter Combination at 0 p.u. active power . . . . .	102
4.6	Robustness Measure for Common Mode Converter Combination at 0.5 p.u. active power . . . . .	104
4.7	Robustness Measure for Converter 1 Differential Mode at 0 p.u. active power . . . . .	105
4.8	Robustness Measure for Converter 1 Differential Mode at 0.5 p.u. active power . . . . .	107

## List of Figures

4.9	Robustness Measure for Converter 2 Differential Mode at 0 p.u. active power . . . . .	109
4.10	Robustness Measure for Converter 2 Differential Mode at 0.5 p.u. active power . . . . .	110
5.1	GFL and GFM connected to network . . . . .	127
5.2	GFM system point of view . . . . .	128
5.3	GFL system point of view . . . . .	128
5.4	GSIM for configurations: (a) $Y_{sys1}$ - SCR 1 (b) $Y_{sys1}$ -SCR 3 (c) $Y_{sys2}$ -SCR 1 (d) $Y_{sys2}$ -SCR 3 (e) $Y_{sys3}$ -SCR 1 (f) $Y_{sys3}$ -SCR 3 . . . . .	132
5.5	GSIM at power limit for configurations: (a) $Y_{sys1}$ - SCR 1 (b) $Y_{sys1}$ -SCR 3 (c) $Y_{sys2}$ -SCR 1 (d) $Y_{sys2}$ -SCR 3 (e) $Y_{sys3}$ -SCR 1 (f) $Y_{sys3}$ -SCR 3 . . . . .	137
5.6	GSIM for Two Converter System at 0 p.u. active power . . . . .	140
5.7	GSIM for Two Converter System at 0.5 p.u. active power . . . . .	142
5.8	Comparison of GSIM for Controller Combinations Varying Reactive Droop Gain at 0.5 pu SCR = 2 . . . . .	143
5.9	Comparison of Common Mode Robustness for Controller Combinations Varying Reactive Droop Gain at 0.5 pu SCR = 2 . . . . .	144
5.10	Comparison of Differential Mode Robustness for Controller Combinations Varying Reactive Droop Gain at 0.5 pu SCR = 2 . . . . .	145
5.11	Comparison of Frequency Dependent GSIM for Controller Combinations 0 pu SCR = 2 . . . . .	147
5.12	Comparison of Frequency Dependent GSIM for Controller Combinations 0.5 pu SCR = 2 . . . . .	149
5.13	Comparison of Frequency Dependent GSIM for Controller Combinations 1 pu SCR = 4 . . . . .	151
5.14	Comparison of Reactive Droop Gain using GSIM for Controller Combinations 0.5 pu SCR = 2 . . . . .	152
5.15	Comparison of Reactive Droop Gain using GSIM for Controller Combinations 0.5 pu SCR = 2 . . . . .	153

List of Figures

5.16 Comparison of Reactive Droop Gain on CM Robustness for Controller Combinations 0.5 pu SCR = 2 . . . . .	154
5.17 Comparison of Voltage Control Gains using GSIM for Controller Combinations 0.5 pu SCR = 2 . . . . .	155
5.18 Comparison of Voltage Control Gains on CM Robustness for Controller Combinations 0.5 pu SCR = 2 . . . . .	156
6.1 Step response comparing generator side DC link voltage controller tunings	161
6.2 Bode plot comparing generator side DC link voltage controller tunings .	162
6.3 Bode plot showing effect of DC link controller bandwidth on VSM frequency response . . . . .	163
6.4 Step response showing effect of DC link controller bandwidth on VSM frequency response . . . . .	164
6.5 Bode plot showing effect of DC link controller bandwidth on PVCCI frequency response . . . . .	165
6.6 Current Control Equivalent Converter Admittance in the Sequence Frame	166
6.7 Example model of programmable wind farm . . . . .	172
6.8 Disk Margin and GSIM Different Penetrations of GFM Turbine at 0.5 p.u. active power . . . . .	180
6.9 Disk Margin and GSIM Different Penetrations of GFM Turbine at 0 p.u. active power . . . . .	182
6.10 Disk Margin and GSIM Different Penetrations of GFM Turbine at 0 p.u. active power . . . . .	183
6.11 Disk Margin and GSIM Different Penetrations of GFM Turbine at 0 p.u. active power . . . . .	184
6.12 First Eigenloci for Critical Penetration with 100 km Line Connection . .	185
6.13 First Eigenloci for Optimal Penetration with 100 km Line Connection .	186
6.14 Second Eigenloci for Optimal Penetration with 100 km Line Connection	187
B.1 Comparison of Diagonal Dominance of Controllers for Varying Operating Point at SCR = 4 . . . . .	216

List of Figures

B.2	Comparison of Diagonal Dominance of Controllers for Varying Operating Point at SCR = 6 . . . . .	217
C.1	Robustness Measure for Converter 1 Differential Mode at 1 p.u. active power . . . . .	218
C.2	Robustness Measure for Converter 2 Differential Mode at 1 p.u. active power . . . . .	219
D.1	GSIM for Two Converter System at 1 p.u. active power . . . . .	220
D.2	Comparison of Frequency Dependent GSIM for Controller Combinations 1 pu SCR = 2 . . . . .	221

# List of Tables

3.1	Comparison of SISO gain margins for controllers . . . . .	70
3.2	Percentage error for SISO gain margins . . . . .	73
3.3	Comparison of SISO phase margins for controllers . . . . .	73
3.4	Percentage error for SISO phase margins . . . . .	76
3.5	Comparison of Loop-at-a-time disk margins for controllers . . . . .	77
3.6	Comparison of Multi-loop disk margins for controllers . . . . .	78
4.1	Summary of Stability Modes . . . . .	101
4.2	Summary of Controller Acronyms . . . . .	101
5.1	Comparison of grid-strength metrics . . . . .	131
5.2	Comparing GSIM to MIMO Stability Margins . . . . .	134
5.3	Voltage Disturbance Ratios . . . . .	135
5.4	Comparing GSIM to MIMO Stability Margins . . . . .	138
6.1	Single Line GFM Investigations, Red = GFL, Green = GFM . . . . .	173
6.2	Single Line, 2 GFM Turbine Investigation, Red = GFL, Green = GFM	175
6.3	Single Line, 3 GFM Turbine Investigation, Red = GFL, Green = GFM	176
6.4	Single Line, 4 GFM Turbine Investigation, Red = GFL, Green = GFM	177
6.5	2 Line GFM Turbine Investigation, Red = GFL, Green = GFM . . . . .	178
A.1	Common Converter Parameters . . . . .	213
A.2	PVCC Parameters . . . . .	213
A.3	PVCCI Parameters . . . . .	214

List of Tables

A.4	PVCCD Parameters . . . . .	214
A.5	GFMD Parameters . . . . .	214
A.6	VSMCC Parameters . . . . .	215
A.7	VSM Parameters . . . . .	215
E.1	Wind Farm Parameters . . . . .	222



# List of Abbreviations

AC	Alternating-Current.
AVR	Automatic Voltage Regulator.
CB	Crossing Boundaries.
CC	Current Control.
CSCR	Composite Short Circuit Ratio.
D	Denominator.
DC	Direct-Current.
DD	Diagonally Dominant.
DFIG	Doubly Fed Induction Generator.
DG	Distributed Generation.
ESCR	Equivalent Circuit Short Circuit Ratio.
ESS	Energy Storage Solution.
FF	Fundamental Frequency.
FLL	Frequency Locked Loop.
FRC	Fully Rated Converter.
FRT	Fault Ride Through.
GBC	Generalised Bode Criterion.
GFL	Grid-following Converter.

## List of Abbreviations

GFM	Grid-Forming Converter.
GFMD	Grid-Forming Droop Controller.
GNC	Generalised Nyquist Criterion.
GS	Grid-Supporting Converter.
GSC	Grid-Side Converter.
GSIM	Grid Strength Impedance Metric.
HVAC	High-Voltage Alternating-Current.
HVDC	High-Voltage Direct-Current.
HVT	High Voltage Transformer.
I/O	Input/Output.
IBR	Inverter Based Resource.
LAT	Loop-at-a-Time.
LHP	Left-Hand Plane.
LPF	Low Pass Filter.
MFD	Mirror Frequency Decoupled.
MIMO	Multiple-Input Multiple-Output.
ML	Multi-Loop.
MMC	Modular Multi-Level Converter.
MSC	Machine-Side Converter.
MTTF	Mean Time to Failure.
MVT	Medium Voltage Transformer.
N	Numerator.
NMP	Non-minimum Phase.
NREL	National Renewable Energy Laboratory.
NSC	Negative Sequence Control.

## List of Abbreviations

PC	Power Control.
PCC	Point of Common Coupling.
PI	Proportional-Integral.
PLL	Phase-locked Loop.
PMSG	Permanent Magnet Synchronous Generator.
PoV	Point of View.
PSC	Power Synchronising Control.
PSS	Power System Stabiliser.
PVCC	Power Voltage Current Controller.
PVCCD	Power Voltage Current Controller with Droop.
PVCCI	Power Voltage Current Controller with Inertia Emulation.
PVCCN	Power Voltage Current Controller with Negative Sequence Regulation.
PWM	Pulse Width Modulation.
RES	Renewable Energy System.
RHP	Right-Half Plane.
RMS	Root Mean Square.
RoCoF	Rate of Change of Frequency.
SCL	Short-Circuit Level.
SCR	Short-Circuit Ratio.
SCRIF	Short Circuit Ratio with Interaction Factors.
SG	Synchronous Generator.
SISO	Single-Input Single-Output.
SO	System Operator.
SRF	Synchronous Reference Frame.

## List of Abbreviations

SSO	Sub-synchronous Oscillation.
TL	Transmission Line.
TR1	Transmission Line 1.
TR2	Transmission Line 2.
VC	Voltage Control.
VSC	Voltage Source Converter.
VSM	Virtual Synchronous Machine.
VSMCC	Virtual Synchronous Machine with Current Control.
WSCR	Weighted Short Circuit Ratio.

# List of Symbols

$\alpha_{cc}$	Current Controller Tuning Time Constant.
$L_b$	Scalar Base Inductance.
$R_b$	Scalar Base Resistance.
$Z_b$	Scalar Base Impedance.
$C^-$	Crossings of 180 degrees from above.
$C^+$	Crossings of 180 degrees from below.
$CSC_{MVA}$	Fault Level Contribution Excluding Converters.
$MW_{VER}$	Sum of Connected Converter Nominal Power Ratings.
$P_{RMW_i}$	Rated Power Output of $i$ th Converter.
$SCMVA_i$	Short Circuit Capacity at Bus $i$ .
$D$	Machine Damping.
$\alpha$	Disk Margin Limit.
$D(\alpha, \sigma)$	Complex Set of Perturbations for Disk Margin.
$\zeta$	Damping Factor.
$i_{DC}$	DC Link Current.
$v_{DC}^*$	DC Link Voltage Setpoint.

## List of Symbols

$v_{DC}$	DC Link Voltage.
$\sigma$	Disk Margin Skew Factor.
$f$	Disk Margin Multiplicative Factor.
$i_{d,g}$	Generator d-axis Stator Current.
$i_{q,g}$	Generator q-axis Stator Current.
$J_{gen}$	Generator Inertia.
$\lambda$	Generator Flux Linkage.
$p$	Generator Pole Pairs.
$\tau_e$	Generator Electromagnetic Torque.
$\tau_{gen}$	Generator Torque.
$v_{d,g}$	Generator d-axis Stator Voltage.
$v_{q,g}$	Generator q-axis Stator Voltage.
$\omega_{gen}$	Generator Speed.
$GM$	Gain Margin.
$G_{c,dd}^-$	dd negative sequence SRF Component.
$G_{c,dq}^-$	dq negative sequence SRF Component.
$G_{c,qd}^-$	qd negative sequence SRF Component.
$G_{c,qq}^-$	qq negative sequence SRF Component.
$H$	Inertia Constant.
$i_{d,cc}$	d-axis Converter Current Cross-Coupling.
$i_{q,cc}$	q-axis Converter Current Cross-Coupling.
$i_d$	Converter d-axis Current.
$i_q$	Converter q-axis Current.
$IF_{ij}$	Interaction Factor of Bus j on Bus i.
$P_i$	Power Rating at Bus i.
$P_j$	Power Rating at Bus j.

## List of Symbols

$S_j$	Fault Level Contribution at Bus i.
$\Delta V_i$	Voltage Deviation at Bus i.
$\Delta V_j$	Voltage Deviation at Bus j.
$J$	Machine Inertia.
$K_{i,ncc}$	NSC Integral Gain.
$K_{p,ncc}$	NSC Proportional Gain.
$K_{i,cc}$	Current Controller Integral Gain.
$K_{p,cc}$	Current Controller Proportional Gain.
$K_{i,DC}$	DC Link Voltage Control Integral Gain.
$K_{p,DC}$	DC Link Voltage Control Proportional Gain.
$K_{gm}$	Gain Margin Mathematical Gain.
$K_{inert}$	Inertia Emulation Constant.
$k_m$	Machine Design Constant.
$K_{i,pll}$	PLL Integral Gain.
$K_{p,pll}$	PLL Proportional Gain.
$K_{i,P}$	Power Controller Integral Gain.
$K_{p,P}$	Power Controller Proportional Gain.
$K_{i,U}$	Voltage Controller Integral Gain.
$K_{p,U}$	Voltage Controller Proportional Gain.
$k_{i,vsm}$	VSM Integral Gain.
$k_{p,vsm}$	VSM Proportional Gain.
$L_f$	Converter Filter Inductance.
$L_{s,d}$	Generator d-axis Stator Inductance.
$L_{s,q}$	Generator q-axis Stator Inductance.
$L_{tf}$	Transformer Inductance.
$L_{tr}$	Transmission Line Inductance.

## List of Symbols

$\mathbf{I}_{c,qd}$	Converter qd Current Matrix.
$\mathbf{I}_{C1,qd}$	Converter 1 qd Current Matrix.
$\mathbf{I}_{C2,qd}$	Converter 2 qd Current Matrix.
$\mathbf{I}_{PCC,qd}$	PCC qd Current Matrix.
$\lambda(\mathbf{Y}_{sys}(s))$	Eigenvalues of System Amittance Matrix.
$\lambda(\mathbf{Z}_b(s))$	Eigenvalues of Base Impedance Matrix.
$\mathbf{V}_{g,qd}$	Grid qd Voltage Matrix.
$\mathbf{V}_{v,qd}$	VSM qd Voltage Matrix.
$\mathbf{Y}_{c,qd}$	Converter qd Admittance Matrix.
$\mathbf{Y}_{C1,qd}$	Converter 1 qd Admittance Matrix.
$\mathbf{Y}_{C2,qd}$	Converter 2 qd Admittance Matrix.
$\mathbf{Y}_{g,qd}$	Grid qd Admittance Matrix.
$\mathbf{Y}_{sys}(s)$	System Amittance Matrix.
$\mathbf{Y}_{p,qd}$	Parallel Admittance Matrix.
$\mathbf{Y}_{sys}(s)$	System Amittance Matrix.
$\mathbf{Y}_{v,qd}$	VSM qd Admittance Matrix.
$\mathbf{Z}_{b,qd}$	Base Impedance Matrix.
$\mathbf{Z}_{b,e}$	Example Base Impedance Matrix.
$\mathbf{Z}_{p,qd}$	Parallel Impedance Matrix.
$\mathbf{Z}_{sys,e}$	Example System Impedance Matrix.
$\mathbf{I}_c$	MIMO Converter Current.
$\mathbf{A}$	Model State Matrix.
$\lambda_{ss}$	Eigenvalues of Model State Matrix.
$\mathbf{U}_{pcc}$	MIMO PCC Voltage.
$N_c^-$	Counter Clockwise Encirclements.
$N_c^+$	Clockwise Encirclements.
$\mathbf{x}_{c,qd}^+$	Negative Sequence SRF Components.
$P$	Transfer Function Poles.



## List of Symbols

$PM$	Phase Margin.
$P_e$	Machine Electrical Power.
$P_m$	Machine Mechanical Power.
$P^*$	Power Setpoint.
$P_{GSC}$	Grid-Side Converter Power.
$P_{MSC}$	Machine Side Converter Power.
$Q$	Notch Filter Quality Factor.
$R_f$	Converter Filter Resistance.
$R_s$	Generator Stator Resistance.
$R_{tf}$	Transformer Resistance.
$R_{tr}$	Transmission Line Resistance.
$R/X$	Ratio of Resistance to Reactance.
$C_{scale}$	GFL Scaling Factor.
$GC_{scale}$	Network Scaling Factor for GFL.
$GV_{scale}$	Network Scaling Factor for GFM.
$s_n$	nth Scaling Factor.
$V_{scale}$	GFM Scaling Factor.
$c$	Shaft Damping Factor.
$\gamma$	Shaft Twist Angle.
$k_{dt}$	Shaft Stiffness.
$k_{dtd}$	Drivetrain Damping Control Gain.
$\omega_{dt}$	Drivetrain First Eigenfrequency.
$S_{rated}$	Machine Rated Power.
$\theta_m$	Machine Angle.
$\theta_{pll}$	PLL Angle Output.
$\tau_{if}$	Inertia Emulation Filter Time Constant.

## List of Symbols

$\tau_{meas}$	Measurement Filter Time Constant.
$\tau_{nf}$	Negative Sequence Voltage Feedforward Time Constant.
$\tau_P$	Grid-Forming Active Power Filter Time Constant.
$\tau_{Pade}$	Padé Time Constant.
$\tau_{pf}$	Power Loop Filter Time Constant.
$\tau_Q$	Grid-Forming Reactive Power Filter Time Constant.
$\tau_V$	Grid-Forming Voltage Filter Constant.
$\tau_{vf}$	Voltage Loop Filter Time Constant.
$\tau_{vff}$	Voltage Feedforward Time Constant.
$J_t$	Turbine Inertia.
$\tau_t$	Turbine Torque.
$\omega_t$	Turbine Speed.
$u_d$	d-axis PCC Voltage.
$u_q$	q-axis PCC Voltage.
$\omega$	Machine Speed.
$\omega_b$	Base Frequency.
$\omega_g$	Nominal Grid Frequency.
$\omega_n$	Undamped Natural Frequency.
$x_d$	d-axis Component of Variable.
$x_{d,n}$	d-axis Negative Sequence Component of Variable.
$x_{d,pn}$	Park Transformed d-axis Negative Sequence Component of Variable.

## List of Symbols

$x_{d,p}$	Park Transformed d-axis Component of Variable.
$x_q$	q-axis Component of Variable.
$x_{q,n}$	q-axis Negative Sequence Component of Variable.
$x_{q,pn}$	Park Transformed q-axis Negative Sequence Component of Variable.
$x_{q,p}$	Park Transformed q-axis Component of Variable.
$Y_c$	Converter Admittance.
$Y_{dd,c}$	dd Admittance Component.
$Y_{dq,c}$	dq Admittance Component.
$Y_{qd,c}$	qd Admittance Component.
$Y_{qq,c}$	qq Admittance Component.
$Y_{nn}$	nn Admittance Component.
$Y_{np}$	np Admittance Component.
$Y_{pn}$	pn Admittance Component.
$Y_{pp}$	pp Admittance Component.
$Y_{sys,pu}$	Per-unit System Admittance.
$Z$	Transfer Function Zeros.
$Z_c$	Converter Impedance.
$Z_g$	Grid Impedance.
$Z_{sys,pu}$	Per-unit System Impedance.

# Acknowledgements

Firstly, I would like to express my gratitude to my supervisors, Agusti Egea-Alvarez, Derrick Holliday and Lie Xu. Their guidance and support throughout my research has been invaluable. The many long discussions have allowed me to gain a deeper understanding than any textbook or research paper could provide. I would also like to thank my supervisor on academic secondment at DTU, Guangya Yang. His fresh perspective and knowledge allowed me to further develop my own ideas to a point I did not think possible. I would like to acknowledge my industrial sponsor Siemens Gamesa Renewable Energy and specifically Paul Brogan who provided insights that helped to shape the research plan and Thyge Kneuppel whose guidance and support during my time in Denmark was greatly appreciated. A final thank you goes out to my family and friends who have provided fantastic support throughout the years of my study.

# Chapter 1

## Introduction

Climate change has led to decarbonisation of electrical generation in the strive for cleaner renewable energy and caused a paradigm shift in the way electrical networks are operated and studied [1]. Largely due to increasing social and political influences, more renewable energy systems (RES) are being connected to the network phasing out old, synchronous coal and oil power stations at a rapid rate [2]. RES were responsible for 37.8 % of the total UK energy generation as of Q1 2022 [3] and wind energy is the fastest growing renewable technology forming a large proportion of energy generation in Europe [4]. Numerous RES, including a significant percentage of wind farms are connected to the network via power electronic converters and known as inverter based resources (IBRs). These provide increased flexibility and control but also new challenges in maintaining stability of the network [5–7].

A number of studies have suggested that the system may become unstable when IBR penetration surpasses a certain threshold if standard converter control techniques are not updated to support the modern network [8]. Couple this with electrical demand rising at unprecedented rates due to the electrification of heat, transport and industry, the need for new analysis techniques capable of representing all interactions of the modern network becomes increasingly evident. This thesis explores new methods of analysing such converter dominated networks, proposing new stability and screening techniques similar to the traditional short-circuit ratio (SCR) but capable of accurately representing the future generation mix.

The opinion of academia and industry has long been that grid-forming (GFM) structures increase the system strength and hence stability in locations where they are deployed. However, quantitative verification of this has avoided significant attention and could offer a promising metric for determining the balance of GFM penetration on the network. The approaches designed for for wind park applications utilise the equivalent converter output impedance to accurately represent modern control action and other legacy equipment on the network. These techniques are utilised to investigate interactions within a full scale wind farm with the final goal of determining the optimal penetration and placement of GFM converters within the wind park and what factors affect this result. Moreover, what GFM structure provides the greatest benefit to system operation, which grid-following (GFL) structures provide the largest detriment and can the GFL structures be enhanced and tuned to provide some much needed security and stability the the future network with pre-existing assets.

The modelling approach applied is highly modular allowing various wind farm architectures in terms of transmission lines, array cables, turbine effects and control actions to be investigated. The main findings suggest that GFM converters do improve the system strength and stability when they are deployed but there are limits and increasing strength too far can be detrimental to overall system stability. While the main focus is wind farm applications, the techniques proposed are applicable to any IBR providing an impedance trace can be obtained.

## 1.1 Challenges of a Converter Dominated Network

The challenges of the modern network are often explored in the context of two main categories. Firstly, how will the increasing number of IBRs impact the network in terms of design, governability and protection and how can the modern system be adequately analysed to identify these issues. Secondly, what is the result in removing synchronous generators (SGs) with heavy, spinning masses masses from the network that have been the topic of intense study for decades. Hence, the numerous problems associated with SGs are well understood and therefore, they provide a sense of security and stability

to network operation.

The mechanical structure of these machines provides inertia and damping and through appropriate design and tuning can increase the frequency and voltage stability of system. The electrical design of the machines provides voltage source behaviour enhancing the system strength and voltage stability of the network. When this behaviour is removed, the onus falls to IBRs to support the network requiring the design and testing of novel control structures that fit this purpose. The main challenges facing the modern network are cited in [9] as: increased rate of change of frequency (RoCoF), loss of synchronising torque and reference voltage, high frequency instability and controller interaction, difficulty modelling RMS models, reduced and delayed fault infeed current during or post fault voltage instability, sub-synchronous oscillations (SSO), increased load imbalance and harmonic sensitivity. These issues were organised in to eight key challenges from a system operators (SO) perspective [10]:

1. Inertia and Frequency Stability
2. System Strength and Voltage Stability
3. Disturbance Ride-Through
4. Adverse System Interaction
5. Protection System Impact
6. Contingency Frequency Control During Islanding Conditions
7. Initiate/Support System Restoration
8. Accurate and Fast Simulation Models

Islanded conditions and system restoration are not a focus of this work and are not explored further.

### **1.1.1 Inertia and Frequency Stability**

The reduction of system inertia has been considered as one of the key factors that may endanger system stability [7, 11, 12]. Having large, heavy spinning masses connected

to the network is beneficial as they provide significant inertia and damping to smooth large power deviations. However, the UK network may see as large as 40 % reduction in inertia by 2025 [13]. Remedial action, such as inertia and enhanced frequency response from unconventional sources such as batteries [14], electric vehicles [15, 16] and wind turbines [17, 18] has been suggested. The goal of these systems is to support the network in the minutes directly following a frequency event with inertia slowing the initial RoCoF in the first few seconds to allow time for the primary frequency response to activate. The primary frequency response follows this and is used to provide time for secondary and tertiary frequency responses to activate, normally in the form of setpoint changes. Several researchers have suggested that the provision of inertia from converter-based systems might be beneficial for the power system [19] but current control, the most popular type of GFL converter control for the integration of renewable power into the grid, cannot support this service at present.

Several approaches have been suggested to facilitate a response from IBRs during a frequency event such as adding an inertia loop to a standard current controller [18] or a new type of converter control known as GFM [20]. An issue common to both families is obtaining the required energy to provide a response [21]. Most IBRs utilise all the available energy for feeding into the grid. Therefore, when a frequency imbalance occurs there is no extra energy to provide a response. Curtailment has been suggested as a possible remedy to allow the IBR headroom to respond if needed [22, 23]. This is likely inefficient and wasteful as large scale frequency response is not required often. A second option, specifically related to wind farms that has experienced real-world testing is to extract kinetic energy from the spinning turbine [24]. This approach offers some useful behaviour in terms of power smoothing but does not provide enough energy to react to large scale events. Moreover, restoring the speed of the turbine post event may cause further frequency stability issues if not managed appropriately. Furthermore, linking the mechanical drivetrain to the electrical network may result in unwanted propagation of oscillations between the two. The more realistic option is to consider energy storage, normally in the form of batteries. This allow utilisation of otherwise wasted energy that can be fed into the grid as virtual inertia when required. However,



if the battery storage is designed to provide inertia, essentially mimicking the behaviour of a SG, similar lower frequency mechanical oscillations may remain despite the lack of mechanical components. In reality, these interactions stem from the control structure and new methods of representing this control action on the network are required.

Interestingly, the terms 'synthetic inertia', 'virtual inertia' and 'inherent inertia' are used with a degree of ambiguity in literature [9]. In general, synthetic inertia is viewed as an adaptation of the power loop in the standard current controller, with a RoCoF measurement and an inertia constant based on the swing equation. However, this is an emulation of the swing equation, the synchronisation of the converter is still achieved via phase-locked loop (PLL). This provides a fast frequency response but may not be fast enough to replace traditional mechanical inertia while remaining stable. Inherent inertia is provided by synchronous machines as it occurs due to the physical composition of the machine. However, it also tends to be thought of as inertia provided via the emulation of synchronous machine behaviour or synchronisation via the power synchronising loop. This is due to the inertia not forming part of an augmented control loop but instead constitutes a core part of the synchronisation algorithm.

Inherent inertia from converters occurs to slow action of the control structure. When a network change is observed the converter acts slowly to correct the error and the mismatch between network and converter voltage constitutes inherent inertia. When responding, the converter exhibits behaviour more similar to that of a voltage source rather than the conventional current source behaviour that is widely accepted. When the network angle deviates, a converter with inherent inertia will now follow the angle quickly, instead a delay is observed and the resultant current flow resulting from the angle mismatch is the inertia delivered to the network. This is likely the most accurate representation of the mechanical inertia connected to the traditional network. Virtual inertia lies somewhere in the middle of these terms and is perhaps used in the most ambiguous manner throughout literature.

### 1.1.2 System Strength and Voltage Stability

While inertia and frequency stability is of great importance, the voltage stability of the network including converters employing different frequency regulating algorithms has avoided significant attention. Traditionally, literature has stated that synchronous generation plays a crucial role in maintaining voltage stability by contributing to fault level [25]. When removed, the fault current is reduced as IBRs are limited in providing increased current beyond limits by the thermal capacity of the power electronic devices. Moreover, removing parallel SGs and adding distributed generation connected electrically distant increases the impedance seen from a fault and further contributes to reduced fault level. The reduction in fault current increases the likelihood of voltage instability and possible voltage collapse on the system [26].

However, this is likely not the case for the modern network where fault current and system strength cannot be considered as a single entity. The operation of the system during faults is directly related to how much fault current can be provided as this governs the protections. The system strength during normal operation is determined by the electrical distance to a stiff voltage source. Since the fault current in the conventional network is determined via the physical impedances on the network, the two are linked. IBRs do useful work in maintaining voltage stability and providing system strength that is not reflected in the fault current contribution or the physical impedances. Hence, fault current and system strength are no longer linked in the modern network and new techniques are required to analyse the normal operation of the network outwith faults.

High impedance or systems with low strength, known as weak grids have received significant attention in literature as they offer higher risk of adverse interactions leading to voltage instability [27]. This is mainly due to the increased impedance offering a greater electrical distance to a stiff voltage source which results in poorer damping of unwanted oscillations. One further issue with weak grids is the non-linear coupling between active power and voltage when transmitting through a high impedance line [15]. This requires control structures to be fitted with augmented control loops to aid operation in these systems [28]. However, this only deals with voltage deviations

during changes in active power flow. It does not allow the converter to contribute to removing the increased voltage oscillations associated with the poor damping provided in weak network [29]. The stability of these systems considering the connection of more advanced control structures looking to mitigate the challenges caused by reduced system strength is of key concern. New methods of modelling and analysis will be required to accurately represent both the positive and negative behaviour of various control structures in terms of voltage stability and system strength.

Impedance-based stability analysis has been widely applied for traditional GFL structures and provides a reliable method of analysing complex inter-system interactions related to voltage stability. However, model complexity is often lacking, utilising current controllers with complex functions disabled to facilitate easier analysis [30,31]. With more large power sources and loads becoming converter interfaced, grid conditions can vary rapidly and it is important that the remaining converters have the robustness to stay connected. The most recent work involves modelling of more complex control systems including negative sequence control (NSC), power and voltage control [32,33], power synchronising control [34] and synchronous machine emulation [35]. However, analysis of wider converter dominated networks employing these advanced control algorithms is lacking. These systems present unique challenges in terms of analysis by reducing the symmetry of frequency responses in different reference frames and hence, previous impedance based stability techniques may not be valid as converter control structures become further advanced.

Furthermore, impedance based methods rely heavily on the point of view (PoV) of the studied system or where the network is 'cut'. Applying complex stability techniques to large systems can be time consuming and computationally demanding. Moreover, a significant proportion of the PoVs will offer no stability concerns. SCR has been used in this manner to classify system strength in traditional networks and identify locations that may pose problems. However, SCR cannot accurately represent the behaviour of converters providing enhanced grid services as control action is not accounted for [36]. Moreover, new indices looking to study the strength of the modern system continue to fail in using a proper description of converters during analysis. Most methods focus on

fault current procurement over other voltage stability concerns associated with weak networks. It is therefore important to develop new methods for screening stability issues to offer fast and accurate determination of problematic system locations including all control interactions.

### 1.1.3 Disturbance Ride-Through and Protection System Impact

As discussed, it is becoming crucial in the modern network to disseminate between system strength and disturbance ride-through. Converters can contribute in various ways to system strength depending on the control topology selected [29]. However, all converters are limited by hardware in provided assistance during low-voltage ride through. Overcurrent protections will prevent the converter from reaching above 1.1 - 1.2 p.u. current in most cases unless significant headroom is installed. Unfortunately, the general approach in converter design is to utilise all available power capability as reserving capacity for fault current provision is inefficient and costly. While most converters cannot contribute readily during faults, systems will be required to allow them to ride through these problems.

The network will still require adequate protections as reduced fault current has been reported to cause issues with the operation of distance relays [37]. This effect was also reported by Li et al. in [38] which looked at the performance of distance relays under varying degrees of converter penetration. Problems specific to Type IV wind turbines were explored by Roy et al. in [39] with similar findings claiming that low fault current and poor procurement of negative and zero sequence currents caused a detriment to the performance of the relays used. However, [37] does claim that IBRs offer unmatched flexibility in controlling fault current and could be a major advantage for IBRs to respond to unbalanced faults. Nevertheless, the reduction of fault current will still remain an issue and other sources such as synchronous condensers should be utilised to maintain the fault level [40]. Moreover, IBRs should not be judged on the inability to procure fault current when they can provide useful behaviour to aid the system in other ways. In reality, this is a purely hardware related issue which relates to efficiencies and costs. The headroom created for fault current could also be utilised

for inertia and frequency support. The correct market for enhanced grid services could provide incentive to build extra headroom into the IBRs to provide these services [41].

#### 1.1.4 Adverse System Interaction and Accurate Simulation Models

Adverse network interactions have been experienced in the traditional network for decades. Hence, they are well understood and multiple systems are in place to mitigate the negative effects. However, control interactions are significantly more complex and exist over a wider range of frequencies. What makes these interactions more worrying is that they can be initiated outwith specific operating points or system outages [10]. However, the likelihood of these interactions occurring can be identified in some ways by analysing system strength. As discussed, the way in which system strength requires updating for the modern system. In doing this, adverse reactions in converter dominated system may become identifiable. It is possible the reason that interactions tend to appear from nowhere is because the rating of strength used is not appropriately defining the system [29,36]. These problems stem for the lack of appropriate representation of converter behaviour into the network.

Simplified power converter models may lead to inaccurate stability assessments when trying to reduce computational burden. In some cases, networks are modelled using single-input single-output (SISO) impedances or utilise transformations so that systems become diagonally dominant and can be analysed in a loop-at-a-time method [42–45]. In these cases, traditional stability techniques and margins can be applied with confidence. However, a proper system description requires multiple-input multiple-output (MIMO) impedances to account for channel interactions which is a topic of current research [46,47]. In some cases, these impedances can be diagonally dominant which simplifies analysis. Additionally, work has been completed in [48] to transform a system that exhibits channel interactions in the dq-frame to a diagonally dominant system in the sequence frame. Stability of these system can often produce misleading results. For example, the system may be correctly labelled as stable but at the wrong point e.g., a pole is closer to the unstable region than originally thought. The stability definition is correct but the stability margins will be significantly different which could

cause issue for further analysis with more components. If a diagonally dominant system is not possible, gain and phase margins can be misleading as simultaneous variations can occur significantly reducing the safety net [49]. Hence, accurate modelling methods and analysis techniques are required to properly describe the modern network.

## 1.2 The Role of Wind Energy in Achieving Net-Zero

Wind energy is the largest and fastest growing renewable energy technology in the UK at the time of writing [4]. The combined onshore and offshore wind capacity of the UK was 28.5 GW in Q3 2022, representing 54.15 % of the entire installed renewable capacity. This also represents a 12.3 % increase in total installed wind capacity since Q3 2021 and a massive 25 % increase within offshore wind alone. Moreover, wind power is being further utilised with a 41.4 % and 25 % increase in electrical generation from onshore and offshore wind, respectively from Q3 2021 to Q3 2022. The growth has been consistent for the past 10 years and looks set to continue with the UK targeting 50 GW of installed wind capacity by 2030. Hence, wind parks could become an important tool in providing the much needed grid services being removed with the loss of traditional synchronous machines.

### 1.2.1 Enhanced Grid Services from Wind Farms

Large wind parks themselves offer a large store of inertia within the combined masses of the spinning turbines, especially in offshore farms where the turbine size is increasing dramatically [50]. These systems tend to employ fully-rated back-to-back converters decoupling the wind turbine dynamics from the network. However, the energy can be harnessed utilising creative control topology to provide inertia and frequency support services as well as voltage stability services. Moreover, energy storage can be fitted to further enhance the capabilities of the control systems without causing harm to the turbine. These topics have been the focus on significant academic literature in previous years [51].

[52] states that both Type I and Type II turbines can provide some form of inertia

or frequency response naturally but the response is somewhat limited. However, Type III and Type IV turbines could offer a promising source of frequency response services despite the lack of natural inertia provision due to the decoupling provided from the converters. Conventional solutions to this can involve reducing the penetration of wind during periods of low load and/or low system inertia. However, this method is likely not viable in the modern network when IBRs represent a significant proportion of connected generation.

One study completed by Gloe et al. investigated how frequency support from wind turbines could have altered the events of a blackout that occurred in Flensburg, Germany in 2019 due to extended islanded operation [53]. It was found that the response from wind turbines could have prevented the disconnection of one genset and restored the system frequency to 50 Hz soon after the initial event. Diaz-Gonzalez et al. conducted a review of the grid code requirements and control methods relating to wind power plants participating in system frequency control in [54]. The work found that some islanded European networks already specify wind turbines should run deloaded from the maximum available output to provide headroom for frequency response. However, stronger grids do not consider this and in most cases only specify for reduction in power due to over-frequency concerns. Different methodologies exist for deloading such as pitching or over-speeding which offer optimal operation at different wind speeds both of which caused enhanced mechanical stress on the turbine.

Work has been completed to consider improved operation from a deloaded converter via the combination of pitch angle and rotor speed control in [55] and claims novelty in utilising the rotor kinetic inertia to contribute to frequency stability more readily. Further control structures aim to provide synthetic inertia which are split into three main categories: RoCoF based response, fixed trajectory response and frequency deviation response [56]. In reality, a number of these systems are somewhat ambiguous with exactly what service is being provided whether that be: synthetic inertia, fast frequency response or regular frequency response. Eriksson et al. claims to provide a definitive definition of synthetic inertia in [57] where synthetic inertia related to the supply of electrical torque in proportion to RoCoF whereas fast frequency response is

based on the frequency deviation which agrees with the definitions from [56]. What is clear however, is the capability of wind energy for providing frequency response services.

In terms of RoCoF response or inertia, control structures can utilise a power command based on the RoCoF provided from the PLL [18, 58]. However, significant issues with obtaining an accurate measure of RoCoF while coping with significant noise from instrumentation reduces the efficacy of these methods. Fixed trajectory responses aim to remedy this by using a frequency measurement to detect an event before following a pre-determine power injection envelope to contribute to the frequency deviation [59]. However, issues with accurately determining events can cause issue and the response can be somewhat conservative.

Droop control based methods are considered as frequency deviation responses and have been explored by Liu et al. which utilise an overspeed based variable frequency droop that considers optimal rotor kinetic energy [60]. The proposed control structure enhanced the frequency regulation capability over conventional over-speed reserve strategies by ensuring all available energy in the rotor was utilised. Another alternative frequency droop scheme was proposed by Boyle et al. which shifts the power tracking curve to facilitate frequency regulation [61]. The proposed method provided fast frequency regulation as well as steady-state regulation which improved the frequency nadir in the conducted tests. Work completed by Mauricio et al. in [62] proposed a communications based approach where the fast response seen from the wind park was communicated to nearby SGs which improved the overall reaction of the system.

One key issue with providing frequency response from wind parks using any method without energy storage is variability of wind. Prakash et al. analysed the frequency support from wind park considering uncertain wind generation [63]. A stochastic scheduling framework was applied to model the frequency support of the turbines which improved the capabilities of the system when operating in uncertain conditions. The method determined that a decreased cost and wind curtailment was observed when providing synthetic inertia and primary frequency response when compared to conventional methods. This suggests that the high variability of wind may not be as harbouring as initially thought when large scale penetration of wind is reached. Since



farms are often located some distance from each other, it is unlikely the entire network will suffer from a complete drop in wind simultaneously.

Grid-forming technology is the latest trend in both academia and industry at present and the latest research involves equipping wind turbines with GFM capabilities [64]. This allows the wind turbines to respond with an inherent inertia response while providing other services such as system strength, enhanced voltage stability as well as islanding and black start capabilities. While this is an enhanced form of operation beyond augmented grid-followers, it is likely the new GFM technologies will exhibit new interactions on the network. Moreover, while trying to emulate SG behaviour the control system may interact with lower frequency mechanical modes in the turbine drivetrain. This problem could be exacerbated in future years as turbine size increases and the resonant frequencies in the drivetrain lower. These systems have seen real world testing at the Dersalloch wind farm in Scotland operated by ScottishPower Renewables [65]. The 23 turbine farm operated for six months in a GFM mode and responded successfully to a number of unscheduled frequency events due to tripping components on the system. One key point to note here is that the wind park was not operated in a curtailed mode and instead the energy was extracted from the turbines. While an important milestone for grid-forming wind farms, further study is required to determine the optimal number of grid-forming turbines within the farm to provide enhanced system stability.

As new control topology continue to emerge, intensive study is required on a wider scale considering realistic wind farms and all possible interactions. Moreover, with new control structures looking to represent the useful behaviour of synchronous machines, unwanted interactions may occur. For example, 'swinging' between wind farms or low-frequency inter-area oscillations which have been reported previously between synchronous machines. This phenomena is well studied for for synchronous generators and is often solved with the use of a power system stabiliser (PSS) [66–68]. However, wind farms offer different challenges due to the range of possible frequencies from various mechanical components such as the tower, blades and drivetrain which all resonate at different frequencies to traditional synchronous machines. Couple this with

the high degree of power variability from the wind and remote connection through long transmission lines and the possibility for low frequency inter-area oscillations increases significantly. Work has been completed utilising Type III wind turbines, to damp inter-area oscillations based on PSS style algorithms [69, 70]. In terms of Type IV turbines, it has been found that the capacitive impedance of these systems can react in weak grids to form SSOs [71]. Shair et al. builds on this in [72], where SSOs are found to be influenced by a number of factors including number and type of turbine, wind speed and control topology used. Both sub and super-synchronous oscillations were observed and concluded that present analysis techniques are not sufficient for accurate study of these interactions.

The massive and ever increasing penetration of wind energy coupled with the versatility of the power converters they utilise to connect to the network makes wind energy one of the most promising sources to supply enhanced grid services in the modern network. However, the interactions that may occur between new GFM devices, enhanced GFL devices and legacy equipment on the network will require accurate modelling and analysis techniques. This thesis proposes new methodologies for analysing converter controllers for wind park applications via the equivalent converter output impedance which accurately represents the behaviour of each of these components.

### 1.3 Objectives and Summary of Work

With the emergence of new converter control structures and the widespread utilisation of wind energy it has become increasingly important to realise new methods of analysing the effect of these wind parks on the modern electricity network. Both detailed stability techniques and faster screening metrics will be required to further facilitate the transition to a cleaner energy system. This thesis proposes both a stability technique and screening metric to allow the analysis of large scale wind parks operating both grid-following and grid-forming control. Multiple converter structures are analysed to determine unique benefits and problems of each. To achieve this impedance modelling is utilised considering the equivalent converter output impedance. The generation of these models from the control structures is provided and mathematical considerations

## Chapter 1. Introduction

of the obtained impedance for different control structures is discussed. Using the constructed impedance models a MIMO generalised stability criterion is proposed that improves over previous techniques by not requiring a specific system description. This allows the system to be accurately studied from different PoVs looking the the common and differential mode contribution of the converter connected generation. A novel screening metric known as the Grid Strength Impedance Metric (GSIM) is proposed to analyse the system strength including converter control action. The proposed methods are used in tandem to analyse two converter systems operating differing control methodologies. The analysis then extends to the interactions of a full wind park operating with 25 3 MW Type IV turbines. The main goal of this study is to determine the optimal penetration and location of GFM turbines within a wind park to enhance system strength and stability.

The objective of the thesis are:

1. Analyse how different control components effect the mathematical composition of the obtained impedance models
2. Investigate the effect of complex converter control structures on stability analysis techniques
3. Develop small-signal stability analysis and screening techniques capable of representing the modern network
4. Employ the techniques to investigate the interactions between GFL and GFM control structures in multi-converter systems
5. Utilise the proposed methodology and rules to investigate interactions between wind turbines, arrays and parks
6. Determine the optimum balance of grid-forming to grid-following turbines within a wind park in terms of stability and system strength

The outline of the thesis is:

## Chapter 1. Introduction

**Chapter 2** Provides an overview of all modelling approaches for converters and control including all systems components and the linearisations required to achieve small-signal models.

**Chapter 3** Presents the methodology for obtaining the equivalent converter output impedances from the small-signal models provided and analyses the effect of controller topology on the shape of the converter output impedance across a range of frequencies with a specific focus on diagonal dominance.

**Chapter 4** Discusses impedance-based stability analysis for single and multi-converter systems employing GFL and GFM structures and proposes a new technique based on eigenvalue analysis capable of achieving new system descriptions avoided in the past

**Chapter 5** Presents an overview of present screening methods based on system strength and the proposal of a new metric, known as the grid strength impedance metric that includes the converter behaviour via the equivalent converter output impedance.

**Chapter 6** Investigates wind park interactions between turbines first focusing on mechanical oscillations that can propagate to the network before utilising the proposed stability and screening methods to determine the optimal penetration of GFM turbine for various lengths of export cable.

**Chapter 7** Summarises the thesis and provides suggestions of future work.

### 1.4 Scientific Contributions

The scientific contributions of the work are as follows:

- A novel method of determining diagonal dominance of MIMO equivalent converter output impedances is proposed. The metric is then employed to determine limits on where traditional SISO stability margins are valid and where more advanced concepts should be applied.
- The impedance-based stability method has been extended to utilise MIMO equivalent converter impedances of GFL and GFM control structures while counteracting identified issues with open loop right half-plane poles and zeros. This differs

from previous approaches as the full-closed loop transfer function is utilised while considering contributions from multiple sources.

- The proposed stability metric allows the system to be cut in new ways allowing the investigation of novel system views in terms of impedance based stability known as the common and differential mode stability between a converter and the grid or between converters
- The issues with coupling system strength and fault current in converter dominated systems have been identified with a review of present methods determining that no metric at present is capable of representing GFM structures correctly.
- The grid strength impedance metric (GSIM) is proposed as a novel method of determining system strength in converter dominated systems that decouples quasi-steady state dynamics from fault behaviour. The metric can represent the system weakening from GFL structures with high impedance and the strengthening from GFM topology with low impedance, the only measure capable at present of doing so.
- The effect of mechanical wind turbine dynamics such as shaft stiffness and blade bending on GS structures employing inertia emulation has been investigated with the DC link tuning being the key factor as to whether oscillations are damped by the mechanical systems or the electrical network.
- The penetration of GFM turbines has been determined to impact significantly on the strength and stability of a wind farm operating under weak grid conditions. A critical penetration is required to stabilise the system and an optimal penetration can be obtained beyond which adding further GFM turbines increases the virtual stiffness of the connection but but reduces the robustness of the system

## 1.5 List of Publications

This thesis has resulted in the following publications:

## Chapter 1. Introduction

- I C. Henderson, A. Egea-Alvarez, T. Kneuppel, G. Yang, and L. Xu, "Grid Strength Impedance Metric: An Alternative to SCR for Evaluating System Strength in Converter Dominated Systems," *IEEE Transactions on Power Delivery*, pp. 1-10, 2023, doi: 10.1109/tpwrd.2022.3233455.
- II C. Henderson, L. Xu, A. Egea-Alvarez, 'Analysis of Multi-Converter Network Impedance Using MIMO Stability Criterion for Multi-Loop Systems', *Electric Power Systems Research*, vol. 211, pp. 108542, Oct 2022.
- III C. Henderson, A. Egea-Alvarez, S. Fekriasl, T. Kneuppel, G. Amico, L. Xu, "The effect of grid-connected converter control topology on the diagonal dominance of converter output impedance," submitted to *IEEE Open Access Journal of Power and Energy*, Nov 2022.
- IV C. Henderson, D. Vozikis, D. Holliday, X. Bian, A. Egea-Alvarez, 'Assessment of grid-connected wind turbines with inertia response considering internal dynamics', *Energies*, vol. 13, no. 5, pp. 1038, Feb 2020.

The following conference works have been published as a result of this thesis:

- V C. Henderson, A. Egea-Alvarez, P. Papadopoulos, R. Li, L. Xu, R. Da Silva, A. Kinsella, I. Gutierrez, R. Pabat-Stroe, 'Exploring an Impedance-Based SCR for Accurate Representation of Grid-Forming Converters', *PESGM'22*, Denver, Colorado, USA, 2022.
- VI C. Henderson, L. Xu, A. Egea-Alvarez, 'PN admittance characterisation of grid support VSC controllers with negative sequence regulation and inertia emulation', in *EPE'21*, Online Conference, 2021.
- VII C. Henderson, N. McNeill, G. Wu, D. Holliday, and A. Egea-Àlvarez, "Vector Control of a Single-Phase Voltage Source Converter For the Supply of Inertia to Weak Grids," 2021 2020: Institution of Engineering and Technology.

The author has also published the following articles during the course of the Ph.D study:

## Chapter 1. Introduction

VIII C. Henderson, A. Egea-Alvarez, J. Rull-Duran, M. Nedd, P. Papadopoulos, L. Xu, 'Inertia and Frequency Support from Britain's AC Powered Trains', *IEEE Transactions of Sustainable Energy*, vol. 0, pp. 1-10, Nov 2022.

The author has also co-authored the following works during the course of the Ph.D study:

IX Q. Hong, M. Khan, C. Henderson, A. Egea-Alvarez, D. Tzelepis, C. Booth, 'Addressing frequency control challenges in future low-inertia power systems: a Great Britain perspective', *Engineering*, vol. 7, no. 8, June 2021.

X S. Harrison, C. Henderson, P. Papadopoulos, A. Egea-Alvarez, "Demystifying inertial specifications; arguing the inclusion of grid-followers", submitted to IET Renewable Power Generation, Nov 2022

The has also co-authored the following conference works during the course of the Ph.D study:

XI S. Harrison, C. Henderson, P. Papadopoulos, A. Egea-Alvarez, 'Assessment of droop and VSM equivalence considering the cascaded control dynamics', *ACDC 2021*, pp. 126 - 131, online conference, Dec 2021.

## Chapter 2

# Converter Modelling

### 2.1 Introduction

This chapter describes the modelling processes for all converters, controllers and other network devices used within this work and provides the linearisations to generate appropriate small-signal models. The recent developments of GFL and GFM techniques are explored first before modelling of the converter hardware is detailed and following this the GFL and GFM structures utilised are described. Six control structures are investigated split equally between GFL and GFM all looking to provide enhanced grid services with a conventional current based structure provided for reference. The components behind the grid-side converter are presented and other system elements such as synchronous machines, transformers and lines are detailed. Finally, the construction of the small-signal models is discussed with the linearisation of all non-linear system components provided.

### 2.2 Grid-connected Converter Control

The issues facing power converter dominated system have been well documented and new advanced control structures have been suggested to mitigate the negative effects of new connections to the network. IBRs will be required to provide inertia and frequency response as well as voltage stability services all while riding through faults and remaining robust or even mitigating adverse system interactions. Luckily, power converters are a



versatile technology which allow almost any voltage waveform to be synthesised subject to transistor current and voltage limits. Converter control techniques can be loosely split into three main families: GFL, grid-supporting (GS) and GFM.

### 2.2.1 Grid-following converters

GFLs are widely adopted in the traditional power system. The name stems from the utilisation of a PLL or frequency-locked loop (FLL) that 'follows' a pre-existing voltage signal to provide synchronisation with the network. Almost all GFLs utilise an inner loop current controller to regulate the converter current in the synchronous reference frame with appropriate voltage feed-forward and cross-coupling terms [73]. Beyond this, traditional outer loop controls looks to independently regulate active and reactive power. The ability to alter active power flow means that GFLs can contribute in some way to maintaining the frequency stability and support the network by re-balancing power flows which is considered as secondary or tertiary frequency reponse [74]. However, since IBRs can respond much quicker than this ( $< 100ms$ ), research has been completed utilising augmented control loops that change GFL to GS to allow them to participate more actively in primary frequency and inertia response [75]. Moreover, due to the versatility of power converters the inertia and damping provided can be easily altered via parameter tuning [76]. The damping provided from a power converter could be vastly different than that of an SG offering a similar inertia constant. Morren et al. proposed an inertia emulation method that provided a power command based on rate of change of frequency. This allowed the GFL to provide fast frequency response and arguably inertia. However, a clear trade off can be seen between speed of response and overall magnitude of response. In terms of other IBRs, Zhu et al. proposed a method for high-voltage direct-current (HVDC) systems where inertia emulation could be achieved by harnessing energy from the direct-current (DC) link capacitor [19]. It was found that the system could be utilised to provide multiple inertia constants with DC link voltage variations limited within a specific range. Fang et al. extended this approach to propose a system that utilised the DC link energy of a large variety of grid-connected power converters in [77]. However, one issue with these systems is the lack of ability

to provide an extended frequency response due to the limited energy available in the DC link. It is important to provide enough damping to smooth network oscillation but not so great that the converter response time is slowed significantly to avoid harming the frequency response.

While important for the frequency stability of the network, GFL structures incorporating these control loops may be unable to enhance the voltage stability of the network or increase the system strength due to their current source behaviour [78]. Therefore, other remedial action must be taken to provide these services otherwise the network will be unable to utilise the increased inertia and frequency response. Moreover, GFL structures experience poor performance when connected in weak grids normally due to the PLL [36, 79, 80]. It has been suggested in literature that GFLs can be tuned to provide fast terminal voltage control and may replicate some useful characteristics normally associated with grid forming implementations [81]. However, it is noted that tuning this behaviour is very dependent on the remaining system topology. For example, if the network is already too weak when the GFL attempts to connect, the PLL will not synchronise and the benefits of the fast terminal control will not be realised. Moreover, the specific tuning may cause instabilities at different frequencies far from the fundamental frequency and could offer issues in stronger grids by causing further interactions with system capacitance. While it has been suggested that GFM structures enhance system strength in locations where they are deployed [29, 36], this behaviour has not been explored for GFL converters employing fast voltage control.

### 2.2.2 Grid-forming converters

GFM converters are a new family of converter control that impose a voltage of set magnitude and angle on to the grid, offering favourable operation in antagonistic network conditions. These structures do not require a measure of the network voltage and can operate grid-connected or independently in islanded conditions [82]. GFM structures are drawing significant attention in literature in terms of frequency stability due to the inherent inertia present in the algorithms [83]. However, the term grid-forming has yet to achieve a fully established description that is agreed upon in literature [10, 20]. At

present the definition states that a GFM converter imposes the frequency and voltage output actively and independently of the grid voltage to support the network [84, 85]. Further definitions focus on the ability to operate without a PLL and therefore isolated from the grid [20], this also results in GFM techniques possessing black start capabilities [86]. Some literature suggests voltage and current source representations where GFM is considered as a controlled voltage source behind a small series impedance representing a Z-type system [36, 87, 88].

Work completed as part of the Migrate project defines a GFM as a power converter which generates an alternating-current (AC) voltage at a specific magnitude and frequency at the point of common coupling (PCC) [89]. Moreover, GFM should operate like an SG where each GFM must “play an identical role” in order to form the electrical system and perform independently, without communication with other devices. The National Renewable Energy Laboratory (NREL) specifies GFM as any inverter that regulates instantaneous terminal voltages and can coexist with other grid-following, grid-forming inverters and any synchronous generation present on the same system without the use of a PLL [90]. [91] states that GFM control can be divided into three sections: frequency control, DC link and AC side voltage magnitude, and inner loop current and voltage control. Interestingly, the low impedance associated with GFM converters that provides greater voltage stability also results in the converter requiring extremely accurate synchronisation in order to operate in parallel with other GFMs [87]. When multiple GFMs are connected in parallel, a very low impedance is observed where small changes in angle cause large deviations in active power offering issues with synchronisation when the grid is very stiff [92]. Therefore, a maximum penetration of GFM is certainly possible and will likely be related to interactions between the synchronisation loops similar to that seen for GFL synchronisation loops in weak grids but in a different manner.

Many GFM topology exist, most with a focus on recreating the useful behaviour of SGs commonly known as virtual synchronous machines (VSM) with simple structures looking to achieve this operating mode with less control complexity [93]. Two main forms exist with the key difference being the inclusion of an internal current loop. The

system presented in [94] utilises a current loop alongside other features such as a virtual impedance as a protection strategy and active damping to improve the paralleling of multiple machines. The system is used to investigate the parametric sensitivity of the VSM controller which is challenging due to the high order nature of the system. It is concluded that the slowest system poles are largely affected by the mechanical time constant, frequency droop gain and the virtual impedance. However, since other parameters do not greatly influence the poles, the parameters can be varied to speed up the transient response without greatly harming stability. It is also found that VSM control exhibits a faster and more damped response when operating in islanded conditions feeding a local load than when grid connected. Sakimoto et al. present a further simplified VSM topology without the internal current loop [95].

Similar improvements in stability are observed for various scenarios with different volumes of SG and distributed generation (DG). The paper also presents a method for handling overcurrents during voltage dips by utilising a virtual resistor similar to [94], which produced viable results. The current loop makes protection of the converter easier and allows for simpler, more conventional methods of fault ride through (FRT) [96]. If current control is not utilised the converter can be prone to damage, especially during faults. Work has been completed on FRT without the presence of a PLL or current loop which could help to remedy this issue [97]. The VSM approach is improved by Shintai in [98] where a reactive droop is included to allow operation while grid connected or in an islanded condition while maintaining a constant voltage at the converter terminals. A similar approach by Cheng et al. implements an automatic voltage regulator (AVR) to regulate the converter voltage and provide support in microgrids which achieves good results [99]. It has been reported that the transient tolerance of inverter connected generation is less than that of real SGs. However, since inverter parameters are easily altered work has been completed to design VSM control systems that can change parameters to improve transient response based on converter conditions [14,100]. These systems change the value of virtual inertia based on the virtual angular velocity and acceleration. The system successfully dissipates the transient energy usually absorbed by damping factor in real SGs and improves stability of the VSM controlled machine

as well as other converters on the network. However, the reduction of the inertia term may decrease the VSMS response to network frequency events.

Moving away from conventional control structures will require intense review and adaptations of new topology to ensure stability is maintained [101]. New control interactions may occur as the frequency response of controllers change. For example, sub-synchronous oscillations that can be observed between SGs may be present between converters when the converter is behaving as an SG. Any control system that looks to control active power can exhibit reduced performance due to interaction with pre-existing power control [102]. The control structure significantly effects the output impedance of the converter and therefore the response to grid frequency and voltage events.

### 2.2.3 Grid-supporting converters

Grid supporting tends to be the name given to traditional GFL structures augmented with extra control loops to provide a virtual form of the behaviour they are replicating. However, the term has been used to describe GFMs and a definition is required. In reality, using the term grid supporting is ambiguous. For example, [103] states that a grid supporting mode is created by implementing a droop control on the active and reactive power references which is a capability of both GFL and GFM structures. A grid forming converter that acts in grid supporting mode can provide synthetic inertia, which a VSM also does. [87] was one of the early works to introduce grid supporting converters representing them as an ideal controlled current source with a shunt impedance in parallel, or an ideal voltage source with series link impedance. The exact source form may not be the important point, what should be considered is the size of the impedance. GFLs have large impedance and therefore exhibit good current source behaviour and the opposite is observed for GFM with low impedance and good voltage source behaviour. GS structures likely have an impedance somewhere in the middle and care should be taken to ensure poor tuning does not cause these systems to exhibit the worst characteristics of each type of system. The main purpose of a GS is to maintain the reference values of active and reactive power in order to regulate

grid frequency and voltage. If it is implemented as a current source, at least one grid former is required in the system as well as the GS, but if the GS represents a voltage source, grid connected and islanded mode operation can be achieved. Therefore, in this work all structures are considered as GFL or GFM as GS is ambiguous. GFL require synchronisation via a PLL and require a pre-existing network whereas GFM synchronise via active power balance. The supporting services described can likely be provided from either type and therefore the term GS is disregarded to avoid confusion.

## 2.3 Converter Modelling

Power electronic converters are versatile devices and with appropriate control can be operated as voltage sources which is achieved via fast switching of the semiconductor devices. Many topology exists with the most popular being two-level, three-level or modular multi-level converters (MMCs). The focus of this work is on the control topology governing the operation of the converter with respect to the grid. Therefore, it is necessary to use appropriate simplifications to ensure the hardware is properly represented while maintaining a low level of computational burden, especially when modelling the behaviour of multiple converters.

Multiple filters and delays are included to try and represent the true dynamics of the converter. Each measurement signal is low-pass filtered (LPF) to emulate the bandwidth of the measurement instrumentation, the filter is applied in the abc-frame and is therefore transformed to dq:

$$K_{meas}(s) = \begin{bmatrix} \frac{1}{\tau_{meas}} & -\omega_g \\ \omega_g & \frac{1}{\tau_{meas}} \end{bmatrix} \quad (2.1)$$

Where  $\tau_{meas}$  is the measurement filter time constant and  $\omega_g$  is the nominal grid frequency. The use of this system is verified via matching of impedance sweeps using a time domain model employing the filters in the abc-frame in Chapter 3. The pulse width modulation (PWM) switching method plays a significant factor in power system dynamics. However, appropriate passive filters tend to be installed alongside converter to mitigate the negative effects. Moreover, PWM represents a non-linear system and

provides a large computational burden. Therefore, it is assumed that the harmonics due to switching are appropriately mitigated and an average converter model is used for analysis. The measurement and switching delay introduced by the control system and PWM is approximated using a 1st order Padé delay:

$$K_{Pade}(s) = \frac{2 - \tau_{pa}}{2 + \tau_{pa}} \quad (2.2)$$

Where  $\tau_{pa}$  is the Padé delay time constant,

### 2.3.1 Grid-Following Control Topology

Grid-following converters are the most common converter control approach present on the electricity network today. The name stems from the fact the the controller synchronises with the external grid by 'following' a pre-existing voltage signal.

A standard GFL structure use widely in literature is provided in Figure 2.1 [28,79]. The main components include: PLL, positive and negative sequence current loops, outer-loop power and voltage control as well as transformations, filters and delays.

### 2.3.2 Synchronisation

All converter controllers used within this work are described in the synchronous reference frame. For correct operation, the controller reference frame must be synchronised with the global reference frame that the network is described in. Synchronisation of three-phase converter controllers is normally achieved via PLL (shown in the light-blue box in Figure 2.1). The PLL acts on either the q or d axis voltage measurement at the PCC, outputting the converter angle for transformation and aims to reduce one qd voltage component to zero. In this case an a-phase to q-axis alignment is used and the d-axis voltage component is set to zero via a proportional-integral (PI) controller:

$$\theta_{pll} = \frac{-V_{d,PCC}K_{pll}(s)}{s} \quad (2.3)$$

$$K_{pll}(s) = K_{p,pll} + \frac{K_{i,pll}}{s} \quad (2.4)$$

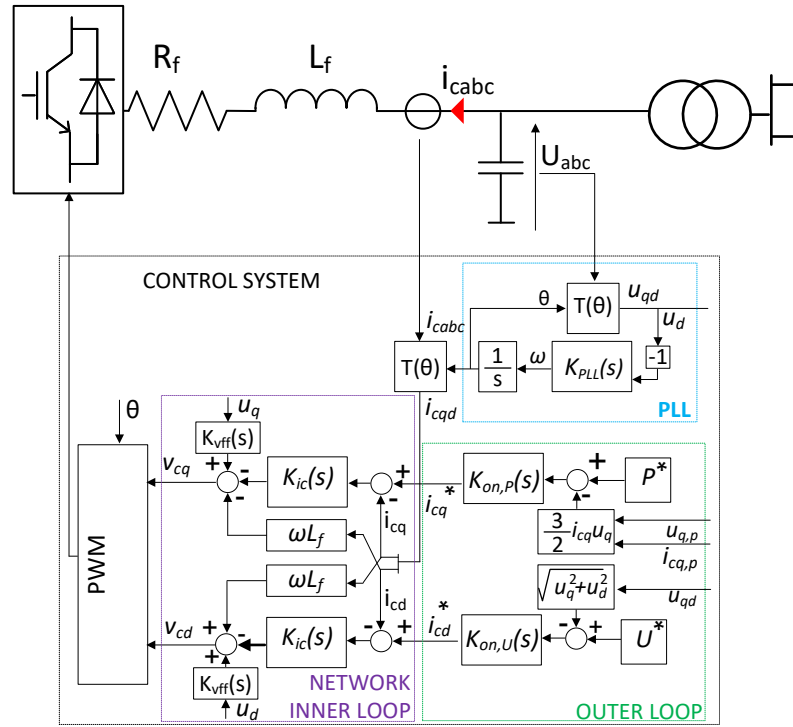


Figure 2.1: GFL Control Diagram

Where  $\theta_{pll}$  is the PLL angle output,  $V_{d,PCC}$  is the PCC d-axis voltage and  $K_{p,pll}$  and  $K_{i,pll}$  are the PLL proportional and integral gains, respectively. The PLL operation can only be achieved using the correct converter angle in the Park and inverse Park transforms when the controller frame is synchronised to the network frame. The Park transform used for the frame alignment is as follows:

$$T(\theta) = \begin{bmatrix} \cos(\theta_{pll}) & -\sin(\theta_{pll}) \\ \sin(\theta_{pll}) & \cos(\theta_{pll}) \end{bmatrix} \quad (2.5)$$

### 2.3.3 Inner Loop Control

In almost all GFL converters, inner loop current control is present. The controller regulates the synchronous reference frame converter currents by altering the terminal voltage commands of the converter. This subsystem is shown in purple in Figure 2.1. Current is controlled via a PI controller on each axis with proportional and integral gains tuned via the modulus optimum criterion with tuning constant  $\alpha$  used to produce



a desired settling time [104]:

$$K_{ic}(s) = K_{p,cc} + \frac{K_{i,cc}}{s} \quad (2.6)$$

$$K_{p,cc} = \frac{L_f}{\alpha} \quad (2.7)$$

$$K_{i,cc} = \frac{R_f}{\alpha} \quad (2.8)$$

Two feedforward terms are included in the control. The first deals with the cross-coupling between the q and d axes:

$$i_{q,cc} = i_d L_f \omega_g \quad (2.9)$$

$$i_{d,cc} = -i_q L_f \omega_g \quad (2.10)$$

Where  $i_q$  and  $i_d$  are the q and d-axis current, respectively and  $i_{q,cc}$  and  $i_{d,cc}$  are the q and d-axis converter current cross-coupling terms. The second feedforward provides the PCC voltage to reduce the strain on the current controller. The qd PCC voltages must be filtered appropriately to maintain stability as the grid impedance increases:

$$K_{vff}(s) = \frac{1}{s\tau_{vff} + 1} \quad (2.11)$$

Where  $\tau_{vff}$  is the voltage feedforward time constant. In addition to the positive sequence loop, a negative sequence current controller is often present to cope with unbalanced network conditions. When included the control structure alters slightly as both positive and negative sequence components are required in the synchronous reference frame. A diagram is provided in Figure 2.2.

The additional components are shown in dark blue 'processing' box in Figure 2.2 and are used to obtain the negative sequence qd converter signals via a modified Park transform:

$$T_n(-\theta) = \begin{bmatrix} \cos(-\theta_{pll}) & -\sin(-\theta_{pll}) \\ \sin(-\theta_{pll}) & \cos(-\theta_{pll}) \end{bmatrix} \quad (2.12)$$

Followed by a notch filters tuned at 100 Hz to remove the unwanted opposite sequence

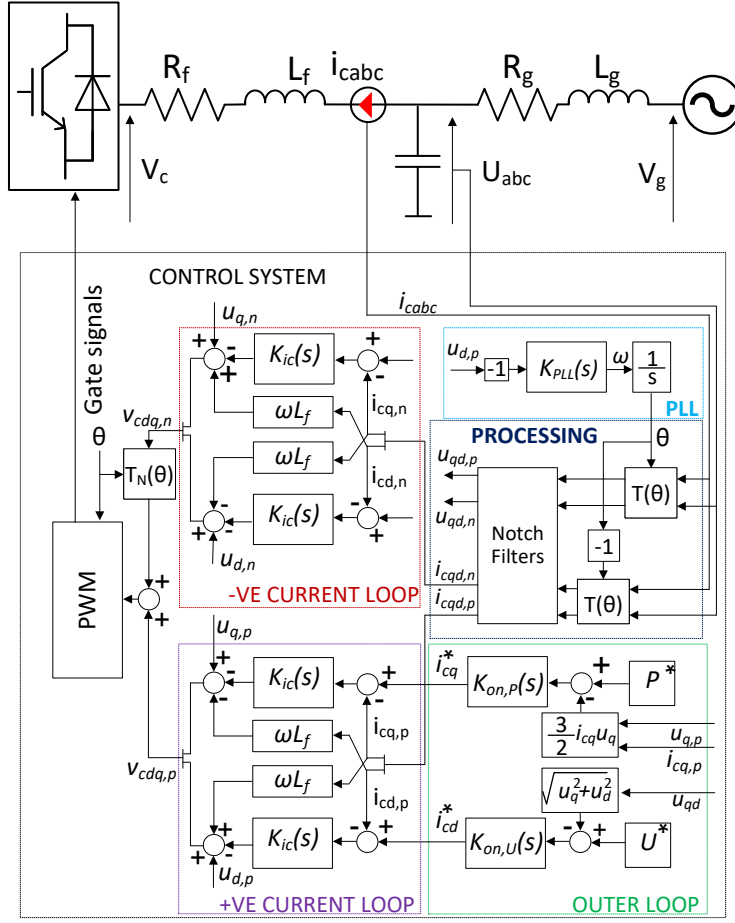


Figure 2.2: GFL Control Diagram with NSC

components:

$$H(s) = \frac{s^2 + (2\omega_g)^2}{s^2 + \frac{2\omega_g}{Q} + (2\omega_g)^2} \quad (2.13)$$

Where  $Q$  is the notch filter quality factor. Note that when the negative sequence control is enabled, notch filters are also applied to the positive sequence signals in the same manner. The same filtering is applied to the negative sequence voltage feedforwards and the PI controllers are initially tuned to match the positive sequence. The remaining negative sequence structure is analogous with the positive sequence counterpart.

### 2.3.4 Outer Loop Control

The outer loop controller allows for various operating modes of the GFL converter two of which can be considered GS. Three outer loop structures are considered in this work: standard power voltage control (PVCC) and two GS structures, power and voltage droop control (PVCCD) and power voltage control with inertia emulation (PVCCI). The negative sequence control can be enabled on these systems at which point a suffix N is added e.g. PVCCN. The standard power voltage control can be seen in the green box in either Figure 2.1 or Figure 2.2. Two PI controllers regulate the active power flowing from the converter and the voltage magnitude at the PCC by provided the reference signals for the internal current loops:

$$K_{on,P}(s) = K_{p,P} + \frac{K_{i,P}}{s} \quad (2.14)$$

$$K_{on,U}(s) = K_{p,U} + \frac{K_{i,U}}{s} \quad (2.15)$$

Where  $K_{p,P}$  and  $K_{i,P}$  are the power controller proportional and integral gains, respectively and  $K_{p,U}$  and  $K_{i,U}$  are the voltage controller proportional and integral gains, respectively. Various tunings are used for these controllers with the only general rule being that the outer loop control should be tuned sufficiently slowly so as not to interfere with the inner loop. This allows the GFL converter to maintain the characteristic current source behaviour. However, in GS mode a faster outer loop is likely preferable as current source behaviour is not always the most beneficial for the network. Note that the active power control is only used when the DC link is not included. Otherwise, a DC link voltage controller is present. Power and voltage filters can be applied to the outer-loop feedback signal if required using similar LPFs with filter constants denoted by  $\tau_{pf}$  and  $\tau_{uf}$ , respectively.

#### Droop Control

Droop control has been widely applied in literature [105–108] and allows for better paralleling and power sharing of multiple converters. A frequency droop is applied to

allow the converter to participate actively in frequency regulation by altering power output accordingly. The control structure has been validated utilising time domain models indicating realistic power sharing relative to the droop gains selected and similar frequency response to that shown in literature [26]. A voltage droop and reactive power setpoint are applied on the other axis. In this case, the PI controllers are replaced with P controllers to provide the droop, a diagram of the outer loop is provided in Figure 2.3.

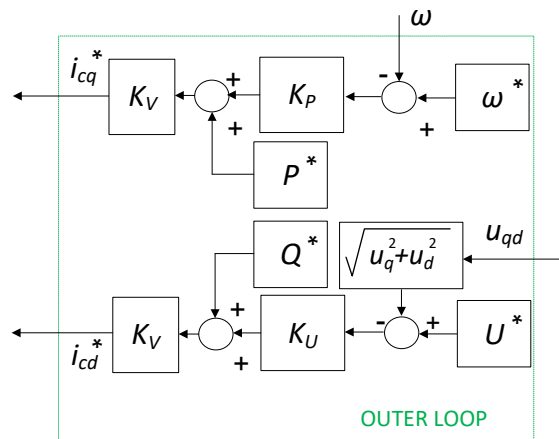


Figure 2.3: Droop Control Outer Loop Diagram

### Inertia Emulation

Control structures that utilise inertia emulation link RoCoF to active power via an augmented control loop allowing for increased participation in frequency regulation. In theory, this lets the converter respond faster to changing network conditions similar to traditional synchronous machines. Conversely, a droop based approach has to wait for a disparity between setpoints instead of being able to pre-empt the frequency event via RoCoF detection. The power and voltage controllers remain the same as in Figure 2.1 but now an addition is made to the power command, a control diagram is provided in Figure 2.4. Validation of the inertia emulation control has been completed by matching the frequency response to the original work detailing the structure [18] and against the frequency response of a real machine providing inertia [26].

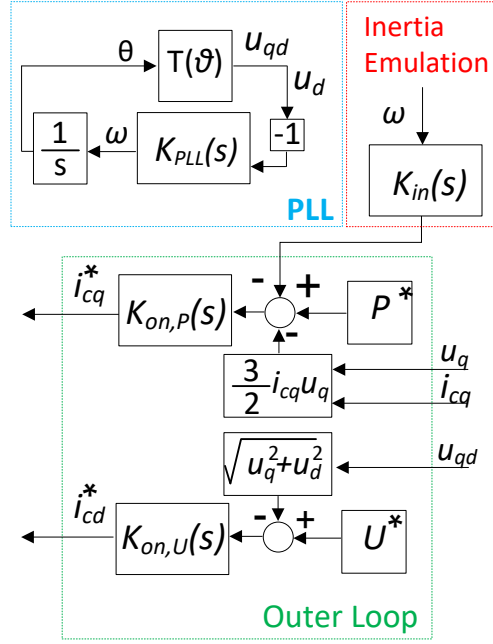


Figure 2.4: Inertia Emulation Control Outer Loop Diagram

The PLL estimation  $\omega_{PLL}$  is passed through  $K_{in}(s)$  before being added to the power setpoint where:

$$K_{in}(s) = K_{inert} \frac{1}{\tau_{if}s + 1} \quad (2.16)$$

Where  $K_{inert}$  is the inertial gain used to determine the magnitude of response and  $\tau_{if}$  is the filter time constant used to remove derivative noise. A second pre-filter may be necessary in very noisy conditions, but this significantly slows the response of the control loop and reduces the effectiveness of the 'inertia'. The operation of each GFL control structure is verified in Chapter 3.

## 2.4 Grid-Forming Control Topology

Grid-forming converters have received significant attention due to their favourable behaviour in antagonistic grid conditions. Instead of following a pre-existing voltage signal, GFM converters impose a voltage on to the network of set magnitude and an-

gle. This voltage source behaviour results in improved voltage strength in locations where they are deployed. Additionally, the synchronisation loops of GFM controllers often provide damping and inertia similar to traditional synchronous machines and are viewed as a key component of the modern converter dominated network to ensure stability [10]. This section discusses three GFM structures: GFM droop control (GFMD), Virtual synchronous machine with current control (VSMCC) and a virtual synchronous machine (VSM). Most GFM structures can operate with or without an internal current loop. Hence, both implementations are presented here and analysis conducted to determine the unique characteristics of both and is presented in later chapters. Unless otherwise stated, each GFM structure employs similar frame transformations and incorporates the same control delays as the previously described GFL structures. One key difference in filtering exists due to the slow response nature of GFM structure requiring a LPF to be applied to the active and reactive power as well as PCC voltage feedback signals when they are utilised tuned via filter constants  $\tau_P$ ,  $\tau_Q$  and  $\tau_V$ , respectively.

#### 2.4.1 Grid-Forming Droop Control

Droop control has been widely applied for GFL controllers [87]. In the case of GFM, the power control no longer employs a frequency droop and power setpoint to determine the active current command. Similar to the GFL droop, validation of the GMFD is completed by matching responses against the PSC proposed in [109] as the mathematical structure of each is identical. Moreover, the frequency response is matched against similarly sized traditional SGs [26]. Instead, an active power droop is used to vary the frequency around the nominal setpoint. A diagram is provided in 2.5.

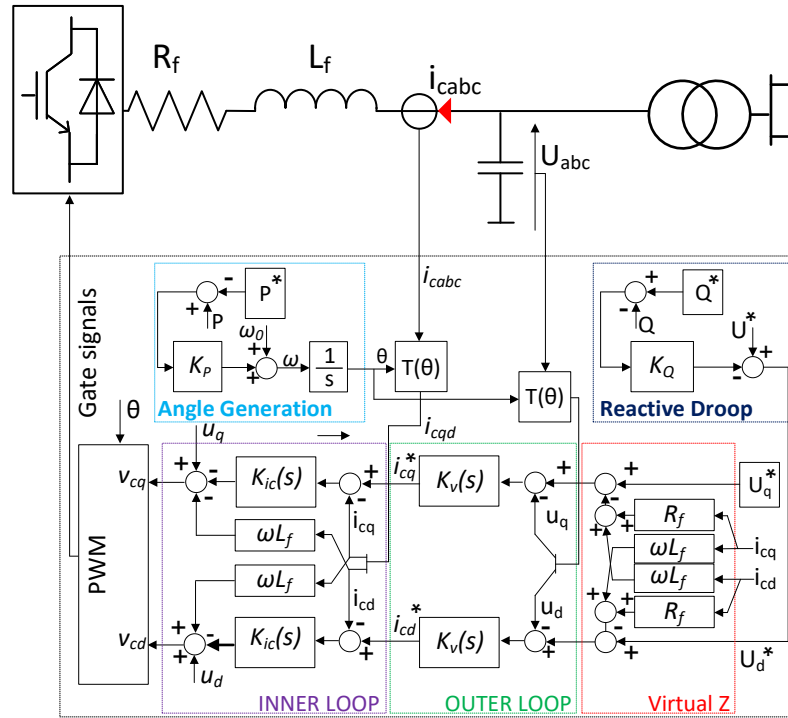


Figure 2.5: Grid-forming Droop Control Diagram

From 2.5, a reactive droop controller is used to produce the desired setpoint for PCC voltage while maintaining reactive power balancing between multiple machines. A virtual impedance is then utilised. This provides increased damping, improved paralleling of multiple machines and fault current limitation in some cases [110]. However, the impedance can be omitted in some scenarios via careful tuning of the voltage control if fault ride through is not of concern. Since the structure contains an inner loop current controller a more traditional current limiting algorithm can be employed when required. The independent synchronous reference frame voltage are then controlled to provide setpoint for the inner loop current controller. The angle calculated in the synchronising loop is used for the Park transforms.

### 2.4.2 Virtual Synchronous Machine

The virtual synchronous machine concept was first introduced in 2007 with the VISMA [111] and a similar approach known as the Synchronverter soon followed [112]. Both topology replicate the full behaviour of a synchronous machine by modelling the stator

voltage dynamics. However, not all work done by synchronous machines is beneficial and therefore more modern approaches simplify and recreate only the useful behaviour [113]. A widely adopted approach is to generate the converter angle by means of the power swing equation. This provides an angle for the Park transforms and facilitates independent control of the synchronous reference frame current and voltage via inner and outer loop control respectively. The VSM achieves synchronisation and regulates active power via the same control loop which recreates the power swing equation:

$$J \frac{d^2 \theta_m}{dt^2} + D \frac{d\theta_m}{dt} = \Delta(P_m - P_e) \quad (2.17)$$

Where  $\theta_m$  is the machine angle,  $J$  and  $D$  and the inertia and damping, respectively and  $P_m$  and  $P_e$  are the mechanical and electrical power, respectively. This means the VSM structure provides inertia and damping to the system while the previous droop only provided the latter. In fact, when the VSM is designed to include current control denoted VSMCC, the control structure is almost the same as GFMD with control of the synchronous reference frame voltages and currents independently. For VSMCC, the virtual impedance is removed to illustrate that it is not required for steady-state operation. The VSM structures used within this work do not model the whole power swing equation and instead utilise an active power based synchronising technique to generate the angle including an inertia term via a PI controller. A diagram is provided for the VSMCC in Figure 2.6.



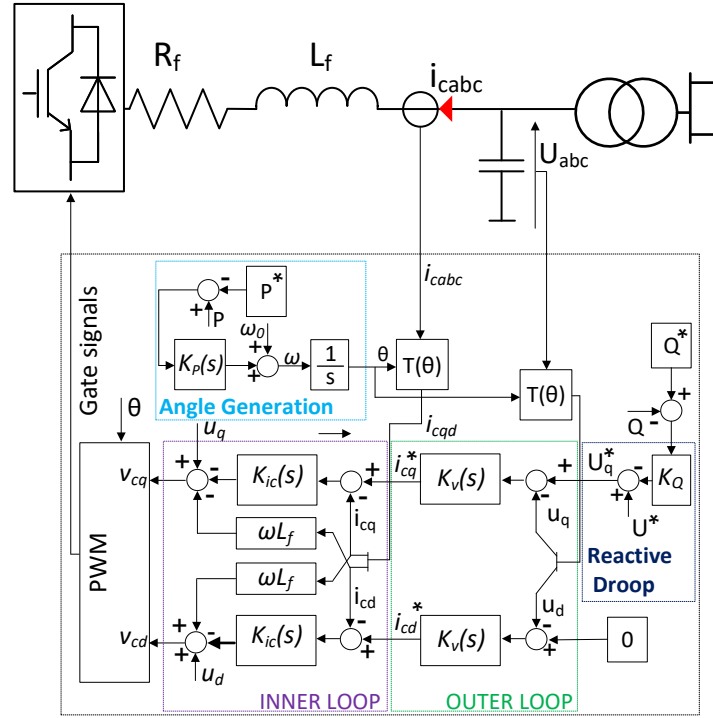


Figure 2.6: Simplified VSM Structure with Current Control

Synchronisation is achieved via active power balance, similar to droop control. However, the proportional control is now replaced with a PI controller. The PI controller in the VSM controllers now represents both damping with the proportional term and inertia with the integral term. The PI controller can be tuned accordingly to represent the dynamics of the power swing equation in a very simple form. If 2.17 is expressed in the Laplace domain with the inertia represented as a function of the inertia constant  $H$ , machine speed  $\omega$  and rated power  $S_{rated}$ :

$$\frac{2H}{\omega} S_{rated} \theta(s) s^2 + D \theta(s) s = P_m(s) - P_e(s) \quad (2.18)$$

The forward path relation between machine power and angle can then be represented as:

$$G_1(s) = \frac{\theta(s)}{P_m(s) - P_e(s)} = \frac{1}{\frac{2H}{\omega} S_{rated} s^2 + Ds} \quad (2.19)$$

Moreover, the feedback path can be written as:

$$H_1(s) = k_m \quad (2.20)$$

Where  $k_m$  is the machine design constant which remains the same for the real and virtual machine. The characteristic equation can then be constructed:

$$s^2 + D \frac{\omega}{2HS_{rated}} s + \frac{k_m \omega}{2HS_{rated}} = 0 \quad (2.21)$$

Comparing this to the standard second order characteristic equation:

$$s^2 + 2\zeta\omega_n s + \omega_n^2 = 0 \quad (2.22)$$

The undamped natural frequency,  $\omega_n$  and damping factor,  $\zeta$  can be expressed as:

$$\omega_n = \sqrt{\frac{\omega}{2HS_{rated}} k_m} \quad (2.23)$$

$$\zeta = \frac{D}{2} \sqrt{\frac{\omega}{2HS_{rated} k_m}} \quad (2.24)$$

The active power loop of the VSM can then be compared to this system to determine values for the VSM proportional,  $k_{p,vsm}$  and integral,  $k_{i,vsm}$  gains. The two closed loop systems are compared with the physical machine loop shown in Figure 2.7 and the VSM loop shown in Figure 2.8.

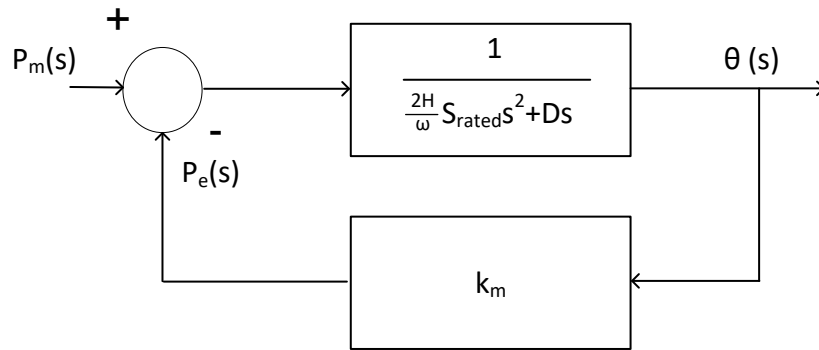


Figure 2.7: Synchronous Machine Closed Loop Function

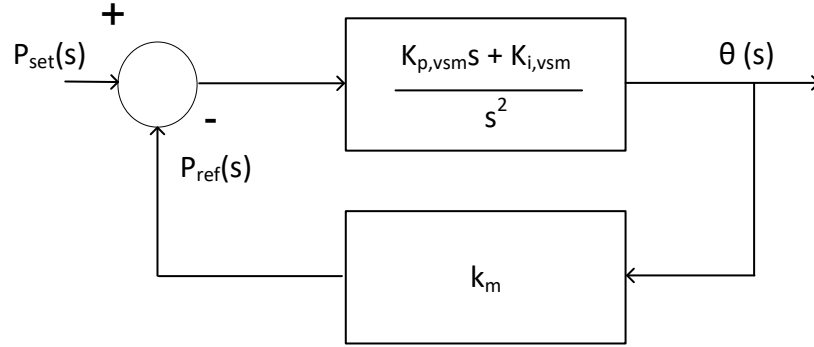


Figure 2.8: Virtual Synchronous Machine Closed Loop Function

Comparing the two loops the VSM structure is obtained by writing the forward path of the active power synchronisation loop as:

$$G_2(s) = \frac{k_{p,vsm}s + k_{i,vsm}}{s} \frac{1}{s} \quad (2.25)$$

The system has the same feedback gain as in 2.20:

$$H_2(s) = H_1(s) = k_m \quad (2.26)$$

The closed-loop characteristic equation can be written as:

$$s^2 + k_m k_{p,vsm} s + k_m k_{i,vsm} = 0 \quad (2.27)$$

Comparing this to the standard second order transfer function 2.22, the undamped natural frequency and damping factor can be expressed as:

$$\omega_n = \sqrt{k_{i,vsm} k_m} \quad (2.28)$$

$$\zeta = \frac{k_{p,vsm}}{2} \sqrt{\frac{k_m}{k_{i,vsm}}} \quad (2.29)$$

If both systems are to exhibit the same behaviour the natural frequency and damping factors for each system should be matched which provides the tuning for the propor-

tional and integral terms:

$$k_{i,vsm} = \frac{\omega}{2HS_{rated}} \quad (2.30)$$

$$k_{p,vsm} = \frac{D\omega}{2HS_{rated}k_m} = \frac{Dk_{i,vsm}}{k_m} \quad (2.31)$$

Following this tuning ensures that the active power loop correctly replicates the inertia of a real machine. However, the tuning of inertia is not limited to replicate real machines and in some cases can be made much larger. This assuming there is sufficient energy stored to provide response and that the increased gain does not cause the system to become unstable. Voltage control in the VSMCC is achieved via two PI controllers regulating the synchronous reference frame voltages independently similar to GFMD. One axis command is left at zero while the other achieves the desired voltage at the PCC which can be augmented with a reactive power droop controller input if required. The two voltage controllers provide the set points for the inner loop current control similar to GFMD. The proper operation of both VSM controllers has been validated by comparing the response to that of real SGs [26] as well as offering a similar response to the deployment of VSM control to real wind farms [65].

The VSM approach can be further simplified by removing the internal current control to offer a stripped back version of the topology. A diagram of this is provided in 2.9.

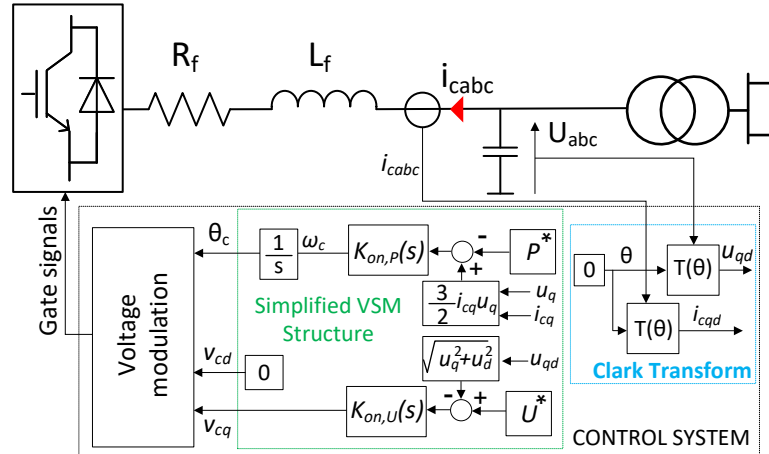


Figure 2.9: VSM Structure

The magnitude of voltage at the PCC can be directly regulated by altering the terminal voltage command without an inner loop current controller. While this may provide more favourable grid-forming behaviour in quasi-steady state conditions, it does offer some concerns in terms of fault ride through capability. Most converter structures rely on the current loop to limit current during the fault and protect the converter [114]. In fact, almost all GFM structures currently in use switch back to current control mode using a back-up PLL during faults to prevent damaging the device [115]. While acceptable at present, switching converter modes to and from current control results in discontinuities on the network and should be avoided if possible. Some work has been completed on FRT for GFM converters without an internal current loop but is limited to three-phase balanced faults at present [97]. This should not be a limiting factor in future for this type of control topology with further research into FRT. However, there is likely no need for grid-forming behaviour during faults. Since the converter will be limited in some way, the impedance and therefore response of the converter will no longer be determined via the control topology and any designed GFM behaviour will not be utilised during faults under present structures. The operation of each GFM structure is validated in Chapter 3.

### 2.5 Behind and Beyond the Grid-Side Converter

To fully represent the interactions of the system, it is important in some cases to include the dynamics occurring behind and beyond the converter. In this work, the main source of generation used is the Type IV turbine as the fully-rated back-to-back converter provides excellent versatility in terms of control. This makes implemented GFM algorithms simpler than with the Type III Doubly-fed induction (DFIG) counterparts. Further to this, offshore wind is the fastest growing sector within the wind industry where the Type IV turbine is preferred due to increased reliability and lower maintenance costs due to the lack of gearbox [116]. For wind farm interaction studies of the individual wind turbines are obviously of interest in certain scenarios. Back-to-back converters are known for decoupling the turbine and network dynamics via the use of a DC link. However, regulation of the DC link voltage from the grid-side converter

results in some oscillations due to blade bending, tower sway and torsional resonances propagating through the DC link to the network [102]. Usually, some form of damping control is used in the turbine control to reduce these unwanted oscillations. However, this uses energy from the DC link and continues to provide interactions between the network and the turbines. Hence, it is important to include these dynamics to ensure interactions are included across the entire frequency range. A diagram of the Type IV turbine used within this work is provided in Figure 2.10 and the sub-components are described in the following subsections.

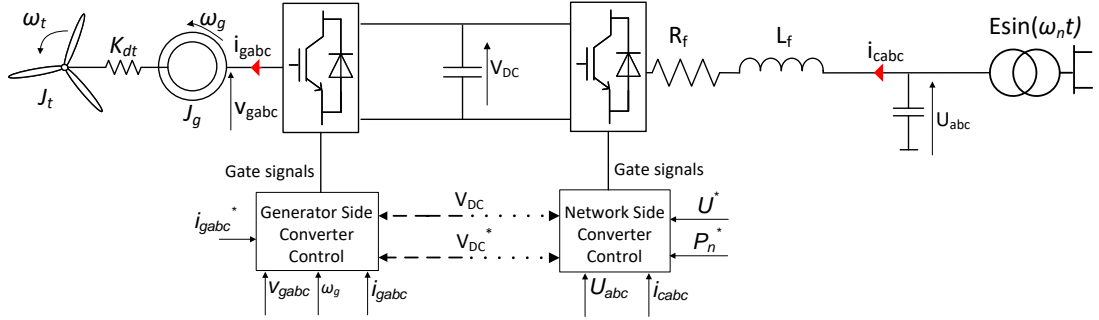


Figure 2.10: Simplified Type-4 Turbine Diagram

### 2.5.1 Permanent Magnet Synchronous Generator

The permanent magnet synchronous generator (PMSG) is modelling via the stator terminal voltage equations:

$$s i_{q,g} = \frac{v_{q,g}}{L_{s,q}} - \frac{R_s}{L_{s,q}} i_{q,g} - \frac{L_{s,d}}{L_{s,q}} p \omega_g i_{d,g} - \frac{\lambda p \omega_m}{L_{s,q}} \quad (2.32)$$

$$s i_{d,g} = \frac{v_{d,g}}{L_{s,d}} - \frac{R_s}{L_{s,d}} i_{d,g} - \frac{L_{s,q}}{L_{s,d}} p \omega_g i_{q,g} \quad (2.33)$$

$$\tau_e = \frac{3}{2} p \lambda i_{q,g} \quad (2.34)$$

Where  $i_{q,g}$  and  $i_{d,g}$  are the generator Q and D-axis stator current components, respectively,  $v_{q,g}$  and  $v_{d,g}$  are the Q and D-axis stator voltage components, respectively,  $L_{q,s}$  and  $L_{d,s}$  are the Q and D-axis stator inductances, respectively,  $R_s$  is the stator resistance,  $\lambda$  is the flux linkage,  $p$  is the number of pole pairs and  $\tau_e$  is the electromagnetic

torque.

### 2.5.2 Two-mass drive-train

Many different drivetrain models of varying complexity exist from single-mass rigid models [117] to flexible two-mass models [118] and beyond to complex six-mass models [119]. Previous studies have indicated that two mass-models are sufficient for interactions on the electrical network [120]. Single-mass models do not contain the required flexibility to allow oscillations and models including more than two masses exhibit modes that are not of concern for the electrical network at this time due to their higher frequency nature [119]. However, this is only a valid assumption for the present generation of turbines, especially of the 3 MW size. As turbine sizes increase, the natural frequencies of various mechanical subsystem will lower which may make them of concern in future. The two-mass drivetrain is described as follows:

$$\omega_t = \frac{\tau_t - \gamma K_{dt}}{s J_t} \quad (2.35)$$

$$\omega_{gen} = \frac{\gamma K_{dt} - \tau_{gen}}{s J_{gen}} \quad (2.36)$$

$$\gamma = \frac{\omega_t - \omega_{gen}}{s} \quad (2.37)$$

Where  $\omega_t$  and  $\omega_{gen}$  are the turbine and generator speeds, respectively,  $\tau_t$  and  $\tau_{gen}$  are the turbine and generator torque, respectively,  $J_t$  and  $J_{gen}$  are the turbine and generator inertias, respectively,  $K_{dt}$  is the shaft stiffness and  $\gamma$  is the shaft twist angle. The natural frequency of the drivetrain is determined by the mass and inertia of the turbine and PMSG, respectively as well as the stiffness of the connecting shaft.

### 2.5.3 Machine Side Control

The machine-side converter (MSC) controller is similar in structure to the grid-side controller in this case regulating the machine stator currents to alter the electromagnetic torque and flux by varying the machine terminal voltages. A diagram is provided in Figure 2.11.

No PLL is required for the MSC as the exact generator speed is known. Damping

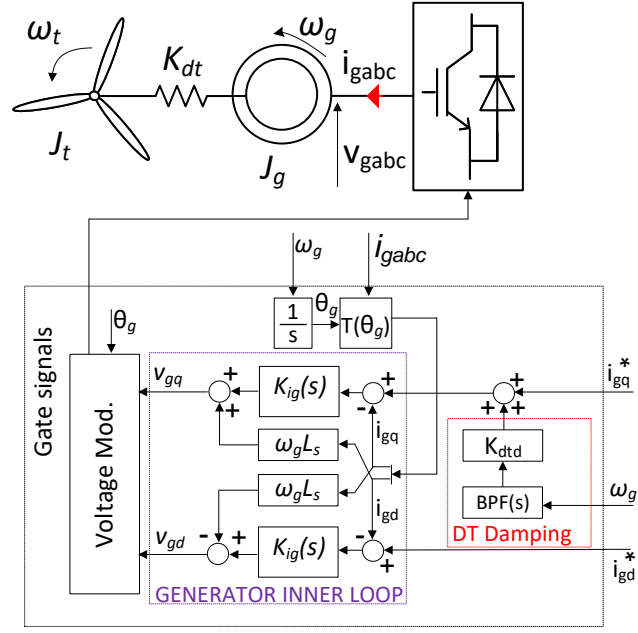


Figure 2.11: Generator Control Structure

of mechanical oscillations in the drivetrain is achieved via the application of a torque deviation provided by filtering the generator speed signal. A bandpass filter is utilised with the centre frequency tuned to the first eigenfrequency of the drivetrain. The gain  $K_{dtd}$  is used to adjust the strength of the damping:

$$BPF(s) = \frac{2c\omega_{dt}s}{s^2 + 2c\omega_{dt}s + \omega_{dt}^2} \quad (2.38)$$

Where  $c$  is the shaft damping factor and  $\omega_{dt}$  is the first eigenfrequency of the drivetrain.

#### 2.5.4 DC Link

In all cases the converters on each side of the DC link are average models and the switching is approximated using a Padé delay. The DC link operates by balancing the power with the machine side and network side power are the inputs with the output



being the DC link voltage.:

$$i_{DC} = \frac{P_{MSC} - P_{GSC}}{v_{DC}} \quad (2.39)$$

$$v_{DC} = \frac{i_{DC}}{sC_{DC}v_{DC}} \quad (2.40)$$

Where  $v_{DC}$ ,  $i_{DC}$  and  $C_{DC}$  are the DC link voltage, current and capacitance, respectively and  $P_{MSC}$  and  $P_{GSC}$  are the machine and grid-side converter active powers, respectively. The DC link voltage is then controlled via the grid-side converter (GSC) with a PI controller acting on the DC link voltage error to provide the active power command to the GSC:

$$P^* = (v_{DC}^* - v_{DC})K_{DC}(s) \quad (2.41)$$

$$K_{DC}(s) = K_{p,DC} + \frac{K_{i,DC}}{s} \quad (2.42)$$

Where  $P^*$  is the active power setpoint,  $v_{DC}^*$  is the DC link voltage setpoint and  $K_{p,DC}$  and  $K_{i,DC}$  are the DC link voltage controller proportional and integral gains, respectively.

## 2.6 Further Network Components

To ensure a full system description other passive network components were also modelled including transformers and transmission lines. Since all studies focused on small-signal models the transformers were modelled as an RL impedance:

$$Z_{qd,Tf}(s) = \begin{bmatrix} R_{tf} + sL_{tf} & \omega_g L_{tf} \\ -\omega_g L_{tf} & R_{tf} + sL_{tf} \end{bmatrix} \quad (2.43)$$

Where  $R_{tf}$  and  $L_{tf}$  are the transformer resistance and inductance, respectively. The short transmission line (< 50 km) impedances are modelled using the same form using the transmission line resistance ( $R_{tr}$ ) and inductance ( $L_{tr}$ ). For longer longer lines, PI sections were utilised including capacitances alongside reactive compensation fitted at

both ends and mid-line.

## 2.7 Small-Signal Modelling

A state-space model is created to facilitate the generation of the component admittance, in this case representing a grid-connected converter:

$$\Delta \dot{\mathbf{x}} = \Delta \mathbf{x} \mathbf{A} + \Delta \mathbf{u} \mathbf{B} \quad (2.44)$$

$$\Delta \mathbf{y} = \Delta \mathbf{x} \mathbf{C} + \Delta \mathbf{u} \mathbf{D} \quad (2.45)$$

Where  $\mathbf{x}$ ,  $\mathbf{u}$  and  $\mathbf{y}$  are the model state, input and output vectors respectively, and  $\mathbf{A}$ ,  $\mathbf{B}$ ,  $\mathbf{C}$  and  $\mathbf{D}$  are the state, input, output and feedthrough matrices respectively. Each non-linear system must be linearised around a system operating point. These non-linear systems are described in this section. Diagrams showcasing the general linearised systems for the GFL and GFM structures are provided using PVCC in Figure 2.12 and VSM in Figure 2.13, respectively.

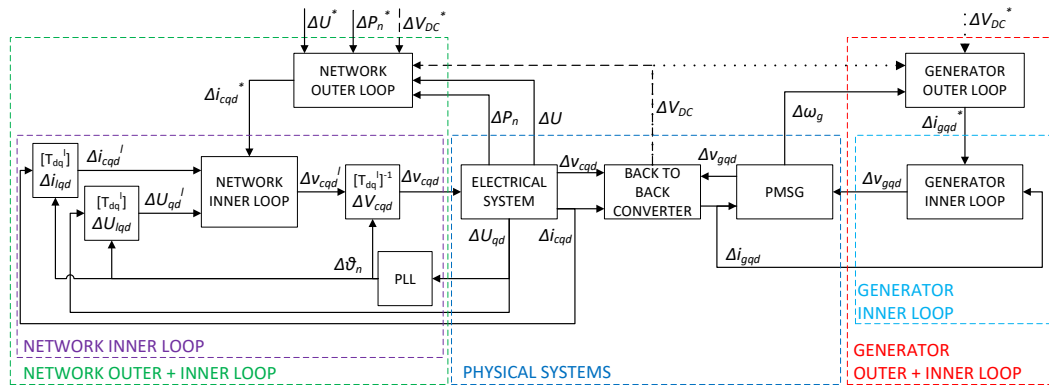


Figure 2.12: General Linearised Small-signal Model of GFL Controllers

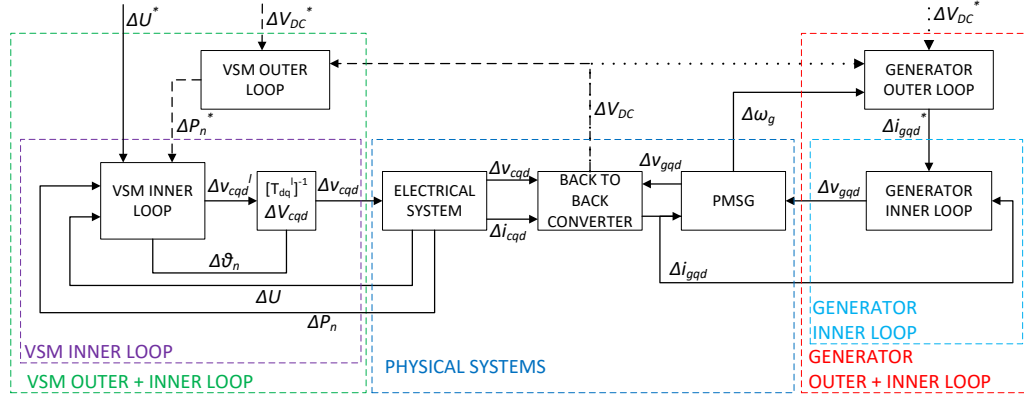


Figure 2.13: General Linearised Small-signal Model of GFM Controllers

This represents the small-signal models of the full system. In some studies the generator side is disregarded and the model only consists of components on the left side of the back to back converter. The DC link voltage control is disabled in these cases.

### 2.7.1 Power Calculation

Active and reactive power are calculated in the positive sequence synchronous reference frame (SRF) via:

$$P = i_q u_q + i_d u_d \quad (2.46)$$

$$Q = i_d u_q - i_q u_d \quad (2.47)$$

Where  $I_q$  and  $I_d$  are the converter q and d-axis current components, respectively and  $U_q$  and  $U_d$  are the PCC q and d-axis voltage components, respectively. Linearisation of each where subscript 0 denotes the initial operating point of the previously defined variables:

$$\Delta P = \frac{3}{2} (u_{q0} \Delta i_q + u_{d0} \Delta i_d + i_{q0} \Delta u_q + i_{d0} \Delta u_d) \quad (2.48)$$

$$\Delta Q = \frac{3}{2} (u_{q0} \Delta i_d - u_{d0} \Delta i_q - i_{q0} \Delta u_d + i_{d0} \Delta u_q) \quad (2.49)$$

### 2.7.2 PLL

The PLL has two linearisation possibilities depending on whether the negative sequence control is enabled, this is due to the inclusion of notch filters. The PLL is considered as a independent closed loop system described by a transfer function in the Laplace domain with d-axis PCC voltage input and converter angle output. For positive sequence only, assuming the frames are in alignment and the initial d-axis PCC voltage is zero:

$$\Delta\theta = -\frac{K_{p,PLL} \cos(\theta_0)s + K_{i,PLL} \cos(\theta_0)}{s^2 + K_{p,PLL} \cos(\theta_0)U_{q0}s + K_{i,PLL} \cos(\theta_0)U_{q0}} \Delta U_d \quad (2.50)$$

### 2.7.3 Park Transforms

The assumptions used to simplify the PLL equation can be applied to the Park and inverse Park transforms. Assuming the PLL has locked the converter frame to the global frame  $\theta_0 = 0^\circ$ . The only effect of the linearised transform is then due to a changing angle input:

$$T_{Park}(\theta) \rightarrow \begin{bmatrix} \Delta X_{q,p} \\ \Delta X_{d,p} \end{bmatrix} = \begin{bmatrix} 1 & 0 & -X_{d0} \\ 0 & 1 & X_{q0} \end{bmatrix} \begin{bmatrix} \Delta X_q \\ \Delta X_d \\ \Delta\theta \end{bmatrix} \quad (2.51)$$

$$T_{Inv,Park}(\theta) \rightarrow \begin{bmatrix} \Delta X_q \\ \Delta X_d \end{bmatrix} = \begin{bmatrix} 1 & 0 & X_{d0} \\ 0 & 1 & -X_{q0} \end{bmatrix} \begin{bmatrix} \Delta X_{q,p} \\ \Delta X_{d,p} \\ \Delta\theta \end{bmatrix} \quad (2.52)$$

Where  $X_q$  and  $X_d$  are the q and d-axis components of the variable in the initial frame,  $X_{q,p}$  and  $X_{d,p}$  are the Park transformed variables expressed in the converter frame and the subscript 0 denotes the initial conditions of the variable described.

### 2.7.4 Negative Sequence Transformation

Small-signal models can only be specified in a singular reference frame, in this case the positive sequence synchronous frame. Therefore, all negative sequence components must be transformed into the positive sequence frame. This is achieved via the following

transform:

$$\mathbf{X}_{c,qd}^+(s) = \begin{bmatrix} G_{qq}(s) & G_{qd}(s) \\ G_{dq}(s) & G_{dd}(s) \end{bmatrix} \quad (2.53)$$

$$G_{qq}(s) = \frac{1}{2}[G_{c,qq}^-(s - j2\omega_g) + G_{c,qq}^-(s + j2\omega_g)] \quad (2.54)$$

$$G_{qd}(s) = \frac{1}{2}[G_{c,qd}^-(s - j2\omega_g) - G_{c,qd}^-(s + j2\omega_g)] \quad (2.55)$$

$$G_{dq}(s) = \frac{1}{2}[G_{c,dq}^-(s - j2\omega_g) - G_{c,dq}^-(s + j2\omega_g)] \quad (2.56)$$

$$G_{dd}(s) = \frac{1}{2}[G_{c,dd}^-(s - j2\omega_g) + G_{c,dd}^-(s + j2\omega_g)] \quad (2.57)$$

Where  $\mathbf{X}_{c,qd}^+$  are the negative sequence SRF components expressed in the positive sequence SRF and  $G_{c,qq}^-$ ,  $G_{c,qd}^-$ ,  $G_{c,dq}^-$  and  $G_{c,dd}^-$  are the individual qq, qd, dq and dd negative sequence SRF components, respectively.

### 2.7.5 Negative Sequence PLL

When negative sequence control is enabled the PLL equation becomes more complex and to simplify the trigonometric functions are evaluated using an initial converter angle  $\theta_0 = 0^\circ$ . The PLL function is then:

$$\Delta\theta = -\frac{K_{p,PLL}Qs^2 + 4K_{p,PLL}Q\omega_g^2s + 4K_{i,PLL}Q\omega_g^2}{Qs^4 + A_{PLL}s^3 + B_{PLL}s^2 + C_{PLL}s + D_{PLL}}\Delta U_d \quad (2.58)$$

$$A_{PLL} = 2\omega_g + K_{p,PLL}QU_{q0} \quad (2.59)$$

$$B_{PLL} = 4Q\omega_g^2 + K_{i,PLL}QU_{q0} \quad (2.60)$$

$$C_{PLL} = 4K_{p,PLL}QU_{q0}\omega_g^2 \quad (2.61)$$

$$D_{PLL} = 4K_{i,PLL}QU_{q0}\omega_g^2 \quad (2.62)$$

### 2.7.6 Negative Sequence Park Transform

The negative sequence Park transforms can be formulated by multiplying the third column of the transform by  $-1$  and replacing the positive sequence inputs and outputs with the negative sequence counterparts. However, the negative sequence inverse Park

transform is slightly different, noting that due to small-signal modelling the transform is still a function of  $+\theta$ :

$$T_{Inv, Park, n}(\theta) \rightarrow \begin{bmatrix} \Delta X_{q, n} \\ \Delta X_{d, n} \end{bmatrix} = \begin{bmatrix} 1 & 0 & -2X_{d0} \\ 0 & 1 & 2X_{q0} \end{bmatrix} \begin{bmatrix} \Delta X_{q, pn} \\ \Delta X_{d, pn} \\ \Delta \theta \end{bmatrix} \quad (2.63)$$

### 2.7.7 Negative Sequence Notch Filters

The negative sequence notch filter functions are obtained via (2.53):

$$\mathbf{G}_{qd, -ve, notch} = \begin{bmatrix} G_{qq, notch} & G_{qd, notch} \\ G_{dq, notch} & G_{dd, notch} \end{bmatrix} \quad (2.64)$$

$$G_{qq, notch} = \frac{Q^2 s^4 + 2Q\omega_g s^3 + (4Q\omega_g)^2 s^2 + 16Q\omega_g^3 s}{Q^2 s^4 + 4Q\omega_g s^3 + ((4Q\omega_g)^2 + (2\omega_g^2))s^2 + 32Q\omega_g^3 s + 16\omega_g^4} \quad (2.65)$$

$$G_{qd, notch} = \frac{4Q\omega_g^2 s^2}{Q^2 s^4 + 4Q\omega_g s^3 + ((4Q\omega_g)^2 + (2\omega_g^2))s^2 + 32Q\omega_g^3 s + 16\omega_g^4} \quad (2.66)$$

$$G_{dq, notch} = -G_{qd, notch} \quad (2.67)$$

$$G_{dd, notch} = G_{qq, notch} \quad (2.68)$$

### 2.7.8 Negative Sequence Current Control

The two PI controllers regulating negative sequence current can be described in the positive sequence SRF as follows:

$$\begin{bmatrix} \frac{K_{p, ncc} + K_{i, ncc} s}{(s^2 + 2\omega_g^2)} & \frac{2\omega_g K_{i, ncc}}{(s^2 + (2\omega_g)^2)} \\ -\frac{2\omega_g K_{i, ncc}}{(s^2 + (2\omega_g)^2)} & \frac{K_{p, ncc} + K_{i, ncc} s}{(s^2 + 2\omega_g^2)} \end{bmatrix} \quad (2.69)$$

Where  $K_{p, ncc}$  and  $K_{i, ncc}$  are the negative sequence current controller proportional and integral gains, respectively.

### 2.7.9 Negative Sequence Voltage FeedForwards

The filtering of the negative sequence voltage feedforwards is the final component requiring transformation to the positive sequence frame:

$$G_{nff} = \begin{bmatrix} \frac{\tau_{nf}s+1}{\tau_{nf}^2s^2+2\tau_{nf}s+(1+(2\omega_g\tau_{nf})^2)} & \frac{2\tau_{nf}\omega_g}{\tau_{nf}^2s^2+2\tau_{nf}s+(1+(2\omega_g\tau_{nf})^2)} \\ -\frac{2\tau_{nf}\omega_g}{\tau_{nf}^2s^2+2\tau_{nf}s+(1+(2\omega_g\tau_{nf})^2)} & \frac{\tau_{nf}s+1}{\tau_{nf}^2s^2+2\tau_{nf}s+(1+(2\omega_g\tau_{nf})^2)} \end{bmatrix} \quad (2.70)$$

Where  $\tau_{nf}$  is the negative sequence voltage feedforward constant.

### 2.7.10 Grid-forming Park Transform

For small signal analysis the lack of PLL in GFM converters means the controller frame and grid frame are no longer locked together. This means the linearisation of the Park transforms becomes dependent on the angle between the frames and correct implementation is achieved via:

$$T_{Park}(\theta) \rightarrow \begin{bmatrix} \Delta X_{q,p} \\ \Delta X_{d,p} \end{bmatrix} = \begin{bmatrix} \cos(\theta) & -\sin(\theta) & -X_{q0}\sin(\theta) - X_{d0}\cos(\theta) \\ \sin(\theta) & \cos(\theta) & X_{q0}\cos(\theta) - X_{d0}\sin(\theta) \end{bmatrix} \begin{bmatrix} \Delta X_q \\ \Delta X_d \\ \Delta\theta \end{bmatrix} \quad (2.71)$$

$$T_{Inv,Park}(\theta) \rightarrow \begin{bmatrix} \Delta X_q \\ \Delta X_d \end{bmatrix} = \begin{bmatrix} \cos(\theta) & \sin(\theta) & -X_{q0}\sin(\theta) + X_{d0}\cos(\theta) \\ -\sin(\theta) & \cos(\theta) & -X_{q0}\cos(\theta) - X_{d0}\sin(\theta) \end{bmatrix} \begin{bmatrix} \Delta X_{q,p} \\ \Delta X_{d,p} \\ \Delta\theta \end{bmatrix} \quad (2.72)$$

Where  $\theta$  is the angle between the converter frame and the global reference frame that the network is described in and all other variables are the same as with the GFL transforms. The angle  $\theta$  becomes crucial when designing impedance based studies and great care is required to ensure it is correct.

### 2.7.11 DC Link

The power inputs to the DC link must be linearised via:

$$s\Delta\mathbf{v}_{DC} = \Delta\mathbf{v}_{DC} \frac{P_{MSC0} - P_{GSC0}}{C_{DC}V_{DC0}^2} + \frac{\Delta P_{GSC}}{C_{DC}V_{DC0}} - \frac{\Delta P_{MSC}}{C_{DC}V_{DC0}} \quad (2.73)$$

Where subscript 0 denotes the initial conditions of previously defined variables based on operating point.

### 2.7.12 Hardware Implications

It is likely that additional energy might be required to provide frequency enhancing services. Some methods look at running resources away from the maximum power point to leave headroom for response. However, this is wasteful and energy storage solutions (ESS) should be employed to provide extra energy when required. Note that the ESS will be required to be independent of the converter if the pre-existing converter hardware is not to be upgraded. Significant work exists on the review of ESS with technologies such as: flywheels, batteries and electric vehicles offering some promising options [121]. Battery systems are one of the most popular with current studies looking to find optimal sizing, chemical type and placement location [122].

Most RES interface with the grid in some way via a power electronic inverter. In the case of the Type III WT, a partially rated converter is used and others (Type IV WT, PV array, batteries) employ fully rated converters (FRC). In most cases it is favourable to extract maximum power from the resource for infeed to the grid. The power electronic devices impose a strict current limit of around 1.1 - 1.2 p.u. [123]. When operating at rated active power (1 p.u. current) there is little headroom for the RES to provide increased power to the grid for frequency and voltage support without damaging the switches. This can occur very quickly during over-currents as power electronics have very low thermal inertia [124]. Some suggestions are made to run the RES curtailed although this leads to reduced efficiencies in some systems [125], and therefore reduced revenue in normal conditions. However, in situations such as the restoration of the electricity network after a total blackout or during severe frequency



and voltage events, different commercial incentives will apply and it offers significant opportunity. Other studies focused on overrating the converter but this can also lead to reduced performance at rated power. Mondol et al. found that the oversized converter used for study in a grid connected PV system experienced poor performance due to partial load operation of the inverter. The oversized converter had a higher energy threshold, requiring more energy to start operation and caused higher loss at lower input conditions [126]. This may need to be considered depending on how much reserve power is required. In addition, extra cost would be incurred for a higher inverter capacity although some studies have shown increased reliability and reduced mean time to failure (MTTF) for oversized inverters [127].

## Chapter 3

# Equivalent Converter Output Impedance

### 3.1 Introduction

To appropriately select a method for analysing converter impedance, it is important to consider the mathematical structure of the studied system impedance and how that may affect the approach. For example, SISO systems offer ease of modelling and offer few concerns in determining system stability with margins that are intuitive and easy to interpret resulting in widespread application. However, in the context of power converters, SISO systems may not be capable of accurately representing converter control action when the resource is providing enhanced support to the network. In reality, a MIMO system description is required to obtain an accurate stability definition. Impedance based stability has been widely applied for both types of system in literature. However, model complexity is often lacking, utilising only standard grid following current controllers with complex functions disabled to facilitate easier analysis [30,31]. With more large power sources and loads becoming converter interfaced, grid conditions can vary rapidly and it is important that the remaining converters have the robustness to stay connected. These systems present unique analysis challenges by reducing the symmetry of frequency responses in different reference frames and hence, require more complex analysis.

This Chapter explores the use of SISO vs MIMO models for advanced converter controllers and showcases how MIMO admittance models are obtained from the models described in the previous Chapter. Verification is then provided indicating that the admittance models behave as intended. The mathematical structure of the models is investigated with a specific focus on diagonal dominance which is measured using a novel method based on calculating the participation factor between row and column of the admittance matrix across a range of frequencies. When the rating is greater than 0.7 the system can be considered diagonally dominant with the two channels behaving as two independent SISO functions where traditional stability techniques apply. When the rating is less than 0.7 generalised MIMO techniques must be applied to accurately characterise the system. The final contribution of the Chapter showcases that none of the proposed control topologies are diagonally dominant and that traditional stability techniques are not applicable for converters providing any form of enhanced grid service.

### 3.2 SISO vs MIMO

Simplified power converter models may lead to inaccurate small-signal stability assessments when considering IBRs participating in enhanced network support. In some cases, networks are modelled using SISO impedances or utilise transformations so that systems become diagonally dominant and can be analysed in a loop-at-a-time method. However, it is argued that SISO techniques are more intuitive and that the alternative (MIMO analysis) is hard to apply and stability margins are difficult to interpret [128].

To remedy this, work has been completed attempting to take MIMO system descriptions in the synchronous reference frame and analyse them using SISO techniques. Amico et al. proposed a technique stating that MIMO systems that are mirror frequency decoupled (MFD) in the synchronous reference frame can be transformed to the sequence domain where they become diagonally dominant (DD) [48]. A further work then proposes a stability technique based on this approach where a converter controller including negative sequence regulation is presented and shown to be DD in the sequence frame when the PLL is disabled [129]. SISO stability techniques are then applied and appear to offer promising results in determining the system stability. How-

ever, it is likely important interactions from the PLL have been removed from the study resulting in an incorrect stability analysis. This effect will be exacerbated in weak grids where the impact of PLL dynamics is greater. Xu et al. attempted to remedy this by proposing a symmetric admittance model in [130]. The work constructs an equivalent two-port circuit and states that oscillations of the original grid connected converter system can be considered as series resonances of the equivalent circuit meaning that PLL behaviour should be represented in the SISO system. However, the control topology disregards any further outer loop control that could reduce the efficacy of the equivalent system and remove the symmetrical property.

Further work to include the PLL was completed by Zhang et al. in [131] where the effect of PLL was modelled using a SISO system. The work presents both a MIMO and SISO system description and shows that the stability result obtained from the MIMO system can be obtained via analysis of three open-loop SISO systems describing the various controller loops. However, these loops are cascaded which means the method could suffer from issues with open-loop right half plane (RHP) poles leading to incorrect analysis. This issue is explored further in Chapter 4. Furthermore, no information is given on how to determine the robustness of the full MIMO system from analysis of the SISO loops. Work completed by Akhavan looked to extend this approach to include further complex system descriptions such as an asymmetrical grid by decomposing the MIMO system into two decoupled SISO systems [132]. However, in doing this a simplification was made disregarding the effect of PLL which provides an incorrect stability definition in a number of cases. It is clear that most research on SISO systems involves simplification or disregards key control components required to achieve an accurate system description. Therefore MIMO models offer a better approach in replicating the true behaviour of advanced control components and provide a more accurate stability definition. Bolzoni analysed the difference between SISO and MIMO models of power converters participating in grid frequency regulation in [46]. The main finding was that the SISO systems provided a greater deviation from the real model when compared to the MIMO version indicating the poor efficacy of SISO models when describing converter controllers participating in enhanced network support.

The main reason MIMO models are required is due to the reduction of DD of the admittance and impedance matrices when advanced control components are included. It is therefore important to highlight how these control components effect the mathematical composition of the admittance and impedance matrices. This chapter will demonstrate the effect of differing controller topology on the DD of the obtained equivalent converter output admittance. A method of rating DD based on the correlation coefficient between the rows and columns of the converter admittance matrix is proposed. Furthermore, recommendations on suitable situations where traditional stability analysis techniques are valid are provided based on the proposed method of DD rating. The novel contribution of this work lies in the determination of exactly where the limit of DD is for applying traditional SISO stability methods and which control components have the greatest effect on the rating. The chapter extends the understanding of why conventional SISO stability margins are not applicable for advanced grid-connected converters in most situations. Using the differing controller complexity, the failures of traditional margins are illustrated. The work observes that reduction of the DD of the admittance matrix causes SISO analysis techniques to fail. Stability analysis based on disk margins are suggested and implemented as an alternative in this work which can be applied irrespective of DD and offer a more realistic approach to considering robustness in the modern network [49].

### 3.3 Admittance Formulation

Obtaining the admittance of various network components can be achieved in different ways. For passive components, simple equations can be used to construct transfer function matrices. However, for more complex active systems the small-signal models described in Chapter 2 are utilised to obtain an impedance or admittance based on the voltage/current reaction to a current/voltage disturbance. This allows the control systems of converters and machines to be included in the output impedances and allows more accurate representation of the modern grid than just using the physical machine and line impedances.

Once the model is linearised the converter admittance is classified as the ratio of

the response current from the converter ( $\mathbf{I}_c$ ) to the voltage disturbance at the PCC ( $\mathbf{U}_{PCC}$ ):

$$\mathbf{Y}_c = \frac{\Delta \mathbf{I}_c}{\Delta \mathbf{U}_{PCC}} \quad (3.1)$$

The converter admittance is determined by the physical filter components and the control architecture. The capacitor between the RL filter and the PCC is not included but can be modelled as a load effect. To generate the admittance from the state-space matrix the model inputs and outputs are selected to be:

$$\mathbf{u} = \begin{bmatrix} \Delta u_{q,pcc} \\ \Delta u_{d,pcc} \end{bmatrix} \quad (3.2)$$

$$\mathbf{y} = \begin{bmatrix} \Delta i_{q,pcc} \\ \Delta i_{d,pcc} \end{bmatrix} \quad (3.3)$$

The state-space then represents the converter admittance:

$$\begin{bmatrix} Y_{qq,c} & Y_{qd,c} \\ Y_{dq,c} & Y_{dd,c} \end{bmatrix} = \frac{\mathbf{y}}{\mathbf{u}} = \frac{\Delta \mathbf{i}}{\Delta \mathbf{u}} \quad (3.4)$$

The impedances are modelled in the synchronous reference frame to ensure all interactions can be accounted for. This process can be completed for a state-space model of any network component.

### 3.4 Comparison and Verification of Controller Admittance

The different families of controller possess unique qualities in terms of impedance or admittance. GFL controllers act as current sources and therefore exhibit high output impedance. Conversely, GFM controllers operate as voltage sources and hence possess a very low output impedance. GS supporting structures provide an impedance somewhere in the middle depending on controller tuning. The output impedance of all converter control structures has been verified against frequency sweeps of time domain simulations

of the previously validated control structures with the results presented in this section. The frequency sweep is conducted by injecting voltage disturbances at the PCC with the converter disconnected from the grid. The resultant current reaction is measured and the converter admittance calculated by dividing by the injected voltage disturbances. Note the DC link is modelled as an ideal DC voltage source during validation.

### 3.4.1 PVCC

The SRF admittance of the PVCC controller (Figure 2.1) is provided in Figure 3.1.

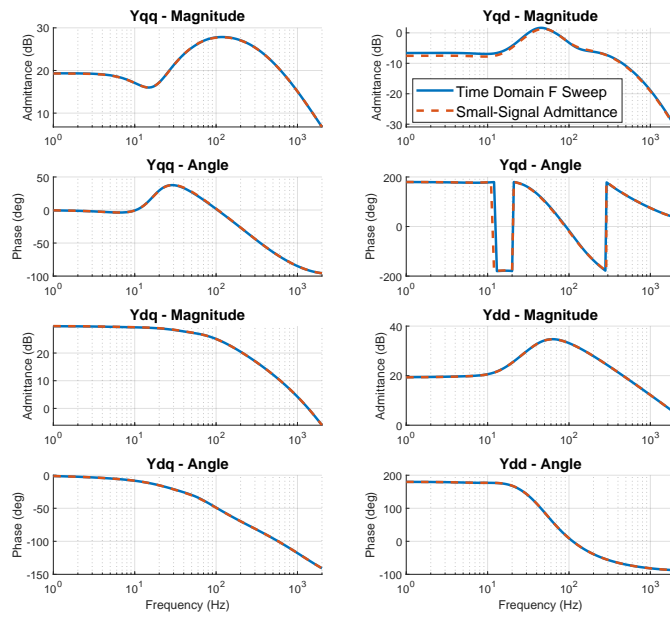


Figure 3.1: PVCC Admittance Model Verification

From Figure 3.1, a good match can be observed in all channels between the small-signal and time domain models. Small deviations in the cross coupling terms can be seen but this is due to a minute mismatch in the angle used for transformation between the abc-frame and SRF

### 3.4.2 PVCCI

The SRF admittance of the PVCCI controller (Figure 2.4) is provided in Figure 3.2.

## Chapter 3. Equivalent Converter Output Impedance

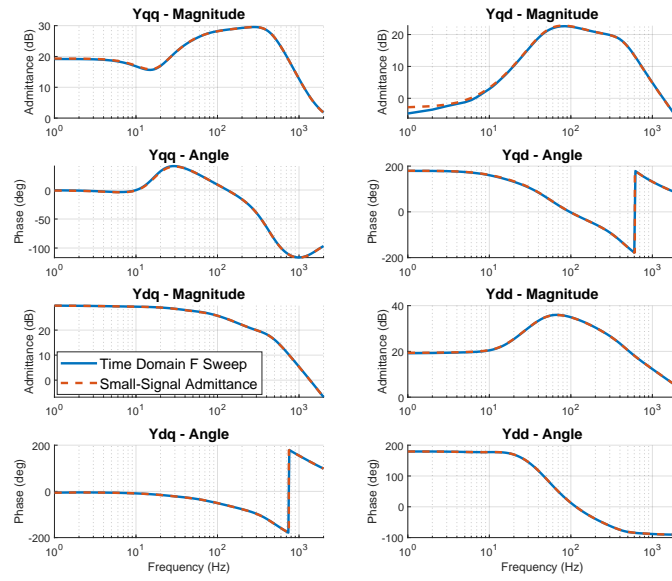


Figure 3.2: PVCCI Admittance Model Verification

From Figure 3.2, a good match between time domain and small-signal model is observed. The addition of the inertia loop has the effect of increasing the  $Y_{qq}$  admittance between (50 - 300 Hz) and a much flatter top is observed than with the standard PVCC controller. The  $Y_{dd}$  admittance is largely the same as the controllers employ the same voltage controller and PLL dynamics. However, the flatter top and larger peaks translate to the cross-coupled  $Y_{qd}$  admittance which is considerably larger and while the shape of the  $Y_{dq}$  admittance changes the magnitude remains similar.

### 3.4.3 PVCCD

The SRF admittance of the PVCCD controller (Figure 2.3) is provided in Figure 3.3.

From Figure 3.3, a good match can be observed in all channels between the small-signal and time domain models. Small deviations in the cross coupling terms can be seen but this is due to a minute mismatch in the angle used for transformation between the abc-frame and SRF.



## Chapter 3. Equivalent Converter Output Impedance

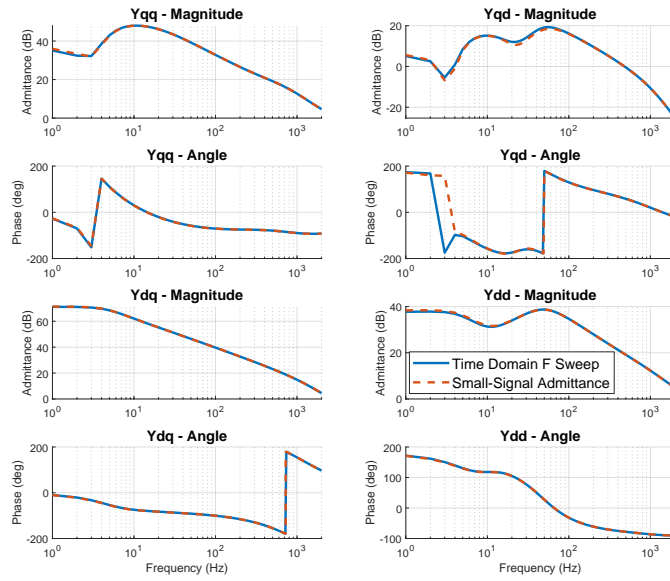


Figure 3.3: PVCCD Admittance Model Verification

### 3.4.4 GFMD

The SRF admittance of the GFMD controller (Figure 2.5) is provided in Figure 3.4.

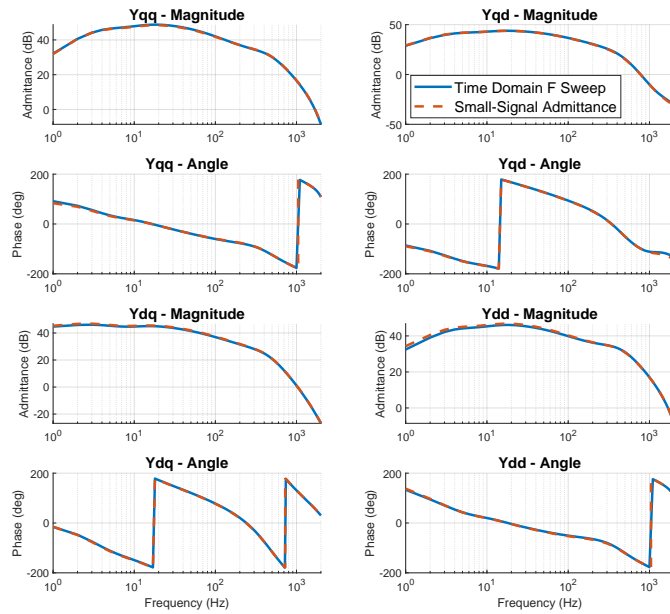


Figure 3.4: GFMD Admittance Model Verification

From Figure 3.4, it can be seen that the admittance throughout the frequency range

is much higher as expected with a GFM control structure. The trace is significantly smoother than any previous implementation that utilises a PLL.

### 3.4.5 VSMCC

The SRF admittance of the VSMCC controller (Figure 2.6) is provided in Figure 3.5 where a good match can be observed in all channels between the small-signal and time domain models. The small error at low frequency is due to a slight mismatch in dq-transformation angle in the models and poor resolution caused by taking 1 Hz intervals from time domain model. Similar to GFMD, the admittance trace is larger in the diagonal channels than the GFL implementations, a key feature of GFM technologies.

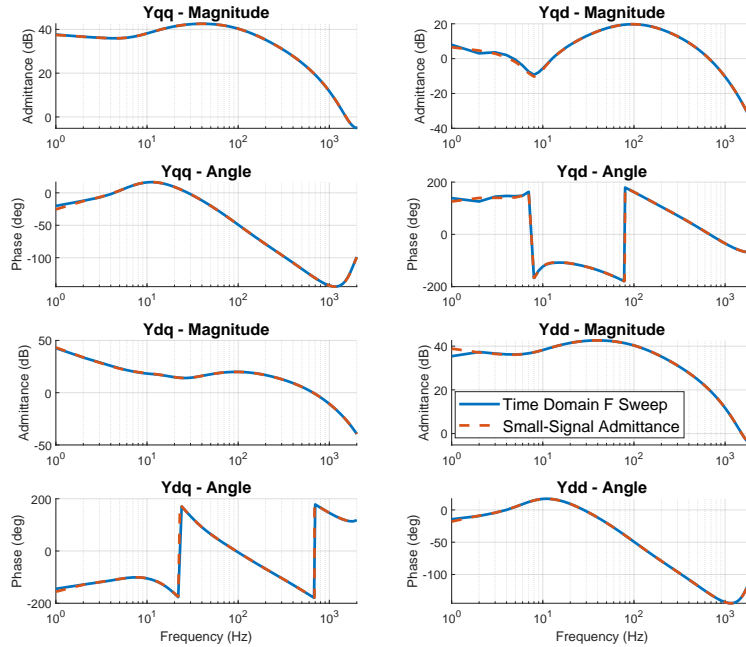


Figure 3.5: VSMCC Admittance Model Verification

### 3.4.6 VSM

The SRF admittance of the VSM controller (Figure 2.9) is provided in Figure 3.6 where a good match can be observed in all channels between the small-signal and time domain models. The small error at low frequency is due to a slight mismatch in dq-transformation angle in the models.

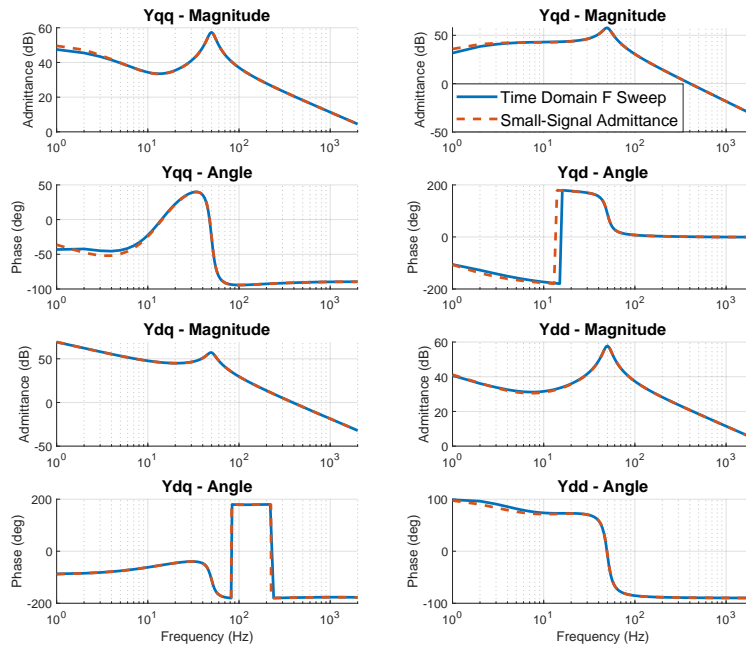


Figure 3.6: VSM Admittance Model Verification

### 3.5 Diagonal Dominance in MIMO Systems

As converter control becomes more complex, methods of determining robustness become increasingly vital to ensure converters remain connected. For SISO systems, this is usually achieved via gain and phase margins. Three issues arise in the case of grid-connected converters. Firstly, since the model usually forms a non-minimum phase (NMP) system the phase margin and associated design rules may not be valid as multiple crossings of 0 dB may be present throughout the frequency range. Secondly for MIMO systems, gain and phase margins can only be employed in a loop-at-a-time method. Therefore, inter-loop interactions are not considered. These interactions become especially important as the matrix off-diagonal terms increase in magnitude. Therefore, traditional phase and gain margins may be applicable for simple current control that is diagonally dominant but not for a fully-functional grid-connected converter. Thirdly, traditional phase and gain margins do not account for simultaneous changes in phase and gain which occur readily in real systems and can cause instability even if the individual phase and gain margins are large.

### Chapter 3. Equivalent Converter Output Impedance

For MIMO systems, approaches have been proposed where MIMO systems that are not DD in the reference frame they are described in are transformed into an alternative reference frame where analysis is simpler. It is extremely rare that any converter control structure will be diagonal dominant when described in the SRF. Even a simple current controller (CC) is not DD and is instead MFD where the off-diagonal terms are of the same magnitude but opposite polarity. The admittance of a simple CC in the SRF is provided in Figure 3.7.

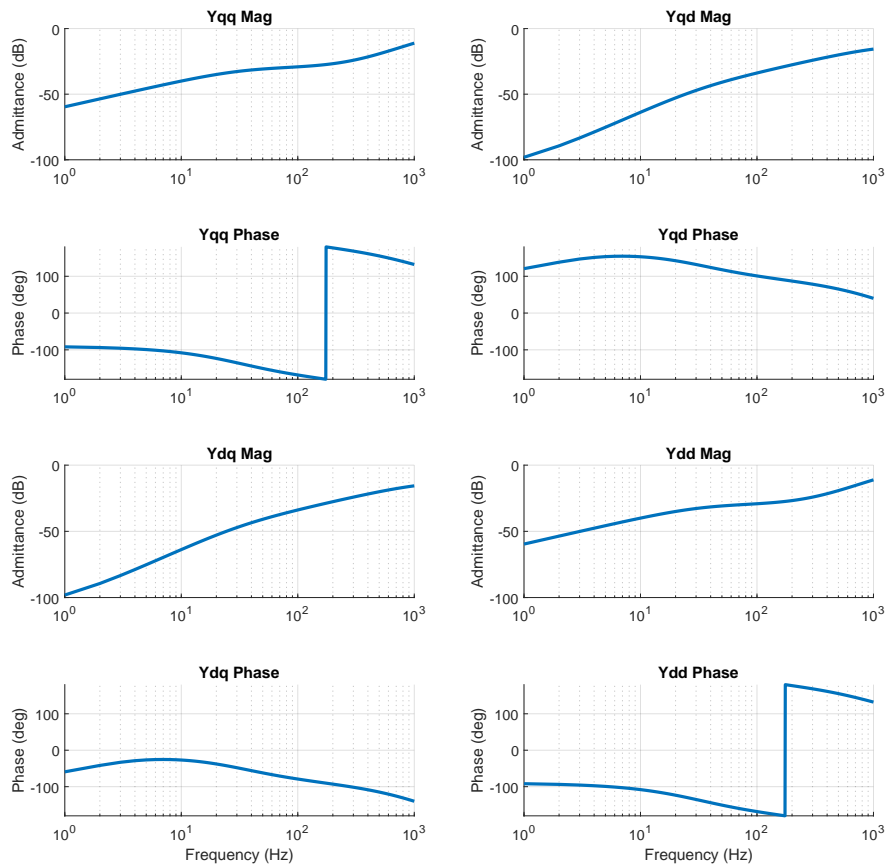


Figure 3.7: Current Control Equivalent Converter Admittance in the SRF

From Figure 3.7, the off diagonal terms have the same magnitude over the entire frequency range but the angles are separated by 180 degrees. Systems that are MFD in the SRF are DD in the modified sequence domain [48]. In this work, the sequence

frame admittances are obtained via transformation for the SRF via:

$$Y_{pp}(s) = \frac{1}{2}[Y_{qq}(s - j\omega_g) + Y_{dd}(s - j\omega_g)] - j[Y_{dq}(s - j\omega_g) - Y_{qd}(s - j\omega_g)] \quad (3.5)$$

$$Y_{pn}(s) = \frac{1}{2}[Y_{qq}(s - j\omega_g) - Y_{dd}(s - j\omega_g)] - j[Y_{dq}(s - j\omega_g) + Y_{qd}(s - j\omega_g)] \quad (3.6)$$

$$Y_{np}(s) = \frac{1}{2}[Y_{qq}(s + j\omega_g) - Y_{dd}(s + j\omega_g)] + j[Y_{dq}(s + j\omega_g) + Y_{qd}(s + j\omega_g)] \quad (3.7)$$

$$Y_{nn}(s) = \frac{1}{2}[Y_{qq}(s + j\omega_g) + Y_{dd}(s + j\omega_g)] + j[Y_{dq}(s + j\omega_g) - Y_{qd}(s + j\omega_g)] \quad (3.8)$$

The same system from Figure 3.7 is transformed to the sequence domain and shown in Figure 3.8. Additionally, a validation of this transform was completed by comparing the small signal admittance of the three GFL control structures with negative sequence enabled against time domain frequency sweeps in the sequence domain and is provided in Figure 3.9. The sequence domain is preferred for validating the NSC structures due to issues that occur with obtaining the correct angle for reference frame transformation when using the SRF for frequency sweeping the NSC structures.

From Figure 3.8, the magnitude of the off-diagonal terms are now approximately zero and the system can be considered DD. This is useful for analysing CC as the stability margins determined are not frame dependent. When CC is augmented with further control loops to regulate power and voltage, this MFD property can be maintained assuming the outer-loop control is tuned slow enough so as not to interfere with the CC. However, this is likely not recommended for the modern grid as tighter control of voltage and power will be required as SGs are removed from the network.

From Figure 3.9, a good agreement can be observed between the small-signal admittance models and the time domain frequency response in the modified sequence domain. This is with the exception of 50 Hz in all cases. This is due to the issues with obtaining an accurate measure of equivalent converter output impedance at 50 Hz where a singularity occurs. The small-signal admittance estimates the response of this pole whereas the response of the time domain simulation is dictated by how quickly the measurement is taken after the disturbance is injected. Since the PCC voltage is fixed and an injection at 50 Hz appears as an operating point change the converter continues to ramp current to try and correct the voltage which cannot be moved. This gives a

## Chapter 3. Equivalent Converter Output Impedance

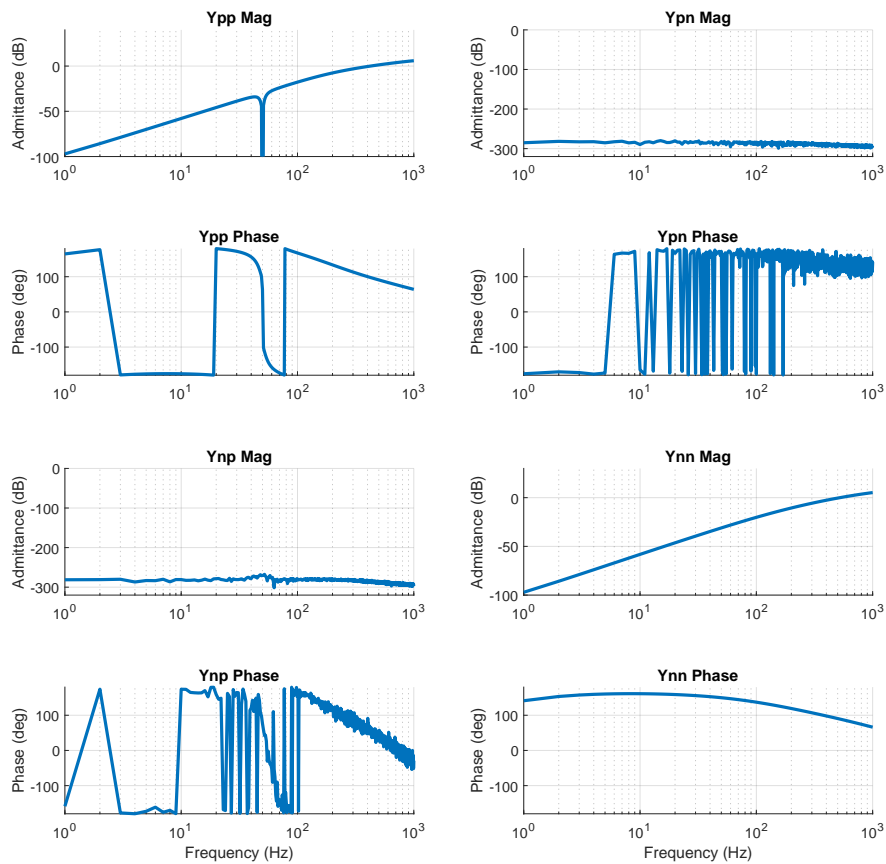


Figure 3.8: Current Control Equivalent Converter Admittance in the Sequence Frame

simplified description of the issues that occur when measuring impedance at 50 Hz. This issue is also present in the SRF but is not visible at the fundamental frequency (FF) in the SRF is 0 Hz which is not show on most Bode plots.

### 3.6 Measuring Diagonal Dominance

As the augmented control loops become more important for network stability the interactions they can cause within the controller may not be visible using traditional analysis techniques. When the power and voltage loops are tuned faster the MFD nature in the SRF is reduced and therefore, SISO analysis cannot be performed in either reference frame with the required confidence. Figure 3.10 illustrates the admittance traces in the sequence frame for the PVCC and PVCCN controllers described in Chapter 2.

From 3.10, it is clear that the addition of the outer loop control reduces the DD

### Chapter 3. Equivalent Converter Output Impedance

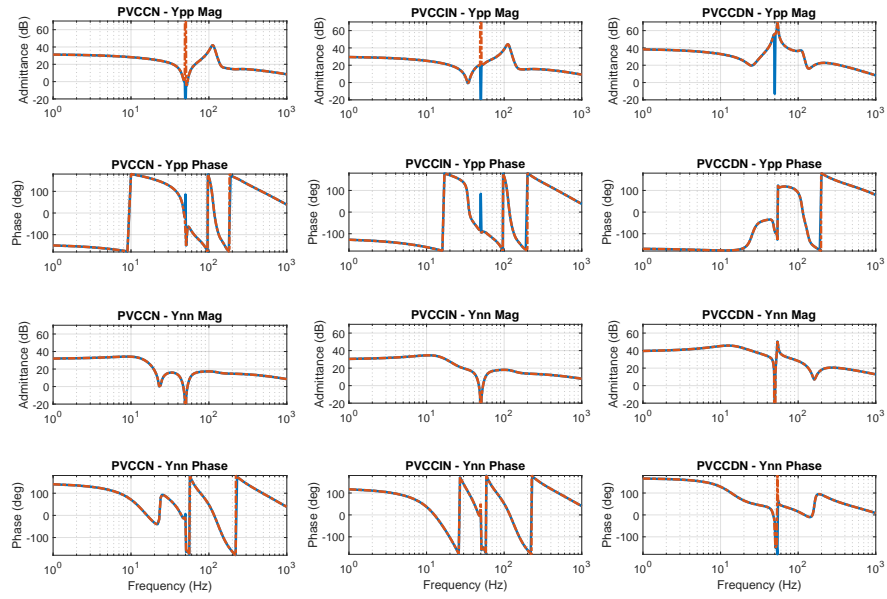


Figure 3.9: Validation of Negative Sequence Controllers in the Sequence Frame (solid blue: Time domain frequency sweep)(Dashed orange: Small-signal admittance)

property in the sequence frame and additionally, a greater variance is observed throughout the frequency range. When the NSC control is enabled, an even more complex trace is obtained due to various filters throughout the control structure which further exacerbates the issues with DD. It can be challenging to determine if a system is DD just from looking at the admittance trace and analysing the frequency response matrices across the range is not practical. Therefore, a novel method of determining the diagonal dominance of a system across a range of frequencies is proposed.

An easily scalable rating of DD can be obtained by calculating the correlation coefficient between rows and columns in the same matrix to obtain an  $r$ -value [133]. This value is equal to one when the matrix is diagonal, around zero when the matrix is uniformly distributed and -1 when the off-diagonal terms are dominant. This process is achieved by considering a square matrix  $A$  of size  $t$  by  $t$ , in this study the square matrix is the impedance ratio  $Z_g Y_c(s)$ , Three vectors then require specification:  $j$ , a  $k$ -long vector of ones,  $r = (1, 2, \dots, k)$  and  $r_2 = (1^2, 2^2, \dots, k^2)$ . The rating of diagonal

### Chapter 3. Equivalent Converter Output Impedance

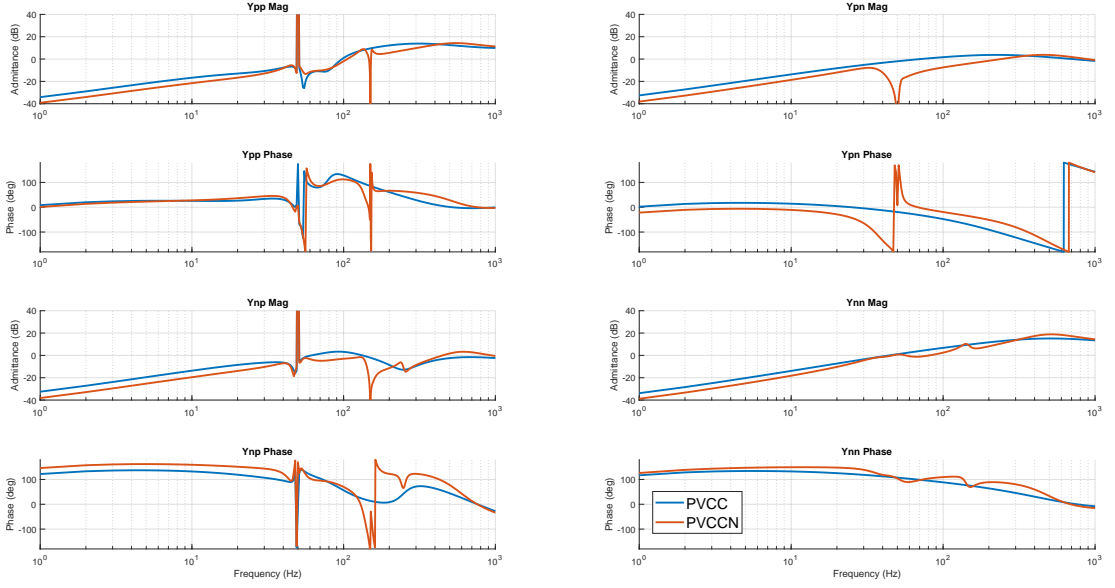


Figure 3.10: Current Control Equivalent Converter Admittance in the Sequence Frame

dominance  $D$  can then be found via:

$$D = \left| \frac{n\Sigma xy - \Sigma x\Sigma y}{\sqrt{n\Sigma x^2 - (\Sigma x)^2} \sqrt{n\Sigma y^2 - (\Sigma y)^2}} \right| \quad (3.9)$$

$$n = \mathbf{jA} \mathbf{j}^T \quad (3.10)$$

$$\Sigma x = \mathbf{rA} \mathbf{j}^T \quad (3.11)$$

$$\Sigma y = \mathbf{jAr}^T \quad (3.12)$$

$$\Sigma x^2 = \mathbf{r}_2 \mathbf{A} \mathbf{j}^T \quad (3.13)$$

$$\Sigma y^2 = \mathbf{jAr}_2^T \quad (3.14)$$

$$\Sigma xy = \mathbf{rAr}^T \quad (3.15)$$

The effect of each control component on DD can be analysed independently in the synchronous and sequence reference frames across a range of frequencies. The standard current control is used as a base case with all other systems including the PLL disabled. Each control component is then enabled independently and a measure of the DD in the SRF and sequence frames from (1 Hz - 1 kHz) is provided in Figure 3.11.



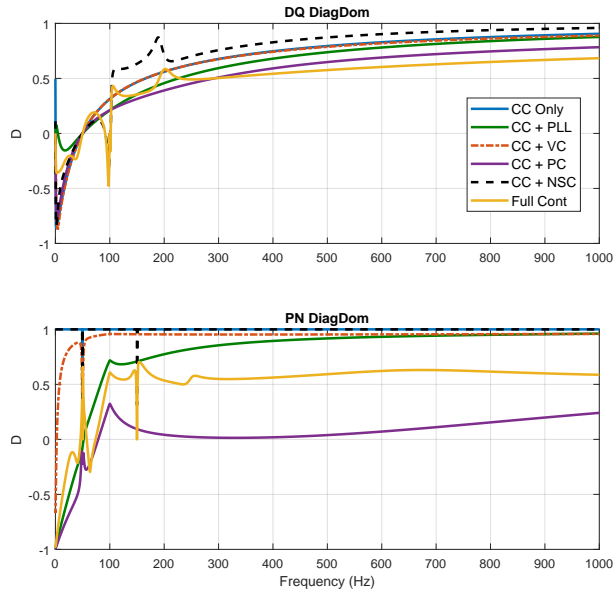


Figure 3.11: Current Control Equivalent Converter Admittance in the Sequence Frame

From Figure 3.11, no system is DD in the DQ domain below 500 Hz. Beyond this point the rating of current control (CC), current and voltage control (CC + VC) and current control with negative sequence (CC + NSC) are above 0.7 and can be considered diagonally dominant. When transformed into the PN frame both the positive and negative sequence current controllers retain DD despite the increased complexity introduced from NSC. The PLL provides a significant reduction in DD in both frames and is a crucial component for inclusion in stability studies. The VC reduces the DD at low frequencies but this effect is reduced at higher frequencies. The power control (PC) individually represents the worst rating of DD in both frames across a range of frequencies. However, it is the one control configuration that provides a greater D rating in the dq-frame compared to the pn. The DD in the pn-frame for VC and PC are directly related to the bandwidths of the outer-loop control. Traditional tuning rules would suggest that the outer-loop should be at least 10 times slower than the inner-loop to avoid interactions [134]. When this occurs the shape of the impedance ratio trace is dominated by the faster current loop and DD is maintained when the outer-loop control is enabled. However, this traditional tuning recommendation may not be sufficient for the more antagonistic grid conditions observed in the modern network. When the

outer-loop control is faster the system is no longer DD.

### 3.7 The effect of Diagonal Dominance on SISO Stability Analysis

This section explores how the rating of DD effects the efficacy of traditional stability margin techniques and determines an appropriate limit for their application.

#### 3.7.1 Traditional SISO Gain Margin

Traditional SISO gain margins determine the amount of gain variation a system can tolerate before going unstable. Mathematical, if gain margins denoted  $K_{gm}$  are determined for a system  $Y(s)$  then the system at the stability limit is given by  $K_{gm}Y(s)$ . This can be extended to MIMO systems that are diagonally dominant, in this case a 2x2 transfer function matrix  $\mathbf{M}(s)$  via:

$$\mathbf{M}_{lim}(s) = k_{gm}\mathbf{I}_2\mathbf{M}(s) \quad (3.16)$$

Where  $\mathbf{M}_{lim}(s)$  is the function on the limit of stability and  $\mathbf{I}_2$  is an identity matrix of rank two. This approach is applied to the systems shown in Figure 3.11 by first calculating the SISO gain margins of each systems impedance ratio in both the SRF and the sequence frame. The minimum value across the 2x2 matrix is taken to be the gain margin in each case. The results are provided in Table 3.1.

Table 3.1: Comparison of SISO gain margins for controllers

Controller	Gain Margin (GM)		GM Freq. (Hz)		D at GM Freq.	
	dq	pn	dq	pn	dq	pn
CC	12.2	3.85	3.18	53.2	-0.844	1
CC+ PLL	3.47	3.1	57	102	0.035	0.712
CC+ VC	12.4	3.95	3.26	53.3	-0.835	0.868
CC+ PC	25.1	$\infty$	13.1	n/a	-0.176	n/a
CC+NS	10	2.07	3.17	151.7	-0.787	1
Full Cont	10.2	2.1	45.3	151.7	-0.116	0.638

From Table 3.1, the rating of DD for the DQ-frame margins is always approximately zero or lower and the gain margins are significantly larger in most cases compared to the pn-frame where the DD is larger. The margins are frame independent meaning the pn-frame margins can be applied to the dq-frame system and vice versa. This is shown in Figure 3.12 which compares the application of the SISO gain margins determined in each frame via Nyquist plots of the most sensitive eigenloci.

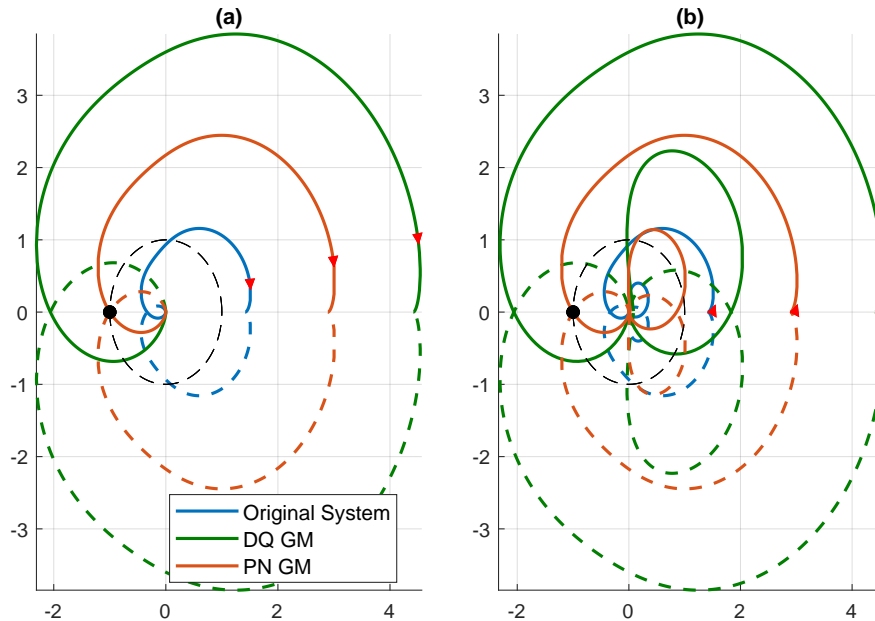


Figure 3.12: Comparison of SISO gain margins for CC (a) SRF (b) sequence frame

From Figure 3.12(a), the dq-frame GM overshoots the critical point while the pn-frame GM estimates the limits of stability correctly. This is expected from the DD ratings obtained in Table 3.1. The same result is obtained when the GM is applied to the pn-frame system in Figure 3.12 (b). The GMs obtained for the remaining systems have been applied to the dq-frame system and the resultant Nyquist plots of the most sensitive eigenloci are provided in Figure 3.13. The percentage error measuring the minimum distance from the Nyquist plot to the critical point is shown in Table 3.2.

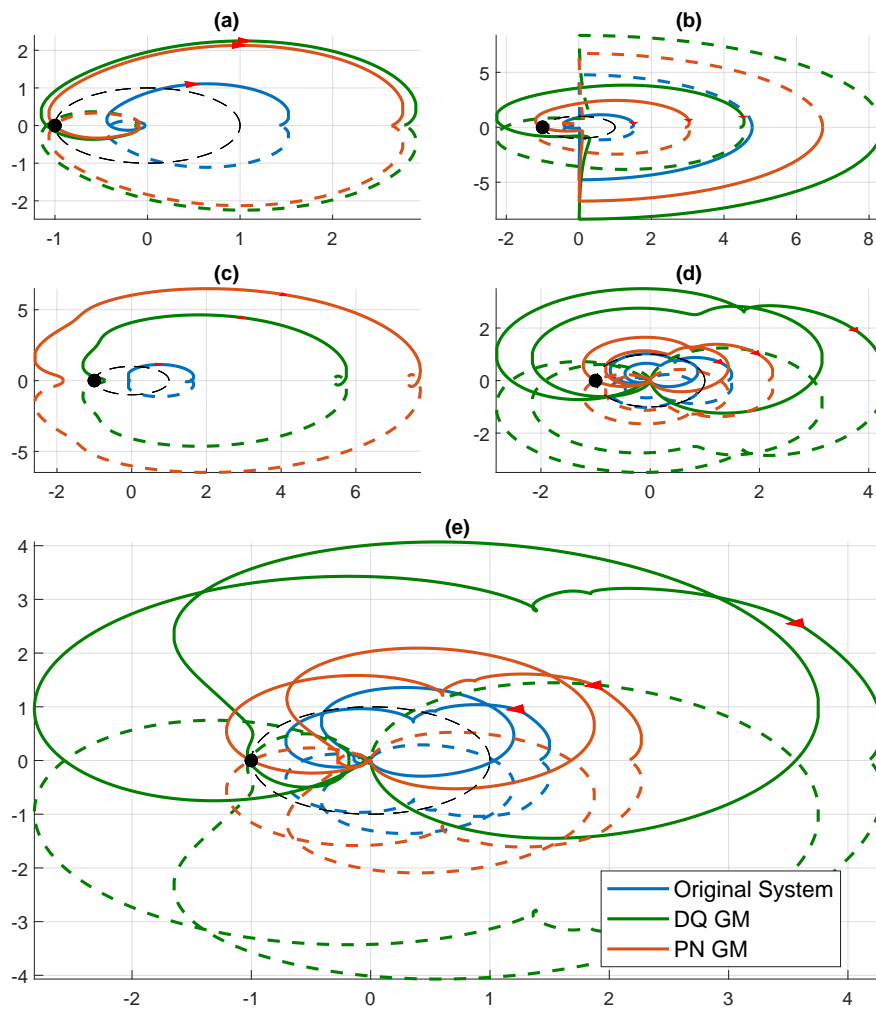


Figure 3.13: Application of SISO dq and pn phase margins to (a) CC + PLL (b) CC +VC (c) CC + PC (d) CC + NSC (e) Full Control

From Figure 3.13 (a), the GM obtained when the PLL is included is similar in both frames with the dq-frame providing a slightly higher GM. This results in the Nyquist plot passing through the critical point when the pn-frame GM is used. The percentage error is still small for the pn-frame margin but significantly larger than the error obtained for CC when the system was completely DD. Similar results are obtained with the plots shown in Figure 3.13 (b)(d)(e) with the pn-frame margin always obtaining a better rating of stability margins due to the higher DD rating. From the obtained results, a D rating of 0.6 or higher appears sufficient for the system to be considered diagonally dominant and the for the application of traditional SISO gain margins to

be valid. The addition of the PC shown in Figure 3.13 (c) offers some concern as GM could be obtained in pn-frame, likely due to reduced DD throughout the entire frequency range. While the dq-frame GM appears to provide a correct measure, the trace significantly undershoots the critical point very close to the real axis. The pn-frame margin is assumed a very large number of 100 as infinite is not possible. This overshoots the critical point and indicates that the original margin of infinity is clearly incorrect. The DD for the PC in pn-frame only reaches above 0.6 when singularities occur in the impedance ratio and are likely not representative of the real system at that frequency.

Table 3.2: Percentage error for SISO gain margins

Controller	Percentage Error (%)		D	
	dq	pn	dq	pn
CC	106	0.05	-0.844	1
CC + PLL	9	0.6	0.035	0.712
CC + VC	104	-0.03	-0.835	0.868
CC + PC	-28.65	82.7	-0.176	n/a
CC + NS	154	0.06	-0.787	1
Full Cont	157	0.23	-0.116	0.638

### 3.7.2 Traditional SISO Phase Margin

The rating of DD can further analysed by the traditional SISO phase margins (PM) on the considered systems which are provided in Table 3.3.

Table 3.3: Comparison of SISO phase margins for controllers

Controller	Phase Margin (PM)		PM Freq. (Hz)		D at PM Freq.	
	dq	pn	dq	pn	dq	pn
CC	-126 °	-95 °	126	96.3	0.403	1
CC+ PLL	-108 °	-100 °	509	448	0.761	0.907
CC+ VC	-126 °	-96.8 °	127	96.8	0.408	0.956
CC+ PC	-108 °	-101 °	511	391	0.692	0.709
CC+NS	-119 °	-59.5 °	183	153	0.817	1
Full Cont	-61.1 °	-60.5 °	254	258	0.491	0.578

From Table 3.3, the phase margins are generally obtained at higher frequencies where the impedance ratio is naturally more diagonally dominant as the physical inductance becomes more prevalent with increasing frequency. The DD rating in the pn-frame is large enough to be considered almost perfectly DD in most cases excluding the full controller. The dq-frame phase margins should be more applicable than the GM due to the increased value of D at higher frequencies. The application of the PMs is provided Figure 3.14 by rotating the Nyquist plots of the original system. Note that both eigenloci are provided for CC + PC in Figure 3.14 (d)(e) and CC + NSC in Figure 3.14 (f)(g) as both eigenloci were sensitive to phase variations unlike the previous applied gain variations. The percentage error indicating the maximum error in the direction of the imaginary axis is shown in Table 3.4.

From Figure 3.14 (a)(b)(c), similar results are obtained for PM application as for GM. The pn-frame PM provide the most accurate stability margins due to the significantly higher D rating. The percentage error for the dq-frame margins are also lower which is in agreement with the D rating obtained compared to the GM errors shown in Table 3.2. The only exception is when the PLL is added. For the PM, the D rating is 0.761 and an error of 14 % is obtained, which is acceptable but slightly higher than expected. The rating of DD does not have a linear relationship with the error obtained due to the complex nature of analysing the MIMO eigenloci. This is most obvious around for margins obtained around 50 Hz in the dq-frame, likely due to harmonics and control components providing singularities around these frequencies. The error obtained for the margins is not only dependent on DD but the magnitude and phase of the impedance ratio at the given frequency. However, when the D rating is above 0.7 the efficacy of traditional margins is evident and independent of these other factors. When the rating is below 0.7, an error will be obtained and generally, the lower the D rating the greater the error obtained with some exceptions.

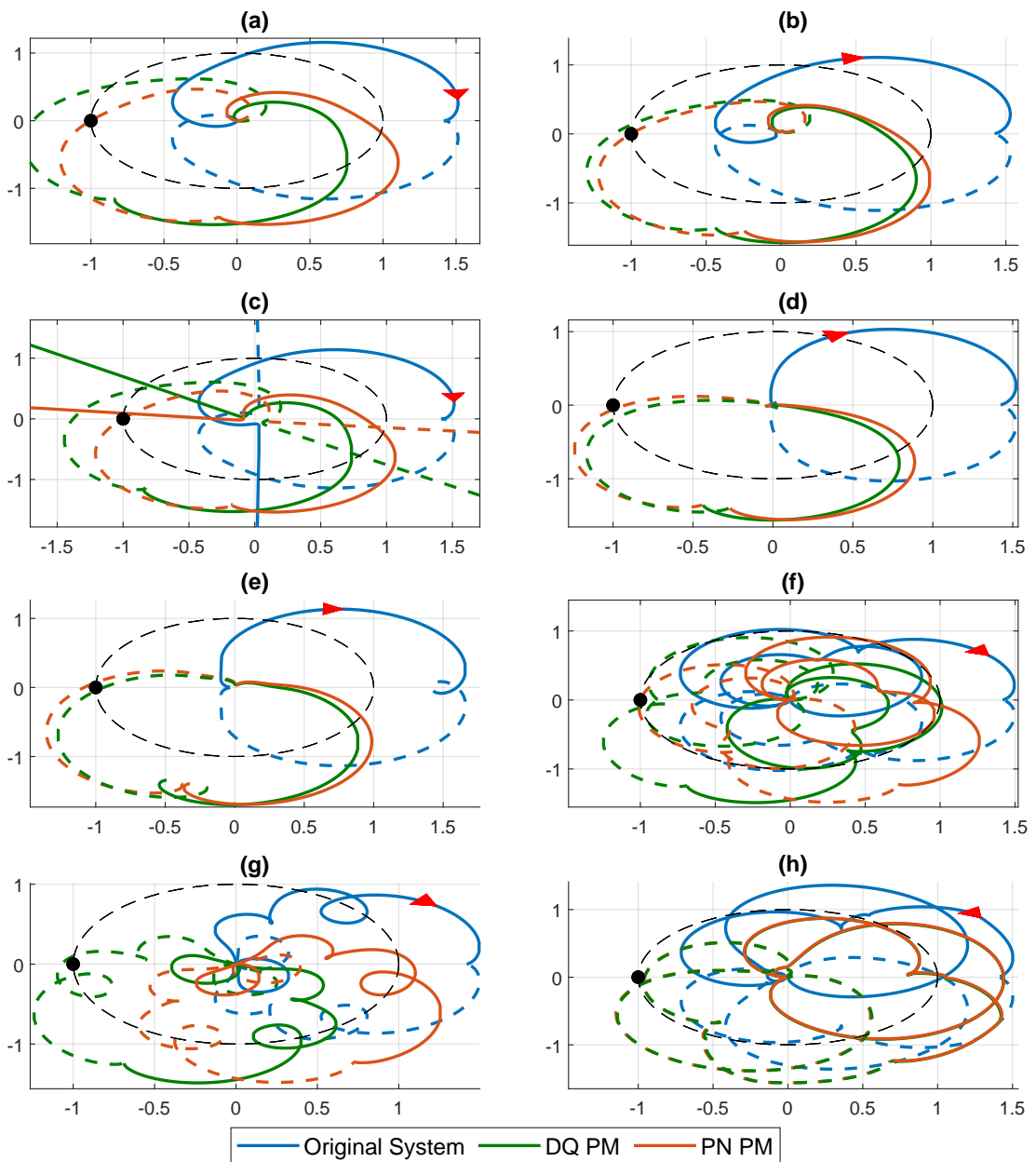


Figure 3.14: Application of SISO dq and pn phase margins to (a) CC (b) CC +PLL (c) CC + VC (d) CC + PC 1st Loci (e) CC + PC 2nd Loci (f) CC + NSC 1st Loci (g) CC + NSC 2nd Loci (h) Full

Table 3.4: Percentage error for SISO phase margins

Controller	Percentage Error (%)		D	
	dq	pn	dq	pn
CC	45	0.11	0.403	1
CC + PLL	14	0.3	0.761	0.907
CC + VC	43	0.3	0.408	0.956
CC + PC	-4.9	-5.9	0.692	0.709
CC + NS	9.8	0.05	0.817	1
Full Cont	-13.1	-11.8	0.491	0.578

### 3.8 Disk Margins for Robust MIMO Stability Analysis

Disk margins have been proposed as a method to tackle these issues in MIMO systems and can be applied irrespective of DD [49]. Disk margins can consider complex perturbations in all loops at once to give a better idea of real stability margins and are applicable to NMP systems. This is particularly important in grid-connected converters considering that  $3\phi$  perturbations from the network will extremely rarely result in a single channel reaction in the synchronous reference frame controller. With disk margins, gain and phase margins are considered as a complex multiplicative factor  $f$ , of the form:

$$f \in D(\alpha, \sigma) = \left\{ \frac{1 + \frac{1-\sigma}{2}\delta}{1 - \frac{1-\sigma}{2}\delta} : \delta \in \mathbb{C}, |\delta| < \alpha \right\} \quad (3.17)$$

Where the set  $D(\alpha, \sigma)$  defines the complex set of perturbations. If the disk skew factor  $\sigma$ , is selected to be 0 the overall perturbation gain can increase or decrease by the same magnitude. In this case the open-loop system is the impedance ratio:

$$L = Z_g Y_c \quad (3.18)$$

Where  $L$  is the loop gain,  $Z_g$  is the grid impedance and  $Y_c$  is the converter admittance. The disk margin can then be defined as the maximum value of  $\alpha$  that allows  $fL$  to remain stable for all  $f \in D(\alpha, \sigma)$ . If the set of possible system perturbations is known, the disk skew can be altered to more accurately cover the real system variations. For MIMO systems, the multiplicative factor  $f$  is applied to each channel individually for



loop-at-a-time (LAT) margins or two factors  $f_1, f_2 \in D(\alpha, \sigma)$  applied simultaneously to both input channels for multi-loop (ML) margins. The loop-at-a-time and all-loop disk margins for each system in the dq-frame are compared in Table 3.5 and Table 3.6, respectively. The dq-frame is used to indicate the improvement in determining stability margins in systems that are not diagonally dominant.

Table 3.5: Comparison of Loop-at-a-time disk margins for controllers

<b>Cont</b>	<b>Disk GM</b>	<b>Disk PM</b>	<b>Frequency (Hz)</b>	<b>D</b>
CC	8.37	$\pm 76^\circ$	4.8	-0.792
	8.37	$\pm 76^\circ$	4.8	
CC+ PLL	8.48	$\pm 76^\circ$	10.7	-0.126
	3.29	$\pm 56^\circ$	11	
CC+VC	8.53	$\pm 76^\circ$	4.8	-0.860
	10.8	$\pm 79^\circ$	4.8	
CC+ PC	49.2	$\pm 88^\circ$	0	0
	10.8	$\pm 79^\circ$	103	0.218
CC+ NSC	2.36	$\pm 44^\circ$	102	-0.070
	2.36	$\pm 44^\circ$	102	
FULL	2.67	$\pm 49^\circ$	102	-0.077
	2.27	$\pm 42^\circ$	102	

From Table 3.5, the minimum LAT GM is always lower than the SISO gain margins determined in Table 3.1 in the dq-frame. However, in most cases the LAT GM is higher than the pn-frame GM obtained. This is due to the LAT GM being designed for a single channel and will overestimate margins if applied to more than one channel simultaneously. Despite the pn-frame margins being of a similar SISO nature to LAT, the same effect is not observed due to the increased DD in the pn-frame. Hence, the gain variation is smaller and can be applied to both channels. Furthermore, the LAT PMs obtained are also significantly lower than the traditional SISO PMs found in Table 3.3. This effect is exacerbated for the more complex control, especially when including NSC due to the complex nature of the Nyquist trace previously discussed. This indicates that the disk margin method may offer a more realistic measure of stability irrespective of the D rating which is low in each case with no system being considered close to DD.

Table 3.6: Comparison of Multi-loop disk margins for controllers

Cont	Disk GM	Disk PM	Frequency (Hz)	D
CC	2.85	$\pm 51^\circ$	5.6	-0.763
CC + PLL	2.78	$\pm 50^\circ$	10.8	-0.123
CC + VC	2.97	$\pm 53^\circ$	5.7	-0.821
CC + PC	8.28	$\pm 76^\circ$	95.4	0.197
CC +NSC	1.65	$\pm 28^\circ$	102	0.07
FULL	1.69	$\pm 29^\circ$	102	0.077

From Table 3.6, the ML disk margins offer the most conservative measure of stability with the smallest ratings. This is expected and guarantees stability for a range of combinations of perturbation that could be possible in the electrical network. The frequencies at which the system is considered sensitive to gain and phase variations are largely in agreement with the frequencies obtained for the LAT margins and hence, the D rating is the same. The ML GMs are much lower showing that the system is far more sensitive to variation than previously thought with traditional SISO margins and LAT margins. The same is observed for the phase margins. This effect increases as the complexity of the system increases and appears independent of DD. The LAT and ML disk margins are applied to the CC system in Figure 3.15 via Nyquist plots of the worst case eigenloci. The remaining systems are plotted in Fig. 13. Note that both eigenloci are plotted in Fig. 13 (c)(d) for the CC + PC system due to the differing effect of the applied margins.

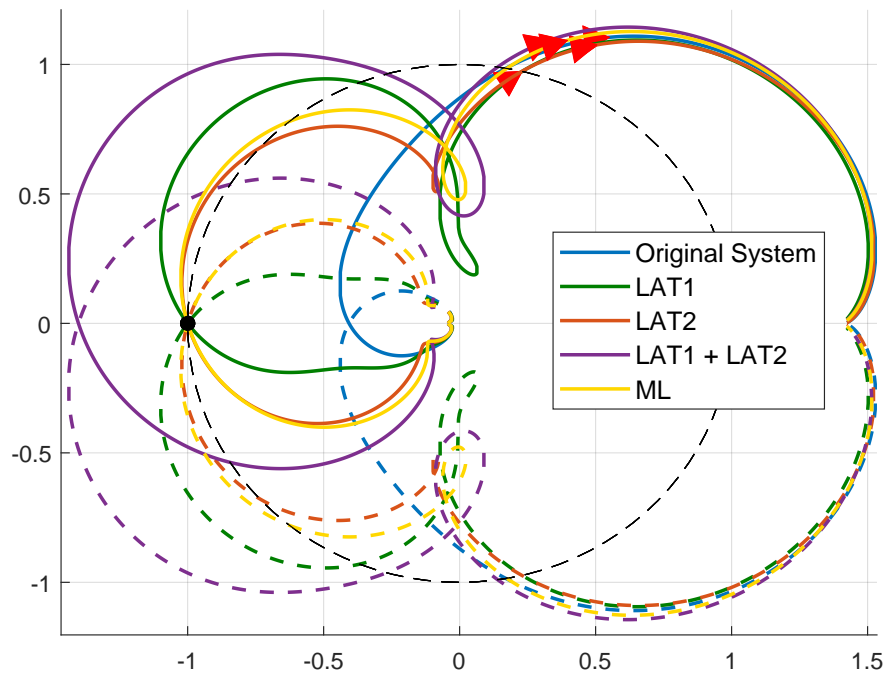


Figure 3.15: Comparison of LAT and ML disk margins for CC system

From Figure 3.15, each LAT and the ML margin predicts the stability limit exactly with simultaneous gain and phase variations. When the LAT margins are combined the stability limit is largely overestimated in the case of the CC system. The introductions of the simultaneous gain and phase variations does introduce some complicated loops in the Nyquist traces that are not previously present. A table of errors is not provided as the error is always less than 0.5 % except for the combined LAT margins where the error is very large with one exception.

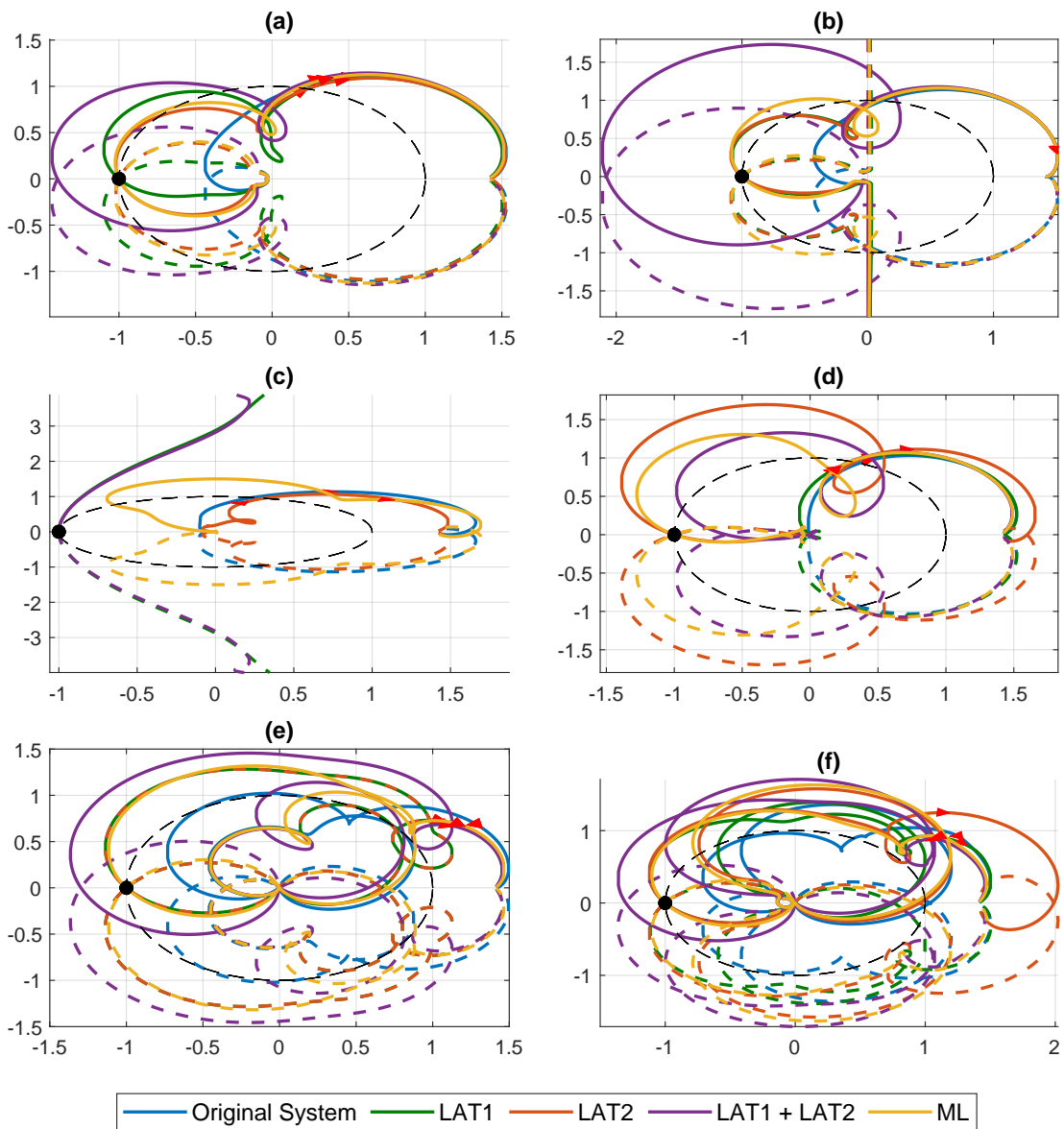


Figure 3.16: Comparison of LAT and ML disk margins for (a) CC + PLL (b) CC + VC (c) CC + PC 1st loci (d) CC + PC 2nd loci (e) CC + NSC (f) Full Control

From Figure 3.16, the result that was observed for CC is repeated for most of the more complicated systems. The LAT disk margins provide the most accurate assessment of simultaneous gain and phase variation for a single channel perturbation. However, this very rarely occurs and in most cases using the traditional SISO margins is likely preferable in the pn-frame where the D rating is above 0.7. The CC + PC system eigenloci shown in Figure 3.16 (c)(d) provide an interesting result where the

combination of the two LAT margins provide almost the same results as the ML margins. Moreover, the individual LAT margins effect the 2nd eigenloci driving it towards instability while the combined LAT and ML margins shift the 1st eigenloci toward the critical point. This is interesting as the ML margin appears much smaller than the combination of LAT margins but suggests that the axis with the large LAT margin is actually very robust to any variation. This also explains the reason for the poor measure from the traditional SISO margins which provided the greatest error.

The SISO margins are simpler and more widely recognised so should be used where applicable. However, for the real network ML disk margins offer the best approach achieving the exact stability margins envelope that the system can handle. This includes simultaneous gain and phase variations in all loops at once which is representative of the real system. This allows the control design to be more robust for the modern network with a higher penetration of converter connected generation which does not form diagonally dominant impedances across the frequency range.

To showcase the requirement for both MIMO modelling and generalised stability techniques for converter controllers providing enhanced grid services, the diagonal dominance of each control structure admittance described in Chapter 2 is provided in both the synchronous and modified sequence domains in Figure 3.17. Three active power operating points are used considering connection to a network with SCR of 2. Plots for the same control structures at SCR of 4 and 6 are shown in Figure B.1 and Figure B.2, respectively in Appendix B. From Figure 3.17, it can be seen that no control structure is DD in either reference frame in the frequency ranges of interest. If a traditional margin was obtained above 300 Hz in the SRF for the GFM control the robustness could be valid. However, due to the poor DD in the lower frequency ranges it is highly likely less robust point will be missed. In the sequence domain the grid formers again offer better DD above 100 Hz but the ratings of -1 at lower frequencies cause issue. This further proves the requirement for MIMO modelling and MIMO analysis techniques. The disk margin approach used in this chapter is applicable for any of the control structures discussed while the traditional SISO margins would fail spectacularly.

Chapter 3. Equivalent Converter Output Impedance

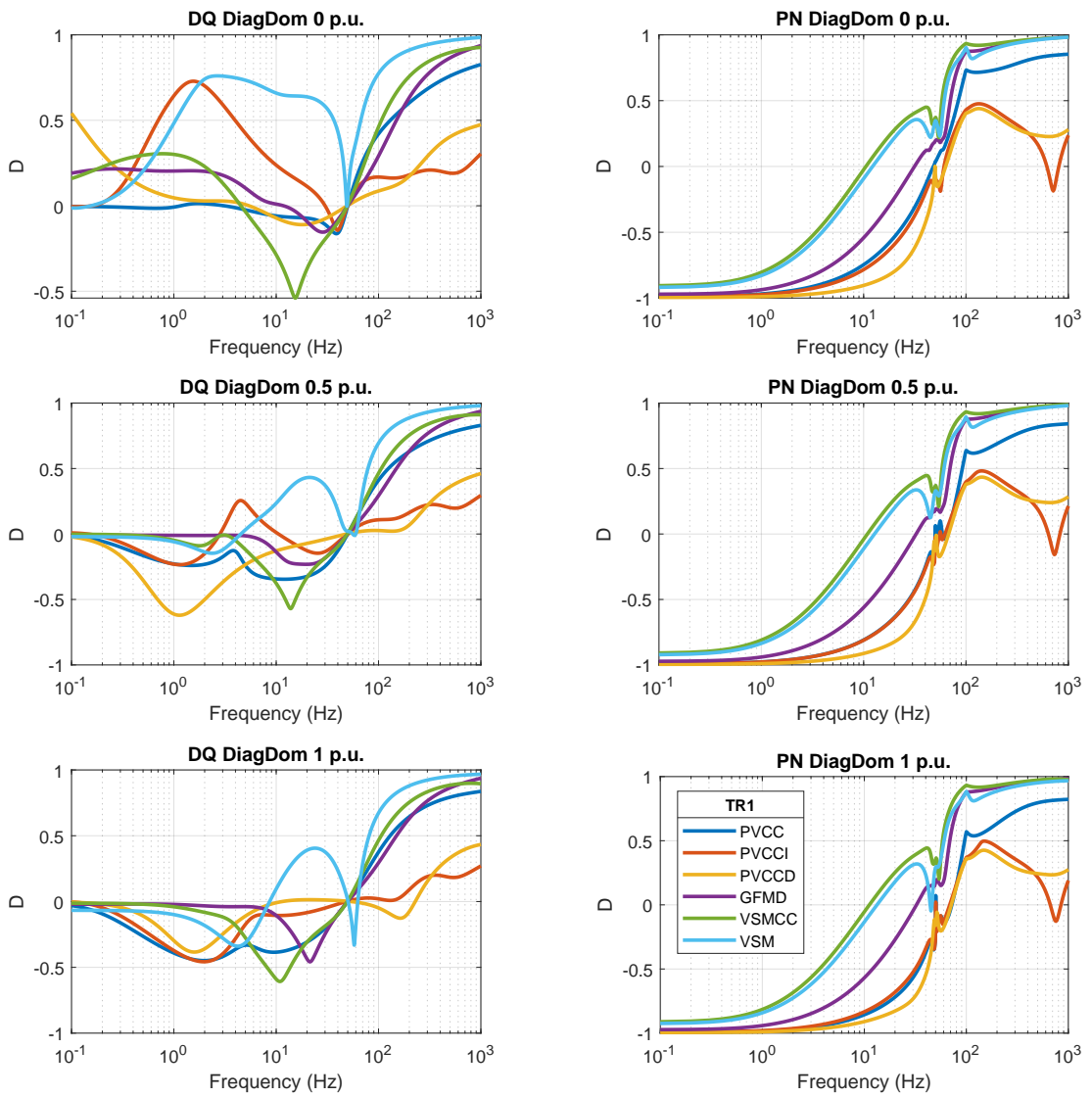


Figure 3.17: Comparison of Diagonal Dominance of Controllers for Varying Operating Point at SCR = 2

## Chapter 4

# Impedance-Based Stability

### 4.1 Introduction

Impedance-based stability analysis has been widely applied for decades [135]. Studying the impedance between sources provides useful information on how they may interact. A number of approaches exist and will be discussed in this chapter. Both SISO and MIMO techniques are explored with SISO analysis only applicable in some specific simplified scenarios. Some methods are more applicable in black-box scenarios where the converter control structure is unknown. However, if an accurate converter is available similar to the topology listed in Chapter 3, then other methods can be more efficient and intuitive. The chapter begins by describing the methodology for a single-converter system using SISO descriptions before showing the adaptations required for MIMO analysis. The idea is then extended to multi-converter systems where a novel analysis approach is presented which is a distinct contribution of this work. The method reduces the reliance on avoiding open-loop RHPs and allows a more varied selection of system views. This approach means different modes of stability can now be investigated. The common mode of converters which is the combined effect of all converter on the network and the differential mode of a single converter which is the effect of the remaining network on the specific converter.

The main findings from the common mode study indicate that the network experiences more stable operation when GFM converters are connected at a further electrical

distance while GFL converters should be closer. However, from the point of view of the converter at the end of the long line, the converter exhibits better operation if the GFM converter is connected closer to the network to strengthen the overall system. Finally, from the point of view of the converter connected electrically close to the network, better operation is observed when the GFM is connected further away, a similar conclusion to the common mode. If the GFL is connected at the end of a long line, the PCC exhibits significant voltage deviations due to poor operation of the GFL connected to the weak grid and if the converter electrically close is GFM it must do more work to stabilise the network which likely causes increased interactions.

## 4.2 Single Converter Systems

Impedance-based stability has been intensively studied utilising SISO techniques as far back as 1976 where Undrill and Kostyniak studied subsynchronous oscillations between synchronous generators and the transmission network [135]. In terms of converters, Middlebrook applied a similar method to study DC-DC converters around the same time [136]. Since then, numerous methodologies have been proposed to study all types of system topology but usually the system is cut to provide a load and a source subsystem. In the case of IBR studies, the converter is viewed as the load and the network is seen as the source. The ratio between these two systems is obtained and conclusions can be made regarding possible system interactions and stability using an appropriate stability technique.

One common approach, based on the Nyquist Stability Criterion [137] is applied by J. Sun in [138] where the effect of grid impedance on grid-connected converter stability is explored. The main contribution of this work showcased that existing impedance-based stability methods were only applicable for voltage-source systems and developed a stability criterion that is applicable for current-source systems. Moreover, it was found that the external behaviour of an inverter is more useful for system stability analysis than the inverter inner loop stability. This is important as converters cannot be viewed strictly as loads and do possess source behaviour. This work is specifically relevant for GFL converter structures that exhibit this type of current source behaviour.



It is also noted that this analysis requires a linear system description of which IBRs are not. Therefore, these approaches are only valid for small-signals analysis where linear behaviour is maintained. A single-phase solar inverter is utilised to showcase a new form of the stability criterion. A diagram showing the simplified source/load subsystem is provided in Figure 4.1.

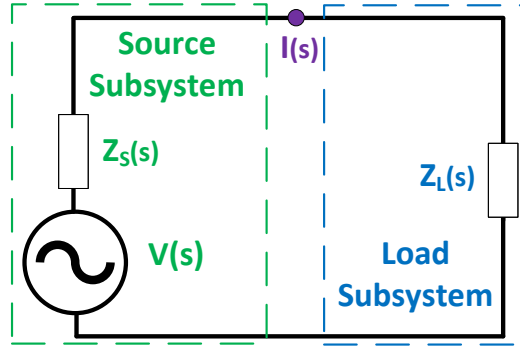


Figure 4.1: Source and Load Subsystem Representation

The current flowing from source to load in this case can be calculated via:

$$I(s) = \frac{V_s(s)}{Z_l(s) + Z_s(s)} \quad (4.1)$$

This can be rearranged to form:

$$I(s) = \frac{V_s(s)}{Z_l(s)} \frac{1}{1 + \frac{Z_s(s)}{Z_l(s)}} \quad (4.2)$$

The right fraction represents a closed loop transfer function governing the interaction between the source and load. If this transfer function contains no right half plane (RHP) poles, the system can be viewed as stable. This is often determined by synthesising the Nyquist contour of minor loop gain to identify any RHP zeros in the characteristic equation, utilising Cauchy's argument principle. If the contour does not encircle the critical point (0,-1) on the real imaginary axes, the characteristic equation contains no RHP zeros and hence, the closed loop system does not contain any unstable poles. In this case, the minor loop gain is the impedance ratio between the source and load impedances.

The Middlebrook Criterion [136] is perhaps the most restrictive Nyquist based stability technique and has been found to result in overly conservative designs [139]. The criterion states that if the Nyquist contour always remains within the unity circle, then the system must be stable as the critical point cannot be encircled. The Opposing Component criterion proposed by J. Carrol [140] or the small gain theorem discussed by Belkhat in [141] looks to extend the stable region by stating that stability is maintained if the Nyquist contour lies to the right of a line at a point  $s = 1/GM$  where GM is the gain margin. An extension of this which provides an even less conservative measure is the the Gain Margin Phase Margin (GMPM) criterion [142]. In this case the vertical line is replaced with a line drawn at an angle of  $\pm PM$ , where PM is the phase margin. The region to the left is considered forbidden. It should be noted that the forbidden regions do not guarantee instability, only that avoiding the forbidden regions will guarantee stability. One final Nyquist approach based on forbidden regions is the ESAC criterion [139]. This region is specified first by two line segments starting at infinity and parallel the negative real axis and stop at the boundary of the unit circle. Two more lines are used to join these lines converging at the point  $s = -1/GM$ . This method opens more of the s-plane and reduces artificial conservativeness.

More forbidden region approaches do exist but certain challenges reduces the efficacy of all these methods. One such issue of using Nyquist based techniques is the lack of obvious frequency information which can make converter design more challenging. Moreover, the impedance ratio is analysed as a whole and the individual impedances can not be analysed and altered to provide a better response. Interestingly, the same information can be displayed on Bode plots which allows for stability analysis and impedance shaping to improve system response. Y. Liao explores translating the previously discussed Nyquist based criterion to bode plots [143]. Instead of plotting the impedance ratio, the individual impedances traces are plotted and compared against each other. This allows the identification of regions where the converter impedance could be shaped to avoid falling into the forbidden regions. This approach has been applied for a grid-connected inverter in weak grid conditions by Yang et al. in [144]. Utilising the bode plot method, the interactions between the converter impedance and

weak grid impedance were studied and the converter impedance was shaped to improve the performance and stability of the system.

The previous stability techniques all make the assumption that there are no unstable open-loop poles present in the minor loop gain. When these poles are present the analysis becomes challenging, the unstable open-loop poles may not result in the closed loop system being unstable. The only conclusion that can be made is that the system will be unstable without feedback applied. However, determining the efficacy of the applied feedback is challenging as the unstable pole can become hidden.

GFL converters are viewed as current sources behind parallel admittances and are known as Y-type systems. Conversely, the network is seen as a voltage source behind a series impedance or a Z-type system. Combining the two provides a Z+Y system and the minor loop gain is unlikely to contain any open-loop unstable poles. If unstable poles do exist, the inverse Nyquist criterion can be applied essentially studying the inverse of the minor loop gain which changes the unstable open-loop poles to open loop RHZ which do not result in instability [145]. There may be some problems as RHZ often indicate that the system is of the non-minimum phase type which can offer some further complications. Moreover, if the minor loop gain contains both open-loop right half plane poles and zeros simultaneously then the inverse Nyquist criterion cannot be applied as unstable poles are present either way. Conversely, GFM converters are viewed as voltage sources behind a series impedance and therefore when combined with the network form Z+Z systems which are far more likely to contain problematic open-loop poles as discussed by Fangcheng et al in [146]. The same can be said for multiple GFL converters connected together forming Y+Y systems.

Zhang et al. proposed a method that lumped all Z-type systems together to create a single numerator impedance while lumping all Y-type system together to provide the denominator impedance [147]. However, this may cause certain system interactions to be lost. Another approach for dealing with open loop RHP poles in Z+Z systems is the impedance sum method [146]. This analyses the transfer function using the form shown in 4.1. This means any problematic poles cannot appear however, the interactions between the two impedances cannot be studied, only the overall stability. Liao extended

the work completed using bode plots to account for open-loop RHP poles in [42] which allows the study of the individual impedances. The bode plots are used to identify singularities in the individual impedance where a magnitude slope of  $-20\text{dB/decade}$  and phase change of  $+90^\circ$  represents a RHP pole and a slope of  $+20\text{dB/decade}$  and phase change of  $-90^\circ$  represents a RHP zero. With this information known, the Nyquist contour or Bode plots of the minor loop gain can then be studied to ensure that any encirclements cancel the open loop poles and zeros. This approach is applicable for simpler systems and does provide a black box approach but as more advanced control components are included, it can be more difficult to distinguish exactly what poles and zeros are present from the bode plot alone.

### 4.3 MIMO Stability Analysis

All of the previously discussed works are based on SISO systems. As discussed in Chapter 3, when modelling requires increased converter control complexity, SISO representations of the converter admittance are not applicable as they do not provide a full description of possible interactions within the converter. This is especially important when converters are participating in frequency regulation which is true for GFM structures and more modern GFL and GS structures. Bolzoni explores this in [46] and finds that MIMO stability techniques provide more precise identification of the stability boundaries of these types of system compared to SISO analysis. Additionally, analysis techniques that rely on the MIMO system being DD or MFD no longer apply and full MIMO stability analysis techniques are required. Fortunately, significant work has been completed to extend the SISO stability techniques to generalised MIMO approaches three of which are explored here.

#### 4.3.1 Generalised Nyquist Criterion

The Generalised Nyquist Criterion (GNC) utilises Cauchy's argument principle to determine the number of RHP poles and zeros present in a transfer function using the Nyquist contour of the MIMO system eigenvalues. This means for a  $2 \times 2$  MIMO sys-

tem there will be two Nyquist contours to study. The contour encapsulates the entire complex RHP in a counter-clockwise direction with small indentations into the RHP to avoid poles and zeros that may lie on the imaginary axis. When the contour is applied to the minor loop gain, in this case the impedance ratio, any excess RHP poles and zeros will appear as encirclements of the origin in opposing directions. To determine stability of the closed loop system shown in Figure 4.1, the process counts encirclements around the critical point (0,-1). This determines the poles and zeros of the characteristic equation which in this case is constructed utilising MIMO impedance and admittance matrices:

$$\mathbf{I}_{PCC,qd} = (\mathbf{V}_{g,qd}\mathbf{Y}_{c,qd} - \mathbf{I}_{c,qd})\mathbf{I}_2(\mathbf{I}_2 + \mathbf{Z}_{g,qd}\mathbf{Y}_{c,qd})^{-1} \quad (4.3)$$

Any zeros that appear in the characteristic equation are unstable closed loop poles and indicate an instability. Some impedance ratios may already contain open-loop RHP poles, in this case the system can still be stable if encirclements of the critical point in Nyquist plot of the eigenloci counteract the open loop poles:

$$Z = P + (N_c^+ - N_c^-) \quad (4.4)$$

Where P is the number of open-loop RHP poles,  $N_c^+, N_c^-$  are the clockwise and counterclockwise encirclements of the critical point and Z is the number of closed-loop RHP poles. Z must be 0 to guarantee stability. The Nyquist plot also provides graphical feedback on how close the system is to becoming unstable but this can be challenging to quantify. The GNC is most effective during real-world testing to ensure a converter will remain stable when connected to the system [148]. The frequency response of the converter can be readily obtained and the stability of the connected system can be determined from the eigenloci of the measured response. Other methods require a state-space model or prior knowledge of system transfer functions.

Theoretically, GNC can cope with any complexity of system. However, in practice measurements will have accuracy issues and it may be difficult to capture all system components. Situations may arise where the knowledge of the open-loop poles are re-

quired. Some systems can remain stable even with the presence of a RHP pole in the open-loop gain. This condition can occur if multiple converters connected to the grid are considered. If the Nyquist diagram provides an encirclement in the correct direction to counteract the unstable open-loop pole the system can remain stable. Conversely, a diagnosis that the system is unstable due to an encirclement may be incorrect if a RHP pole is already present in the open loop gain. While in some cases RHP poles can be identified from a bode plot of the system, this becomes increasingly challenging as system complexity grows. Especially if the poles lie extremely close to the imaginary axis. In reality, accurate knowledge of the system transfer functions is required. This is relatively straightforward process via system identification for a simple system where it is unlikely that any RHP poles will exist if the controller has been designed properly. However, challenges arise when trying to account for complex system components especially in NMP systems.

### 4.3.2 Generalised Bode Criterion

The MIMO Generalized Bode criterion (GBC) has been proposed as a remedy to the issues of implementing the traditional Bode stability criterion in MIMO systems [47]. While the method closely follows the GNC some components lead to a more difficult implementation. The process involves identifying encirclements of the critical point via a Bode plot of the eigenloci. This is achieved by locating regions where the eigenloci phase crosses  $\pm 180^\circ$  while the magnitude is greater than 0 dB. The following equation is then applied similar to Nyquist:

$$P = 2(C^+ - C^-) + C_0 \quad (4.5)$$

Where  $P$  is the number of open-loop RHP,  $C^+$  and  $C^-$  are the crossing of  $\pm 180^\circ$  from below and above respectively and  $C_0$  represents the crossings at 0 Hz. Using a Bode plot or Nyquist plot is largely a personal choice with both approaches similar. In some cases with a large number of poles or zeros it can be difficult to determine exactly how many times the trace crosses the boundary and in what direction on a bode plot. In

addition, the key parameter  $C_0$  accounts for possible encirclements at 0 Hz which the Bode plot cannot represent. This parameter becomes increasingly difficult to compute as the system becomes more complex. Exact knowledge of the admittance transfer functions is required so that the Smith-MacMillan form can be obtained. The number of pure integrators in system characteristic equation must also be known which is non-trivial with greater system intricacy. This makes it extremely difficult to implement in a laboratory setting as identifying the transfer functions of a system with the required complexity would be near impossible. If the assumption is made that the phase of the eigenloci does not cross  $\pm 180^\circ$  at 0 Hz the method could still be valid. However, all systems containing PIs will have at least one pure integrator in the characteristic equation which greatly increases the odds of having a crossing around 0 Hz.

### 4.3.3 Eigenvalue Analysis

State-space eigenvalue analysis is an alternative technique that is often employed [32]. In fact, Fan et al. suggested that eigenvalue analysis provides the most accurate stability analysis independent of system topology and uses a voltage source converter (VSC) connected to a weak grid as an example in [33]. This provides an interesting insight into the techniques that should be used for offshore windfarm connections as they are normally of the weak to very weak rating due to the distance of the connection from the network.

Consider one of the state-space models described in chapter 2. The stability of the system can be determined by finding if all eigenvalues of  $A$  lie in the left-hand plane (LHP). The eigenvalues are obtained and a stability condition applied:

$$\det(A - \lambda_{ss}I) = 0 \quad (4.6)$$

$$\operatorname{Re}\{\lambda_{ss}\} < 0 \quad (4.7)$$

Where  $A$  is the model state matrix,  $\lambda_{ss}$  are eigenvalues of  $A$  and  $I$  is an identity matrix of the same rank as  $A$ . If the condition 4.7 is satisfied the system is then

asymptotically stable. In the case of state-space analysis the impedance method is utilised to obtain the correct amalgamation of network impedances. This method is straightforward to implement if a state-space model is available. It is often easier to interpret a pole-zero map than encirclements on a Nyquist diagram. If the converter admittance is obtained from a state-space model, it is likely the model could be quickly adapted to provide other closed-loop responses such as power and voltage to investigate control performance. However, the state-space model cannot be obtained through experimental procedure.

Eigenvalue analysis is most useful during the design stage where the converter model is readily available. The eigenvalues can be used to determine stability and the control performance by using different input/output (I/O) pairs. The method also allows for analysis of sufficiently complex models. If eigenvalue analysis is employed to guarantee no open-loop RHP poles during the design process, the GNC can be more readily applied during laboratory testing.

### 4.3.4 Comparison of Stability Techniques

The stability methods are compared in Figure 4.2 which provides Bode and Nyquist plots of a single eigenloci for an arbitrary MIMO converter impedance as an example.



## Chapter 4. Impedance-Based Stability

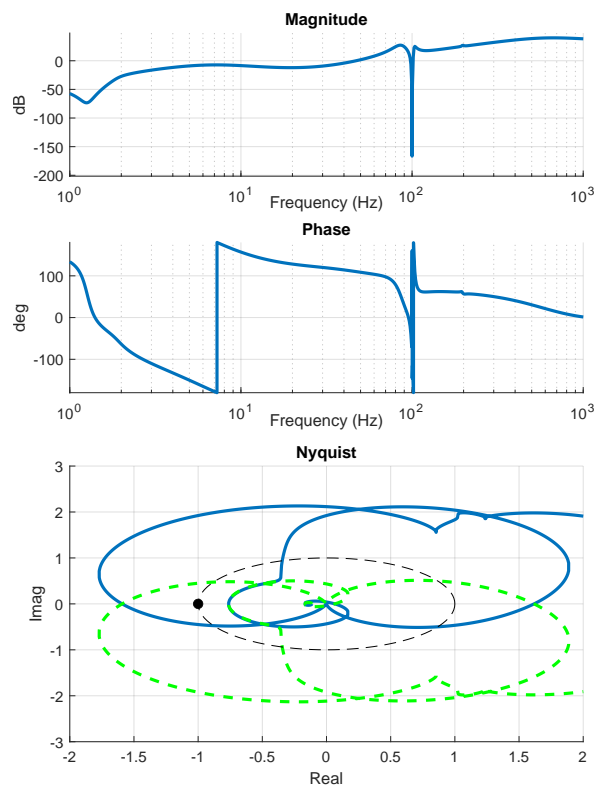


Figure 4.2: Multi-converter system diagram

From Figure 4.2, around 100 Hz a thick line indicating multiple crossings of  $\pm 180^\circ$  are present. Due to the nature of the magnitude trace it is challenging to determine if the magnitude is above 0 dB when the phase makes the crossings. It is also difficult to determine the direction of the crossing without closer inspection. If the Nyquist plot is used there is still a lot of messy complex behaviour however it is very easy to see two encirclements of the critical point indicating instability in this case. This is not as obvious from the bode plot and the instability is challenging to find, on close inspection with a large zoom factor one crossing can be found at 102 Hz. If the eigenvalues of the closed loop are calculated a complex conjugate pair of unstable poles are found:  $1.835 \pm j637.72$ . This is in agreement with the Bode and Nyquist analyses and has been validation with time-domain simulation. These types of issues become more prevalent of converter complexity increases and components such as PLLs, notch filters and delays are introduced.

### 4.3.5 Applications of MIMO Techniques

The emergence of GFM technologies has resulted in a significant volume of research on MIMO models utilising the discussed techniques. One such study looked at power synchronising control (PSC) which was originally proposed by Zhang et al. in [115]. Khazaei et al. constructed and analysed a MIMO impedance model of this control structure in [34] and studied the effect when connected to a very weak grid. The MIMO impedance model successfully determined that PSC had better operation in weak grids compared to traditional GFL structures and enhanced the volume of possible active power flow. A similar study was completed by Unamuno et al. in [35] instead looking at a VSM implementation via MIMO impedance analysis. Interestingly, both a current-controlled and voltage-controlled VSM structure were studied and a clear difference was discovered, especially in the low frequency range. The voltage-controlled machine showed lower stability margins when compared to the current-controlled version but it is stated that the problems could be improved by adding some form of active damping loop to the voltage-controlled system. This work may suffer from some of the issues of stability for  $Z+Z$  type systems previously discussed when operating as the voltage controlled VSM and may be the reason for the poor stability definition.

Quite often combining the different techniques allows some of the pitfalls to be negated and allows both stability determination and performance enhancement. Li et al. applied combinations of these techniques to investigate the stability of a power controlled grid-connected inverter in [32]. The work applies eigenvalue analysis to identify problematic roots and identify their frequency. An adaptation of the Bode criterion is then used to analyse each impedance independently to determine if any impedance shaping could be applied to reduce the interactions between systems similar to some of the SISO based works previously discussed. In terms of these types of power controlled converter, the inertia and frequency response is one unique component compared to most GFL structures. However, most impedance-based models do not contain terms that are dependent on the grid frequency. It is then difficult to deduce if the stability analysis provides the whole picture of the converter in grid connected mode.

## 4.4 Multi-Converter System

With the penetration of IBRs ever increasing on the network all with unique control topology, investigation of single converters even when lumped is likely not sufficient for network studies. Considering impedance-based stability for multi-converter systems is challenging as previous issues pertaining to open-loop RHP poles become more prevalent as system complexity increases. Work completed by Wang et al. in [43] looked at creating a Nyquist based stability criterion for two converters connected to the network. The method involves first determining if converter 1 is stable when grid connected. If the system is stable, converter 1 is combined in parallel with the network to form a new parallel impedance. The new impedance ratio of minor loop gain is then formed between converter 2 and the new parallel combination of converter 1 and the network. By analysing the system as a series of loops, the open loop RHP poles present in the final description are determined. This provides a good result but can be time consuming and complicated as more and more loops are considered.

Liao et al. explored a Bode criterion based stability method in [42] for a two converter system using forbidden regions. Auxiliary regions are created  $\pm 180^\circ$  from the first converter impedance known as the crossing boundaries (CB). Locations where the second converter impedance crosses these boundaries are analysed with the crossing direction determined from the derivatives of the frequency response. This provides a method of counting the encirclements that may be present on the Nyquist contour of the full system. Similar to previous graphical methods, this becomes increasingly complicated as system complexity increases. Moreover, all of the multi-converter studies have only been studied thus far utilising SISO impedance models which as discussed are not sufficient for a full system description especially when considering converters providing advanced grid services.

One important consideration of multi-converter impedance studies (especially when considering MIMO impedance models) is the reference frame that the converter impedances are expressed in. This is explored by Xiao et al. in [149] where four different approaches are studied and found to be equivalent. One of the most applied techniques is stipulated

by Rygg et al. in [150]. The importance of applying one of the rotational methods is stated and validated using impedance sweeps in simulation showing that not utilising a rotation provides an incorrect system description.

This work is extended by Zhang et al. in [151] which states that the reason for the required transformation is due to the impedance models of the VSCs being evaluated locally via linearisation which requires the reference frame angle. Hence, they all must be rotated into a global reference frame before study can commence. One further point highlighted by Zhang is the difficulties encountered when considering multi-converter systems containing converter branches of similar impedance. Stating that the rotation and combination of these impedances can cause information to be lost. If a system is considered with a network impedance,  $Z_g$ , and two identical converter impedances, ( $Z_1, Z_2 = Z_c$ ) one loop impedance of the system combining the converters in parallel and expressing the transfer function numerators (N) and denominators (D) could be:

$$Z_l = \frac{(N_{Z_c}(s)D_{Z_c}(s)^{-1})^2}{2N_{Z_c}(s)D_{Z_c}(s)^{-1}} + \frac{N_{Z_g}(s)}{D_{Z_g}(s)} \quad (4.8)$$

If the system is cancelled before obtaining the modes, the new numerator loses the zero information of one converter:

$$N_{new}(s) = N_{Z_c}(s)D_{Z_g}(s) + 2D_{Z_c}(s)N_{Z_g}(s) \quad (4.9)$$

However, including all information the numerator should be:

$$N_{correct} = N_{Z_c}(s)N_{new}(s) \quad (4.10)$$

It is obvious to see the loss of information for identical branches, but less obvious issues occur in complex systems. Problematic modes that should be visible but are cancelled during manipulations of matrices. For this reason, it has been suggested that analysis via the Norton admittance matrix is preferred as it prevents incorrect network operations during simplification. However, this is time consuming and correct analysis can be achieved in several cases by constructing a simplified closed-loop system. Some

important steps should be taken to ensure that information is not being lost during the construction of the simplified loop.

## 4.5 MIMO Multi-Converter System

A novel contribution of this work looks to extend impedance-based stability analysis to wider networks with multiple converters employing MIMO impedance definitions [88]. Careful consideration of converter type to ensure the correct representation either Z-type or Y-type is utilised. As more converters are considered it becomes apparent that solving for the stability of the system solely through the characteristic equation is no longer sufficient due to the presence of complex admittance descriptions in the transfer function numerator. An example system is provided in Figure 4.3.

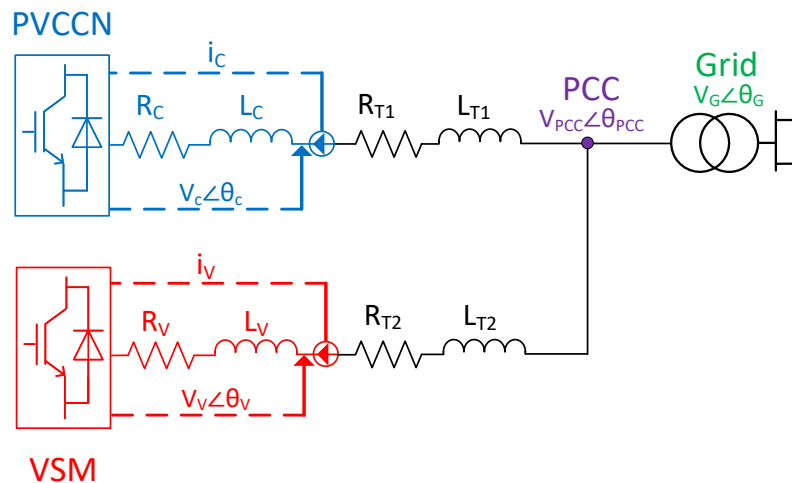


Figure 4.3: Multi-converter system diagram

From Figure 4.3, the network and GFM converter are both represented as voltage sources to begin with the GFL shown as a current source. In order to ensure correct circuit manipulations it is simpler to convert each source to a current source before solving for the current at the PCC essentially obtaining the Norton equivalent of the system. This equivalent circuit is shown in Figure 4.4.

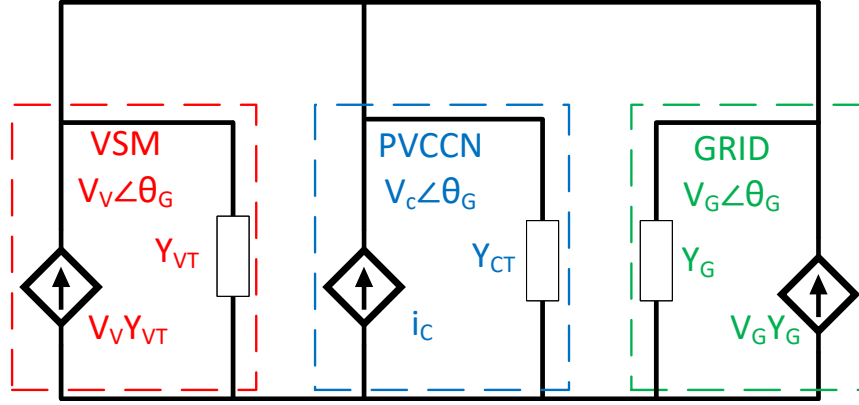


Figure 4.4: Norton Equivalent Circuit for Multi-converter system

From Figure 4.4, it is important to note that the conversion from voltage to current source is maintained by including the extra admittance matrix multiplying the voltage sources in any analysis. Using the equivalent circuit two sources are now combined in parallel to reduce the system to a two converter network. Technically any combination is possible and the way in which the system is split would allow investigation of different interactions. Initially, the Z-type systems are combined to form a single Z-type system with parallel impedance:

$$\mathbf{Y}_{p,qd} = \mathbf{I}_2 \mathbf{Z}_{p,qd}^{-1} = \mathbf{Y}_{g,qd} + \mathbf{Y}_{v,qd} \quad (4.11)$$

The current at the PCC can now be determined utilising the parallel impedance:

$$\begin{aligned} \mathbf{I}_{PCC,qd} = & \mathbf{I}_{c,qd} \mathbf{I}_2 (\mathbf{I}_2 + \mathbf{Z}_{p,qd} \mathbf{Y}_{c,qd})^{-1} - \mathbf{V}_{v,qd} \mathbf{Y}_{v,qd} \mathbf{Z}_{p,qd} \mathbf{Y}_{c,qd} (\mathbf{I}_2 + \mathbf{Z}_{p,qd} \mathbf{Y}_{c,qd})^{-1} \\ & - \mathbf{V}_{g,qd} \mathbf{Y}_{g,qd} \mathbf{Z}_{p,qd} \mathbf{Y}_{c,qd} (\mathbf{I}_2 + \mathbf{Z}_{p,qd} \mathbf{Y}_{c,qd})^{-1} \end{aligned} \quad (4.12)$$

From 4.12, the system is now more complex but each component has the same characteristic equation which normally determines stability. However, due to the inclusion of the GFM converter analysis via the characteristic equation is now no longer sufficient. The GFM converter admittance  $\mathbf{Y}_{v,qd}$  is now present in the numerator of the central transfer function in 4.12 and must be accounted for as it could result in extra

poles and zeros being present in the closed loop function.

It should be noted that this approach has not been required previously for the network voltage source conversion as the grid admittance is entirely passive and will not impose unstable poles on the system and can therefore be disregarded. Since each transfer function has the same characteristic equation and the central function including the GFM admittance is the most complex, it is selected for analysis. When the numerator is considered one key issue arises such that graphical techniques like GNC become insufficient to properly analyse the stability of the system. Instead an eigenvalue analysis approach is preferred since state-space models of all network components are available. Using eigenvalue analysis makes the approach easily automated and allows for analysis of multiple system operating points, network conditions and controller tunings.

## 4.6 Multi-Converter Case Studies

This section showcases a range of case studies with various GFL and GFM structures connected in pairs to a network similar to the diagram shown in Figure 4.3. Stability assessments are conducted via the impedance ratios formed for a range of network conditions. The process for determining stability is the same as outlined in the previous section however, the stability of the systems can be compared by utilising the disk margins described in 3. Since the disk margins look at the forward loop gain assuming a unity feedback system they can be applied readily to the transfer functions shown in 4.12. To ensure no RHP poles are present the full system is analysed via the closed loop transfer function. Once confirmed stable, the robustness is tested by applying the disk margins to the forward loop gain equal to the ratio between one component and the parallel combination of the other two.

Until this point in literature, the goal has always been to avoid  $Y + Y$  and  $Z + Z$  types systems when constructing the impedance ratio to avoid open loop RHP poles. This would mean when considering two GFL converters, the converters are combined to lump the  $Y$ -type systems before the ratio is formed with the network to give a  $Z + Y$  system. For a mix of GFM and GFL, the GFM converter is combined with the

grid before the ratio is formed with the GFL again providing a  $Z + Y$  system. When considering two GFM converters the analysis becomes more challenging as there are only Z-type systems. The impedance sum method can be used to solve for stability but is not applicable for disk margins as it does not construct the correct type of forward loop gain. One approach could be to combine source of the same type. A different impedance ratio could be selected and the same stability conclusion would be reached but the disk margins and therefore robustness would vary. This is due to how the worst case perturbation from the disk margin affects the system from specific point of view.

This brings an interesting point, since the eigenvalue analysis proposed can identify these problematic poles the analysis can change slightly to construct the impedance ratio to view the system from a different point of view. In fact, if the previous method is followed lumping same type systems, the system containing a mix of converters always appears significantly more robust. Now this may not be strictly true, one possible explanation for this is that the way in which the first parallel system is connected, effects which mode is studied. If the converters are combined in parallel this can be seen as the common mode robustness of the converters or how the converters combine to interact with the network. However, if a converter is combined first with the grid this can be seen as the common mode interaction between the network and converter 1 or the differential mode between converter 2 and the remaining system. This also allows a degree of commonality to be maintained when studying the various systems.

This idea is explored considering all three possible modes for each converter combination e.g. converter common mode, differential mode of converter 1 and differential mode of converter 2. The parameters for all following analyses are provided in Appendix A. These cases are summarised in Table 4.1. It should be noted that the impedance of TR1 is three times larger the TR2 which is the reason for the different robustness measures. Table 4.2 provides a reminder of the different controller acronyms used within the Thesis.



Table 4.1: Summary of Stability Modes

Stability Mode	Parallel Combination	Studied Effect
Common Mode	C1 + C2	Converters on Network
Differential Mode 1	Network + C2	Network on C1
Differential Mode 2	Network + C1	Network on C2

Table 4.2: Summary of Controller Acronyms

Acronym	Controller Description
PVCC	Outer loop power and voltage PI control with inner loop current control
PVCCI	Outer loop power and voltage PI control with Inertia emulation and inner loop current control
PVCCD	Outer loop power and voltage droops with inner loop current control
GFMD	Active power to angle and Reactive power to voltage droop, outer loop voltage and inner loop current control
VSMCC	VSM power to angle control with outer loop voltage and inner loop current control
VSM	VSM power to angle control with voltage control only

#### 4.6.1 Converter Common Mode

When investigating the common mode the following combination is made to construct the system:

$$\mathbf{Y}_{p,qd} = \mathbf{Z}_{p,qd}^{-1} = \mathbf{Y}_{C1,qd} + \mathbf{Y}_{C2,qd} \quad (4.13)$$

The current at the PCC can then be determined as:

$$\begin{aligned} \mathbf{I}_{PCC,qd} = & \mathbf{I}_{g,qd}(\mathbf{I}_2 + \mathbf{Z}_{p,qd}\mathbf{Y}_{g,qd})^{-1} - \mathbf{I}_{C1,qd}\mathbf{Z}_{p,qd}\mathbf{Y}_{g,qd}(\mathbf{I}_2 + \mathbf{Z}_{p,qd}\mathbf{Y}_{g,qd})^{-1} \\ & - \mathbf{I}_{C2,qd}\mathbf{Z}_{p,qd}\mathbf{Y}_{g,qd}(\mathbf{I}_2 + \mathbf{Z}_{p,qd}\mathbf{Y}_{g,qd})^{-1} \end{aligned} \quad (4.14)$$

## Chapter 4. Impedance-Based Stability

Note that when Z-type systems are included, the correct source conversion is applied and the corresponding admittance added to the transfer function numerator. Eigenvalue analysis is used to determine the stability at first to account for open loop RHP poles. Once confirmed as stable, this part of the numerator is disregarded. The disk margins are then applied to the minor loop gain impedance ratio to determine system robustness. This essentially looks from the point of view of how much the rest of the system can vary while maintaining the admittance characteristic of the equivalent admittance of the single source in the numerator.

The disk margins are compared for the common mode for a range of SCRs for an operating point of 0 and 0.5 p.u. active power in Figure 4.5 and Figure 4.6, respectively. An SCR of 1.8 was the minimum strength that all converters could remain connected.

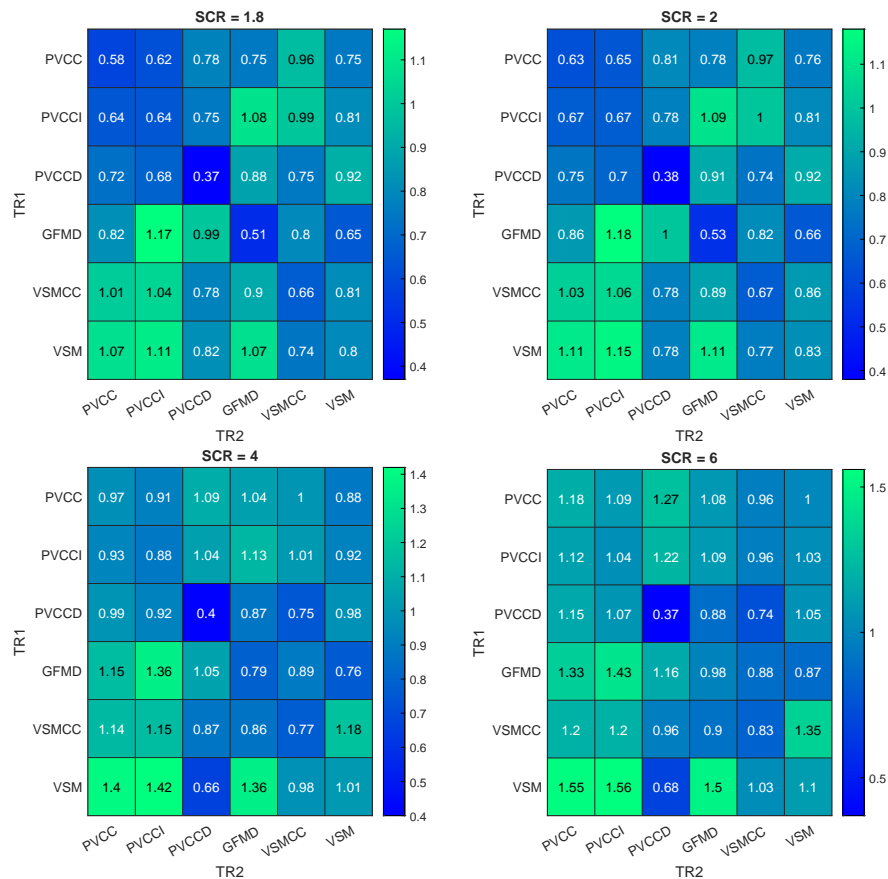


Figure 4.5: Robustness Measure for Common Mode Converter Combination at 0 p.u. active power

From Figure 4.5 when no active power is flowing, the GFL structures appear only slightly less stable than the GFM controller when combining two converters from the same family. Greater robustness is observed when combining GFL and GFM together when the GFM is connected on the longer line. When the GFL is connected to the longer line the robustness is significantly worse than any other case. The stability improves significantly for each GFL structure as the SCR increases as expected but the effect is less pronounced for GFM converters. As the operating point increased, the system containing two PVCCD was driven the closest to instability, especially in weak networks. This is likely due to no strict control of power and voltage, instead reacting to what happens on the network. The addition of the inertia emulation in the PVCCI appears to increase the stability of the system when deployed offering some voltage source like behaviour. The improvement from PVCCI over PVCC becomes more apparent at higher operating points. There are some cases involving the GFM controller utilising current control where the robustness increases with SCR suggesting that these structures relying on current control become more susceptible to interactions when operating in weak grids. The GFMD does useful work in improving the system stability but is significantly worse when connected to the longer transmission line. Moreover, when two GFMD controllers are included the robustness is very low in weak grids. This could be due to the lack of inherent inertia offered by the system. The VSM based controller tend to offer better operation in weak grids. The performance of the VSM controllers is improved when connected via the longer transmission line. Additionally, the detrimental effect of GFL structures is worsened when they are connected to longer lines.

From Figure 4.6, the higher operating point significantly worsens the stability of any system operating only GFL structures. Moreover, a small degradation in stability is observed when the operating point of the GFM converters is increased in weak grids. Conversely in stiff grids, the robustness of the system is increased at higher operating points when a GFM structure is present. Moreover, the PVCCD controller is right on the limit of stability when operating near the converter power limit. This behaviour can be improved by incorporating some other GFL controller that offers more strict

control of the PCC voltage. A large jump in robustness is observed when the SCR is increased beyond 4 and the robustness is similar to the lower operating points.

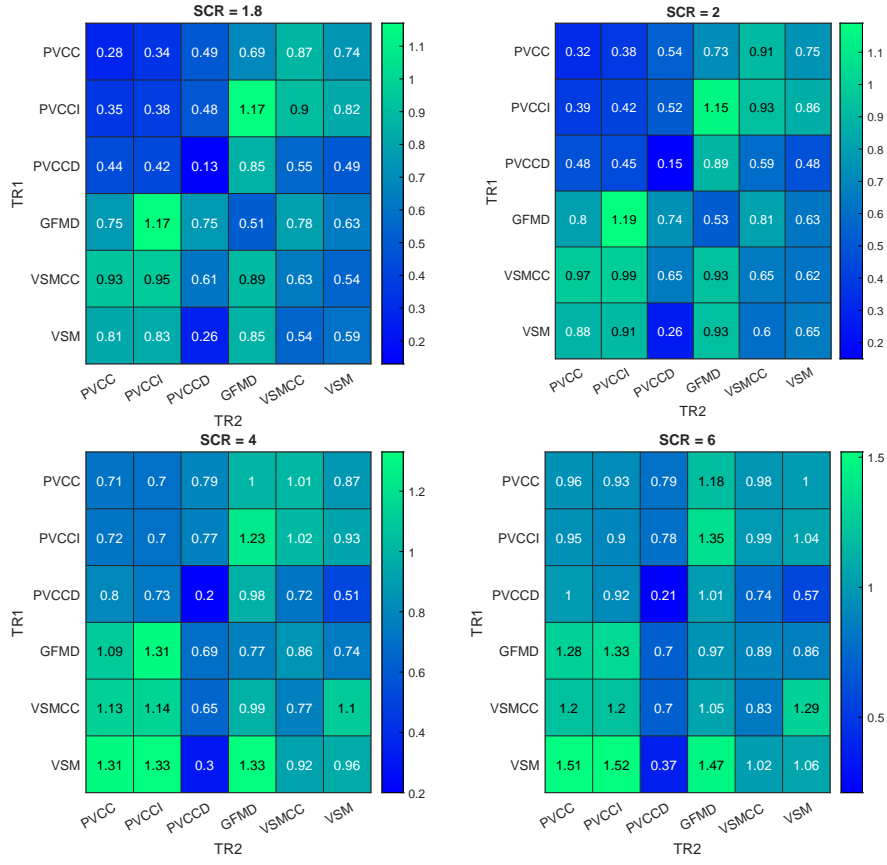


Figure 4.6: Robustness Measure for Common Mode Converter Combination at 0.5 p.u. active power

#### 4.6.2 Converter 1 Differential Mode

When investigating the differential mode of converter 1 the following combination is made to construct the system:

$$\mathbf{Y}_{p,qd} = \mathbf{Z}_{p,qd}^{-1} = \mathbf{Y}_{g,qd} + \mathbf{Y}_{C2,qd} \quad (4.15)$$

## Chapter 4. Impedance-Based Stability

The current at the PCC can then be determined as:

$$\begin{aligned} \mathbf{I}_{PCC,qd} = & \mathbf{I}_{C1,qd}(\mathbf{I}_2 + \mathbf{Z}_{p,qd}\mathbf{Y}_{C1,qd})^{-1} - \mathbf{I}_{g,qd}\mathbf{Z}_{p,qd}\mathbf{Y}_{C1,qd}(\mathbf{I}_2 + \mathbf{Z}_{p,qd}\mathbf{Y}_{C1,qd})^{-1} \\ & - \mathbf{I}_{C2,qd}\mathbf{Z}_{p,qd}\mathbf{Y}_{C1,qd}(\mathbf{I}_2 + \mathbf{Z}_{p,qd}\mathbf{Y}_{C1,qd})^{-1} \quad (4.16) \end{aligned}$$

The disk margins are compared for the differential mode of converter 1 for a range of SCRs for an operating point of 0 and 0.5 p.u. active power in Figure 4.7 and Figure 4.8, respectively. One further operating point of 1 p.u. is provided in Figure C.1 in Appendix C.

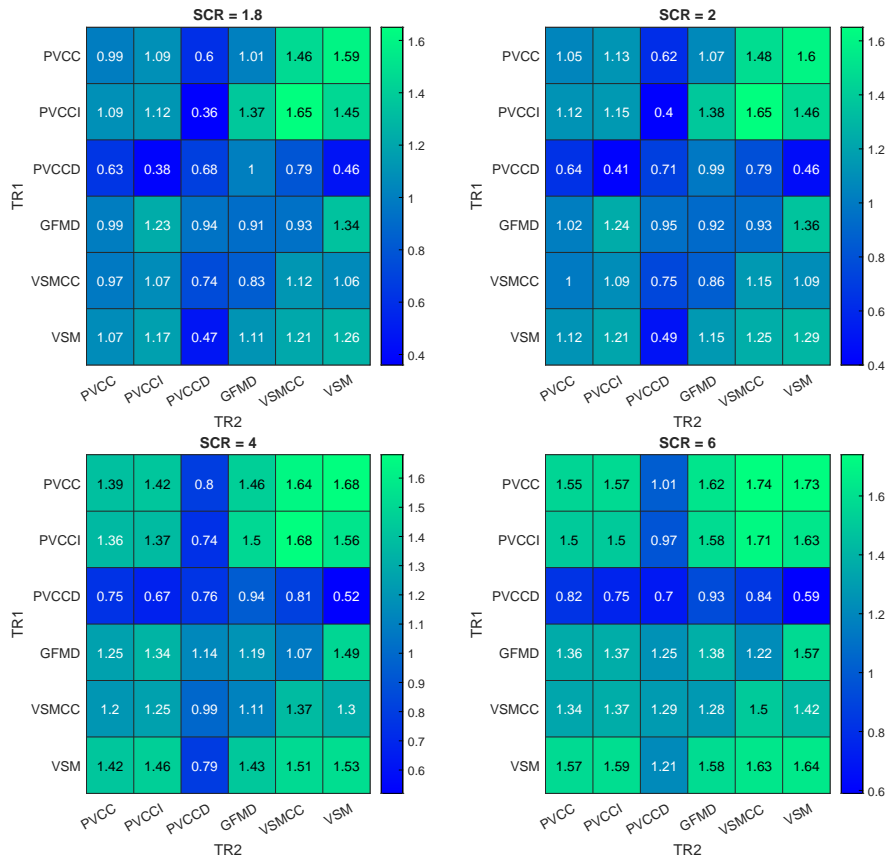


Figure 4.7: Robustness Measure for Converter 1 Differential Mode at 0 p.u. active power

From Figure 4.7, the differential mode robustness is significantly larger than the common mode for all controller combinations yet similar conclusions can be made comparing the differential mode relatively. The combination of GFM and GFL seems

to offer the most stable approach, a similar conclusion to the common mode analysis. However, the common mode analysis suggested having the GFM controller connected on the longer line offered more favourable performance. Conversely, the differential mode appears to offer the opposite conclusion with a higher robustness observed when the GFM controller is connected to the short line.

It is important here to consider the point of view. The differential mode of converter one considers the interaction between the converter at the end of the long line and the rest of the system. When converter 1 is GFL, the GFM converter combines with the network to provide an artificially stiff grid which improves the performance of the GFL and hence provides a higher robustness. However, when converter 1 is GFM at the end of the long line the view from converter 1 is that the grid it is connecting to is weaker due to the combination of the grid and the GFL and the GFM must do more work to stabilise the system which is more challenging with the long line in the way. Moreover, the GFL connected on the short line does not see any improvement from the GFM at the end of the longer line and must connect to the weak grid with less assistance.

The robustness improves significantly at higher SCRs likely due to the better combination of the GFL and the stiffer grid, This indicates the importance of considering different points of view as the common mode suggests the network will experience better operation when the GFM converter is connected further from the PCC as the common mode robustness is higher. However, from the converter 1 PoV greater stability is observed when the GFM combines closer to the network to strengthen the connection before the transmission line. If the converters are reversed the GFM can do less useful work to stabilise the system and sees a weaker connection overall. However, it is clear that the inclusion of a GFM converter always enhances the stability of the system regardless of where it is connected.

## Chapter 4. Impedance-Based Stability

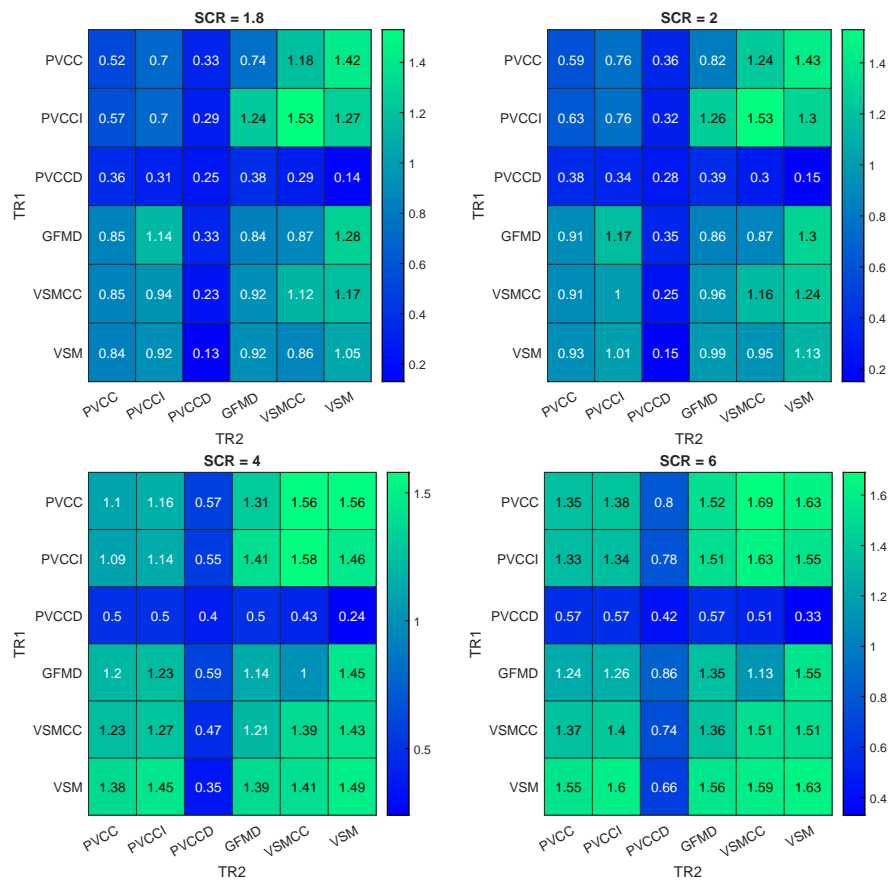


Figure 4.8: Robustness Measure for Converter 1 Differential Mode at 0.5 p.u. active power

From Figure 4.8, the operating point has a similar effect as with the common mode stability. The higher operating points harm stability further in weak networks but offers little concern in stronger networks. The difference between connecting a GFM to the longer or shorter line remains largely unchanged with the increase in operating point. Both measures of robustness alter by roughly the same amount. The differential mode stability from converter 1 appears to be affected more by the operating point when considering the GFL structures, with the value reducing further as the operating point increases. The discrepancy between GFM and GFL controllers becomes smaller at higher operating points for a larger SCR as the robustness increases for the GFM while reducing for GFL as operating point becomes bigger. This is exacerbated when the GFM is connected to the longer line and cannot help to mitigate the problems associated

with increased power flow from the GFL structures. In terms of GFL controllers the PVCCD offers the worst operating across the board while the PVCCI performs best, a similar conclusion as with the common mode analysis. However, from Figure 4.8 the PVCCD controller appears to have greater differential mode robustness when compared to the common mode at high operating points. In terms of GFM, the VSM and VSMCC are very closely tied in terms of robustness with each performing better in some specific scenarios.

### 4.6.3 Converter 2 Differential Mode

When investigating the differential mode of converter 2 the following combination is made to construct the system:

$$\mathbf{Y}_{p,qd} = \mathbf{Z}_{p,qd}^{-1} = \mathbf{Y}_{g,qd} + \mathbf{Y}_{C1,qd} \quad (4.17)$$

The current at the PCC can then be determined as:

$$\begin{aligned} \mathbf{I}_{PCC,qd} = & \mathbf{I}_{C2,qd}(\mathbf{I}_2 + \mathbf{Z}_{p,qd}\mathbf{Y}_{C2,qd})^{-1} - \mathbf{I}_{g,qd}\mathbf{Z}_{p,qd}\mathbf{Y}_{C2,qd}(\mathbf{I}_2 + \mathbf{Z}_{p,qd}\mathbf{Y}_{C2,qd})^{-1} \\ & - \mathbf{I}_{C1,qd}\mathbf{Z}_{p,qd}\mathbf{Y}_{C2,qd}(\mathbf{I}_2 + \mathbf{Z}_{p,qd}\mathbf{Y}_{C2,qd})^{-1} \end{aligned} \quad (4.18)$$

The disk margins are compared for the differential mode of converter 2 for a range of SCRs for an operating point of 0 and 0.5 p.u. active power in Figure 4.9 and Figure 4.10, respectively. The disk margins for an operating point of 1 p.u. are shown in Figure C.2 in Appendix C.



## Chapter 4. Impedance-Based Stability

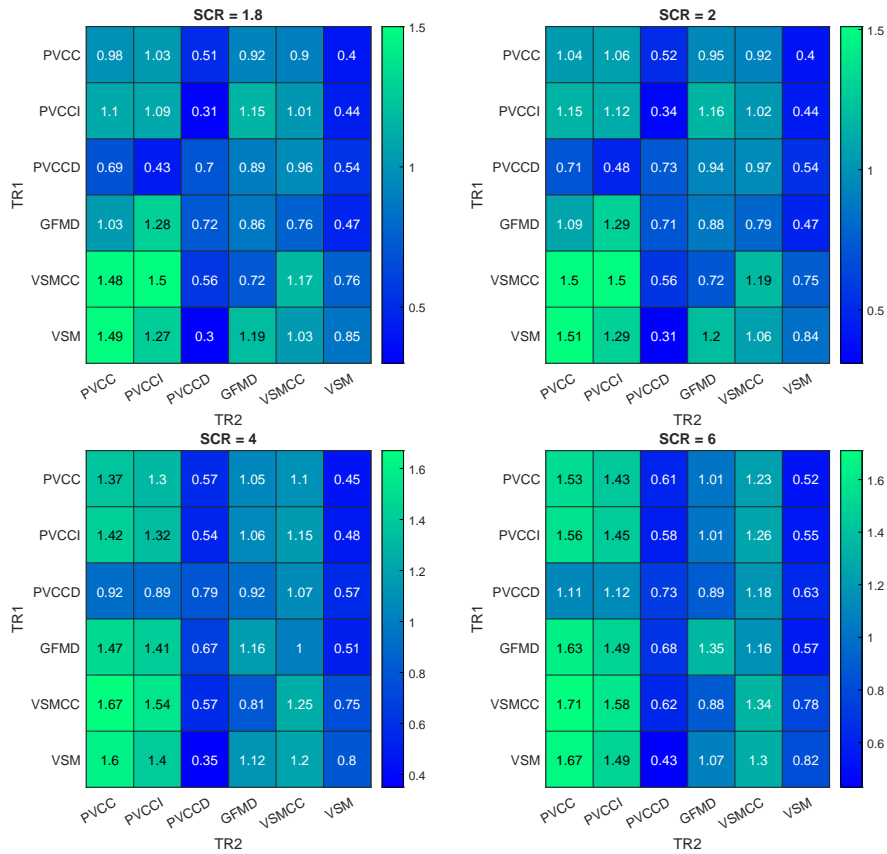


Figure 4.9: Robustness Measure for Converter 2 Differential Mode at 0 p.u. active power

From Figure 4.9, the differential mode stability is approximately the same from both points of view when the system incorporates only GFL structures. However, when analysing from the point of view of converter 2 the GFM structures become less robust for all SCRs. When considering a combination of GFL and GFM, again since the system is now concerned with the independent operation of converter 2 the robustness now suggests that converter 2 will experience better operation if it is GFM connected to the long line. This is an opposite conclusion to the previous converter 1 differential mode but similar to the common mode. If the SCR is high, considering that converter 2 is already connected electrically close to the network, it tracks that the the GFL should be connected as it will experience the least degradation to robustness independent of converter 1. It becomes slightly more complex at lower SCRs.

If converter 2 is GFM the combination of converter 1 which is GFL and the weak grid

## Chapter 4. Impedance-Based Stability

will further degrade the stability of the system and it will be worse than the differential mode 1 stability as the GFL is now connected further away. However, when converter 2 is GFL the weak grid is combined with GFM with a smaller equivalent impedance which strengthens the network and provides greater robustness albeit the increased robustness is reduced somewhat compared to if the GFM was connected closer.

When converter 2 is GFM it will experience greater detriment if a GFL converter is connected further away as it will need to do more work to support this. However, from the point of view of the GFL converter at the end of the long line, the GFL converter will experience better robustness in weak grids when the weak grid is combined with the GFM as this provides a stiffer network. Overall, these analyses suggest that the three points of view, common mode and differential modes 1 and 2 are all in agreement when considering the point of view at which they are applied.

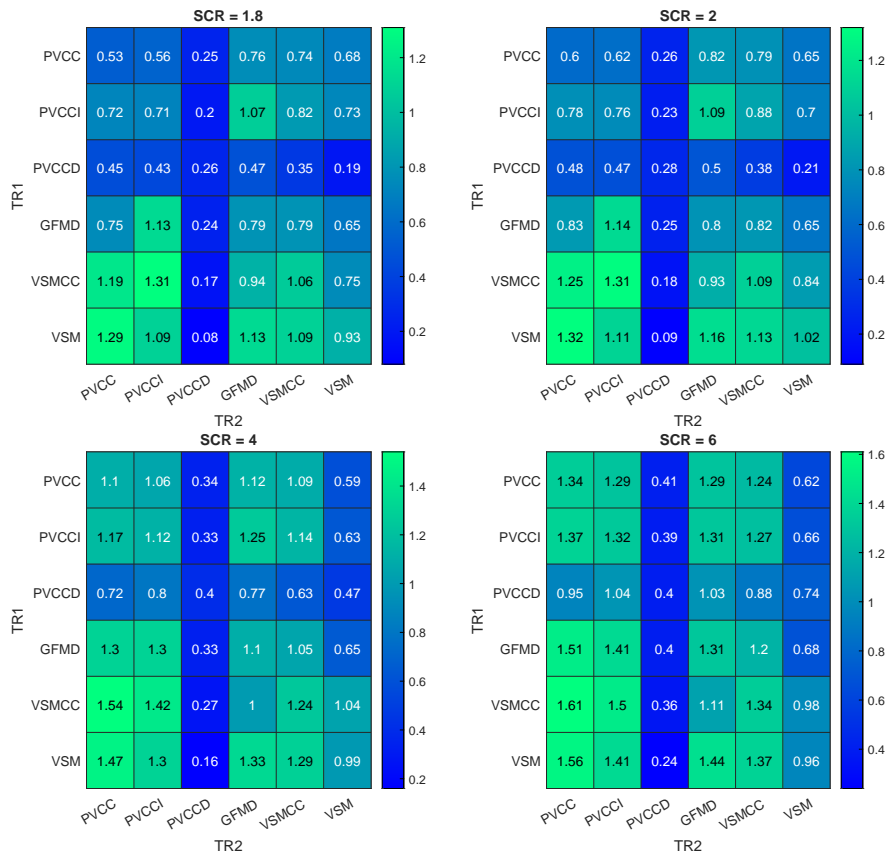


Figure 4.10: Robustness Measure for Converter 2 Differential Mode at 0.5 p.u. active power

From Figure 4.10, an interesting difference is observed in that the increased operating does not appear to balance out the difference between connecting GFL and GFM at the ends of the different transmission line. Even at large operating points the result suggests that the VSM should be connected to the longer transmission line. This does again track, if the GFL is connected at the end of a longer line the deviation to the PCC will be larger and from the point of view of the GFM converter as converter 2 it will have to do more work to remedy this and the system will appear less robust. Moreover, when the GFL is connected as converter 2 it sees better performance as it does not need to deal with the issues of the longer transmission line. Furthermore, the GFM converter reduces the equivalent impedance to the PCC and when combined with the grid offers a stiffer PCC for the GFL to connect to. When the GFL is connected to the longer line the GFM converter can still only do work to reduce the equivalent distance to the PCC. Therefore, the voltage deviations cause by the GFL converter cannot be remedied until the end of the longer line resulting in more work for the GFM.

All of these effects are exacerbated when the power flow is larger as more work must be done to support the voltage. Even when the SCR is higher, the GFL at the end of the long line still shows poor performance as that stiffness cannot be seen fully due to the extra impedance of the longer line. One final important point to consider is that when the network becomes suitably strong at an SCR of 6, the system appears more robust when both converters are GFL than when a VSM is connected, which may appear different to previous conclusions. However, what is likely happening is that both the grid and the VSM converter are fighting to control the PCC voltage so from the point of view of the VSM the system appears less robust. However, when a GFL is connected as converter two it immediately see the stiff grid impedance and does not care what is happening at the end of the long line. The GFL converter at the end of the long line however, will experience worse robustness due to the other GFL as seen when analysis differential mode 1.

From the analysis the following conclusions can be drawn:

1. GFL structures are significantly less stable at low SCRs
2. This effect is worsened at higher operating points

## Chapter 4. Impedance-Based Stability

3. The PVCCD structure offers the least stable system while PVCCI appears the most stable in terms of GFL
4. GFM structures offer preferable performance in weak grids and improve the performance of any GFL connected
5. The robustness provided from GFM tends to improve with increases in both SCR and operating point
6. Both VSM and VSMCC offer greater robustness over GMFD from all points of view
7. The most stable system incorporates both GFM and GFL
8. The point of view of the system is important for determining the best system topology
9. Common mode and both differential modes appear to be consistent with absolute stability but offer different robustness
10. This is mainly due to which system component they are considering e.g. common mode = network stability, differential mode 1 = stability of converter 1 and differential mode two = stability of converter 2
11. From the point of view of the network the best approach is to connect a GFM converter at the furthest possible point as GFL tend to harm stability further when operating at the end of a longer line
12. From the point of view of converter 1 at the end of a long line, the type of converter is not particularly important but better operation is observed when converter 1 is GFL as this allow the GFM to stiffen the connection and improve the performance at the end of the line.
13. Conversely to this, when the converter 1 is GFM the network is artificially weaker due the combination of the GFL and the grid provided poorer operation from the point of view of the GFM

## Chapter 4. Impedance-Based Stability

14. From the point of view of converter 2 connected to the short line, if converter 2 is GFL it is better to have a GFM connected at the end of the long line as this again increases the stiffness of the PCC albeit less than if the GFM was connected electrically closer
15. Conversely, if converter 2 is GFM, worse operation is observed from the point of view of this converter as it must do more work to remedy the poor behaviour of the GFL and the system it connects to is weakened by the GFL
16. What is slightly easier to see is that from the point of view of the network and a GFL converter, connecting a GFM creates a more stable system, but from the point of view of a GFM connecting a GFL has a negative effect when the operating point is above 0.

## Chapter 5

# Screening Stability Issues

Stability analysis of any form is a rigorous technique that can accurately determine problematic interactions of a system. However, the methods are often complex, computationally demanding and require significant experience to utilise correctly for complex systems. Moreover, the impedance of the system changes significantly depending on the point of view of the study, e.g. where the system is cut. Before using in-depth analysis it is often useful to employ some kind of screening technique and traditionally the grid strength or short-circuit level (SCL) is used. In traditional systems, with a large number of SGs the SCL can also be expressed as the short-circuit ratio (SCR) which is the ratio between the current provided during a three-phase fault to the nominal current.

Presently, the terms SCL and grid strength are used analogously. The definition of system strength is well defined for traditional networks and links three main aspects: available short-circuit current, susceptibility to voltage disturbances and maximum power transfer. In traditional networks dominated by SGs, the SCL is determined by the physical machine and line impedances. A high SCL is delivered by a low impedance and results in the generator being seen as a stiffer voltage source from the PCC. This increases the resistance to voltage disturbances. A strong network characterised by a high SCR ( $> 3$ ) will have a large volume of short-circuit current, better short-term voltage stability and a larger capability for active power transfer. When IBRs are considered, the physical network impedances are no longer sufficient to characterise

the system [36]. The fault current is determined by the inverter limit instead of the physical impedance and traditional definitions of SCR are invalid.

To avoid this, the most common approach is to ignore the contribution of IBRs from SCR calculations or use an alternative definition [152]. These methods include composite short circuit ratio (CSCR) [153], weighted short circuit ratio (WSCR) [154], short circuit ratio with interaction factors (SCRIF) and equivalent circuit short circuit ratio (ESCR) [155]. Literature surrounding these methods is poorly explained and lacking implementation. The approaches may be correct for determining the available fault current but incorrectly characterize the strength of the network often suggesting reduced voltage stability. Hence, in IBR dominated systems SCL and grid strength should be considered separately. If considered as a single entity, the system can become needlessly strong in terms of voltage disturbances while trying to procure increased fault current and the useful behaviour of converters is not represented. Conversely, representing increased grid strength as a higher SCL results in ‘synthetic’ fault current which is not actually available and risky to consider [156].

This chapter will explore the current screening metrics in the forms of various types of augmented SCR and discuss the drawbacks of each. A new screening concept that combines the complex interactions of impedance based stability and the simplicity and ease of understanding of SCR is then presented. The method known as the Grid Strength Impedance Metric (GSIM) utilises the converter output admittance to give a more accurate system description than is currently utilised with other forms of SCR. The analysis finds that GFM controllers provide the most stable method of provided enhanced system strength with significant gains made at low SCRs. GFL converters can provide system strength at the fundamental frequency via appropriate tuning of the voltage control loop but this often creates issues at higher frequencies and reduced robustness. Cases are provided showcasing the importance of considering the system strength as a function of frequency as the system may not be weakest at the fundamental frequency. Finally, each of the control structures is compared and the VSM based approaches provide the most stable and strong system with the consensus being that controllers that react less to external events exhibit stronger characteristics. The

differences between VSM both with and without current control can largely be negated with appropriate tuning.

## 5.1 Short-Circuit Ratio and Weak Networks

The traditional definition of SCR is based on the SCL or the volume of extra current available during a three-phase balanced fault. In the traditional network SCL is determined by the physical impedances of the system:

$$SCR = \frac{SCL_{MVA}}{S_{rated}} \quad (5.1)$$

$$SCL_{MVA} = \frac{1}{Z_{sys,pu}} \quad (5.2)$$

In general, a large impedance results in poor fault current provision and a low SCR. Since the SCL is determined via the impedances of the network, the SCR value can be used to determine the electrical distance from a network connection point to a stiff voltage source e.g. a synchronous machine. A high SCR results in a low impedance, short electrical distance and improved voltage strength. For the traditional network, fault current and voltage strength are inexplicably linked to the SCR. However, this may not be applicable in modern converter dominated systems. The fault current provision from converters is significantly different. Instead of being determined from physical impedances, the current is now limited to around 1.1 - 1.2 p.u. to protect the converter from damage [157].

In comparison, synchronous machines can provide significant overcurrents of 3-4 p.u. for some seconds without damaging the machine [158]. As the penetration of converters increases and synchronous machines are removed from the network the available fault current will reduce. Additionally, the present definition likely provides an incorrect rating of the available current as converters are entirely disregarded. This is clearly an issue for fault conditions and remedial action will be required to either provide increased fault current from devices such as synchronous condensers [156]. The alternative is to re-calibrate protections to operate with reduced fault current.

Low SCR is a common concern for the connection of offshore wind farms as the



transmission distance is often large. This provides issues as most wind farms are designed to operate based on the SCR at the point of connection which may lead to an over conservative design since the possible interactions of converters are not included, especially considering possible GFM structures. Numerous issues have been discovered related to the connection of traditional GFL controllers in weak grids, mainly due to the action of the PLL. Wu et al. found that the PLL introduces a large phase lag around the PLL bandwidth frequency when operating in weak grids and significantly decreases the oscillation damping and proposes a PI + Clegg integrator to improve the damping provided [79].

Building on this, work has been completed to further enhance regular GFL controllers to facilitate operation in these systems. One approach completed by Davari et al. applied robust vector control techniques to design a different type of voltage controller that allowed operation in very weak grids ( $SCR = 1$ ) while considering the influence of the PLL [80]. The work discovered that the overall converter system stability was based on the ac-voltage stability at the PCC and with appropriate voltage control this can appear virtually stiff and improve performance. Egea-Alvarez et al. proposed a technique to provide GFL controllers with a non-linear coupling term to improve the performance in weak grids by accounting for the non-linear relationship between voltage and active power in a line with large impedance [28]. However, these systems are complicated and require further studies as different unwanted interactions may occur. Moreover, they may not be required if the voltage signal at the PCC is provided from a GFM converter with low impedance providing a stiff voltage source instead of the large network impedance which provides non-linear voltage deviations during active power changes. However, a metric capable of showcasing this behaviour had not been suggested until work completed by Henderson et al. explored a system strength rating based on converter output impedance including control action [36].

Ray et al. reported that the impact of the PLL in weak networks is directly positively correlated to the penetration of IBRs [159]. This is due to three main interactions: the self-synchronisation loop due to converter injection current, grid-synchronisation loop through the grid voltage and inter-synchronisation loop through

the system impedance. Clearly, the first loop is not sensitive to network changes. However, the grid-synchronisation loop is dependent on the grid impedance and will exhibit worse interactions when the grid impedance becomes large, which is a similar finding to [80]. Finally, the impedance between converters will determine the sensitivity of the inter-synchronisation loops. If the physical impedance is used to calculate this, there will be no dissemination between GFL and GFM converters and the system can only be improved by altering the lines between converters. However, when control action is considered, the GFM converters represent a small impedance and can work to reduce interactions with the PLL in any GFLs present. Moreover, if the GFM impedance becomes lower than the network impedance, the interaction with the grid impedance is reduced and the GFM converter provides the stiff voltage source required for good GFL operation.

While the reduction of fault current is an obvious problem, the lower value of SCR may not result in reduced voltage strength in the modern network. As suggested in literature, the presence of a virtually stiff grid is possible with appropriate voltage control. While previous work has focused on equipping GFL converters with this behavior a better approach is to utilise the inherently low impedance of GFM structures. This reduces the need for complicated non-linear functions or  $\mu$ -synthesis based controller design. Converters do useful work in terms of voltage strength that is not represented by the fault current contribution. GFM converters are viewed as voltage sources and tend to have a very low output impedance [36]. Therefore, when GFM converters are introduced to a network they provide a small electrical distance to a stiff voltage source and improve voltage strength in quasi-steady state conditions [29]. However, if only the physical impedance of the converter is considered there is no way to differentiate between GFM and GFL control structures both of which have a very different effect on the voltage strength of the system. Clearly, a new method of determining system strength including the useful interactions of all types of converter control is required. With this information, it is likely more GFL can be connected safely to the network and will exhibit greater stability and performance. Moreover, a metric will allow the investigation of the appropriate penetration of GFM vs GFL converters on the network

in terms of grid stiffness and voltage stability.

## 5.2 Alternative Definitions

Present work looks to include the contribution of converters to the SCR of the system. However, most approaches continue to link fault current and voltage strength which should be avoided in the modern network. Any increased fault current determined from the converter is likely synthetic and risky to consider as it may not actually be available. Additionally, no method presently incorporates the converter control action and therefore the true behaviour of GFM converter cannot be represented.

### 5.2.1 Composite Short Circuit Ratio

Initially proposed by GE, CSCR calculates the grid strength considering all electrically close converters [154]. All converters of interest are assumed to be connected to a single bus and the strength is calculated including power contributions from converters but without fault current contribution:

$$CSCR = \frac{CSC_{MVA}}{MW_{VER}} \quad (5.3)$$

Where  $CSC_{MVA}$  is the fault level contribution excluding converters and  $MW_{VER}$  is the sum of nominal power ratings of the connected converters.

### 5.2.2 Weighted Short Circuit Ratio

WSCR has been most notably applied in defining operational limits in Texas [27]. The approach is similar to CSCR but now analyses key points on the network by considering multiple buses:

$$WSCR = \frac{\sum_i^N SCMVA_i P_{RMW_i}}{\sum_i^N P_{RNW_i}^2} \quad (5.4)$$

Where  $SCMVA_i$  is the short circuit capacity at bus  $i$  and  $P_{RMW_i}$  is the rated power output of the  $i$ th converter.

### 5.2.3 Short Circuit Ratio with Interaction Factors

The SCRIF looks to augment previous definitions of SCR with a component that captures voltage deviations [155]. This voltage sensitivity is captured via an interaction factor:

$$IF_{ij} = \frac{\Delta V_i}{\Delta V_j} \quad (5.5)$$

The SCRIF is then determined:

$$SCRIF_i = \frac{S_i}{P_i + \sum_j (IF_{ij} \times P_j)} \quad (5.6)$$

Subscript j represents all electrically close converters or buses.  $IF_{ij}$  is the interaction factor of bus j on bus i,  $\Delta V_i$  and  $\Delta V_j$  are the voltage deviations at the ith and jth bus, respectively,  $S_i$  and  $P_i$  are the fault level contribution and nominal power rating at bus i and  $P_j$  is the nominal power at bus j. This suggests that a stiff voltage source inserted at bus i, would decrease the interaction factor, raise the SCRIF and bus i would become more stable. Converters are considered here in terms of power and line impedance, but the control action represented by the equivalent impedance appears to be disregarded preventing dissemination between grid friendly and grid harming devices. It is challenging to determine exactly how the converter is represented in literature surrounding SCRIF as the calculation of the voltage disturbances for the IF is not well described. Approaches looking at the steady state reaction to disturbance injection at the fundamental frequency likely do not accurately represent the converter action in quasi-steady state conditions.

### 5.2.4 Equivalent Circuit Short Circuit Ratio

The ESCR is very similar to the traditional SCR, but now considers all physical impedances on the network:

$$ESCR = \frac{1}{Z_{sys,PU}} = Y_{sys,PU} \quad (5.7)$$

Where  $Z_{sys,PU}$  and  $Y_{sys,PU}$  are the system impedance and admittance, respectively. The ESCR is not necessarily novel, it is the traditional SCR determined at a different point on the network, closer to the device of interest. The metric suggests the maximum network impedance that the converter can operate under. However, the impedance due to converter control is not considered. This method forms the basis for the novel approach proposed in this paper utilizing converter admittance models to extract an equivalent rating of strength.

### 5.2.5 Drawbacks of Present Methods

The drawbacks of the previous methods include: the inability to differentiate between grid friendly and harmful devices, only representing strength at the FF and continuing to describe the network as if it was dominated by SGs. For example, CSCR and WSCR cannot represent different types of converter behaviour as they consider the power contribution which is the same for both GFL and GFM. ESCR only considers the physical line impedances of the converters which is again not dependent on converter type. SCRIF begins to study interactions however, it is only described at the FF where the true behaviour of the converters is challenging to represent using conventional measurement techniques such as IF. Additionally, the IF is based on physical impedances and does not include any converter control components that act to reduce the equivalent electrical impedance to a voltage source. Hence, the SCRIF will underestimate the strength of the network when GFM converters are included.

All methods continue to couple voltage stiffness and fault current into one metric which is not valid for the modern system. The behaviour of converters during faults is vastly different from the quasi-steady state behaviour and therefore characterising the normal operating behaviour via the fault characteristic is futile. The voltage strength provided by converters must be calculated considering the behaviour of the converter in the quasi-steady state which is achievable by utilising the equivalent converter output impedance. When considering quasi-steady state conditions, increased voltage stability from IBRs can occur without increased fault current with appropriate control. Any suggested increase in fault current without a lower physical impedance is synthetic and

possibly risky to consider [156].

### 5.3 Grid Strength Impedance Metric

Using the defined impedance models the grid strength impedance metric (GSIM) for classifying the network strength can be postulated. GSIM is equivalent to previous definitions of SCR for SG based networks in terms of grid strength but does not indicate a presence of available fault current. This is achieved by using the admittance models discussed that describe the performance of the converter in quasi-steady state. This normal operating behaviour is vastly different from fault conditions and allows the decoupling of voltage strength from fault current provision. However, the admittances and hence GSIM are operating point dependent and a range of cases should be studied. Additionally, the poor accuracy of some small-signal models at high frequencies should be considered [160].

#### 5.3.1 Defining GSIM

Firstly, the base impedance of the network must be specified using the conventional method:

$$Z_b = \frac{V_b^2}{S_b} \quad (5.8)$$

Where  $Z_b$ ,  $V_b$  and  $S_b$  are the base impedance, voltage and power, respectively. The base impedance can then be used to determine the resistance and inductance parameters for a Thevenin equivalent base grid:

$$R_b = Z_b \frac{R}{X} \quad (5.9)$$

$$L_b = \frac{Z_b}{\omega_g} \quad (5.10)$$

$$\mathbf{Z}_b = \begin{bmatrix} R_b + sL_b & \omega_b L_b \\ -\omega_b L_b & R_b + sL_b \end{bmatrix} \quad (5.11)$$

Where  $\mathbf{Z}_b$  is the base impedance expressed in the synchronous reference frame,  $\omega_b$  is the FF,  $R_b$  and  $L_b$  are the base resistance and inductance, respectively and  $\frac{R}{X}$  is the desired

ratio of resistance to reactance of the network. The system admittance  $Y_{sys}$  contains all components of the network under study including a Thevenin equivalent grid with SCR applied and any connected inverter-based resources. Since the impedance/admittance matrices form MIMO systems, the eigenloci of the impedance/admittance matrices across the frequency range are considered. This is a common approach in impedance-based stability methods [32, 34, 35, 45, 46, 149, 161]. The impedance/admittance for the base or converter can be obtained from a frequency scan of the physical network which makes GSIM applicable in black box scenarios [162]. Alternatively, a frequency response of a state-space model or transfer function model can be utilised:

$$\mathbf{Y}_{sys}(s) = \begin{bmatrix} Y_{qq}(s) & Y_{qd}(s) \\ Y_{dq}(s) & Y_{dd}(s) \end{bmatrix} \quad (5.12)$$

$$\mathbf{Z}_b(s) = \begin{bmatrix} Z_{qq}(s) & Z_{qd}(s) \\ Z_{dq}(s) & Z_{dd}(s) \end{bmatrix} \quad (5.13)$$

Where  $\mathbf{Y}_{sys}(s)$  is the 2x2 MIMO transfer function matrix describing the selected system admittance and  $\mathbf{Z}_b(s)$  is the 2x2 MIMO transfer function matrix describing the base impedance. Each of the 2x2 matrices then produces two eigenloci denoted q and d:

$$\lambda(\mathbf{Y}_{sys}(s)) = \begin{bmatrix} |\lambda(Y_{sys,q}(s))| \\ |\lambda(Y_{sys,d}(s))| \end{bmatrix} \quad (5.14)$$

$$\lambda(\mathbf{Z}_b(s)) = \begin{bmatrix} |\lambda(Z_{b,q}(s))| \\ |\lambda(Z_{b,d}(s))| \end{bmatrix} \quad (5.15)$$

Where  $\lambda(\mathbf{Y}_{sys}(s))$  and  $\lambda(\mathbf{Z}_b(s))$  are the eigenloci of the system admittance and base impedance, respectively. These eigenvalues represent the magnitude of impedance or admittance in the synchronous reference frame. GSIM is then obtained via the element-wise multiplication (denoted  $\odot$ ) of 5.14 and 5.15 which forms an impedance ratio:

$$\begin{bmatrix} GSIM_q(s) \\ GSIM_d(s) \end{bmatrix} = \lambda(\mathbf{Y}_{sys}(s)) \odot \lambda(\mathbf{Z}_b(s)) \quad (5.16)$$

Where  $GSIM_q(s)$  and  $GSIM_d(s)$  are the q and d axis GSIM components, respectively. These components act in unison with interaction between axes to affect the stability of the grid. Therefore, the final GSIM definition combines these values into a single metric relating to the PCC voltage magnitude:

$$GSIM(s) = \sqrt{\frac{GSIM_q(s)^2 + GSIM_d(s)^2}{2}} \quad (5.17)$$

It should be noted that any converter will have a vastly different impedance during faults compared to normal operation and GSIM is not representative of fault behaviour by design.

### 5.3.2 Exploring the Properties of GSIM

Since system strength is normally obtained at the FF, the 0 Hz component in the synchronous reference frame can be extracted for initial study. If the traditional network is analysed without converters GSIM is equal to the SCR. This can be proven if a base impedance is generated for a 3 MW grid at 690 V with an X/R of 10 and FF of 50 Hz. This gives an example base impedance, resistance and inductance of 159 mΩ, 15.9 mΩ and 505 μH, respectively. If the system impedance is then considered as a Thevenin equivalent network with an SCR of 3 applied then an example system impedance, resistance and inductance of 53 mΩ, 5.3 mΩ and 170 μH, respectively. Constructing the 2x2 base impedance and system impedances using the form described 5.11:

$$\mathbf{Z}_{b,e} = \begin{bmatrix} 0.0159 + s0.505 \times 10^{-3} & 0.159 \\ -0.159 & 0.0159 + s0.505 \times 10^{-3} \end{bmatrix} \quad (5.18)$$

$$\mathbf{Z}_{sys,e} = \begin{bmatrix} 0.0053 + s0.17 \times 10^{-3} & 0.053 \\ -0.053 & 0.0053 + s0.17 \times 10^{-3} \end{bmatrix} \quad (5.19)$$

Where  $\mathbf{Z}_{b,e}$  is the example base impedance matrix and  $\mathbf{Z}_{sys,e}$  is the example system impedance matrix. The frequency response of each impedance can be generated and



the eigenvalues extracted for the FF component:

$$|\lambda(\mathbf{Z}_{b,e}(0Hz))| = \begin{bmatrix} 0.1598 \\ 0.1598 \end{bmatrix} \quad (5.20)$$

$$|\lambda(\mathbf{Z}_{sys,e}(0Hz))| = \begin{bmatrix} 0.0532 \\ 0.0532 \end{bmatrix} \quad (5.21)$$

Where  $\lambda(\mathbf{Z}_{b,e}(0Hz))$  and  $\lambda(\mathbf{Z}_{sys,e}(0Hz))$  are the eigenvalues of the frequency response of the base and system impedances, respectively at the FF. The magnitude of the eigenvalues in each case is equal to the magnitude of the impedance of each of the base and system impedances. If the GSIM is calculated dividing by  $\mathbf{Z}_{sys,e}$  instead of multiplying by the admittance for simplicity, the original SCR of 3 is obtained. The process appears somewhat trivial when RL networks are considered but the addition of converters with complex MIMO admittances begins to provide interesting results that are provided in Section V.

GSIM is mathematically equivalent to SCR as it represents the ratio of base impedance to system impedance. If the per-unit impedance form of SCR is described:

$$SCR = \frac{1}{Z_{sys,pu}} \quad (5.22)$$

Multiplication of both numerator and denominator by the base impedance provides a similar form to GSIM since the eigenloci represent the magnitude of the impedance or admittance. If the FF components are considered then both are equivalent:

$$SCR = \frac{Z_b}{Z_{sys}} \equiv GSIM(0Hz) \quad (5.23)$$

GSIM will have the same implications in terms of voltage stability to traditional SCR definitions. However, the effect of IBRs can now be represented in quasi-steady state. Moreover, the GSIM provides the same value across the frequency range for SG dominated networks. This proves the similarity and provides an initial validation of the method. However, when converters are included, the GSIM varies significantly across

the frequency range and shows areas of large/small impedance previously not present on the traditional network at the FF. Since all network components are now fully represented, this should lead to discovery of components interacting to produce SSO and harmonic interactions which are becoming more prevalent in the modern network [163, 164]. Fast identification of these areas of concern is a key benefit of using GSIM to screen stability issues over conventional metrics where they would be overlooked. This is increasingly important for impedance-based stability techniques which require multiple system ‘views’ from different points for complete analysis. GSIM facilitates fast screening of these problematic points. In the synchronous reference frame, the (0 - 50 Hz) abc components are not directly visible as they would appear (-50 - 0 Hz). However, like most FFTs the impedances are symmetrical around 0 Hz and the 0-50 Hz abc should be reflected accordingly [165]. This may vary when negative sequence components are added but can be address by representing the components in a different reference frame such as the modified sequence domain [166].

Using the developed method, an investigation of different types of control structure on the GSIM can be considered. Note that GSIM is applicable to any control structure and the same methodology as in Chapter 4 is applied looking at different combinations of GFL and GFM. Irrespective of control structure, a new converter to be connected to the network requires information about the strength of the point it is connecting to. This is completed by considering a new system impedance for the network that is the parallel combination of the original Thevenin equivalent and any converters. The GSIM can then be used to quantify the strength of the node for further connections ‘looking’ into the PCC. A system is defined to investigate this containing two converters connected to the network. A diagram is provided in Figure 5.1 considering one converter as a GFL and the other as GFM.

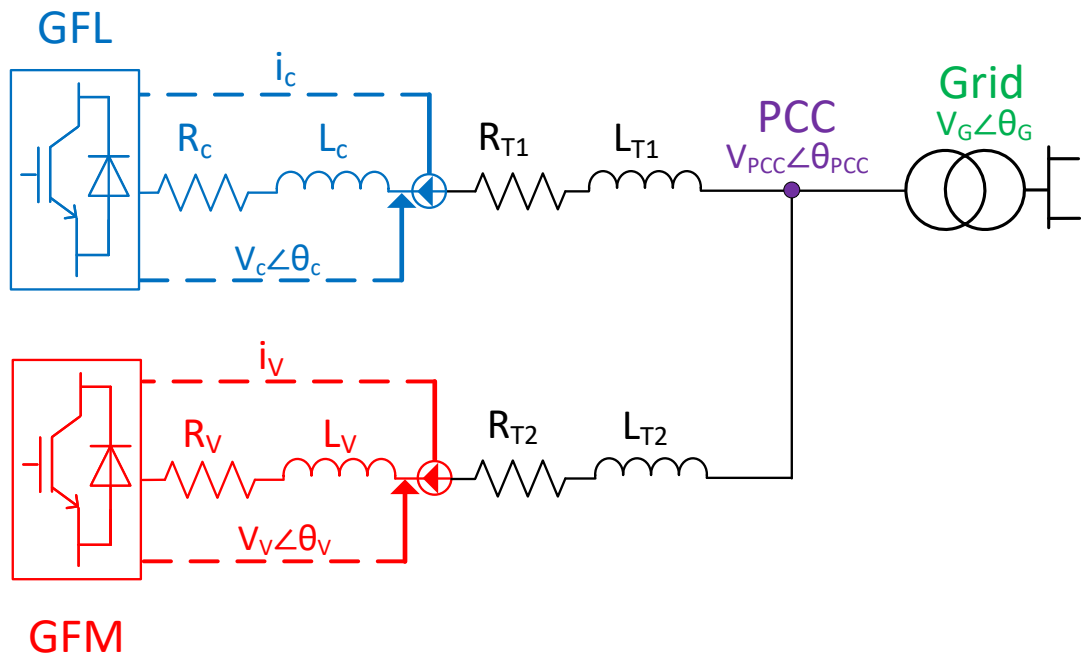


Figure 5.1: GFL and GFM connected to network

Any impedance-based method requires all components to be expressed in a single reference frame. The reference frames on the network can be related to each other via a rotation of which details can be found in GSIM[16]. The nature of the transform means that MFD or DD systems are unaffected. However, as seen from chapter 3 converter impedances rarely form these types of systems across the entire frequency range. Each converter and filter impedance is combined in series with the respective transmission line (TL) impedance and rotated into the global reference frame. The GFM admittance combination is denoted  $Y_{VT}$  and the GFL as  $Y_{CT}$ . The strength of the network is analysed by constructing the equivalent circuit from the point of view of a converter ‘looking’ into the PCC. Two points of view are considered. Firstly, the GFM looking into the network consisting of the grid and the GFL. Secondly, the GFL looking into the network consisting of the grid and GFM. An illustration of these is provided in Figure 5.2 and Figure 5.3.

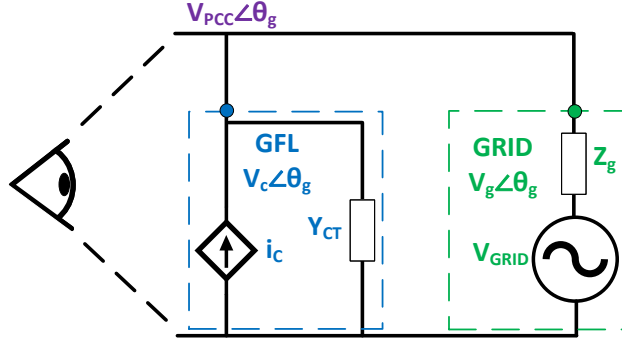


Figure 5.2: GFM system point of view

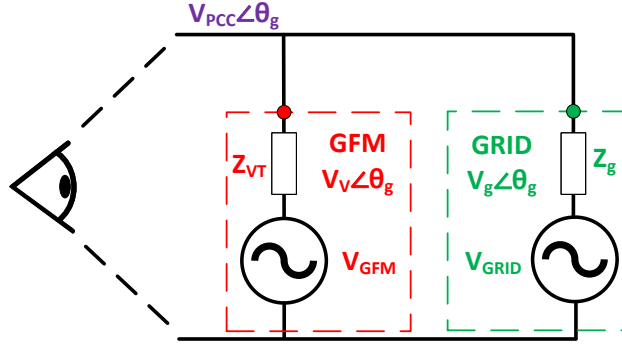


Figure 5.3: GFL system point of view

The system is simplified for initial analysis but any system topology should be possible providing the impedance traces can be obtained; this may require some topology reduction if the individual MIMO port impedances were to be used, which is a common approach in impedance-based methods [32, 161]. Failing this, a frequency sweep can be conducted at the bus in question to obtain the combined impedance of the network.

Each admittance is modelled as a standalone component and therefore the relationship between voltage and current at the terminals is likely different than when grid connected. The full converter behaviour will not be seen at the PCC and will be scaled by some factor. These factors are determined by considering the system as a combination of Thevenin voltage sources and considering the contribution of voltage to the PCC. A Norton equivalent is also possible. A scaling factor for each source is determined using the physical impedance magnitude seen at the FF:

$$C_{scale} = \frac{Z_g}{Z_{CT} + Z_g} \quad (5.24)$$

$$V_{scale} = \frac{Z_g}{Z_{VT} + Z_g} \quad (5.25)$$

$$GV_{scale} = \frac{Z_{VT}}{Z_{VT} + Z_g} \quad (5.26)$$

$$GC_{scale} = \frac{Z_{CT}}{Z_{CT} + Z_g} \quad (5.27)$$

Where  $C_{scale}$  and  $V_{scale}$  are the GFL and GFM scaling factors, respectively and  $GV_{scale}$  and  $GC_{scale}$  are the network scaling factors for the network when the GFM or GFL converter is connected, respectively. If scaling factors are disregarded the ratings of system strength can significantly over or underestimate the network strength depending on the converter of concern. From Figure 5.2 the GFM converter ‘sees’ a combination of the grid and the GFL converter with related line impedances. The stiffness at the PCC is determined by the system impedance which is the parallel combination of the grid and GFL with scaling applied:

$$\mathbf{Y}_{sys1} = C_{scale}\mathbf{Y}_{CT} + GC_{scale}\mathbf{Y}_g \quad (5.28)$$

From Figure 5.3, the GFL converter ‘sees’ a combination of the grid and the GFM converter. The stiffness at the PCC is again determined by this system impedance which is now the parallel combination of the grid and GFM impedances:

$$\mathbf{Y}_{sys2} = V_{scale}\mathbf{Y}_{VT} + GV_{scale}\mathbf{Y}_g \quad (5.29)$$

The application of each scaling factor allows GSIM to match the rating scale of traditional versions of SCR. Using these two parallel combinations, the effect that GFL control has on system strength can be explored using  $\mathbf{Y}_{sys1}$  and the GFM control using  $\mathbf{Y}_{sys2}$ . A final combination of all three components is also defined, with similar scaling terms applied to the voltage sources. However, the scaling factors now become a balance between the converter of concern and the combination of the remaining impedances on the network:

$$s_n = \frac{Z_{p,n}}{Z_n + Z_{p,n}} \quad (5.30)$$

Where  $s_n$  is the scaling factor for the  $n$ th component and  $Z_{p,n}$  is the combination of all other system impedances excluding the  $n$ th component. The third system with scaling applied is:

$$\mathbf{Y}_{sys3} = s_1\mathbf{Y}_g + s_2\mathbf{Y}_{VT} + s_3\mathbf{Y}_{CT} \quad (5.31)$$

The structure of the converter looking into the network is not important, but the power rating should be considered. The base impedance is constant for both systems. Three GSIMs are defined for analysis with a single value obtained via 5.17:

$$GSIM_{GFL} = |\lambda(\mathbf{Y}_{sys1}(s))\lambda(\mathbf{Z}_{b,3}(s))| \quad (5.32)$$

$$GSIM_{GFM} = |\lambda(\mathbf{Y}_{sys2}(s))\lambda(\mathbf{Z}_{b,3}(s))| \quad (5.33)$$

$$GSIM_{FULL} = |\lambda(\mathbf{Y}_{sys3}(s))\lambda(\mathbf{Z}_{b,6}(s))| \quad (5.34)$$

The subscript number (3 or 6) in the base impedances  $Z_{b,3}(s)$  and  $Z_{b,6}(s)$  dictates the base power in MW used for creating the network. The GSIM is used to analyse the effect of each converter type on the voltage stiffness for a weak Thevenin grid (SCR = 1) and a stronger Thevenin grid (SCR = 3). The PVCC controller is used to represent the GFL family with the VSM utilised for the GFM for initial discussion of the new metric. The results showing the scaled GSIM are then compared to alternative SCR methods at the FF in Table 5.1. The SCR shown shows the strength of the initial Thevenin network before the addition of converters. Note the initial Thevenin grid denoted  $\mathbf{Y}_{sys}$  from 5.19 is included to validate that the method is synonymous with other definitions in traditional networks.

From Table 5.1, all the grid-strength metrics are equal for the standard network with no IBRs. Note that all methods become twice as large when considering only one converter. The grid impedance is designed considering both converters, when one is disregarded, the resultant system becomes twice as strong. The CSCR and ESCR methods are equal when considering one converter only. The CSCR and ESCR underestimate the strength of the network for GFM. Moreover, the control action of the GFL is not properly accounted for with the discrepancy being larger for weaker networks. The GSIM clearly indicates an improvement in voltage strength when GFM

Table 5.1: Comparison of grid-strength metrics

<b>System</b>	<b>SCR</b>	<b>CSCR</b>	<b>ESCR</b>	<b>GSIM</b>
Network ( $\mathbf{Y}_{sys}$ )	1 3	1 3	1 3	1 3
GFL ( $\mathbf{Y}_{sys1}$ )	2 6	1.93 5.42	1.93 5.42	1.65 5.61
GFM ( $\mathbf{Y}_{sys2}$ )	2 6	1.93 5.42	1.93 5.42	4.42 7.17
Full ( $\mathbf{Y}_{sys3}$ )	1 3	0.95 2.85	0.97 2.78	1.98 3.5

converters are added to the system.

The value at the FF is conventionally used to infer the strength across the frequency range. This is acceptable as for traditional systems as every impedance component forms an RL system. If it is assumed that the X/R is large, the frequency response of each system is dominated by the inductance. Therefore, the response shape will be similar in all cases with the difference being a scalar multiplier determined by the magnitude of reactance. When converters are introduced, the RL property of the network is reduced. In this case, the GSIM (or traditional SCR) provided at the FF may not cover all the system issues as problems likely occur at different frequencies. The value can still be used however, it is probable the FF GSIM will be larger than the actual limit. For example, a GSIM of 1.1 at the FF may only be required to ensure the minimum GSIM at another frequency remains above a lower threshold. Hence, network strength should be considered across the frequency range and not just at the FF to ensure a proper characterisation of the network is obtained and GSIM is the only metric at present capable of this.

The GSIM is plotted for the three systems against a range of frequencies in Figure 5.4 to showcase the significant variation in system strength with frequency. Additionally, the effect of the GFL PLL bandwidth and GFM voltage control proportional ( $K_p$ ) and integral ( $K_i$ ) gain terms are explored. No high frequency components are modelled therefore, a frequency range of 0-400 Hz is sufficient for analysis. The GSIM is provided

in the synchronous reference frame where 0 Hz is the FF.

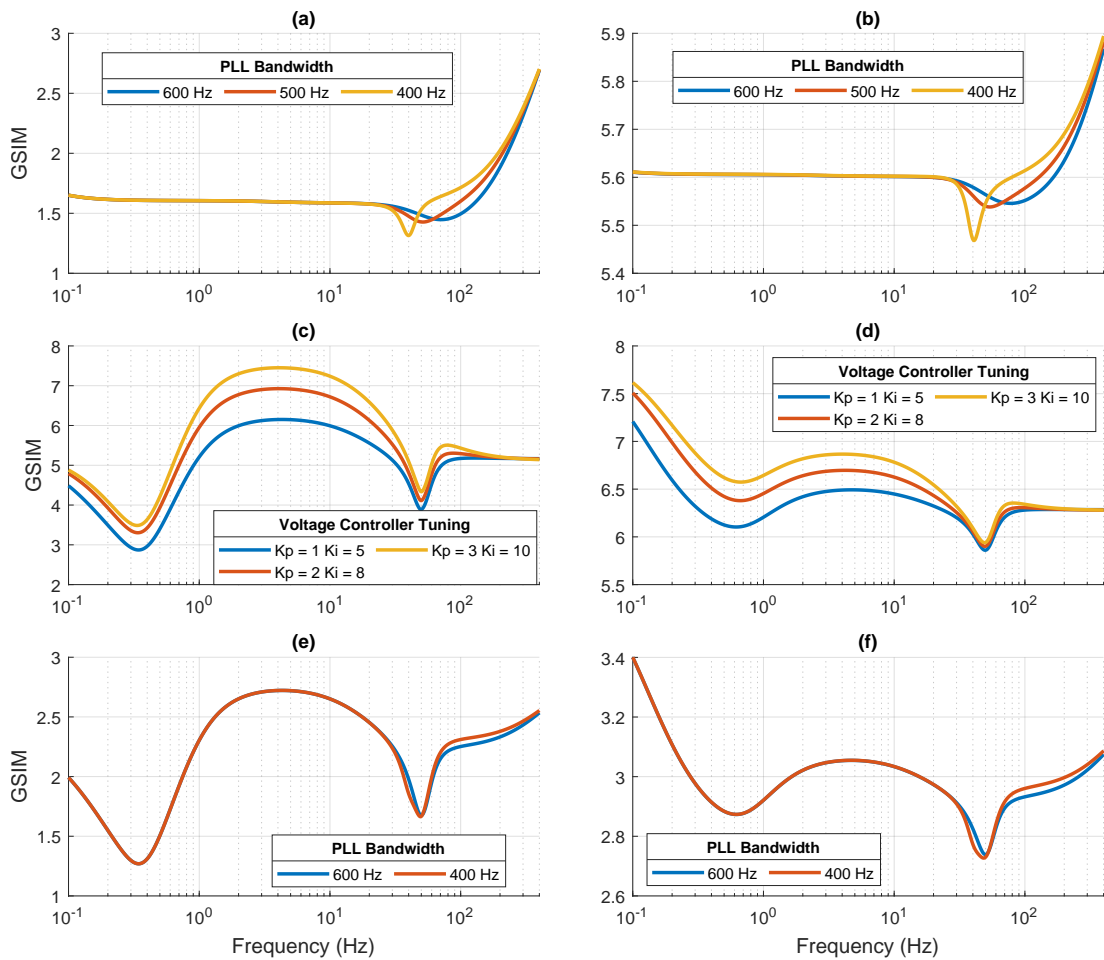


Figure 5.4: GSIM for configurations: (a)  $Y_{sys1}$  - SCR 1 (b)  $Y_{sys1}$ -SCR 3 (c)  $Y_{sys2}$  -SCR 1 (d)  $Y_{sys2}$  -SCR 3 (e)  $Y_{sys3}$  -SCR 1 (f)  $Y_{sys3}$  -SCR 3

From Figure 5.4 (a)(b), the GFL reduces the GSIM below the initial SCR at the FF and up to around 20 Hz. For both SCRs, the GSIM then falls indicating a region of high impedance and poor damping which can be seen to be sensitive to the PLL bandwidth. In Fig. 5 (c)(d), the GFM improves the network strength across most of the frequency range. For both SCRs, the impedance is smaller close to 0 Hz due to the direct voltage control of the GFM and provides a greater strength rating near the FF. This can be increased with faster tunings as shown in Figure 5.4 (c)(d). A similar peak can be formed for the GFL traces if the GFL voltage controller is tuned faster but this may harm strength at higher frequencies. This effect is again visible in Figure 5.4 (e)(f)



around 0 Hz. When the SCR is 1 the GFM converter does more work in supporting the PCC voltage as the GFM scaling factor is larger than the network factor. The PLL bandwidth effects the GSIM over the same range of frequencies as with  $\mathbf{Y}_{sys1}$  but the magnitude is reduced likely due to the increased support from the GFM. When a GFL converter is present GSIM increases at high frequencies due to the system impedance including the converter growing at a slower rate with respect to frequency than the base impedance.

## 5.4 Validation

A validation of system strength including converter control action is challenging as no previous metric exists. However, system strength has three main indicators:

1. A stronger system is more stable and therefore will exhibit greater robustness which can be measured using traditional stability techniques
2. A greater strength will provide more damping of oscillations on the network
3. A greater strength can provide more reactive support and therefore increased active power flow

Hence, when converter behaviour is included and the GSIM is higher it is expected that the system is more stable, oscillations will be better damped and can transfer more power. If GSIM correctly indicates strength considering converters, then the behaviour of the system in terms of the points above containing converters, should be similar to the behaviour of the traditional system with SCR set to the GSIM value obtained when converters are considered. This comparison is made for each indicator in the following section excluding the voltage disturbances as the method used for testing is not applicable to the standalone traditional network model.

### 5.4.1 Stability Analysis

Traditional impedance-based stability methods can be employed to validate the system strength indicated by GSIM. The analysis requires the formulation of transfer functions

that describe the current at the PCC as described in Chapter 4. In this case, the equation formed is:

$$\mathbf{i}_{pcc} = \frac{(\mathbf{i}_{c2})}{\mathbf{I}_2 + \mathbf{Y}_{c2}\mathbf{Z}_p} - \frac{(\mathbf{i}_{c1})\mathbf{Y}_{c2}\mathbf{Z}_p}{\mathbf{I}_2 + \mathbf{Y}_{c2}\mathbf{Z}_p} - \frac{(\mathbf{i}_g)\mathbf{Y}_{c2}\mathbf{Z}_p}{\mathbf{I}_2 + \mathbf{Y}_{c2}\mathbf{Z}_p} \quad (5.35)$$

Where  $i_{PCC}$  is the PCC current,  $\mathbf{i}_{c1}$ ,  $\mathbf{i}_{c2}$  and  $\mathbf{i}_g$  are the first and second converter and grid currents, respectively,  $\mathbf{Y}_{c1}$  and  $\mathbf{Y}_{c2}$  and the first and second converter admittance, respectively,  $\mathbf{Z}_p$  is the parallel impedance of the first converter and the grid and  $\mathbf{I}_2$  is an identity matrix of rank two. Since all terms are matrices the division symbol is used to represent multiplication by a right inverse to aid readability. Disk margins which were introduced in Chapter 3 were then employed to determine the robustness of the system which should have a positive relation with GSIM. This provides a form of validation as the two approaches analyse the system from a different mathematical perspective. The disk margins alongside the scaled and unscaled GSIM values are provided in Table 5.2.

Table 5.2: Comparing GSIM to MIMO Stability Margins

System	GSIM Unscaled	GSIM Scaled	Disk Margin
GFL	2.52	1.65	0.42
( $Y_{sys1}$ )	6.35	5.61	1.08
GFM	8.92	4.42	0.87
( $Y_{sys2}$ )	16.7	7.17	1.32
Full	4.52	1.98	0.86
( $Y_{sys3}$ )	8.51	3.4	1.25

The system robustness using disk margins follows the strength rating provided by GSIM. Note that a disk margin ( $< 1$ ) does not carry the same meaning as traditional margins. The gain and phase perturbation related to the disk are still ( $> 1$ ) and indicate positive stable margins. The largest disk margin of 1.32 occurs for the largest scaled GSIM of 7.17. The ratings of both GSIM and disk margin decrease in the order of  $\mathbf{Y}_{sys2}$ ,  $\mathbf{Y}_{sys3}$  to  $\mathbf{Y}_{sys1}$  from strongest to weakest for each SCR. This suggests that the different values of GSIM are correctly replicating the differing behaviour of GFL and GFM in terms of the first indicator of system strength. Conversely, other metrics

such as ESCR and CSCR which are equal for both structures suggest the behaviour is the same which does not follow the margins deduced. Moreover, if a traditional network is specified with SCRs equal to the GSIM obtained for  $\mathbf{Y}_{sys2}$  of 4.42 and 7.17, respectively. The disk margins obtained from the PoV of the GFL converter looking into the traditional network are 0.89 and 1.22, respectively. These margins are similar to the margins obtained for  $\mathbf{Y}_{sys2}$ . This suggests that the GFM converter is providing the increased system strength captured by GSIM as the system behaves comparably to a stronger traditional network of the same rating. Note, that for the traditional system the SCR and GSIM are equal offering further justification of the values obtained as the same rating of strength is obtained via GSIM for both the converter based and traditional systems despite the SCR being different. When comparing the scaled and unscaled GSIM versions, the unscaled version appears to overestimate the strength of the network greatly in each case.

#### 5.4.2 Voltage Disturbances

The ability of the system to reject voltage disturbances should increase with system strength. To justify the larger GSIM rating for GFM converters, a load of (0.5 + j0.3) MW is suddenly switched into the PCC to disturb the network and the resultant perturbation is studied at three frequencies. The magnitude of voltage disturbance is provided alongside the GSIM at disturbance frequency in Table 5.3.

Table 5.3: Voltage Disturbance Ratios

System	$ \Delta V_i/\Delta V_j $		
	75 Hz	125 Hz	175 Hz
GFL	0.403 (1.45)	0.317 (1.58)	0.235 (1.78)
( $\mathbf{Y}_{sys1}$ )	0.276 (5.55)	0.203 (5.57)	0.178 (5.61)
GFM	0.274 (5.05)	0.208 (5.18)	0.186 (5.21)
( $\mathbf{Y}_{sys2}$ )	0.187 (6.24)	0.159 (6.29)	0.150 (6.29)
Full	0.247 (2.19)	0.151 (2.27)	0.113 (2.31)
( $\mathbf{Y}_{sys3}$ )	0.179 (2.91)	0.143 (2.94)	0.128 (2.96)

From Table 5.3, the voltage disturbances are larger when the GFL converters op-

erates alone for the respective initial SCRs. The size of the perturbation is similar for  $\mathbf{Y}_{sys2}$  and  $\mathbf{Y}_{sys3}$  despite the large difference in GSIM. However, this is due to the different base powers of the system which are specified in 5.33 and 5.34 due to one converter being removed in  $\mathbf{Y}_{sys2}$ . Accounting for this, the magnitude of the disturbances is largely in agreement with the rating of GSIM. This method of validation provides certain drawbacks as the introduction of a load may introduce further interactions in the system. However, it is clear that GFM converters reduce the magnitude of voltage perturbations in the network compared to GFL. This indicates a stronger system which is correctly identified by the GSIM.

### 5.4.3 Power Flow

The traditional SCR is often used to infer the active power transfer capabilities of a system. While instabilities caused by interactions between active power flow and voltage are likely not small-signal issues, the impedances determined from small-signal models can be used to infer the power transfer capabilities of the system. The absolute maximum power is determined by the line impedance to the grid as the power capability cannot be violated. However, the connected generation determines how much of this transfer capability can be utilised. GFLs exhibit instabilities when operating close to the physical line limit due to the non-linear relationship between power and voltage [15]. However, GFMs can operate right up to the maximum angle without instability and allow GFLs to increase their maximum angle. The GSIM can represent this feature. New operating points must be utilised for the impedance models that are closer to the limit of power transfer. For  $\mathbf{Y}_{sys3}$ , the active power contribution is considered solely from the GFL converter. This is to allow comparison between the strength provided from the GFM converter and from the traditional network. The converter is assumed to have no current limit to allow high power operation for validation purposes. The GSIM is plotted for the three systems for each SCR in Figure 5.5.

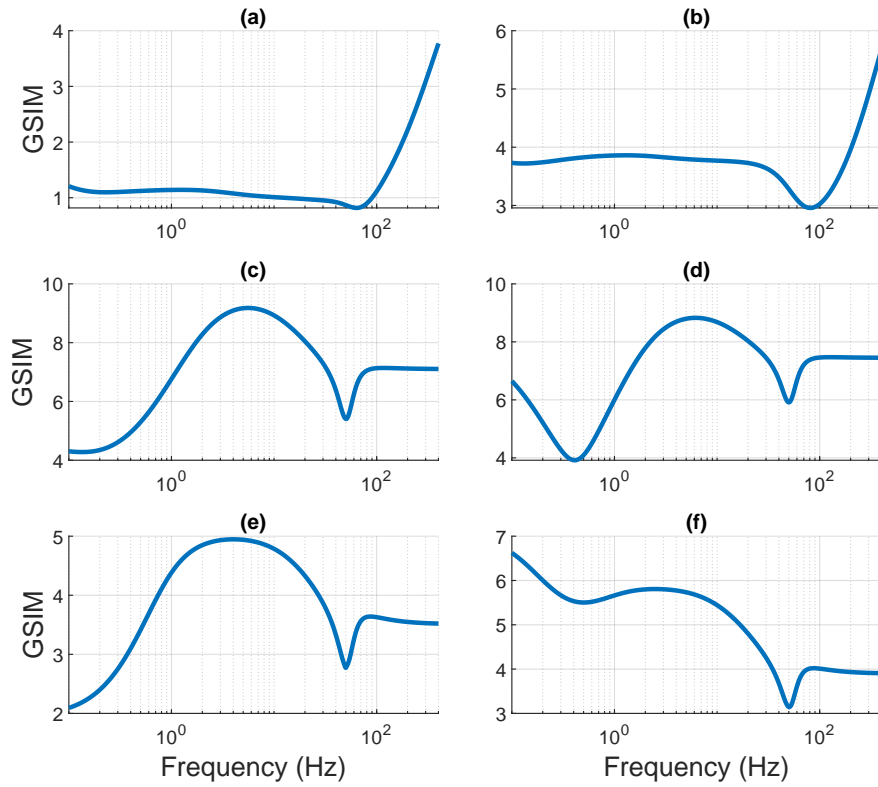


Figure 5.5: GSIM at power limit for configurations: (a)  $Y_{sys1}$  - SCR 1 (b)  $Y_{sys1}$ -SCR 3 (c)  $Y_{sys2}$  -SCR 1 (d)  $Y_{sys2}$  -SCR 3 (e)  $Y_{sys3}$  -SCR 1 (f)  $Y_{sys3}$  -SCR 3

From Figure 5.5 (a)(b), the GFL converter weakens the network more at higher operating points which can be seen from the lower GSIM rating compared to Figure 5.4. This is due to the higher equivalent converter impedance from the increased reactive power contribution to support the PCC. In the case of GFM in Figure 5.5 (c)(d), the strengthening of the network is reduced compared to the normal operating point in Figure 5.4. However, the converter still contributes increased support to the PCC, allowing higher power operation. When considering the combination of converters in Figure 5.5 (e)(f), the GSIM at the FF is higher than when only a single converter is connected. One reason for this is the respective reactive power contribution from each converter is smaller, lowering the effective impedance. The results are compared to time domain simulations where the power output from the respective converter was ramped until the system became unstable. The maximum active power transfer is shown alongside scaled and unscaled GSIMs in Table 5.4.

Table 5.4: Comparing GSIM to MIMO Stability Margins

System	Power Transfer		GSIM (unscaled)	
	SCR 1	SCR 3	SCR 1	SCR 3
$(\mathbf{Y}_{sys1})$	3.8 MW	9.8 MW	1.2 (2.5)	3.73 (15.4)
$(\mathbf{Y}_{sys2})$	5.7 MW	16.8 MW	4.3 (6.2)	6.64 (14.8)
$(\mathbf{Y}_{sys3})$	5.5 MW	15.7 MW	1.82 (9.14)	5.86 (9.0)

From Table 5.4, considering SCR 1, the maximum power transfer is worst for the GFL converter. The GFM converter improves this significantly, which is consistent with the GSIMs calculated. The same agreement can be seen between the time domain simulations and the GSIM calculation at an initial SCR 3. Similar to Section IV, the unscaled GSIMs provide an exaggerated view of system strength. If the unscaled values for GFL and GFM are compared for an SCR of 3, the GFL converter appears to provide more strength than the GFM which is incorrect based on the maximum power flows.

To further validate the approach, a traditional network with SCR equal to the GSIMs obtained for  $\mathbf{Y}_{sys3}$  is specified. A GFL converter is then connected and the maximum power flow is obtained as 5.74 MW when the SCR is 1.82 and 15.6 MW when the SCR is 5.86. Note,  $\mathbf{Y}_{sys3}$  is used instead of  $\mathbf{Y}_{sys2}$  as with the stability margins, as the power flow must be determined after the connection of the converter. These values are similar to that of  $\mathbf{Y}_{sys3}$  with an error of -4 % and 0.64 %, respectively. This indicates that the GSIM provides a similar rating of strength for a converter dominated network, as the SCR provides for the traditional network in terms of power flow.

In a traditional system, the SCR and GSIM are equivalent at the FF and remain the same value across the frequency range. Therefore, the traditional SCR is sufficient to make conclusions across the whole range of frequencies. For converter dominated systems, the result suggests that the strength provided at the FF is not representative of the entire frequency range. In fact, a definition that the minimum operable strength is 1.2 may not be the real cause of issue. The minimum strength at the FF may be required to ensure the strength at a different frequency is above another threshold. Around 0.82 at 64 Hz in the case of Figure 5.5 (a). It is unlikely that instability will occur due to an oscillation at the FF. It is more likely that the system will become unstable during

in the transition between operating points, achieved by injecting disturbances above or below the FF to reach the new operating point.

## 5.5 Case Studies

This section applies the new technique of GSIM to the system configurations studied using impedance stability methods in Chapter 4. To begin only the fundamental frequency component is studied as this allows fast analysis of the most interesting combinations. Following this, the GSIM is plotted across the frequency range for a number of key cases and an investigation of the key tuning parameters is conducted.

### 5.5.1 Fundamental Frequency

The GSIM for the combinations of all six converter types in the same configuration as shown in Figure 4.3 are provided for an active power operating point of 0 and 0.5 p.u. in Figure 5.6 and Figure 5.7, respectively. One further operating point of 1 p.u. is provided in Figure D.1 in Appendix D.

## Chapter 5. Screening Stability Issues

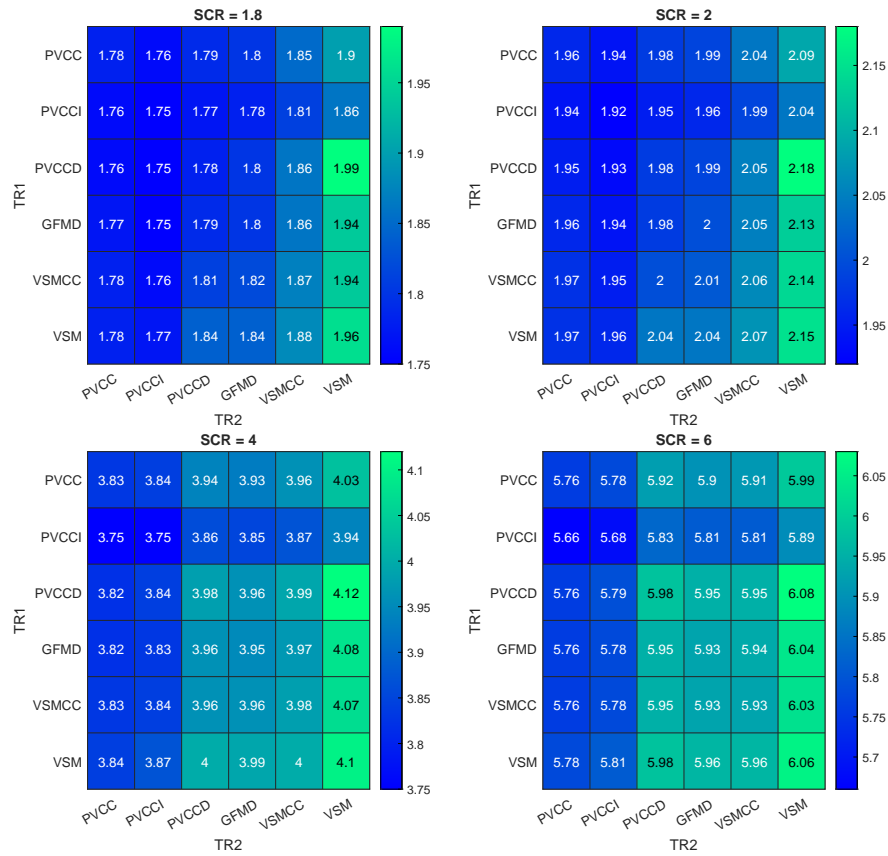


Figure 5.6: GSIM for Two Converter System at 0 p.u. active power

From Figure 5.6, it is clear the GFM structures are providing increased strength when compared to the GFL combinations. Moreover, the system strength is greater when the GFM converter is connected via the shorter transmission line, evident from the green vertical bar on the right hand side VSM column. This behaviour is replicated for the other GFM structures. This is in agreement with the stability analysis in the previous chapter considering the PoV. The GSIM provided in this case would be the PoV of another system component looking to connect to the PCC. Therefore, the closer the GFM converter to the PCC the more artificially stiff the PCC appears. Hence, the differential mode stability from the PoV of the new connection (assuming it was GFL dominated) would show greater robustness if the GFM was connected to the shorter transmission line. Similar to the differential mode 1 analysis in the previous chapter.

In terms of GFL, there is no particular weakening evident but this is due to the lack



of power flow which reduces the apparent GFL impedance and prevents the converter weakening the network. Interestingly, as the SCR of the network increases, the effect of the GFM converter is reduced. This is because the network impedance is small enough to provide most of the system strength, since the grid impedance is lower than the GFM the GFM converter cannot enhance the system strength. Conversely, the effect of the GFL converter is exacerbated at higher SCRs, this does not cause issue as the remaining GSIM is still high.

The VSM structure always provides a strengthening even at high SCRs while the GFMD and VSMCC controllers begin to worsen at a higher SCR. This is likely due to a different droop setting used in the reactive power controller. The higher the droop gain, the less strength provided to the system as the voltage setpoint reacts more to external factors. However, it is interesting to note that the increased reactive droop gain improved the stability robustness in Chapter 4 when considering two VSM controllers. This makes sense logically, if both VSM converters have a small reactive droop gain they both try to dictate the voltage at the PCC which becomes too stiff with too many sources trying to control it which leads to increased interaction between the two and reduced robustness.

From Figure 5.7, the increased flow of active power increases the weakening caused by the GFL converters for all SCR. Additionally, the strengthening provided from the GFM converters is enhanced in most cases. The VSM controller again provides the greatest strengthening. However, the discrepancy between the VSM and VSMCC is worsened as the operating point increases with the VSMCC beginning to weaken the network at higher SCR. Again, this is due to the reactive droop gain. From Figure D.1, the same effect is observed as the operating point increases further. All GFL controllers present a significant weakening of the system. The GFM controllers with a larger reactive droop gain provide a slight weakening of the system but this is not as pronounced as the GFL structures.

## Chapter 5. Screening Stability Issues

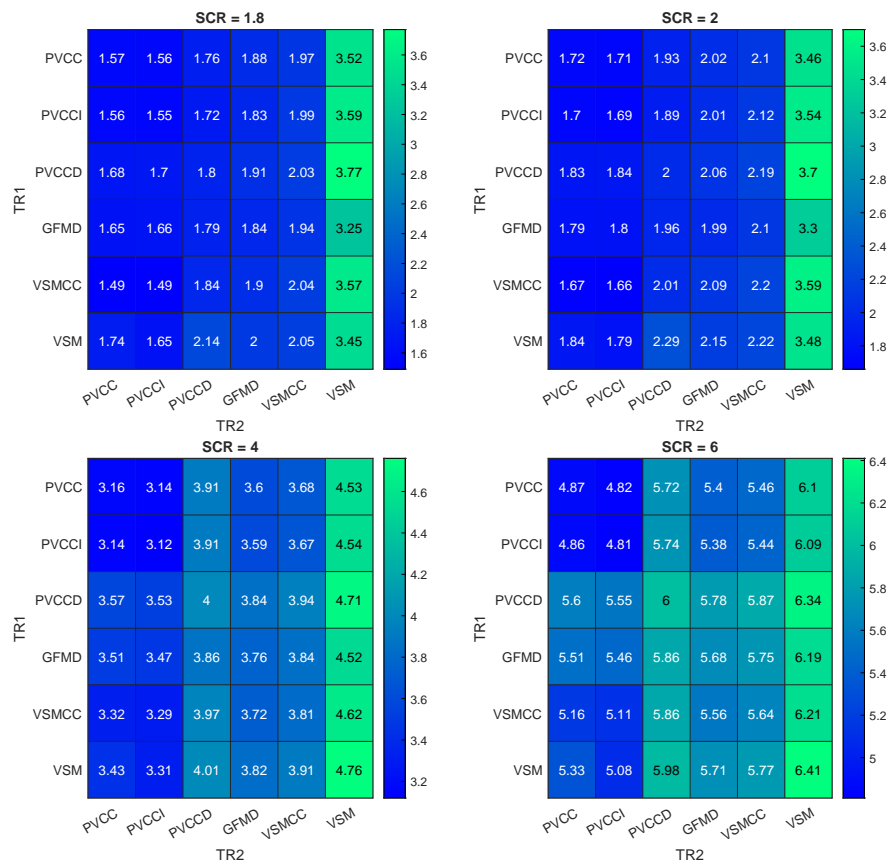


Figure 5.7: GSIM for Two Converter System at 0.5 p.u. active power

The difference in reactive droop gain was deliberately inserted to showcase the effect on system strength. The reactive power droop can be enabled on all controllers except the PVCCD to investigate the effect. An SCR of 2 and an operating point of 0.5 p.u. are used to illustrate this effect as it shows the best balance between GFL weakening and GFM strengthening. Four different reactive droop gains are then applied for each controller and the results are provided in Figure 5.8. The GSIM values obtained for a varying reactive droop gain are compared with measures of the common and differential mode robustness in Figure 5.9 and Figure 5.10, respectively.

## Chapter 5. Screening Stability Issues

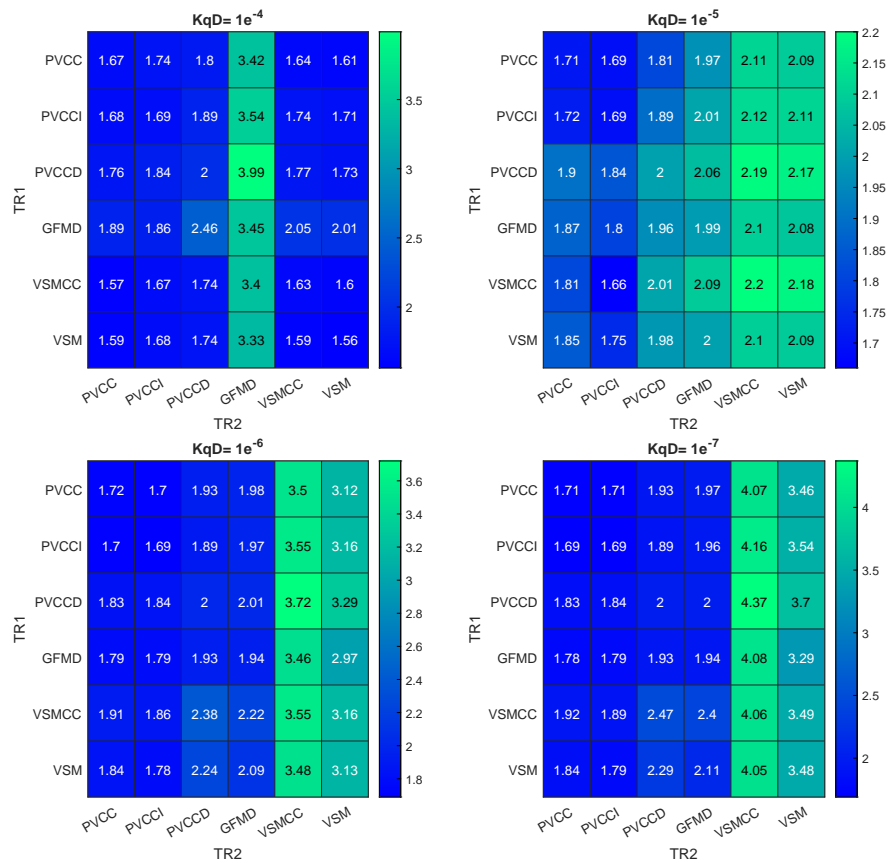


Figure 5.8: Comparison of GSIM for Controller Combinations Varying Reactive Droop Gain at 0.5 pu SCR = 2

From Figure 5.8, it is clear the reactive droop gain  $KqD$  has a significant effect on the GFM ability to provide system strength. In reality, as the gain increases the converter participates more readily in power sharing causing the reactive current to vary greatly which in turn alters the equivalent impedance. The original conclusion that the VSM controller provides the greatest strength is not strictly true. When the droop gains are matched the VSMCC provides the greatest strength. However, the common mode and differential mode robustness shown in Figure 5.9 and Figure 5.10, respectively tell a slightly different story.

Chapter 5. Screening Stability Issues

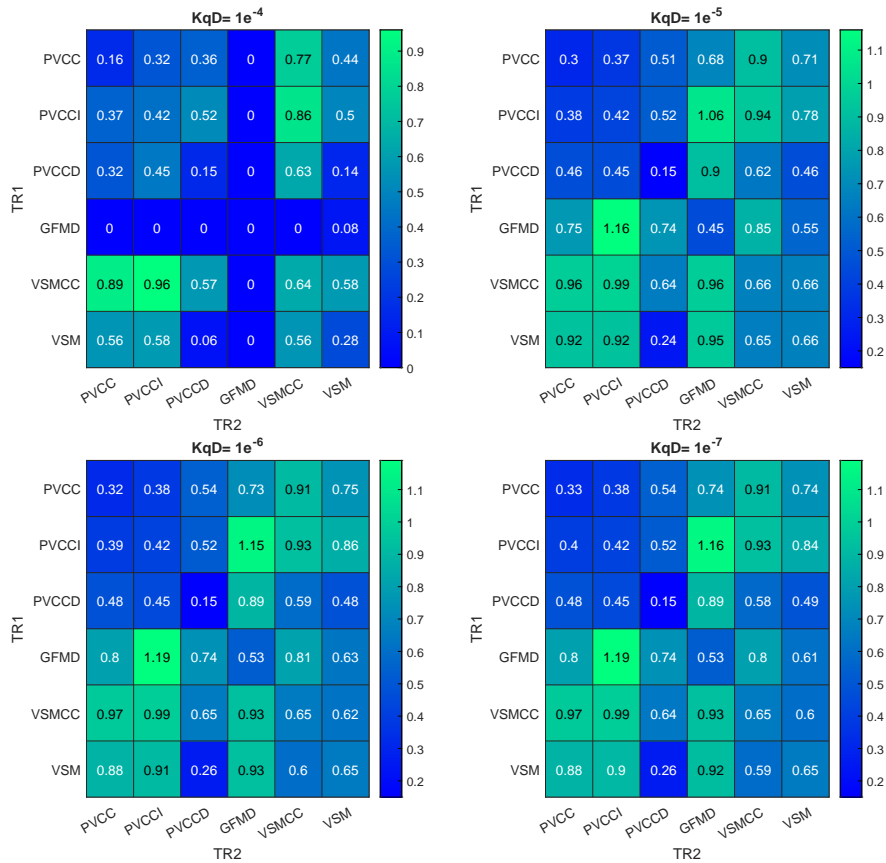


Figure 5.9: Comparison of Common Mode Robustness for Controller Combinations Varying Reactive Droop Gain at  $0.5 \text{ pu SCR} = 2$

For the highest reactive droop gain the system is clearly close to instability in most cases and is in fact unstable for GFMD. Interestingly, it should be noted here that again, despite analysing the different points of view (common or differential mode) the same absolute stability conclusion is reached for both. The GFMD is unstable for the largest droop gain. For the remaining droop gains, the VSM robustness is largely unaffected by droop gain setting while the strength provided significantly increases when the droop gain is reduced. Conversely, the VSMCC controller appears to become less robust as the droop gain reduces yet the system strength has significantly increased. This suggests a fundamental difference in the way these controllers interact despite being largely similar. The droop gain had least effect on the robustness of the GFL structure with the exception of the largest gain as this was clearly too large and was causing

reduced stability in all systems.

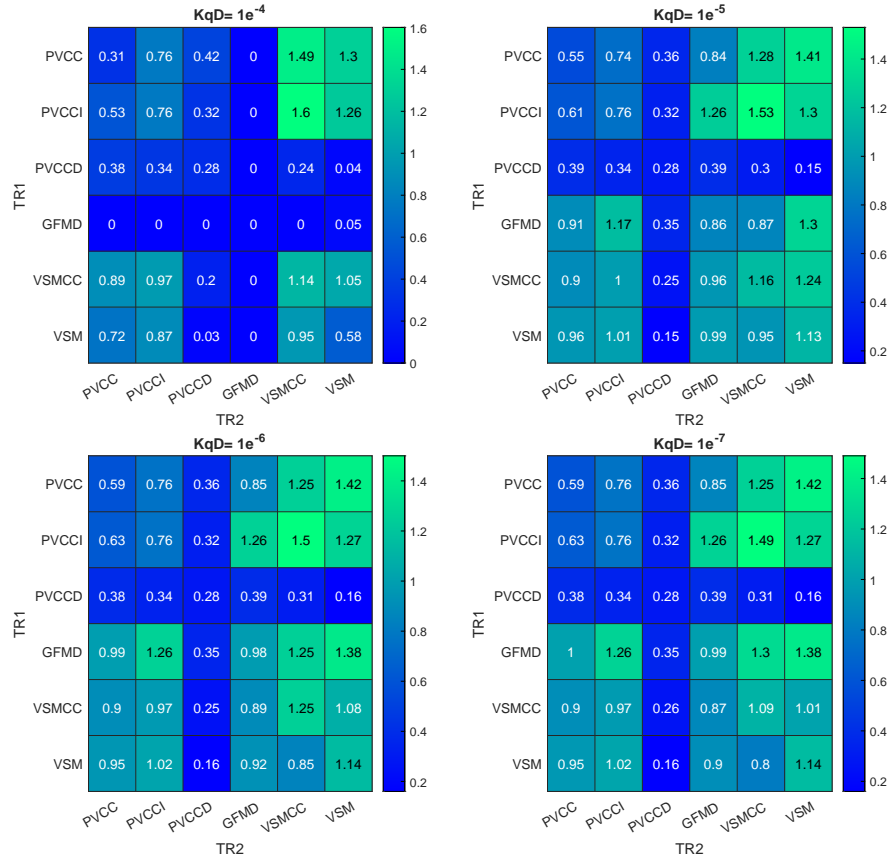


Figure 5.10: Comparison of Differential Mode Robustness for Controller Combinations Varying Reactive Droop Gain at  $0.5 \text{ pu SCR} = 2$

From these studies the following conclusions can be drawn:

1. GFL structures do not harm system strength when active power flow is zero
2. GFL structures do harm system strength when exporting active power and system strength becomes lower as active power increases
3. GFL structures harm system strength more when the SCR is higher
4. PVCCD provides the least weakening followed by PVCC and PVCCI
5. GFM structures enhance system system strength irrespective of operating point but more strengthening is observed at higher operating point

6. GFM structures provide greater strengthening at lower SCR due to increased responsibility of forming the PCC voltage due to high grid impedance
7. The strengthening from the GFM controller is highly dependent on reactive power droop gain as this causes the GFM controller to react more to network changes.
8. The system strength at the PCC is greatest when the GFM converter is connected close to the PCC to provide the greatest strength for further connections to that point
9. This improves network stability and improves the performance of any GFL converter that may be connected, a similar conclusion as when studying the common and differential mode 1 robustness
10. If GSIM was calculated for a single converter, the PoV of the GFM converter would see a weaker network and while stable, would be less robust, a similar conclusion as to when studying the differential mode 2 robustness
11. VSMCC provides the greatest strengthening, followed by VSM and finally GFMD
12. Smaller values of reactive droop gain provide greater strength in VSM and VSMCC
13. Smaller values of reactive droop gain provide greater robustness for VSM yet lower robustness for VSMCC
14. Increasing the system strength may not always lead to enhanced stability, very small impedances between GFM converters will appear strong but will likely cause the converters to fight to control voltage which is seen in differential mode robustness

### 5.5.2 GSIM Across the Frequency Range

While system strength has always been determined at the fundamental frequency, this may only provide adequate information in the traditional network with a low penetration of power converters. As the number of IBRs increases more information may be required at other frequencies that could lie within the bandwidth of the converter as

this is generally much larger than synchronous machines. The frequency dependent nature of GSIM can identify issues at other frequencies which may be more likely to occur as IBR penetration grows. The same analyses conducted at the FF are now explored across a frequency range of (1 - 1000 Hz). The GSIM is shown for a system with  $SCR = 2$  and operating points of 0 and 0.5 p.u. in Figure 5.11 and Figure 5.12, respectively. Figure 5.13, provides the same result at 0.5 p.u. power for an SCR of 4 for further comparison of the impact of the network. Furthermore, Figure D.2 in Appendix D illustrates an operating point of 1 p.u.

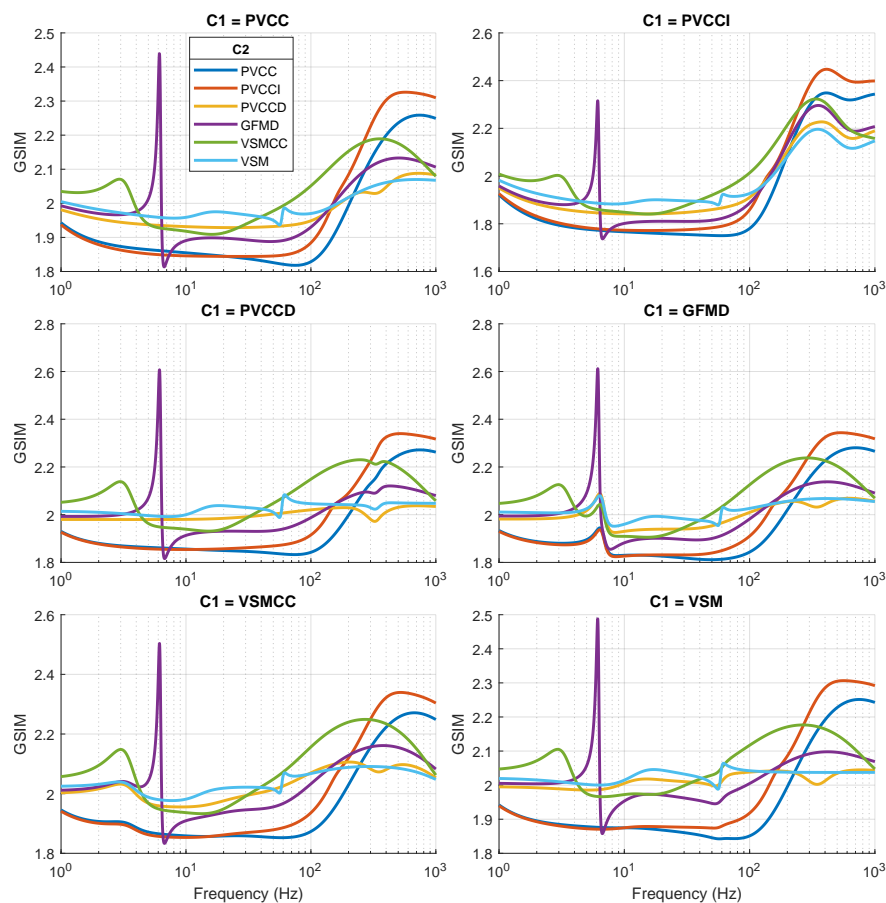


Figure 5.11: Comparison of Frequency Dependent GSIM for Controller Combinations 0 pu  $SCR = 2$

From Figure 5.11, the GFM converters provide increased strength throughout the low frequency range up to around 10 Hz. The GFMD appears to suffer from some form of complex combination of poles and zeros around 6 Hz. While this does not cause a

big deviation in the strength rating, it may cause an issue due to the fast rate of change of strength in this region. If the frequency of the disturbance was to vary around 6 Hz it may cause significant harm to stability. This can be confirmed by analysing the frequency of worst case perturbation calculated as part of the disk margins. From the PoV of the GFMD this frequency is 6.23 Hz. When the GFMD is operating at the end of the longer line the pole-zero issue is much less pronounced indicating the poor robustness could be due to an interaction with the line and not the other converter. This provides a good example of how the problematic points can be identified and suggests it is not only magnitude of GSIM that matters, the rate of change may also provide some important information which may be related to the angle associated with each eigenvalue.

Beyond 10 Hz, the GFM controllers utilising current control appear to cause a reduction in strength last until 30 Hz for VSMCC and as far as 150 Hz for the GFMD. The VSM controller remains largely constant throughout these ranges with a strange pole-zero combination observed around 60 Hz. However, when analysing the worst case perturbation, the frequency returned is over 100 Hz suggesting the pole-zero combination does not cause a significant issue. The trace experiences less of a rate of change of strength compared to the problematic point observed with GFMD. The VSM controller does not appear to increase strength above 100 Hz. However, every other controller including GFL, appears to strengthen at higher frequencies.

Interestingly, the inertia emulation of the PVCCI controller provides a stronger system in the low frequency range compared to the PVCC and removes the region of poor damping due to the PLL. This suggests that the inertia emulation is provided some form of voltage phase response, quick enough to reduce the negative effects of the PLL in weak grids. This indicates that some forms of synthetic inertia may operate more like inherent inertia than previously thought. The PVCCD seems to offer a flat trace, not really altering the strength of the network. However, the stability analyses conducted previously indicated that the PVCCD controllers were the least robust. Hence, the poor behaviour of the controller may not be related to the system strength and is instead poorly tuned.



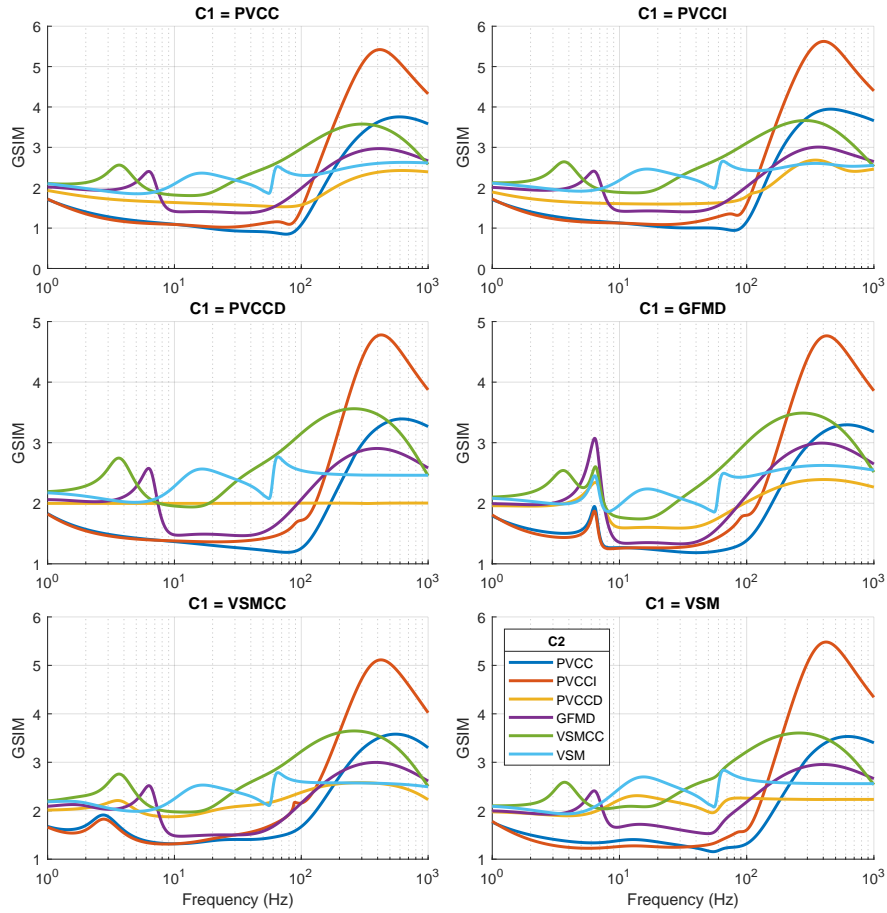


Figure 5.12: Comparison of Frequency Dependent GSIM for Controller Combinations  $0.5 \text{ pu SCR} = 2$

From Figure 5.12, the first noticeable difference is that the problematic singularity related to the GFMD was removed with increased active power flow and this was confirmed by analysing the worst case perturbation which also moved frequency. Additionally, the increased power flow degrades the performance of the GFL controllers in the middle frequency range (10 - 100 Hz). Conversely, the higher operating point increases the strength provided from the VSMCC lowering the frequency at which the strength begins to increase from 30 Hz to around 20 Hz.

The VSMCC appears to have a small admittance pole around 4.5 Hz with the peak growing as the operating point increases. This is due to the reactive droop controller of which the effect is shown in Figure 5.14 for an SCR of 2 and power flow of 0.5 p.u. with the droop gain reduced from  $1 \times 10^{-5} \text{ V / VAr}$  to  $1 \times 10^{-6} \text{ V / VAr}$ . The larger the

droop gain the smaller the effect of this pole. This has an opposite relation with the system strength provided. Since the strength rises sharply around 4.5 Hz which is close to the fundamental frequency, this has the effect of increasing the strength seen at the fundamental frequency. This only occurs when current control is present. It is likely, lowering the droop gain to improve system strength will cause instability sooner in the VSMCC controller over the VSM as this pole will quickly largen and cause problems.

The traces observed for PVCC and PVCCI at each SCR and operating point do provide some insights in to why GFLs exhibit poor performance in weaker systems. There is a poor damping of any frequencies within the range of converter action especially around 60 - 100 Hz which was shown to be due to the PLL tuning in Figure 5.4. The inertia emulation in the PVCCI controller does also appear to enhance the system strength in the region originally affected by the PLL tuning. The range of frequencies affected seems to increase with the operating point. The PVCCI controller does still exhibit poor strength characteristics in the lower frequency ranges. The GFM structures appear to do significant work to remove this negative PLL behaviour when considering two converters but this could be a key point for determining the possible balance of GFL to GFM. It is also important to consider that the GFM has removed the unwanted PLL interaction from the PoV of a new connection. However, poor interactions may still occur between converters and it is important to consider all points of view.

From Figure D.2, when operating at the maximum operating point the previously described effect become even more prevalent. The difference between the PVCC and PVCCI becomes more obvious and highlights that the inertia emulation doe useful work in maintain system strength, not just providing inertia. Furthermore, the high frequency behaviour of every control structure illustrates greater strengthening at higher operating points. Moreover, the problematic pole zero combination for GFMD is significantly reduced. For the VSM and VSMCC the highest operating point appears to reduce strength around the fundamental frequency slightly but a significant improvement is observed at higher frequencies.

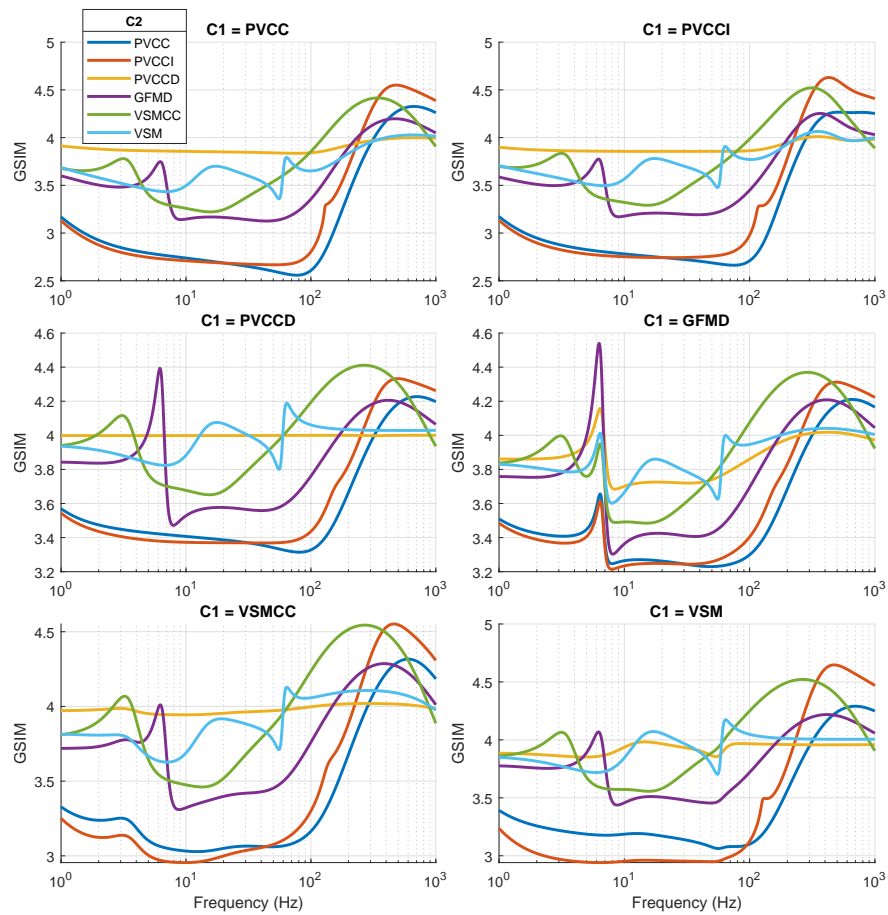


Figure 5.13: Comparison of Frequency Dependent GSIM for Controller Combinations  
 1 pu SCR = 4

From Figure 5.13, the higher SCR appears to enhance the negative effects of each control structure. For the PVCC and PVCCI the relative weakening is higher than at lower SCRs but does not offer concern overall as the GSIM is still high excluding the region affected by the PLL. The sharp dips due to PLL operation are removed at higher SCRs but a more uniform weakening throughout the low and mid frequency ranges is observed. The strengthening provided from the GFM structures is also reduced across the frequency range. The effect of the GFMD pole zero combination is much the same and appears independent of SCR and more related to operating point.

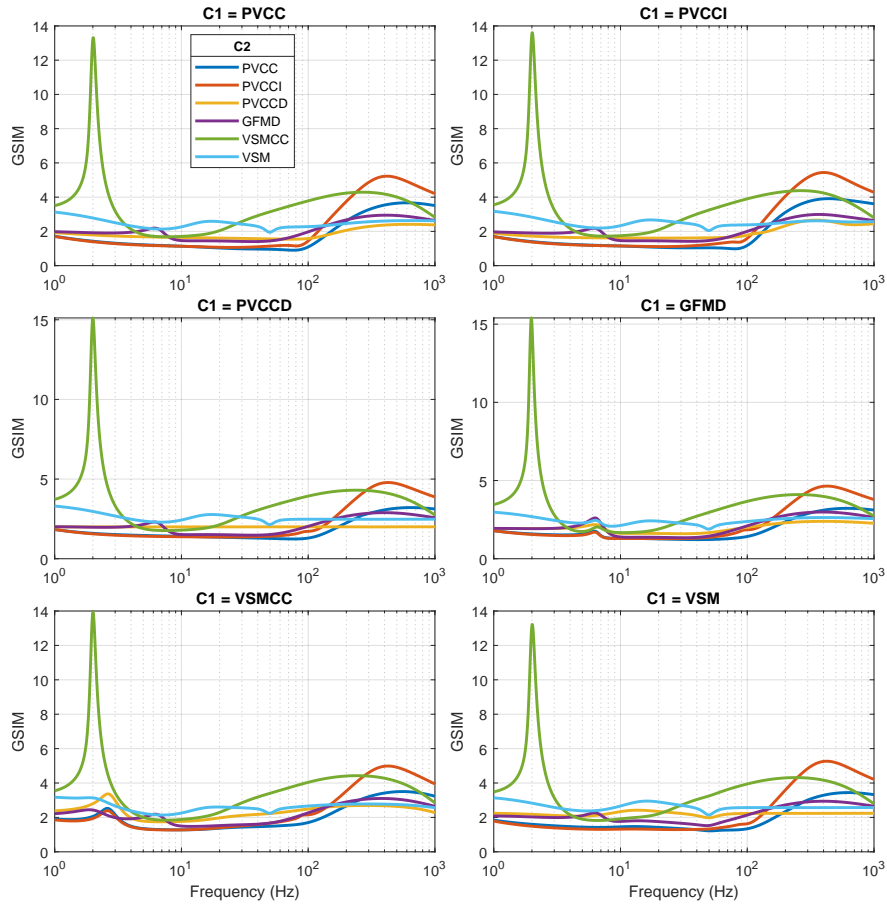


Figure 5.14: Comparison of Reactive Droop Gain using GSIM for Controller Combinations 0.5 pu SCR = 2

From Figure 5.14, the effect of the reactive droop gain on the GFM controller strengthening is evident. Both the VSM and VSMCC create a stronger network at the fundamental frequency when the reactive droop gain is lower as shown in Figure 5.8. However, analysing only the fundamental frequencies misses the large pole close the FF when utilising the VSMCC. This is not observed with the VSM. This large pole is likely the reason for the reduced robustness observed when analysing the effect of the droop gain in the previous section. While this does not cause an instability under the present tuning it offers a similar GSIM trace to capacitance based interactions and could suggest the formation of a region of low frequency negative damping which has been reported in some GFM structures. This behaviour cannot be confirmed using magnitude alone, however GSIM could be extended to include the eigenvalue angle in

future work.

On the topic of reactive droop gain, it has been suggested that tuning the voltage controller of GFLs fast may have a beneficial result on the resultant system strength. This effect is explored using GSIM utilising only the GFL controllers for a varying reactive droop gain and voltage controller tuning constant. PVCCD is excluded as the droop control does not produce strict enough control of the voltage. The frequency dependent GSIM is shown for four reactive droop constants in Figure 5.15. The effect of the voltage controller is explored after in Figure 5.17.

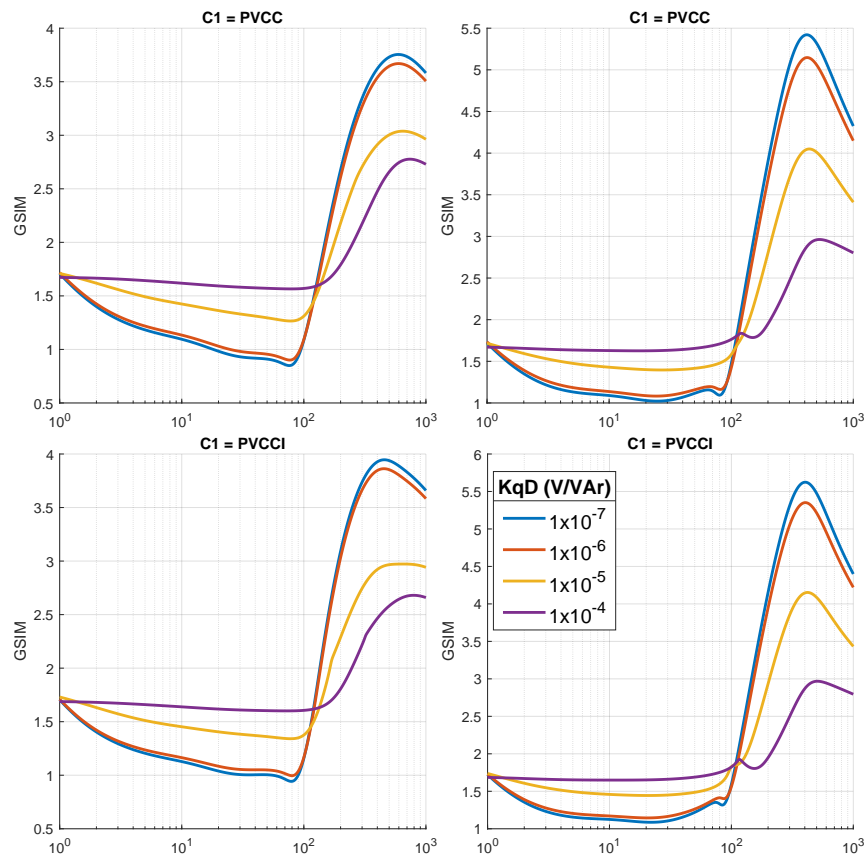


Figure 5.15: Comparison of Reactive Droop Gain using GSIM for Controller Combinations 0.5 pu SCR = 2

From Figure 5.15, the reactive droop gain significantly effects the system strength across a range of frequencies. Interestingly, not much of an effect is observed at the fundamental frequency. The regions of poor damping due to PLL are reduced as the gain enlarges however, the high frequency strength is reduced. This would suggest that a

higher droop gain is better for system stability. However, if the common mode stability robustness shown in Figure 5.16 is consulted, it can be seen the systems appear to be least stable for the highest droop gain. This suggests providing the enhanced system strength from GFL does not provide as much stability as with the VSM. Since the same effect is observed for VSMCC the issue may be related to attempting to provide system strength with controllers utilising current control. However, the robustness of the VSMCC can likely be improved with retuning to remove the low frequency pole interacting with the reactive droop controller.

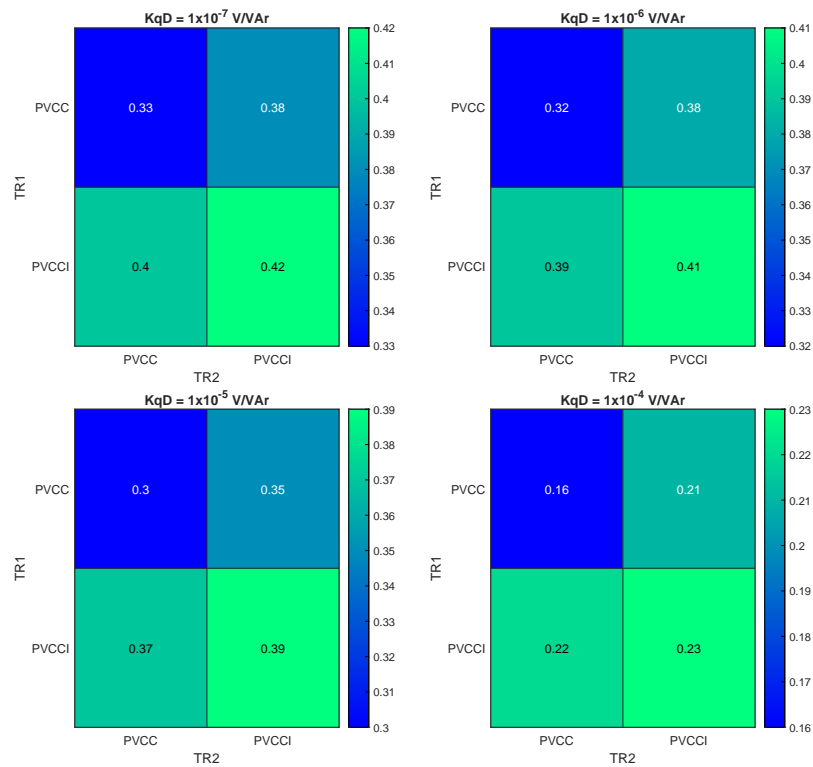


Figure 5.16: Comparison of Reactive Droop Gain on CM Robustness for Controller Combinations 0.5 pu SCR = 2

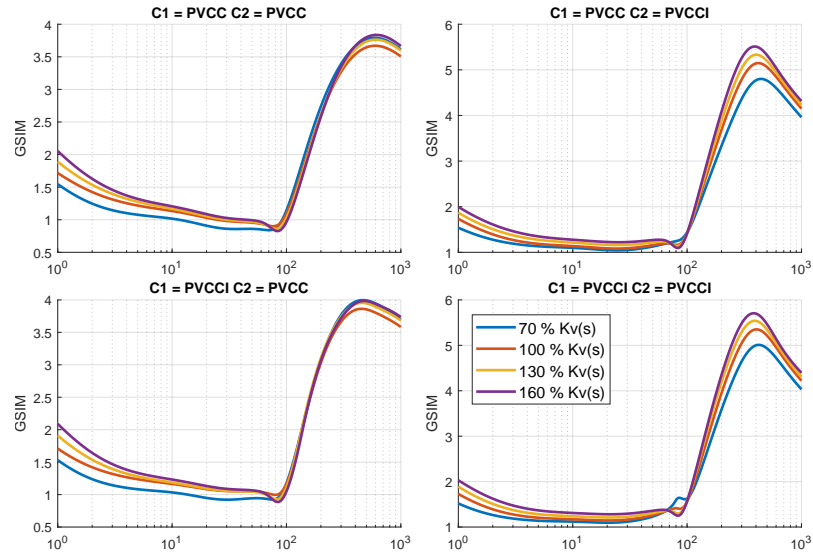


Figure 5.17: Comparison of Voltage Control Gains using GSIM for Controller Combinations 0.5 pu SCR = 2

From Figure 5.17, the voltage controller tuning was achieved by multiplying the proportional gains by the percentage shown in the legend. It is clear that the voltage control has a greater effect at the fundamental frequency. The results follow what is suggested in literature as the system strength appears to increase at the FF as the voltage controller is tuned faster. However, as the controller is tuned faster the negative effect from the PLL around 85 Hz is worsened for all controller combinations. It should be noted that even with the largest voltage controller gains used, the strength did not match either of the VSM topology. The common mode robustness for each voltage control gain is shown in Figure 5.18 where it can be seen that the system becomes significantly less robust as the voltage controller is tuned faster and in the case of the PVCCI becomes unstable for the fastest voltage controller. While tuning the voltage controller may improve the system strength at the fundamental frequency, further issues are caused at other frequencies and this behaviour is not observed when using GFM structures. This indicates the importance of utilising a frequency dependent rating of system strength.

Chapter 5. Screening Stability Issues

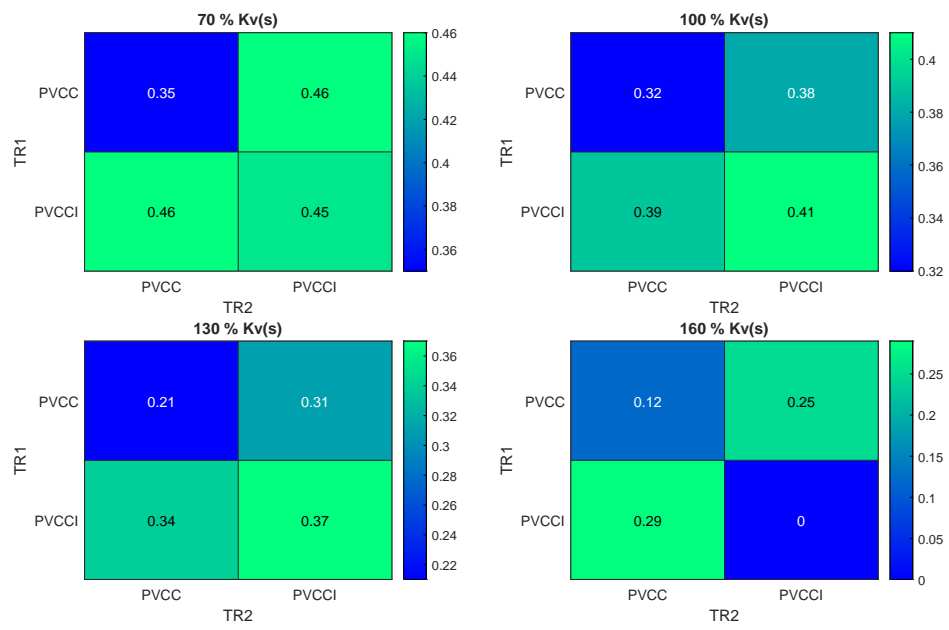


Figure 5.18: Comparison of Voltage Control Gains on CM Robustness for Controller Combinations 0.5 pu SCR = 2



From the frequency dependent GSIM analysis the following conclusions can be made:

1. System strength varies significantly across a range of frequencies and can be vastly different only a few Hz from the fundamental
2. The GFM controllers tend to provide a flatter trace of strength throughout the range
3. The current controlled VSM offered a strange low frequency interaction when the droop gain was tuned too low to enhance strength
4. The GFMD exhibited a low frequency pole zero combination not highlight by the strength at the FF
5. The inertia emulation appears to act more like inherent inertia, reducing the negative effects of the PLL and improving the strength across the range of frequencies
6. Tuning GFL controllers to provide virtual stiffness at the FF causes worse interactions at higher frequencies
7. Even when GFL is tuned to provide stiffness, GFM always perform this better and offer a more robust system
8. The system strength around the FF is improved with faster GFM voltage tuning but this harms stability at higher frequencies

## Chapter 6

# System Interactions of Windfarms

This chapter explores the system interactions that could occur in new wind parks operating a mixture of GFL and GFM control. The interactions of traditional grid followers have been well researched but the new GS and GFM characteristics may offer new challenges. For example, power dense situations like the provision of inertia and frequency support may cause increased wear on wind turbine mechanical components due to increased drivetrain oscillations, blade bending and tower sway. These oscillations can propagate to the network and since they are related to mechanical time constants, occur at lower frequencies and could interact with GFM structures. Moreover, lower energy services such as the provision of system strength and voltage support may cause further local interactions between wind turbines and arrays.

Modelling multiple turbines operating differing control while including the mechanical interactions of each turbine is computationally intensive. Therefore, this chapter is split into two distinct sections. The first section of the chapter focuses on identifying mechanical issues behind the turbine when converters are tasked with increased participation in network frequency and voltage support. The increased power fluctuations will likely cause increased torque steps within the mechanical drivetrain and could reduce the MTTF of the wind turbine. Moreover, the torque steps may cause oscillations at novel frequencies that could propagate to the network. These frequencies could change

and worsen as the turbine experiences faster aging due to the new control algorithms. It is then important to consider to identify possible modes of oscillations and how they can be damped. Moreover, recommendations are provided in terms of controller type, location and tuning to try and remedy any problematic oscillations. If the mechanical frequencies can be damped before reaching the network it is a safe assumption to disregard these component for wider farm studies as they will not affect the results.

The second section then extends the analysis of previous chapters studying interactions between sets of two and three converters by investigating the effect of penetration and placement of GFM converters within a larger wind farm array. Specifically studying the optimum penetration to enhance the strength of the array, increase stability and reduce interactions between turbines. GFM turbines have been discussed to provide system strength and stability in weak systems where they are deployed but this behaviour has yet to be quantitatively measured for a realistic system. Modelling of a wind farm case study capable of representing individual control goals of each turbine is a key step in achieving this measure. The study works through and entirely GFL farm which is initially unstable, enabling GFM control on each turbine until a stable system is obtained and this point is denoted the critical penetration. Further GFM turbines are then enabled until the system reaches the most robust point or the optimal penetration. The GFM turbines are then increased up to a fully GFM farm and the point at which robustness begins to decay rapidly is denoted the maximum penetration. The balance of GFL and GFM turbines within the farm is found to follow a similar trajectory for different line lengths and operating points with the critical penetration never rising above 25 % of the farm and a more optimal approach tends to have more GFL converters than GFM.

The system strength at the point of connection is a key design parameter for wind parks but if this is provided at the beginning of a long transmission line the wind farm may still experience stability issues. Hence, turbine operation will be governed by the strength provided after the long transmission line at the beginning of the array not the connection point on the grid. Moreover, each turbine can only provide strength within the array and this action is likely not seen on the network. The array will then appear

more stable at the end of the long transmission line from the network PoV. Moreover, the array cables connecting the wind turbines offer a much smaller impedance than that of the transmission line connecting the farm to the grid. Hence, studying the strength beyond the medium voltage transformer (MVT) connecting the array will not provide greater insight to system operation as the difference will be negligible. Therefore, it is important to study the farm at array level as this provides the greatest insight to the operation of the GFM converters within the farm.

It has been suggested in literature that too many GFM structures operating in close proximity will cause instability as the low impedance between converters will cause large power swings for very small angle changes [92]. This is similar to the inter-synchronisation loop issues reported by GFL converters due to the PLL but the loss of synchronisation is due to too small an impedance instead of an impedance that is too large. The same problem can occur if the grid connection is extremely strong however, this issue is related to the grid synchronisation loop determined by the network impedance. It is clear that GFM structures solve the issues of GFLs in weak grids but it may be the case that GFL converters are required to improve GFM operation in very stiff grids. Therefore, a mix of GFM and GFL is likely the best option but removing GFM converters will require the GFLs to provide an inertia response.

## 6.1 Mechanical Interactions

A large volume of research has considered the impact of control structure on network stability when the converter of study is connected directly to a suitable energy storage [76, 93]. However, literature considering the impact of internal wind turbine dynamics on network stability is limited especially when considering a GFM control structure. This is only likely an issue with GFM characteristics that use significant energy such as inertia and frequency support. This situation can only be analysed with the inclusion of a back-to-back converter which leads to the necessity of a DC link voltage controller. The location of this controller (network or generator side) can affect the performance of the individual control structures. As the converter attempts to react to an event, the DC link voltage deviates as current flows into or out of the converter. The DC link

voltage control attempts to counteract this action and reduces the converters ability to react.

The wind turbine rotor is a promising source of inertia which is usually decoupled from the grid but with appropriate control this energy can be realised [24]. However, possible issues arise when the generator side converter and mechanical properties of the wind turbine are considered. Certain system components also react at low frequency such as the algorithm to dampen mechanical oscillations in the drivetrain. These low bandwidth systems are normally decoupled but the inclusion of a DC link voltage controller (discussed in Section 2.5.4) can cause interactions. This analysis in this section explores the idea of moving the DC link control to the generator side converter to reduce oscillations propagated to the network. However, the DC link voltage loop appears to oppose the active damping of torsional drivetrain vibrations. The problem is exacerbated when the DC link voltage gains are increased to reduce the settling time from disturbances. Figure 6.1 illustrates this effect with a step response to a  $1 \text{ rads}^{-1}$  step in network frequency. Figure 6.2 shows the bode plot of the system from an input of the network frequency to the outputs of generator mechanical speed and DC link voltage respectively.

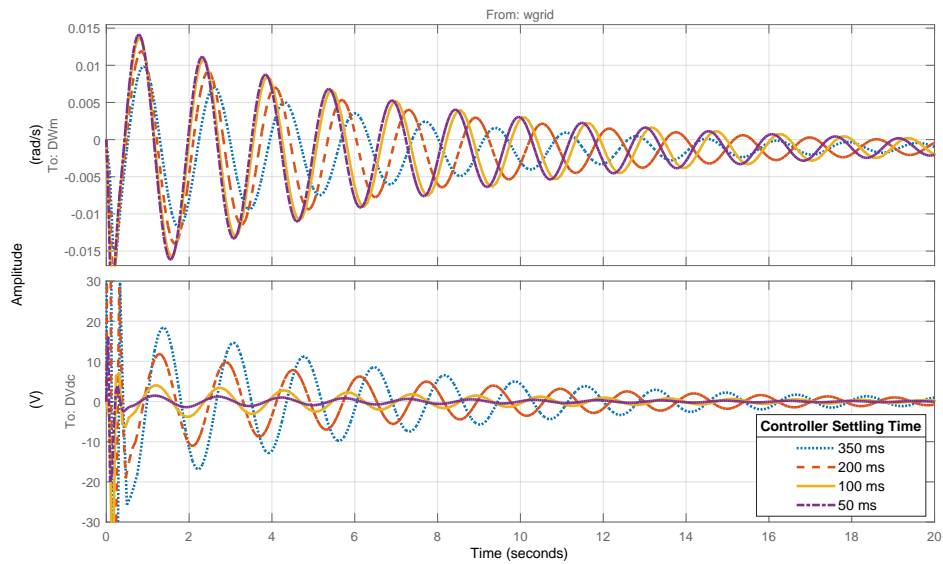


Figure 6.1: Step response comparing generator side DC link voltage controller tunings

From Figure 6.1, the oscillations in mechanical speed (upper plot) were smaller, decayed faster and were of lower frequency as the DC link voltage controller speed was reduced. This indicates that the active damping was better at slow controller tunings. If the lower plot in Figure 6.1 is considered, the DC link voltage experienced larger fluctuations when the DC link voltage controller was tuned slowly (blue dotted line). This suggests a trade-off between drive train damping and DC link voltage disturbance rejection when the control of the DC link is governed by the generator side converter.

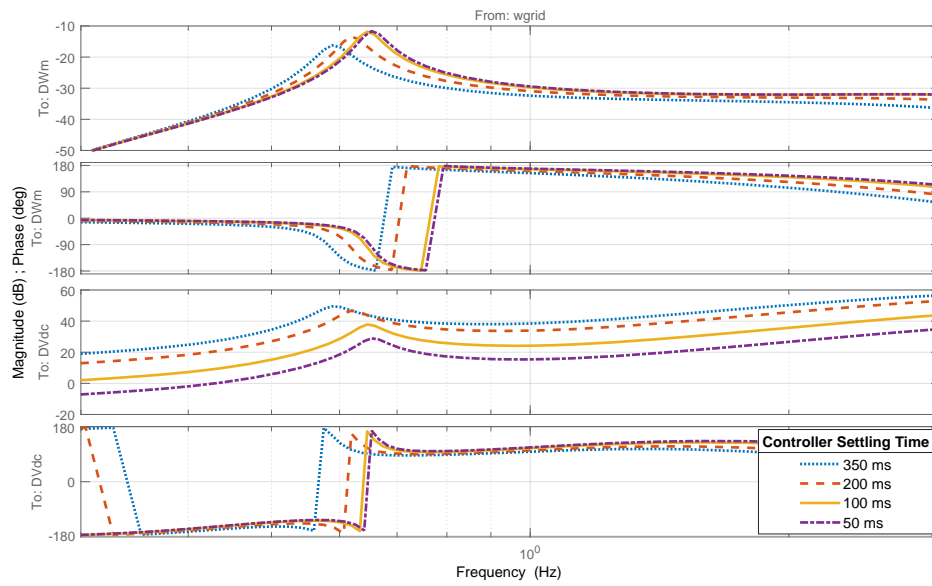


Figure 6.2: Bode plot comparing generator side DC link voltage controller tunings

This idea is further solidified in Figure 6.2, considering the mechanical speed in the upper plot, the peak was lowest for the slowest DC link controller tuning and largest for the fastest tuning confirming improved damping for slower DC link tunings. However, when the lower plot in Figure 6.2 is studied, the magnitude response peak was much greater when the DC link controller was tuned slowly further indicating a large upset in DC voltage when the controller gains were slow.

When the responsibility of controlling the DC link voltage is left to the network side converter the power command is altered when the DC link voltage deviates. Since the DC link voltage varies when the network power changes and this occurs during frequency events for the VSM controller and PVCCI, it is clear there will be an interaction

between the DC link voltage control and the inertial response. To investigate this both the VSM controller and PVCCI were subjected to a frequency step of  $+0.2\text{rads}^{-1}$  and the DC link voltage controller gains were varied. Figure 6.3 presents a bode plot illustrating the effect when the DC link controller proportional and integral gains are increased to alter the controller bandwidth. Figure 6.4 shows the network converter step response.

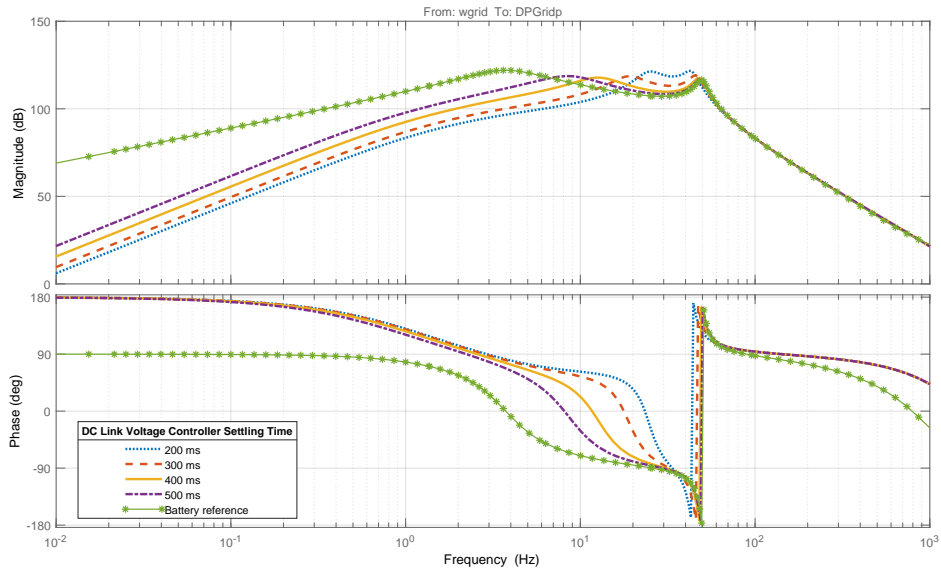


Figure 6.3: Bode plot showing effect of DC link controller bandwidth on VSM frequency response

Figure 6.3 indicates a larger degradation of inertial performance as the speed of the controller was increased. Even with the slowest tuning of 500 ms (purple dash-dot) the performance across the range of inertial frequencies was decreased and the peak response was flattened and its frequency shifted up by 6 Hz. There was a very large difference from the ideal case across the range and the frequency at which the peak response occurred moved to around 25 Hz. The frequency of the peak response increases as the controller speed increases, this could explain the reason for instability if the first peak interacts with the peak at 50 Hz. It should be noted that in order to match the ideal response the controller had to be tuned to a settling time of over 3 seconds. This essentially allowed the inertial response to occur before the DC link controller reacted

to restore the voltage but was too slow for deployment in a real system. Beyond 50 Hz the tuning of the DC link controller had no effect on the output.

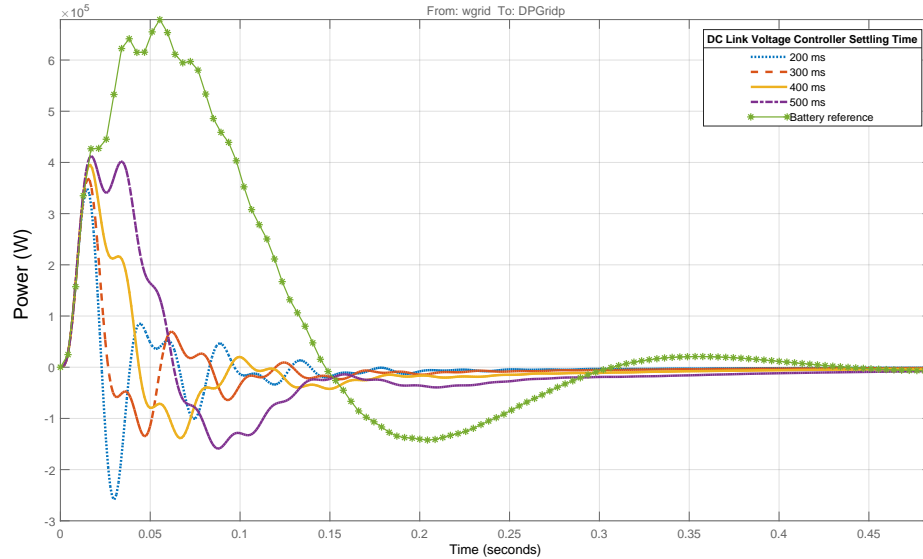


Figure 6.4: Step response showing effect of DC link controller bandwidth on VSM frequency response

Looking at Figure 6.4, the negative impact of the DC link voltage controller is evident. The peak power responses were much lower than the ideal case and reduced steadily as the voltage controller gains are increased. The difference observed between the fastest (blue dotted) and slowest controllers (purple dash-dot) is ( $\approx 50kW$ ). The blue dotted trace exhibits more oscillatory behaviour than the slower tuned controllers. This is thought to be due to the DC link controller and inertial response fighting against each other more aggressively. The same tests were conducted for the PVCCI to ensure the issue was due to the inertia response and not just a result of the VSM controller structure. The Bode plot can be viewed in Figure 6.5 and the response when subjected to a frequency step of  $1 \text{ rads}^{-1}$  in Figure 6.6.

From Figure 6.5, the PVCCI exhibited a similar degradation in inertial performance as the VSM controller when the speed of the DC link voltage controller was increased. Note that the same proportional and integral gains were used for both the PVCCI and VSM however, in the case of the PVCCI the DC link voltage settling time was faster.



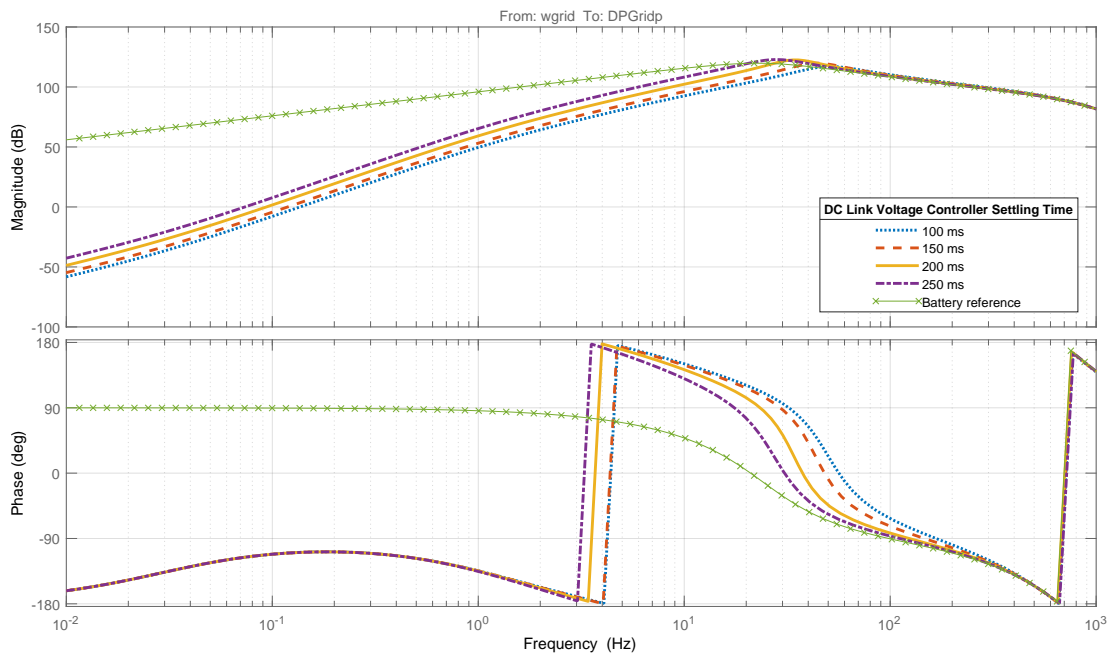


Figure 6.5: Bode plot showing effect of DC link controller bandwidth on PVCCI frequency response

The PVCCI gain response does not contain a peak in the inertial frequency range the frequency of the peak response does not shift as noticeably as with the VSM controller. However, there is a clear reduction in performance across the entire range of inertial frequencies.

Figure 6.6 presents a smoother reaction than that of the VSM controller. This makes it easier to view the reduction in peak power response during a frequency event. A large change was again observed between the ideal battery cases and the wind turbine connected cases. In the case of the PVCCI the difference between the peak power response for an increasing DC link voltage controller speed was larger than that of the VSM controller. Approximately 200 kW for the PVCCI and 50 kW for the VSM controller. The settling time for the event was also much smaller for the PVCCI than the VSM but this was due to the controller structure rather than the DC link voltage control.

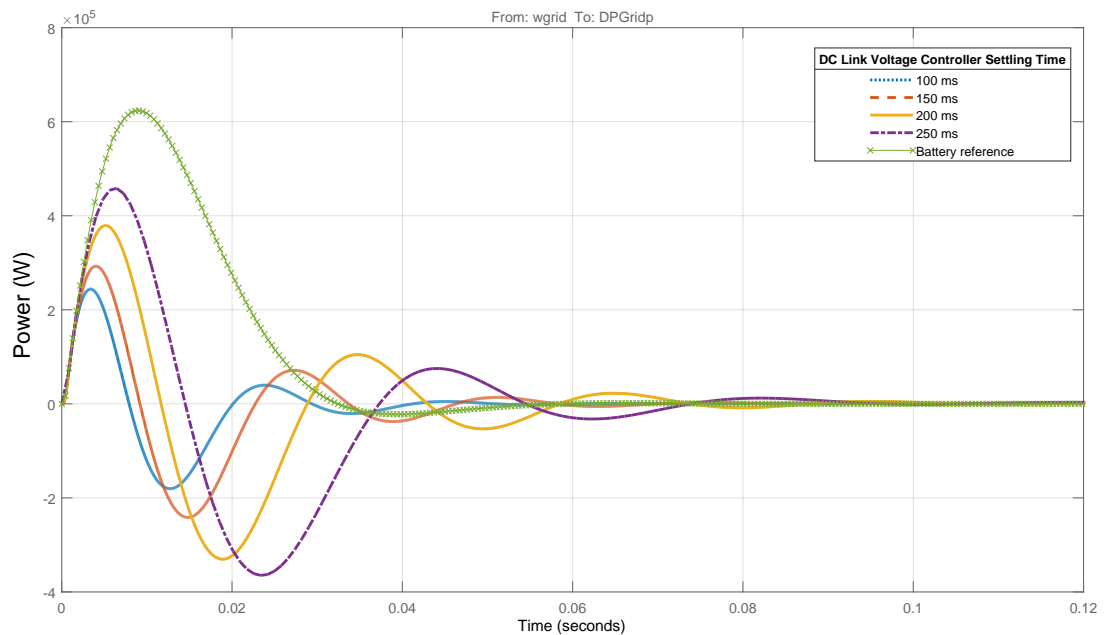


Figure 6.6: Current Control Equivalent Converter Admittance in the Sequence Frame

### 6.1.1 Recommendations Considering Mechanical Effects

The ability of the network side converter to respond to frequency events is important for grid stability in an inverter dominant network. When the DC link controller is added on the network the inertial response performance is reduced therefore degrading network stability. The inertia response also limits how fast the DC link voltage control can be tuned as the interaction worsens as the control speed is increased. However, it could be argued that since the generator converter does not react to the frequency event the energy is not being extracted from the turbine but instead from the DC link itself. This is what causes the interaction. If the network frequency deviation is sufficiently fast, it can cause large, almost instantaneous changes in torque which causes the drivetrain to oscillate. This drivetrain oscillation feeds into the DC link and can cause further issue with the network converter. The problem is more evident with the VSM controller as the control structure is more susceptible to DC link voltage ringing. In normal conditions the rate of change of frequency would be slower. This may have an impact on the interaction between DC link controller and the inertia provision or damping

of mechanical vibrations. Further study is required to characterise this. Conducting further tests on real hardware is challenging, especially using real wind turbines due to time and cost constraints. Limited studies are available applying grid forming control to a wind park [34].

The easiest way to avoid the interaction is to move the DC link voltage control responsibility to the generator side converter. This allows the network side converter to respond freely to frequency events. The DC link control then slows the turbine, extracting energy from the rotor preventing DC link perturbations. However, a similar interaction occurs between the drivetrain active damping and DC link voltage control. The damping of torsional vibrations relies on the altering of electromagnetic torque via the injection or absorption of q-axis current. The DC link controller opposes the action of the active damping preventing smoothing of mechanical oscillations. This could lead to extra strain being placed on drivetrain components.

Another possible solution is to include a form of energy storage [167], essentially shifting the system architecture towards that of an ideal battery connected system. The optimal sizing and location of this energy storage requires further study. It would still be possible to use the inertia included within the turbine to charge the energy storage system (ESS) but this would occur during steady state conditions preventing the interactions observed. Without ESS the selection of DC link voltage control location will either harm network stability or cause extra strain on drivetrain components limiting the effect of the inertia support. A number of differences can be observed between the grid PVCC, PVCCI and VSM. The VSM controller was more susceptible to DC link voltage fluctuations with large vibrations observed throughout the system.

Interestingly, the peak observed in the VSM frequency response bode plot matches with the problematic pole identified with the VSMCC controller when utilising GSIM. The grid following PVCCI coped better with the interaction, successfully dampening the oscillations. This led to an improved inertial response that was not obtainable using the VSM controller. A final issue relates to the converter sizing. The VSM controller has no inherent current limiting. Therefore, if converter was operating near maximum power when a frequency event occurred the controller would attempt to contribute more

current and damage the devices. One option in this case is to oversize the converter to deal with such issues. However, this would depend on cost and frequency at which the converter is expected to exceed the aforementioned current limits. The PVCCI controller contains an inner loop current controller making it easier to prevent this problem.

## 6.2 Adverse System Interactions in Windfarms

The stability interactions of single and multi-turbine systems has been a topic of wide research as presented in previous chapters. However, most of these systems look at three turbines maximum and often simplifications look to aggregate multiple sections of the wind-farm into a lumped model that capture the most important dynamics. One study looking at the simplest representations and comparing the model order of wind turbine generators was conducted by Garcia-Gracia et al. in [168]. It found that 3rd and 5th order models are required to accurately represent behaviour and trying to reduce computation time by using 1st order models was not valid. Instead, computational burden should be removed by aggregating the wind farm and using a higher order model. Further aggregation techniques were explored by Fernandez et al. in [169] where an equivalent single turbine was modelled and the energy input generated from an equivalent wind speed based on the power curve and the wind present at each wind turbine. This method was compared against a more conventional approach aggregating wind turbine experiencing similar wind speeds.

The equivalent method was found to significantly reduce computational burden beyond conventional techniques while still providing an accurate system description. In reality, neither of these works included any advanced control components. Hence, it is possible a different conclusion may be reached and modelling of a greater number of turbines is required when the converter control is equipped with enhanced grid support services. Additionally, the work did not discuss weak grid connections which likely increase interactions between converter controllers. Liu et al. studied the interactions between voltage controllers, current controllers and the PLL in Type IV wind parks with a weak grid connection in [170]. It was found that each control component had

a significant effect on the shaping of the wind park impedance and that interactions between control loops was dependent on overlapping between the PLL and voltage loop bandwidth. With inappropriate tuning of the voltage loop the wind farm was shown to exhibit negative damping characteristics that caused oscillations when connected to a weak grid. However, an aggregated model was applied here with two lumped turbines representing two lines. It is likely that further interactions would exist between control structures if more turbines were represented. Furthermore, with more turbines it should also be possible to study how many GFM converters are required to remove the negative impedance behaviour of the GFL if present. However, it is also possible that GFM converters could add to this negative damping in low frequency ranges and does require further study.

Du et al. focused on small-signal angular stability in [171] and explored two important points. Firstly, what interactions are removed from the network when replacing synchronous generation with a wind park and secondly, what interactions are then added to the system with the inclusion of new converter based generation. Interestingly, it was found that the inclusion of wind farms was detrimental to some electro-mechanical modes but beneficial to others. This suggests that addition of new converter generation is not necessarily bad, it is just not well understood at present unlike interactions between synchronous generation. It is then critical to investigate possible interactions between all different types of converter control to determine which combination provides useful behaviour in different situations.

An interesting conclusion reached by Chen et al. in [172] was that MIMO models provided significantly greater merits when investigating oscillations in wind parks, specifically SSOs. The paper compared both impedance based analysis and open-loop modal analysis but few conclusions were drawn between which is more applicable. Studies on the designs on real wind parks were completed by Kocewiak et al. in [173] where Horns Rev II and Karnice were investigated. It was found that long high-voltage alternating-current (HVAC) cables and Park transformers introduced significant low-frequency series resonances that affect the wind turbine control systems and overall wind farm stability. Moreover, it was discovered that the wind turbine grid

side converter required sufficient harmonic rejection to maintain stability during this phenomena and therefore required tuning differed depending on wind farm location. Interestingly, the study applied standard SISO techniques for analyses such as gain margin and phase margin which may have not provided the full picture incorporating all possible control interactions.

In terms of higher frequency interactions Glasdam et al. explored harmonic interactions of a wind power plant connected to the grid via a VSC-HVDC link [174]. They found that the use of notch filters in the primary control chain reduced influence due to harmonics. However, tuning of the notch filters required study of the wind park in situ to first identify the problematic frequencies.

It is clear from literature that numerous interactions occur across a wide range of frequencies and proper study of this is required. However, many possible wind park architectures are possible with different turbines, controllers and array layouts. Studying possible interactions by manually analysing impedance traces of all possible permutations is likely not feasible. Therefore, steps must be taken to ensure the stability and particularly the screening metrics described in previous chapters can be accurately and efficiently applied to full scale wind parks to identify problematic scenarios.

### 6.2.1 Line Analysis

Using a modular modelling approach, a more detailed small-signal impedance model can be constructed representing full wind farm arrays with each individual turbine. This allows the investigation of the optimum placement of grid-forming turbines measured against grid stability and strength at different operating points which is the main focus of this sub-section. The main components such as pi-section lines, transformers and converter control are all detailed in Chapter 2. The following assumptions are made to allow modelling: each turbine is equally spaced with the same line length, each turbine has a set active power operating point of either 0 or 0.5 p.u. that can be set independently for each turbine but are grouped to reduce the number of results. Moreover, the mechanical sub-systems are disregarded here and the DC-link is modelled as an infinite source to reduce some computational burden. However, the converter

models could easily be replaced to include the mechanical systems if desired. Finally, for strength and stability tests the wind park is assumed to be connected to a simplified Thevenin network with a specific SCR or GSIM.

To achieve this a programmable wind farm model was created. This allows the fast creation of a wind park with  $n_A$  number of array each with  $n_L$  lines of  $n_T$  turbines. Cables are modelled as PI sections with TL representing the longer transmission line from the MVT to the high voltage transformers (HVT). The HVT is modelled as a Thevenin equivalent. Terms denoted subscript L represent the cables between turbines. Each turbine is modelled using the grid side converter only and mechanical dynamics are disabled initially. Each turbine can be enabled with any of the control structures previously discussed. The turbines are connected to the line via the using RLC filter and another RL component representing the turbine transformer. The addition of multiple lines to the bus results in a bus or array capacitance equal to the sum of all the first capacitances on each line:

$$C_a = C_{L(1)} + C_{L(2)} + \dots + C_{L(nL)} \quad (6.1)$$

A diagram showcasing the construction of an example wind park with  $n_L = 2$  and  $n_T = 2$  is shown in Figure 6.7. The red turbines indicate GFL while the green represents GFM. The ellipsis on the diagram indicate where repetition of the same model can occur up to the number of lines and turbines.

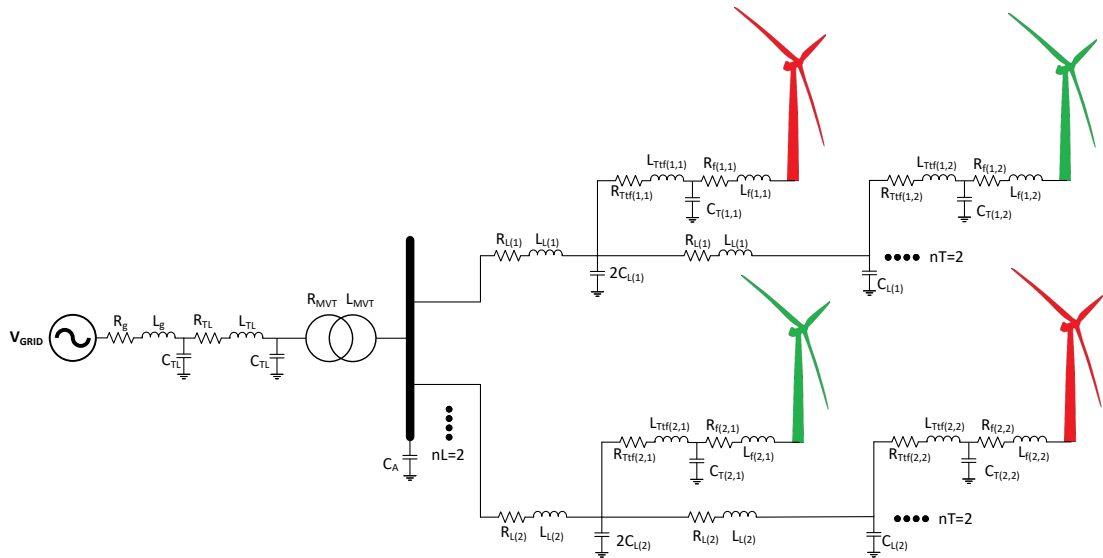







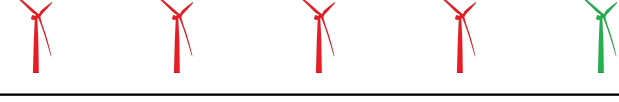
Figure 6.7: Example model of programmable wind farm

The wind park is to be made up of array consisting of five lines of five 3 MW turbines each giving each array a combined power of 75 MW. This implementation is based around the CIGRE benchmark provided in [175] but utilising 3 MW turbines. Parameters for the wind farm model can be found in Appendix E. The HVAC transmission cable is 100 km long and offers significant impedance, for this initial analysis reactive compensation is not considered. This impedance alters depending on the base power used which for all studies matches the total combined power of all connected wind turbines. This method is preferred as using the cable parameters for the full farm when conducting single line studies results in no combination of converters providing a stable system.

The SCR or GSIM provided onshore before the HVAC cable is 2. The first investigation is to determine the optimal number and placement of GFM turbines within a line of five. For this system, the GSIM rating after the HVAC cable is 1.6. Tables comparing the GSIM and disk margins for all an array with a single GFM turbine are shown in Table 6.1 for varying positions. The first position in the table indicates the location closest to the MVT at the start of the line. An array of only GFL is included here for reference. This is repeated for 2, 3 and 4 turbines in Table 6.2, Table 6.3 and Table 6.4, respectively. An array of only GFM is shown in Table 6.4 for comparison.



Table 6.1: Single Line GFM Investigations, Red = GFL, Green = GFM

Topology	GSIM	DM
	0.993	0
	1.476	0.352
	1.473	0.345
	1.470	0.340
	1.467	0.338
	1.465	0.339

From Table 6.1, the array is unstable when operating with only GFL turbines and the system is significantly weakened below the initial SCR of 2. Note that the tuning of GFL converter is designed to offer good operation when the farm is connected directly to a system of SCR 2 without the HVAC cable. It is possible that the GFL could be re-tuned to stabilise the system for a GSIM of 1.6 after the HVAC cable but this would significantly harm performance and likely cause further high frequency oscillations as explored in Chapter 5.

When a GFM turbine is included the GSIM indicates the strength has improved while the disk margin is in agreement. However, the strength is still weaker than the initial SCR as the negative behaviour of the GFLs and the impact of the long export line still outweighs the strengthening of the GFM converter. The position of the GFM turbine on the line is not of concern as approximately the same stability margin and GSIM is obtained for each position with a slight increase observed the the GFM is connected closer. This is due to the array cables being relatively short and offering a

small impedance compared to the long export line.

From Table 6.2, the addition of a second GFM converter increases the strength of the network further. The GFLs now operate with less detriment to overall strength and the weakening due to the export cable is almost fully remedied. With the addition of a second GFM the wind farm strength improves to that of an onshore wind park connected to an SCR of approximately 2. However, a small detriment to the robustness of the system is observed in each case compared to having a single GFM turbine possibly due to the interaction of GFM converters. The most stable configuration is observed when both turbines are at the end of the line but the difference is small. Similar to a single turbine, the position of the two turbines is not of concern.

Table 6.2: Single Line, 2 GFM Turbine Investigation, Red = GFL, Green = GFM







Topology	GSIM	DM
	1.972	0.755
	1.969	0.760
	1.966	0.764
	1.963	0.765
	1.961	0.764
	1.958	0.767
	1.956	0.768
	1.951	0.769
	1.948	0.770
	1.941	0.771

Table 6.3: Single Line, 3 GFM Turbine Investigation, Red = GFL, Green = GFM

Topology	GSIM	DM
	2.442	0.571
	2.439	0.575
	2.436	0.578
	2.431	0.578
	2.429	0.581
	2.422	0.582
	2.420	0.580
	2.417	0.583
	2.398	0.584

From Table 6.3, the third GFM turbine adds more strength to the system increasing the strength beyond what was originally provided from the network by a small amount. However, the robustness is now reduced from the double GFM topology yet still higher than the system with a single GFM. This indicates that providing strength above what is provided at the onshore connection point harms system stability. The robustness is again slightly improved by having the GFM turbines connected at the end of the line but the greater stiffness by connecting at the start of the line.

Table 6.4: Single Line, 4 GFM Turbine Investigation, Red = GFL, Green = GFM





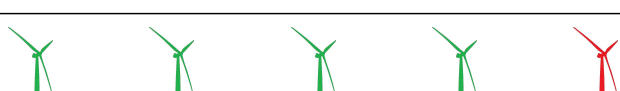
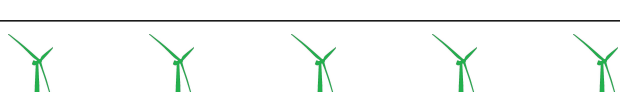
Topology	GSIM	DM
	2.887	0.330
	2.885	0.333
	2.878	0.335
	2.866	0.336
	2.850	0.335
	3.3140	0.005

From Table 6.4, the addition of four GFM turbines provides a significant strengthening to the network but the disk margins are further reduced from the three GFM system. Despite the high strength rating, the robustness is similar to that of having only one GFM connected. Interestingly, a line of all GFM turbines produces the highest GSIM as expected. However, the system is only marginally stable indicating an issue with robustness. This is likely due to every converter trying to dictate the voltage at the PCC without any GFL to increase the impedance and reduce fighting between converters. This indicates that GFL converters still remain of use in these situations.

Utilising a similar approach to the previous section, extra lines can be connected to the array to investigate if further GFM turbines would aid network operation. Analysis determined that a mix of four GFM to one GFL produced the greatest system strength while maintaining stability. Moreover, the position of the GFM turbine on the line was found to have minimal effect on the outcome. Hence, line one is constructed of 4 GFM and 1 GFL, with the GFL connected closest to the array transformer as this

produced the best results. A second line was then connected and the number of GFM turbines was varied with the results provided in Table 6.5. Since the power rating of the connection has doubled, the offshore GSIM is now 1.323.

Table 6.5: 2 Line GFM Turbine Investigation, Red = GFL, Green = GFM

Topology	GSIM	DM
	1.281	0.378
	1.533	0.710
	1.774	0.835
	1.999	0.743
	2.209	0.635
	2.404	0.506

From Table 6.5, the greatest robustness was observed when two GFM turbines were connected on the second line. Having a full line of GFM turbines enhanced the strength the most and since GFL were still present on the first line, the robustness was much greater than a single line with all GFM turbines. The robustness was reduced when restoring the offshore connection point to a GSIM of 2 indicated the high number of GFM turbines were causing adverse interactions. From the analysis of lines within the farm the following conclusions can be drawn:

1. When the grid connection is weak the fully GFL lines would not operate
2. Only one GFM converter is required to stabilise the line

3. The greatest robustness was observed for two GFM converters on a single line, beyond this stability was reduced despite increasing strength
4. Increased strength at the FF may not cover all of the possible system interactions occurring
5. A fully GFM is critically stable and would likely offer poor performance
6. When considering two lines a 40 % penetration of GFM converters provided the greatest robustness despite a GSIM of only 1.774

### 6.2.2 Array Analysis

Finally, the full wind park was connected consisting of five lines of five turbines. The park was connected to the onshore connection point via a transmission line that provided a significant reduction in strength at the offshore connection point. Three cable lengths were used: 50 km, 100 km and 150 km. Each cable was modelled as a PI section with suitable reactive compensation split between both ends and the middle of the line. The strength and robustness is then analysed at the offshore connection point from the PoV of another system looking in. The GSIM of the onshore connection point was set to 2 (equivalent to  $SCR = 2$ ) resulting in a GSIM at the offshore connection point of 1.48, 1.27 and 0.86, for the respective ascending line lengths. The GSIM and common mode robustness is analysed and provided in Figure 6.8 considering all turbines at 0.5 p.u. active power.

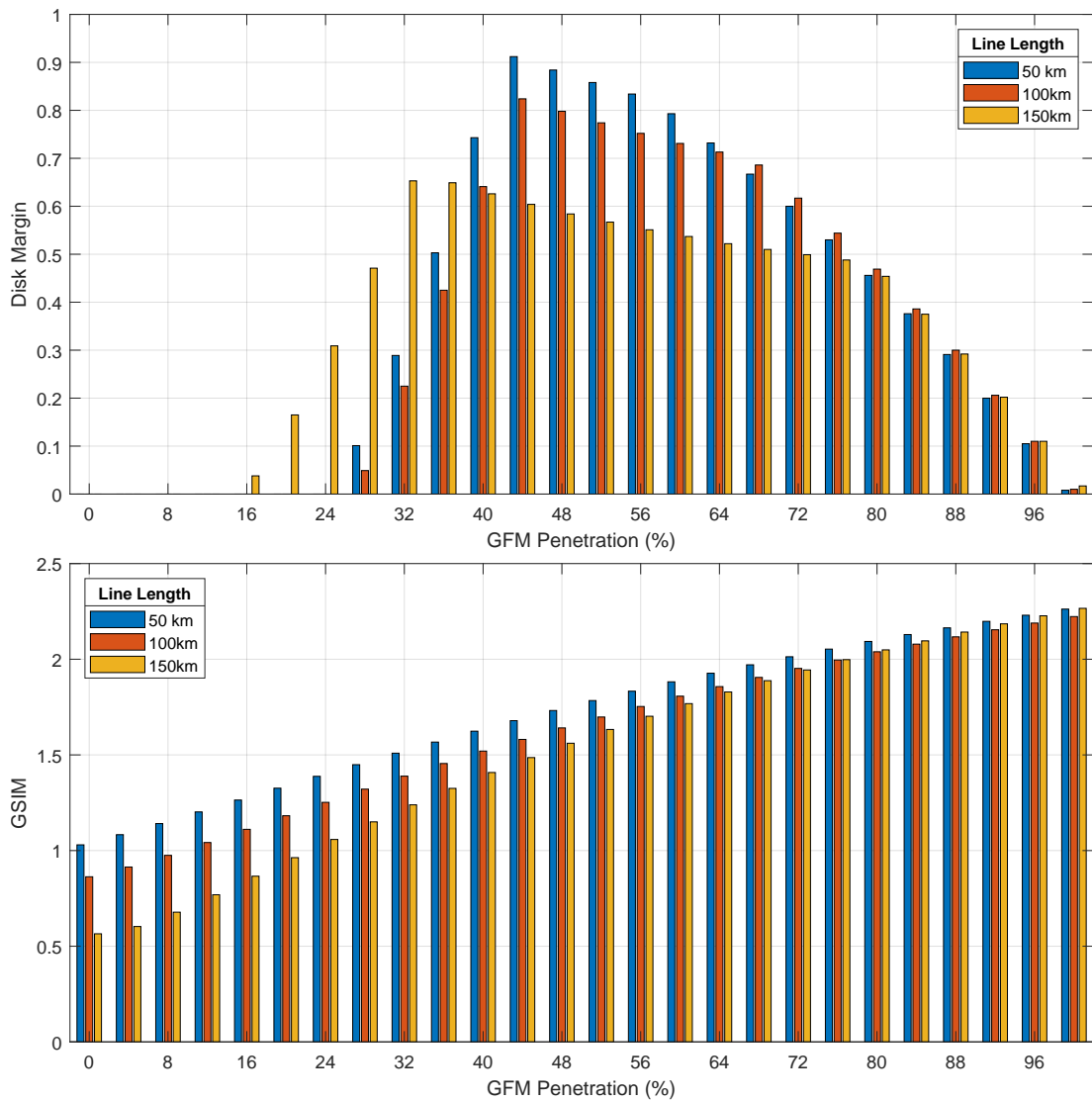


Figure 6.8: Disk Margin and GSIM Different Penetrations of GFM Turbine at 0.5 p.u. active power

From Figure 6.8, the strength of offshore connection point rises steadily with GFM penetration. The initial strength is significantly lower for the longer transmission lines as expected. However, when GFM penetration passes a certain threshold the strength appears to not depend on the length of the line as all of the strength is being provided by the farm. This occurs when the strength of the offshore connection point exceeds that of the onshore connection point therefore negating any detrimental effects of the longer line length. Note that providing all the strength from the wind farm does reduce



the stability of the system significantly.

Three key penetrations are defined for each transmission line length. The critical penetration, which is minimum number of GFM turbines to stabilise the system. This is 16 % for the 150 km line and 24 % for the 50 km and 100 km. Resolution plays a factor here as it is only possible to have integer numbers of turbines placed on the network, hence the same critical penetration for two line lengths. The longer line has a lower critical penetration than the shorter lines which appears counter intuitive but the reason for this can be explained by analysing the frequency dependent GSIM in the next section. For now, despite less GFM being required to initially stabilise the system for a longer line, it is important to consider that the maximum achievable robustness always occurs for the shortest transmission line length.

The second key penetration is the optimal penetration of GFM converters. This is the penetration that provides the largest robustness, NOT the greatest strength. The optimal penetration is 32 % for the 150 km line while 44 % for the 50 km and 100 km lines. Beyond this penetration, the robustness of the wind farm seen from the network begins to reduce slightly with increased GFM. However, the GSIM rating of strength continues to rise. The results suggest that providing too much virtual stiffness beyond the original connection point can result in reduced stability, likely due to the increased work of the GFM converters. From Chapters 4 and 5, the analysis found that GFM converters do less work to strengthen the network as the system became stiffer. Moreover, the negative effect of the GFL was exacerbated. This is the reason for the small reduction after the optimal penetration. The network has reached a level of stiffness where the extra GFM converters added begin to do less work while the remaining GFL converters act to further reduce the stability of the system.

The final key penetration is known as the maximum penetration which is the point after which the stability of the system begins to decay rapidly. This is 80 % for the 150 km line, 72 % for the 100 km line and 68 % for the 50 km line. Interestingly, these penetrations appear to approximately align with the penetration at which the offshore GSIM is restored back to the stiffness provided at the onshore connection point. Strengthening beyond this provides a significant reduction of stability up to

100 % penetration. The fully GFM wind park is stable but is very close to being critically stable and should be avoided.

The power provided from wind has a high degree of variability. Due to this, it is important to investigate what happens if the wind suddenly drops and if the GFM converters will continue to stabilise the system. The same analysis is provided considering all turbines are at 0 p.u. active power in Figure 6.9.

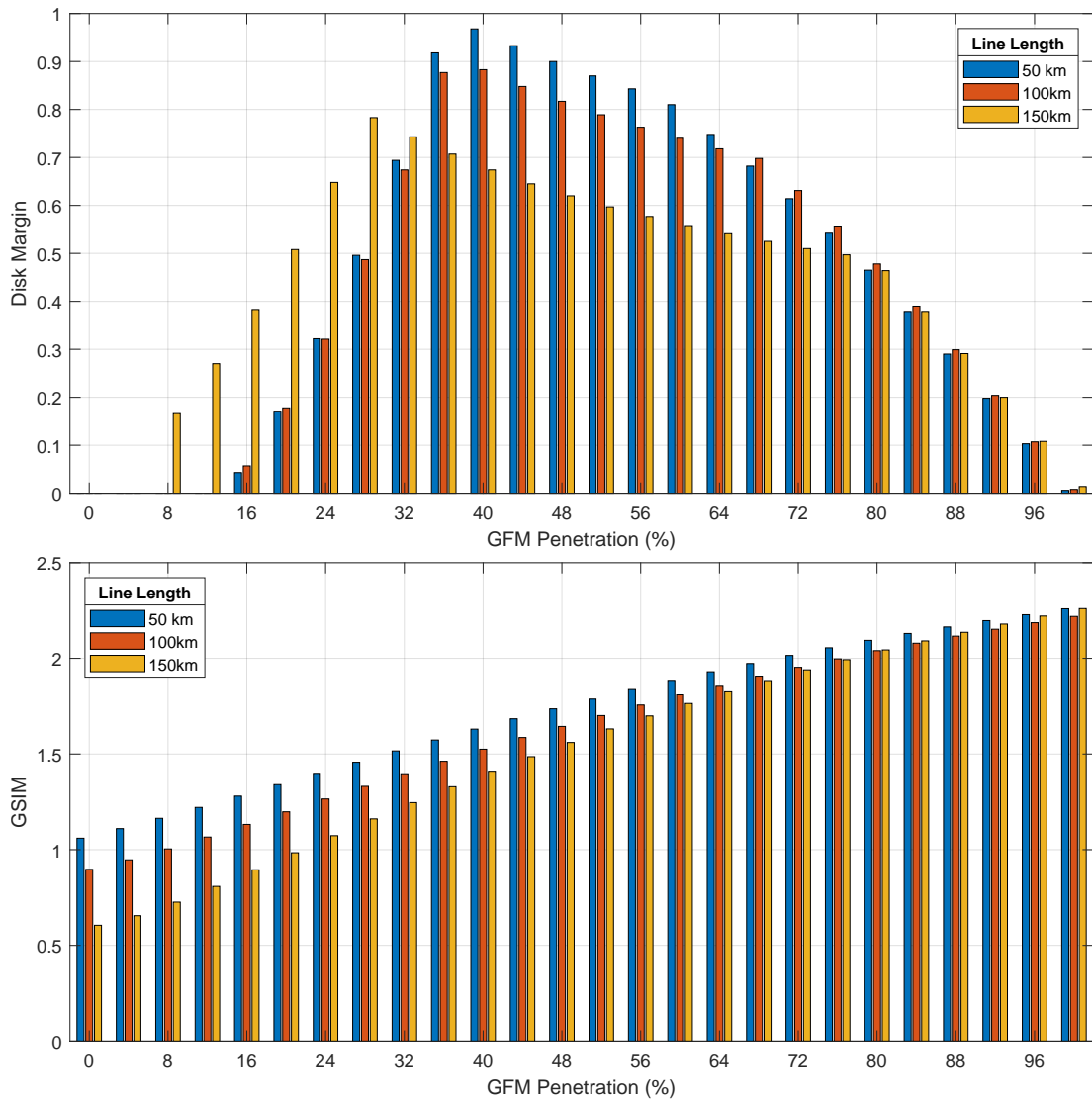


Figure 6.9: Disk Margin and GSIM Different Penetrations of GFM Turbine at 0 p.u. active power

From Figure 6.9, the effect of reduced operating point have a significant effects the

three key penetrations discussed. Less GFM converters are needed to stabilise each system with the critical penetrations dropping to 8 % for the 150 km line and 16 % for the 100 km and 50 km lines. This agrees with the analysis of previous chapters as the GFL converters do less work to reduce system strength and stability at lower operating points while the GFM structures remain largely impervious to operating point changes observing only a small reduction in the stiffness provided. The optimal penetrations fall to 28 % for the 150 km line and 40 % for the the 100 km and 50 km lines. Conversely, the maximum penetration is increased, rising to 84 %, 80 % and 72 % for the 150 km, 100 km and 50 km lines, respectively. The maximum penetration again appears to coincide with the point at which the offshore connection becomes approximately equal to the onshore connection point.

As discussed, the fact that the longer transmission line offers the lowest critical penetration appears counter intuitive. In reality, this problem indicates the requirement to analyse strength as a function of frequency. The GSIM is plotted as a function of frequency for the three transmission lines at the critical penetration for the 150 km line which was 16 % in Figure 6.10.

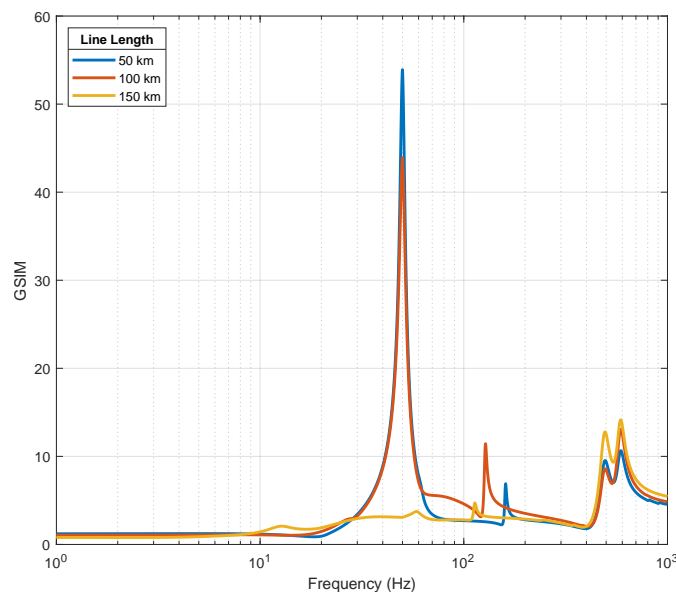


Figure 6.10: Disk Margin and GSIM Different Penetrations of GFM Turbine at 0 p.u. active power

From Figure 6.10, it can be seen that the shorter line offers a slightly higher strength rating which would usually indicate a more stable system. However, two large poles in GSIM can be seen for the 50 km and 100 km lines around 50 Hz representing a high rate of change of strength. As found in Chapter 5 for the GFMD controller, these type of large poles appear to indicate instability. These poles are the reason the system requires further GFM penetration to stability. The system with the 150 km line does not exhibit this same interaction and stabilises for a lower critical penetration. The penetration was increased to the critical value determined for the 50 km and 100 km lines which was 28 % and the resultant frequency dependent GSIM traces are plotted in Figure 6.11.

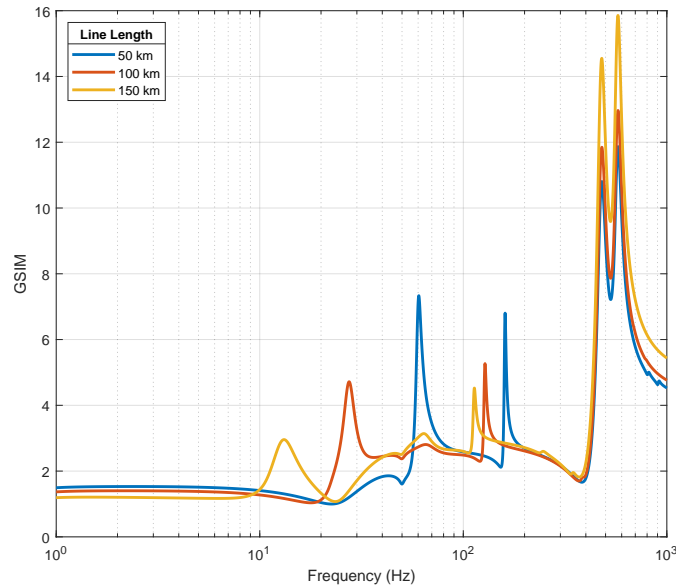


Figure 6.11: Disk Margin and GSIM Different Penetrations of GFM Turbine at 0 p.u. active power

Figure 6.11, the greater penetration of GFM removes the large poles that were of concern previous and results in a stable system. This suggest that the critical penetration of the shorter lines appears to relate to a higher frequency oscillation than with the 150 km, likely due to an interaction between the wind park and the transmission line with poorly designed compensation. Remembering that the compensation was deliberately designed for the 150 km line. Re-tuning of the controllers or properly sizing

the compensation could remove this pole and may reduce the critical penetration of the shorter lines. What is clear is the requirement to analyse the system strength as a function of frequency as the fundamental frequency information is not sufficient for the modern network.

The key penetrations can be further investigated using Nyquist contours to determine which eigenloci offers reduced stability and why. In the case of critical penetration the instability is related to the first eigenloci and a graphical representation of the stability margins at this penetration for the 100 km line is shown in Figure 6.12.

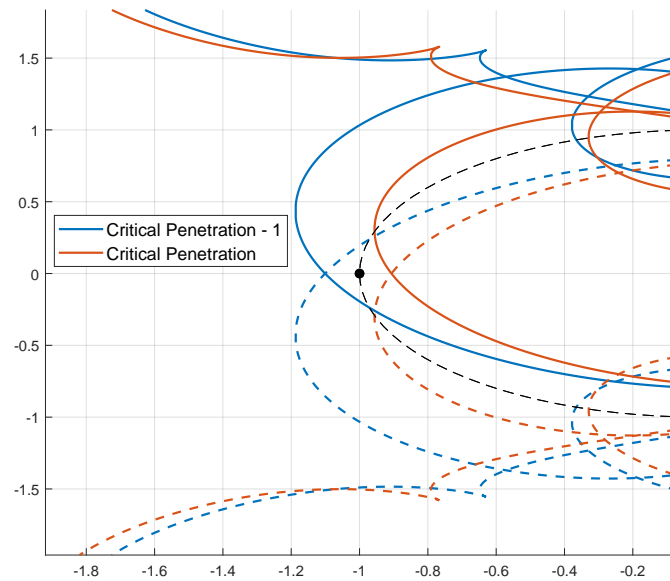


Figure 6.12: First Eigenloci for Critical Penetration with 100 km Line Connection

From Figure 6.12, the encirclement of the critical point is clearly visible when the GFM penetration is 1 turbine below the critical penetration. When another turbine is added the encirclement is removed and moves to the right of the critical point indicating stability. It should be noted that the contour begins to move closer towards the critical point directly above and below the critical point as the penetration is increased. This is important as it provides the cause of the optimal penetration. This is further investigated by considering the Nyquist contour with penetrations surrounding the optimal penetration in Figure 6.13.

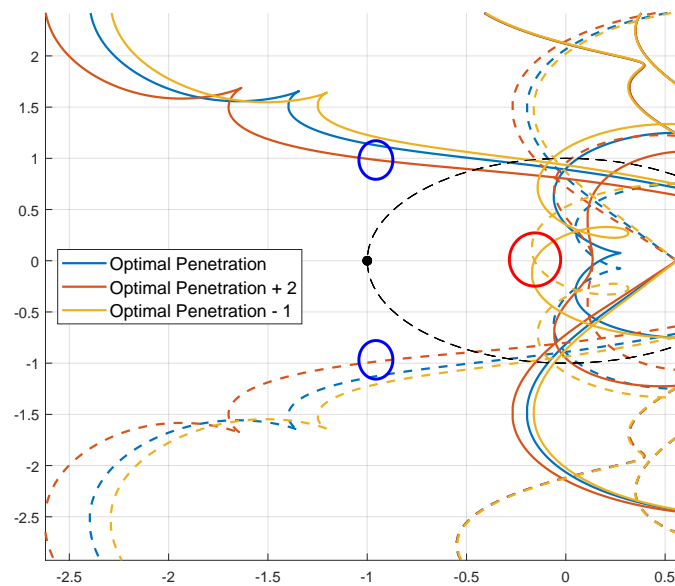


Figure 6.13: First Eigenloci for Optimal Penetration with 100 km Line Connection

From Figure 6.13, the optimal penetration is shown in blue. When the penetration is below this level (shown in yellow), the contour still contains the loop that caused instability around the critical penetration (red circle). At the optimal penetration this loop is moved further away and reduces in size. At this point the disk margin becomes related to the distance directly above and below the critical points (blue circles). As the penetration is increased beyond the critical point, this part of the contour begins to move closer to the critical point reducing the robustness of the system as the strength is further increased. This provides the mechanism for the optimal penetration as balancing these two parts of the traces becomes critical. The loop causing the instability (red circle) occurs at a lower frequency and is the reason the GSIM and disk margin have a strong correlation as penetration increases beyond critical. The loops providing the balance at the optimal penetration (blue circles) are related to higher frequencies. Therefore, as these move closer to the critical point the system strength at the fundamental frequency cannot capture this. Studying the strength across the frequency range is required to identify this point. When considering the mechanism behind the maximum penetration the problem is related to the reduced of the second eigenloci. As the system approaches maximum penetration the second

eigenloci exhibits similarly reduced robustness which is shown in Figure 6.14.

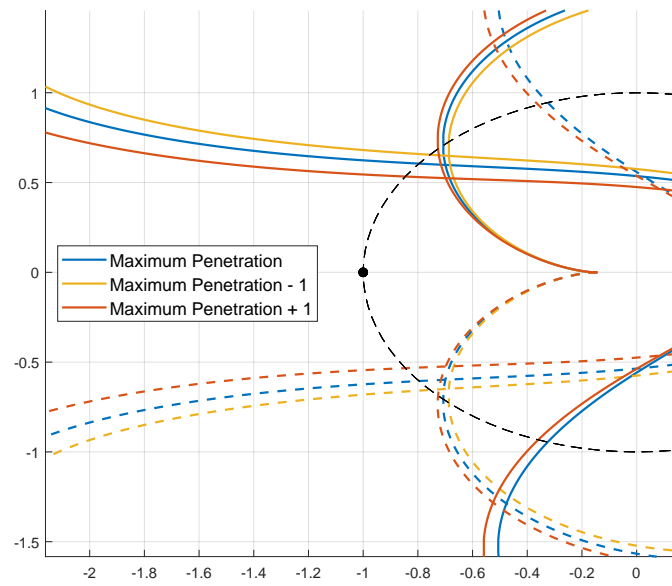


Figure 6.14: Second Eigenloci for Optimal Penetration with 100 km Line Connection

From Figure 6.14, the second eigenloci moves considerably closer to the critical point than at lower penetrations. Moreover, the first eigenloci offers a similar contour directly above and below the critical point (not shown). Beyond the maximum penetration, both eigenloci are close enough to the critical point to worsen the reduction in robustness since the disk margins consider both loops simultaneously. This is the reason a rapid decay in stability is observed after the maximum penetration. Clearly, obtaining the most robust system involves balancing these eigenloci.

## Chapter 7

# Conclusion

The electricity network is evolving with the continued increase in installations of renewable energy systems. The complex nature of the governing control systems is causing new types of instability and interaction on the network. Without novel techniques to identify, analyse and mitigate these problematic scenarios the continued increase in inverter based resource penetration will grind to a halt. Grid-connected converters can be fitted with advanced control systems to allow further participation in actively supporting the network frequency and voltage as synchronous generation is removed from the network.

Conventional grid-following control structures can be fitted to improve the frequency stability of the system by providing synthetic inertia and frequency support. Moreover, a new family of control topology known as grid-forming converters aim to provide frequency support and enhance system strength in locations they are deployed by replicating the useful behaviour of synchronous generation. These new control structures add further complication to network analysis with no techniques in literature capable of accurately representing the differing behaviour of grid-following compared to grid-forming when providing enhanced grid services.

Wind energy is seen as a promising source for these new control structures to be deployed due the large percentage of installed wind capacity which continues to increase at a rapid rate. This thesis has proposed new techniques for studying the stability of these new types of interconnected converter dominated systems and screening pos-



sible system issues by measuring the grid strength including converter action. The techniques have been applied to successfully determine the optimal penetration of grid-forming devices in an offshore wind farm operating under weak conditions with new key parameters specified for determining the best approach.

### **Mathematical Considerations of Converter Impedance**

The modelling of equivalent converter output impedance has been shown to provide the necessary information to represent the differing behaviour of grid-following and grid-forming converters. The impedance traces of these converters require accurate MIMO modelling as SISO representations do not include all possible interactions. A new method of determining the applicability of traditional SISO stability techniques based on the diagonal dominance of the obtained systems has been provided. Any system with a DD rating of 0.7 or above can be accurately described using traditional margins. However, all the advanced grid-following and grid-forming structures exhibited DD significantly lower than this and therefore require more complex MIMO analysis.

### **Impedance-Based Stability**

Impedance-based stability has been widely applied for decades but issues due to open-loop RHP poles and zeros have prevented the approaches from successfully analysing wider systems consisting of grid-following converters (Y-type systems) and grid-forming converters (Z-type systems). Utilising eigenvalue analysis, a novel method of analysing multi-converter systems has been proposed which can utilise any system description and offer differing points of view. Common mode stability of the converter systems showcases the network view of inverter based resources on the network. Conversely, differential mode stability indicates the stability of a certain device against the remaining network. The technique has been applied to study the robustness of different grid-following and forming topology on the network. Overall, the most robust systems consisted of a mix GFM and GFL converter when the network connection was weak. If two connections are made to the grid, the network sees greater robustness if GFL structures are connected closer with GFM converters coping better with longer trans-

mission line lengths. The difference in robustness between GFL and GFM is reduced when the grid connection is stiffer. Moreover, GFL converters reduce the robustness of the system further at higher operating points. GFM also exhibit slightly reduced robustness at higher operating points but the difference is significantly less pronounced.

### **Screening Stability Issues**

The impedance-based technique proposed provides an accurate measure of the stability and robustness of the studied system. However, significant computational power is needed and results can be difficult to interpret without proper experience. Therefore, studying wider systems with a large number of points of view can be time consuming and challenging. Hence, screening metrics are useful for determining which locations may cause issue. Previously, techniques such as SCR have been used for this which have been updated to modern versions such as CSCR and ESCR. However, all techniques coupled fault current and stiffness and did not include converter control action. A new technique was proposed, known as the Grid Strength Impedance Metric which included converter control action and accurately represents the differences between GFL and GFM control structures. GSIM was successfully applied to showcase the strengthening that can be provided to the system via GFM converters and the pitfalls related to trying to achieve the same with GFL structures. Overall, the more GFM connected the greater the stiffness. Moreover, the tuning of the GFM directly relates to the stiffness provided with greater strength observed when the converter reacts less to external events. The greatest strength was provided from VSM based approaches with other GFM techniques provided less strength likely due to no emulation of inertia in the synchronising loop. GFM structures provide greater strength to the system when the SCR is low while GFL cause greater harm for the same conditions. This is reversed for higher SCRs. Moreover, GFL converters harm network strength further when exporting greater levels of active power

### **System Interactions of Wind Farms**

Using the proposed techniques, analysis of the strength and stability of an offshore wind farm connected through varying transmission line lengths was conducted. Three key penetration levels were identified: critical, optimal and maximum penetration. Critical penetration is the minimum number of turbines to stabilise the system where the strength is great enough to connect but the robustness remains low. Note the critical penetration may not always be related to the strength at the fundamental frequency. It has been shown for two cases that an interaction at a higher frequency caused instability when the GSIM calculated at the fundamental frequency suggested a stronger and more stable system. This resulted in the farm connected through the longest line having the lowest critical penetration as the high frequency pole was not present in the system.

The optimal penetration is the number of GFM devices that provide the greatest system robustness, not system strength. The optimal penetration was again lower for the longer transmission line but the stability of the system overall was always greater using shorter lines. Beyond the optimal penetration the robustness begins to reduce as the GFM converters do less useful work while the negative effects of GFLs are enhanced. Finally, the maximum penetration occurs when further increasing the penetration of GFM causes the stability to rapidly decay. The maximum penetration tended to coincide with when the offshore connection point was restored to the initial strength of the onshore connection point effectively negating the negative effect of the long line. The GSIM provided at the fundamental frequency did not provide the full picture of system stability and considering strength as a function of frequency was required to identify problematic interactions that occurred far from the fundamental.

### **Future Work**

Possible future contributions:

1. Further development of impedance-based stability techniques utilising physical converter prototypes. The analysis in this thesis has formulated converter impedances

from state-space models which offer a linearised approximation. The efficacy of the approach could be further validated using laboratory equipment.

2. GSIM requires testing on real system data to ensure the correct identifications of problematic points on the network. While the approach is formulated using frequency response data, real system components may offer complications with calculations.
3. The investigation of mechanical interactions should be extended to higher power turbines. These turbines will have larger masses and therefore possible modes of oscillation will likely be lower than the 3 MW turbines used in these studies. These lower frequency oscillations could interact further with GFM control structures.
4. The wind farm analysis should be extended to include different wind farm architectures including different array cable arrangements and connections. The way in which the arrays connect together will significantly effect how each line impedance is viewed from the MVT and may provide different conclusions to the optimal location of GFM turbines.
5. The wind farm analysis should be extended to include further control architectures to investigate which offer the most promising result. Only one GFM architecture is considered but it may be possible to achieve different optimal penetrations with different GFM structures as the frequency dependent behaviour is highly variable

# Bibliography

- [1] V. Masson-Delmotte, P. Zhai, A. Pirani, S. Connors, C. Pean, B. S., N. Caud, Y. Chen, L. Goldfarb, M. Gomis, M. Huang, K. Leitzell, E. Lonnoy, J. Matthews, T. Maycock, T. Waterfield, O. Yelekci, R. Yu, and Z. B., “Ipcc, 2021: Summary for policymakers,” report, 2021.
- [2] The Rt Hon Anne-Marie Trevelyan MP and The Rt Hon Alok Sharma KCMG MP, “End to coal power brought forward to october 2024,” 2021.
- [3] D. for Business Energy and I. Strategy, “Energy trends and prices statistical release january 2022,” 2022.
- [4] D. for Business Energy & Industrial Strategy, “Energy trends december 2022,” 22/12/22 2022.
- [5] Q. Hong, M. A. U. Khan, C. Henderson, A. Egea-Álvarez, D. Tzelepis, and C. Booth, “Addressing frequency control challenges in future low-inertia power systems: A great britain perspective,” *Engineering*, vol. 7, no. 8, pp. 1057–1063, 2021.
- [6] H. Urdal, R. Ierna, and A. J. Roscoe, “Stability challenges & solutions for power systems operating close to 100interfaced power sources : exchange of experience between hybrid and major power systems,” 2018.
- [7] F. Milano, F. Dorfler, G. Hug, D. J. Hill, and G. Verbic, “Foundations and challenges of low-inertia systems (invited paper),” IEEE.

## Bibliography

- [8] P. Tielens and D. Van Hertem, “Grid inertia and frequency control in power systems with high penetration of renewables,” 2012.
- [9] R. Ierna, J. Zhu, H. Urdal, A. Roscoe, M. Yu, A. Dyśko, and C. Booth, *Effects of VSM Converter Control on Penetration Limits of Non-Synchronous Generation in the GB Power System*. 2016.
- [10] J. Matevosyan, V. Vital, J. O’Sullivan, R. Quint, B. Badrzadeh, T. Prevost, E. Quitmann, D. Ramasubramanian, H. Urdal, S. Achilles, J. Macdowell, and S. H. Huang, “Grid-forming inverters: Are they the key for high renewable penetration?,” *IEEE Power and Energy Magazine*, vol. 17, no. 6, pp. 89–98, 2019.
- [11] M. Yu, A. J. Roscoe, A. Dyśko, C. D. Booth, R. Ierna, J. Zhu, and H. Urdal, “Instantaneous penetration level limits of non-synchronous devices in the british power system,” *IET Renewable Power Generation*, vol. 11, no. 8, pp. 1211–1217, 2017.
- [12] H. Gu, R. Yan, and T. Saha, “Review of system strength and inertia requirements for the national electricity market of australia,” *CSEE Journal of Power and Energy Systems*, vol. 5, no. 3, pp. 295–305, 2019.
- [13] N. G. ESO, “A system operability framework document,” report, 2020.
- [14] J. Alipoor, Y. Miura, and T. Ise, “Power system stabilization using virtual synchronous generator with alternating moment of inertia,” *IEEE Journal of Emerging and Selected Topics in Power Electronics*, vol. 3, no. 2, pp. 451–458, 2015.
- [15] C. Henderson, N. McNeill, G. Wu, D. Holliday, and A. Egea-Álvarez, “Vector control of a single-phase voltage source converter for the supply of inertia to weak grids,” Institution of Engineering and Technology.
- [16] G. Magdy, H. Ali, and D. Xu, “A new synthetic inertia system based on electric vehicles to support the frequency stability of low-inertia modern power grids,” *Journal of Cleaner Production*, vol. 297, p. 126595, 2021.

## Bibliography

- [17] A. Roscoe, T. Knueppel, R. Da Silva, P. Brogan, I. Gutierrez, D. Elliott, and J. Perez Campion, “Response of a grid forming wind farm to system events, and the impact of external and internal damping,” *IET Renewable Power Generation*, vol. 14, no. 19, pp. 3908–3917, 2020.
- [18] J. Morren, S. W. H. De Haan, W. L. Kling, and J. A. Ferreira, “Wind turbines emulating inertia and supporting primary frequency control,” *IEEE Transactions on Power Systems*, vol. 21, no. 1, pp. 433–434, 2006.
- [19] J. Zhu, C. D. Booth, G. P. Adam, A. J. Roscoe, and C. G. Bright, “Inertia emulation control strategy for vsc-hvdc transmission systems,” *IEEE Transactions on Power Systems*, vol. 28, no. 2, pp. 1277–1287, 2013.
- [20] R. Rosso, X. Wang, M. Liserre, X. Lu, and S. Engelken, “Grid-forming converters: Control approaches, grid-synchronization, and future trends—a review,” *IEEE Open Journal of Industry Applications*, vol. 2, pp. 93–109, 2021.
- [21] J. Liu, J. Wen, W. Yao, and Y. Long, “Solution to short-term frequency response of wind farms by using energy storage systems,” *IET Renewable Power Generation*, vol. 10, no. 5, pp. 669–678, 2016.
- [22] R. G. De Almeida and J. A. Pecas Lopes, “Participation of doubly fed induction wind generators in system frequency regulation,” *IEEE Transactions on Power Systems*, vol. 22, no. 3, pp. 944–950, 2007.
- [23] C. Zhong, Y. Zhou, and G. Yan, “A novel frequency regulation strategy for a pv system based on the curtailment power-current curve tracking algorithm,” *IEEE Access*, vol. 8, pp. 77701–77715, 2020.
- [24] J. Morren, J. Pierik, and S. W. H. de Haan, “Inertial response of variable speed wind turbines,” *Electric Power Systems Research*, vol. 76, no. 11, pp. 980–987, 2006.
- [25] M. G. Dozein, P. Mancarella, T. K. Saha, and R. Yan, “System strength and weak grids: Fundamentals, challenges, and mitigation strategies,” *IEEE*.

## Bibliography

- [26] P. Kundur, *Power System Stability and Control*. McGraw-Hill, 1994.
- [27] NERC, “Integrating inverter-based resources into low short circuit strength systems - reliability guideline,” 2017.
- [28] A. Egea-Alvarez, S. Fekriasl, F. Hassan, and O. Gomis-Bellmunt, “Advanced vector control for voltage source converters connected to weak grids,” *IEEE Transactions on Power Systems*, vol. 30, no. 6, pp. 3072–3081, 2015.
- [29] C. Henderson, A. Egea-Alvarez, T. Kneuppel, G. Yang, and L. Xu, “Grid strength impedance metric: An alternative to scr for evaluating system strength in converter dominated systems,” *IEEE Transactions on Power Delivery*, pp. 1–10, 2023.
- [30] H. Xin, Z. Li, W. Dong, Z. Wang, and L. Zhang, “A generalized-impedance based stability criterion for three-phase grid-connected voltage source converters,” *ArXiv*, vol. abs/1703.10514, 2017.
- [31] K. Sun, W. Yao, J. Fang, X. Ai, J. Wen, and S. Cheng, “Impedance modeling and stability analysis of grid-connected dfig-based wind farm with a vsc-hvdc,” *IEEE Journal of Emerging and Selected Topics in Power Electronics*, vol. 8, no. 2, pp. 1375–1390, 2020.
- [32] C. Li, J. Liang, L. M. Cipcigan, W. Ming, F. Colas, and X. Guillaud, “Dq impedance stability analysis for the power-controlled grid-connected inverter,” *IEEE Transactions on Energy Conversion*, vol. 35, no. 4, pp. 1762–1771, 2020.
- [33] L. Fan and Z. Miao, “Admittance-based stability analysis: Bode plots, nyquist diagrams or eigenvalue analysis?,” *IEEE Transactions on Power Systems*, vol. 35, no. 4, pp. 3312–3315, 2020.
- [34] J. Khazaei, Z. Miao, and L. Piyasinghe, “Impedance-model-based mimo analysis of power synchronization control,” *Electric Power Systems Research*, vol. 154, pp. 341–351, 2018.



## Bibliography

- [35] E. Unamuno, A. Rygg, M. Amin, M. Molinas, and J. A. Barrena, “Impedance-based stability evaluation of virtual synchronous machine implementations in converter controllers,” *IEEE*.
- [36] C. Henderson, A. Egea-Alvarez, R. Li, L. Xu, R. Da Silva, A. Kinsella, I. Gutierrez, and R. Pabat-Stroe, “Exploring an impedance-based scr for accurate representation of grid-forming converters,” 17th - 21st July 2022.
- [37] M. Sarkar, J. Jia, and G. Yang, “Distance relay performance in future converter dominated power systems,” *IEEE*.
- [38] L. Ruiqi, A. Dyśko, H. Urdal, A. Roscoe, Z. Jiebei, and C. Booth, “Protection challenges in future converter dominated power systems: demonstration through simulation and hardware tests,” Institution of Engineering and Technology.
- [39] A. Roy and B. K. Johnson, “Transmission side protection performance with type-iv wind turbine system integration,” *IEEE*.
- [40] R. C. Matthews, S. Hossain-Mckenzie, and M. J. Reno, “Fault current correction strategies for effective fault location in inverter-based systems,” *IEEE*.
- [41] K. Oureilidis, K.-N. Malamaki, K. Gallos, A. Tsitsimelis, C. Dikaiakos, S. Gkavanoudis, M. Cvetkovic, J. M. Mauricio, J. M. Maza Ortega, J. L. M. Ramos, G. Papaioannou, and C. Demoulias, “Ancillary services market design in distribution networks: Review and identification of barriers,” *Energies*, vol. 13, no. 4, p. 917, 2020.
- [42] Y. Liao and X. Wang, “Impedance-based stability analysis for interconnected converter systems with open-loop rhp poles,” *IEEE Transactions on Power Electronics*, vol. 35, no. 4, pp. 4388–4397, 2020.
- [43] X. Wang, F. Blaabjerg, and P. C. Loh, “An impedance-based stability analysis method for paralleled voltage source converters,” *IEEE*.

## Bibliography

- [44] H. Wu, X. Wang, and L. H. Kocewiak, “Impedance-based stability analysis of voltage-controlled mmcs feeding linear ac systems,” *IEEE Journal of Emerging and Selected Topics in Power Electronics*, vol. 8, no. 4, pp. 4060–4074, 2020.
- [45] Z. Haoxiang, L. Jing, Z. Chen, C. Xu, M. Molinas, and R. Fangquan, “Mimo impedance based stability analysis of dfig-based wind farm with mmc-hvdc in modified sequence domain,” Institution of Engineering and Technology.
- [46] A. Bolzoni, “Generalized nyquist mimo stability of frequency regulation services in power networks,” IEEE.
- [47] J. Samanes, A. Urtasun, E. L. Barrios, D. Lumbreras, J. Lopez, E. Gubia, and P. Sanchis, “Control design and stability analysis of power converters: The mimo generalized bode criterion,” *IEEE Journal of Emerging and Selected Topics in Power Electronics*, vol. 8, no. 2, pp. 1880–1893, 2020.
- [48] G. Amico, A. Egea-Alvarez, P. Brogan, and S. Zhang, “Small-signal converter admittance in the pn-frame: Systematic derivation and analysis of the cross-coupling terms,” *IEEE Transactions on Energy Conversion*, vol. 34, no. 4, pp. 1829–1838, 2019.
- [49] P. Seiler, A. Packard, and P. A. Gahinet, “An introduction to disk margins,” *IEEE Control Systems Magazine*, 2020.
- [50] M. R. Islam, S. Mekhilef, and R. Saidur, “Progress and recent trends of wind energy technology,” *Renewable and Sustainable Energy Reviews*, vol. 21, pp. 456–468, 2013.
- [51] P. Fernández-Bustamante, O. Barambones, I. Calvo, C. Napole, and M. Derbeli, “Provision of frequency response from wind farms: A review,” *Energies*, vol. 14, no. 20, p. 6689, 2021.
- [52] F. Gonzalez-Longatt, *Frequency Control and Inertial Response Schemes for the Future Power Networks*, pp. 193–231. Springer Singapore, 2014.

## Bibliography

- [53] A. Gloe, C. Jauch, and T. Räther, “Grid support with wind turbines: The case of the 2019 blackout in flensburg,” *Energies*, vol. 14, no. 6, p. 1697, 2021.
- [54] F. Díaz-González, M. Hau, A. Sumper, and O. Gomis-Bellmunt, “Participation of wind power plants in system frequency control: Review of grid code requirements and control methods,” *Renewable and Sustainable Energy Reviews*, vol. 34, pp. 551–564, 2014.
- [55] H. Luo, Z. Hu, H. Zhang, and H. Chen, “Coordinated active power control strategy for deloaded wind turbines to improve regulation performance in agc,” *IEEE Transactions on Power Systems*, vol. 34, no. 1, pp. 98–108, 2019.
- [56] L. Ruttledge and D. Flynn, “Emulated inertial response from wind turbines: Gain scheduling and resource coordination,” *IEEE Transactions on Power Systems*, vol. 31, no. 5, pp. 3747–3755, 2016.
- [57] R. Eriksson, N. Modig, and K. Elkington, “Synthetic inertia versus fast frequency response: a definition,” *IET Renewable Power Generation*, vol. 12, no. 5, pp. 507–514, 2018.
- [58] J. F. Conroy and R. Watson, “Frequency response capability of full converter wind turbine generators in comparison to conventional generation,” *IEEE Transactions on Power Systems*, vol. 23, no. 2, pp. 649–656, 2008.
- [59] C. Henderson, A. Egea-Alvarez, J. Rull-Duran, M. Nedd, P. Papadopoulos, and L. Xu, “Inertia and frequency support from britain’s ac powered trains,” *IEEE Transactions on Sustainable Energy*, pp. 1–10, 2022.
- [60] T. Liu, W. Pan, R. Quan, and M. Liu, “A variable droop frequency control strategy for wind farms that considers optimal rotor kinetic energy,” *IEEE Access*, vol. 7, pp. 68636–68645, 2019.
- [61] J. Boyle, T. Littler, S. M. Muyeen, and A. M. Foley, “An alternative frequency-droop scheme for wind turbines that provide primary frequency regulation via

## Bibliography

- rotor speed control,” *International Journal of Electrical Power & Energy Systems*, vol. 133, p. 107219, 2021.
- [62] J. M. Mauricio, A. Marano, A. Gomez-Exposito, and J. L. Martinez Ramos, “Frequency regulation contribution through variable-speed wind energy conversion systems,” *IEEE Transactions on Power Systems*, vol. 24, no. 1, pp. 173–180, 2009.
- [63] V. Prakash, P. Kushwaha, K. Chand Sharma, and R. Bhakar, “Frequency response support assessment from uncertain wind generation,” *International Journal of Electrical Power & Energy Systems*, vol. 134, p. 107465, 2022.
- [64] Y. Yu, S. K. Chaudhary, S. Golestan, G. D. A. Tinajero, J. C. Vasquez, and J. M. Guerrero, “An overview of grid-forming control for wind turbine converters,” IEEE.
- [65] A. Roscoe, T. Knueppel, R. Da Silva, P. Brogan, I. Gutierrez, D. Elliott, and J. Perez Campion, “Response of a grid forming wind farm to system events, and the impact of external and internal damping,” *IET Renewable Power Generation*, vol. 14, no. 19, pp. 3908–3917, 2020.
- [66] G. Gurrula and I. Sen, “Power system stabilizers design for interconnected power systems,” *IEEE Transactions on Power Systems*, vol. 25, no. 2, pp. 1042–1051, 2010. Export Date: 18 January 2023; Cited By: 157.
- [67] D. M. Lam and H. Yee, “A study of frequency responses of generator electrical torques for power system stabilizer design,” *IEEE Transactions on Power Systems*, vol. 13, no. 3, pp. 1136–1142, 1998. Export Date: 18 January 2023; Cited By: 33.
- [68] J. Khazaie, M. Mokhtari, M. Khalilyan, and D. Nazarpour, “Sub-synchronous resonance damping using distributed static series compensator (dssc) enhanced with fuzzy logic controller,” *International Journal of Electrical Power & Energy Systems*, vol. 43, no. 1, pp. 80–89, 2012.

## Bibliography

- [69] G. Tsourakis, B. M. Nomikos, and C. D. Vournas, “Contribution of doubly fed wind generators to oscillation damping,” *IEEE Transactions on Energy Conversion*, vol. 24, no. 3, pp. 783–791, 2009. Export Date: 18 January 2023; Cited By: 194.
- [70] F. M. Hughes, O. Anaya-Lara, N. Jenkins, and G. Strbac, “A power system stabilizer for dfig-based wind generation,” *IEEE Transactions on Power Systems*, vol. 21, no. 2, pp. 763–772, 2006. Export Date: 18 January 2023; Cited By: 261.
- [71] T. Shi, D. Nayanassiri, and Y. Li, “Sub-synchronous oscillations in wind farms – an overview study of mechanisms and damping methods,” *IET Renewable Power Generation*, vol. 14, no. 19, pp. 3974–3988, 2020. (Ryan).
- [72] J. Shair, X. Xie, L. Wang, W. Liu, J. He, and H. Liu, “Overview of emerging subsynchronous oscillations in practical wind power systems,” *Renewable and Sustainable Energy Reviews*, vol. 99, pp. 159–168, 2019.
- [73] Q. Liu, T. Caldognetto, and S. Buso, “Review and comparison of grid-tied inverter controllers in microgrids,” *IEEE Transactions on Power Electronics*, vol. 35, no. 7, pp. 7624–7639, 2020.
- [74] J. H. Eto, J. Undrill, P. Mackin, R. Daschmans, B. Williams, B. Haney, R. Hunt, J. Ellis, H. Illian, C. Martinez, M. O’Malley, K. Coughlin, and K. H. Lacommaré, “Use of frequency response metrics to assess the planning and operating requirements for reliable integration of variable renewable generation,” report, Office of Scientific and Technical Information (OSTI), 2010.
- [75] M. Dreidy, H. Mokhlis, and S. Mekhilef, “Inertia response and frequency control techniques for renewable energy sources: A review,” *Renewable and Sustainable Energy Reviews*, vol. 69, pp. 144–155, 2017.
- [76] M. A. Torres L, L. A. C. Lopes, L. A. Moran T, and J. R. Espinoza C, “Self-tuning virtual synchronous machine: A control strategy for energy storage systems to support dynamic frequency control,” *IEEE Transactions on Energy Conversion*, vol. 29, no. 4, pp. 833–840, 2014.

## Bibliography

- [77] J. Fang, H. Li, Y. Tang, and F. Blaabjerg, “Distributed power system virtual inertia implemented by grid-connected power converters,” *IEEE Transactions on Power Electronics*, vol. 33, no. 10, pp. 8488–8499, 2018.
- [78] M. Kersic, T. Müller, E. Lewis, T. Schaupp, R. Denninger, P. Ernst, S. Reichert, S. Rogalla, R. Singer, A. Roscoe, K. Jalili, A. Dyško, A. Alvarez, Q. Hong, H. Lens, and C. Schöll, *Testing Characteristics of Grid Forming Converters Part I: Specification and Definition of Behaviour*. 2020.
- [79] G. Wu, H. Sun, B. Zhao, S. Xu, X. Zhang, A. Egea-Alvarez, S. Wang, G. Li, Y. Li, and X. Zhou, “Low-frequency converter-driven oscillations in weak grids: Explanation and damping improvement,” *IEEE Transactions on Power Systems*, vol. 36, no. 6, pp. 5944–5947, 2021.
- [80] M. Davari and Y. A.-R. I. Mohamed, “Robust vector control of a very weak-grid-connected voltage-source converter considering the phase-locked loop dynamics,” *IEEE Transactions on Power Electronics*, vol. 32, no. 2, pp. 977–994, 2017.
- [81] D. Ramasubramanian, W. Baker, J. Matevosyan, S. Pant, and S. Achilles, “Asking for fast terminal voltage control in grid following plants could provide benefits of grid forming behavior,” *IET Generation, Transmission & Distribution*, 2022.
- [82] A. Alassi, K. Ahmed, A. Egea-Alvarez, and C. Foote, “Modified grid-forming converter control for black-start and grid-synchronization applications,” *IEEE*.
- [83] P. Unruh, M. Nuschke, P. Strauß, and F. Welck, “Overview on grid-forming inverter control methods,” *Energies*, vol. 13, no. 10, p. 2589, 2020.
- [84] A. Tayyebi, F. Dorfler, F. Kupzog, Z. Miletic, and W. Hribernik, “Grid-forming converters – inevitability, control strategies and challenges in future grids application,” 7-8th June 2018 2018.
- [85] R. Musca, A. Vasile, and G. Zizzo, “Grid-forming converters. a critical review of pilot projects and demonstrators,” *Renewable and Sustainable Energy Reviews*, vol. 165, p. 112551, 2022.

## Bibliography

- [86] A. Jain, J. N. Sakamuri, and N. A. Cutululis, “Grid-forming control strategies for black start by offshore wind power plants,” *Wind Energy Science*, vol. 5, no. 4, pp. 1297–1313, 2020.
- [87] J. Rocabert, A. Luna, F. Blaabjerg, and P. Rodríguez, “Control of power converters in ac microgrids,” *IEEE Transactions on Power Electronics*, vol. 27, no. 11, pp. 4734–4749, 2012.
- [88] C. Henderson, A. Egea-Alvarez, and L. Xu, “Analysis of multi-converter network impedance using mimo stability criterion for multi-loop systems,” *Electric Power Systems Research*, vol. 211, p. 108542, 2022.
- [89] T. Qoria, Q. Cossart, C. Li, X. Guillaud, F. Colas, F. Gruson, and X. Kestelyn, “Control and operation of a grid with 100 report, 2018.
- [90] Y. Lin, J. H. Eto, B. B. Johnson, J. D. Flicker, R. H. Lasseter, H. N. Pico, G.-S. Seo, B. J. Pierre, and A. Ellis, “Research roadmap on grid-forming inverters,” report, 2020.
- [91] S. Samanta and N. R. Chaudhuri, “Stability analysis of grid-forming converters under dc-side current limitation in primary frequency response regime,” *IEEE Transactions on Power Systems*, vol. 37, no. 4, pp. 3077–3091, 2022.
- [92] L. Zhang, *Modeling and Control of VSC-HVDC Links Connected to Weak AC Systems*. Thesis, 2010.
- [93] S. D’Arco, J. A. Suul, and O. B. Fosso, “A virtual synchronous machine implementation for distributed control of power converters in smartgrids,” *Electric Power Systems Research*, vol. 122, pp. 180–197, 2015.
- [94] S. D’Arco, J. A. Suul, and O. B. Fosso, “Small-signal modelling and parametric sensitivity of a virtual synchronous machine,” *IEEE*.
- [95] K. Sakimoto, Y. Miura, and T. Ise, “Stabilization of a power system with a distributed generator by a virtual synchronous generator function,” *IEEE*.

## Bibliography

- [96] M. G. Taul, X. Wang, P. Davari, and F. Blaabjerg, “Current limiting control with enhanced dynamics of grid-forming converters during fault conditions,” *IEEE Journal of Emerging and Selected Topics in Power Electronics*, vol. 8, no. 2, pp. 1062–1073, 2020.
- [97] A. M. Abdelrahim, P. McKeever, M. Smailes, A. Egea-Álvarez, and K. H. Ahmed, “Modified grid forming converter controller with fault ride through capability without pll or current loop,”
- [98] T. Shintai, Y. Miura, and T. Ise, “Reactive power control for load sharing with virtual synchronous generator control,” *IEEE*.
- [99] C. Cheng, Z. Zeng, H. Yang, and R. Zhao, “Wireless parallel control of three-phase inverters based on virtual synchronous generator theory,” *IEEE*.
- [100] J. Alipoor, Y. Miura, and T. Ise, “Distributed generation grid integration using virtual synchronous generator with adoptive virtual inertia,” *IEEE*.
- [101] H. Bevrani, T. Ise, and Y. Miura, “Virtual synchronous generators: A survey and new perspectives,” *International Journal of Electrical Power & Energy Systems*, vol. 54, pp. 244–254, 2014.
- [102] C. Henderson, D. Vozikis, D. Holliday, X. Bian, and A. Egea-Álvarez, “Assessment of grid-connected wind turbines with an inertia response by considering internal dynamics,” *Energies*, vol. 13, no. 5, 2020.
- [103] F. D’Agostino, S. Massucco, G. P. Schiapparelli, F. Silvestro, and M. Paolone, “Performance comparative assessment of grid connected power converters control strategies,” *IEEE*.
- [104] A. J. J. Rezek, C. A. D. Coelho, J. M. E. Vicente, J. A. Cortez, and P. R. Laurentino, “The modulus optimum ( mo ) method applied to voltage regulation systems : Modeling , tuning and implementation,” in *IPST - International Conference on Power Systems Transients*.



## Bibliography

- [105] C.-T. Lee, C.-C. Chu, and P.-T. Cheng, “A new droop control method for the autonomous operation of distributed energy resource interface converters,” *IEEE Transactions on Power Electronics*, vol. 28, no. 4, pp. 1980–1993, 2013.
- [106] R. Majumder, G. Ledwich, A. Ghosh, S. Chakrabarti, and F. Zare, “Droop control of converter-interfaced microsources in rural distributed generation,” *IEEE Transactions on Power Delivery*, vol. 25, no. 4, pp. 2768–2778, 2010.
- [107] R. Wang, Q. Sun, D. Ma, and Z. Liu, “The small-signal stability analysis of the droop-controlled converter in electromagnetic timescale,” *IEEE Transactions on Sustainable Energy*, vol. 10, no. 3, pp. 1459–1469, 2019.
- [108] C.-T. Lee, C.-C. Chu, and P.-T. Cheng, “A new droop control method for the autonomous operation of distributed energy resource interface converters,” *IEEE Transactions on Power Electronics*, vol. 28, no. 4, pp. 1980–1993, 2013.
- [109] L. Zhang, L. Harnefors, and H.-P. Nee, “Power-synchronization control of grid-connected voltage-source converters,” *IEEE Transactions on Power Systems*, vol. 25, no. 2, pp. 809–820, 2010.
- [110] D. Pattabiraman, R. H. Lasseter, and T. M. Jahns, “Transient stability modeling of droop-controlled grid-forming inverters with fault current limiting,” *IEEE*.
- [111] H.-P. Beck and R. Hesse, “Virtual synchronous machine,” *IEEE*.
- [112] Q.-C. Zhong and G. Weiss, “Synchroverters: Inverters that mimic synchronous generators,” *IEEE Transactions on Industrial Electronics*, vol. 58, no. 4, pp. 1259–1267, 2011.
- [113] S. D’Arco and J. A. Suul, “Virtual synchronous machines; classification of implementations and analysis of equivalence to droop controllers for microgrids,” *IEEE*.
- [114] S. Alepuz, S. Busquets-Monge, J. Bordonau, J. A. Martinez-Velasco, C. A. Silva, J. Pontt, and J. Rodriguez, “Control strategies based on symmetrical compo-

## Bibliography

- nents for grid-connected converters under voltage dips,” *IEEE Transactions on Industrial Electronics*, vol. 56, no. 6, pp. 2162–2173, 2009.
- [115] L. Zhang, L. Harnefors, and H.-P. Nee, “Power-synchronization control of grid-connected voltage-source converters,” *IEEE Transactions on Power Systems*, vol. 25, no. 2, pp. 809–820, 2010.
- [116] D.-J. Bang, H. Polinder, G. Shrestha, and J. Abraham Ferreira, “Promising direct-drive generator system for large wind turbines,” *EPE Journal*, vol. 18, no. 3, pp. 7–13, 2008.
- [117] I. P. Girsang, J. S. Dhupia, E. Muljadi, M. Singh, and L. Y. Pao, “Gearbox and drivetrain models to study dynamic effects of modern wind turbines,” *IEEE Transactions on Industry Applications*, vol. 50, no. 6, pp. 3777–3786, 2014.
- [118] M. Rahimi and A. Beiki, “Efficient modification of the control system in pmsg-based wind turbine for improvement of the wind turbine dynamic response and suppression of torsional oscillations,” *International Transactions on Electrical Energy Systems*, vol. 28, no. 8, p. e2578, 2018.
- [119] S. M. Muyeen, M. Hasan Ali, R. Takahashi, T. Murata, J. Tamura, Y. Tomaki, A. Sakahara, and E. Sasano, “Comparative study on transient stability analysis of wind turbine generator system using different drive train models,” *IET Renewable Power Generation*, vol. 1, no. 2, p. 131, 2007.
- [120] A. D. Hansen and G. Michalke, “Modelling and control of variable-speed multipole permanent magnet synchronous generator wind turbine,” *Wind Energy*, vol. 11, no. 5, pp. 537–554, 2008.
- [121] Y. Yang, S. Bremner, C. Menictas, and M. Kay, “Battery energy storage system size determination in renewable energy systems: A review,” *Renewable and Sustainable Energy Reviews*, vol. 91, pp. 109–125, 2018.

## Bibliography

- [122] H. Beltran, S. Harrison, A. Egea-Álvarez, and L. Xu, “Techno-economic assessment of energy storage technologies for inertia response and frequency support from wind farms,” *Energies*, vol. 13, no. 13, p. 3421, 2020.
- [123] N. Mohan, T. M. Undeland, and W. P. Robbins, *Power Electronics Converters, Applications and Design*. John Wileyand Sons, Inc., 3rd ed., 2003.
- [124] W. Shepherd, L. N. Hulley, and D. T. W. Liang, *Power Electronics and Motor Control*. Cambridge: Cambridge University Press, 2 ed., 1996.
- [125] F. Baumgartner, H. Scholz, A. Breu, and S. Roth, “Mpp voltage monitoring to optimise grid connected system design rules,” 2004.
- [126] J. D. Mondol, Y. G. Yohanis, and B. Norton, “The effect of low insolation conditions and inverter oversizing on the long-term performance of a grid-connected photovoltaic system,” *Progress in Photovoltaics: Research and Applications*, vol. 15, no. 4, pp. 353–368, 2007.
- [127] C. J. Murray, *Reliability Analysis of Single-Phase Photovoltaic Inverter with Reactive Power Support*. Thesis, 2010.
- [128] H. Zhang, X. Wang, L. Harnefors, H. Gong, J.-P. Hasler, and H.-P. Nee, “Siso transfer functions for stability analysis of grid-connected voltage-source converters,” *IEEE Transactions on Industry Applications*, vol. 55, no. 3, pp. 2931–2941, 2019.
- [129] G. Amico, A. Egea-Alvarez, L. Xu, and P. Brogan, “Stability margin definition for a converter-grid system based on diagonal dominance property in the sequence-frame,” IEEE.
- [130] L. Xu, H. Xin, L. Huang, H. Yuan, P. Ju, and D. Wu, “Symmetric admittance modeling for stability analysis of grid-connected converters,” *IEEE Transactions on Energy Conversion*, vol. 35, no. 1, pp. 434–444, 2020.

## Bibliography

- [131] H. Zhang, L. Harnefors, X. Wang, H. Gong, and J.-P. Hasler, “Stability analysis of grid-connected voltage-source converters using siso modeling,” *IEEE Transactions on Power Electronics*, vol. 34, no. 8, pp. 8104–8117, 2019.
- [132] A. Akhavan, S. Golestan, J. C. Vasquez, and J. M. Guerrero, “Control and stability analysis of current-controlled grid-connected inverters in asymmetrical grids,” *IEEE Transactions on Power Electronics*, vol. 37, no. 12, pp. 14252–14264, 2022.
- [133] M. Barrow, *Correlation and regression*, book section 7. Harlow, UK: Pearson, 7 ed., 2017.
- [134] F. D. Freijedo, A. Vidal, A. G. Yepes, J. M. Guerrero, O. Lopez, J. Malvar, and J. Doval-Gandoy, “Tuning of synchronous-frame pi current controllers in grid-connected converters operating at a low sampling rate by mimo root locus,” *IEEE Transactions on Industrial Electronics*, vol. 62, no. 8, pp. 5006–5017, 2015.
- [135] J. M. Undrill and T. E. Kostyniak, “Subsynchronous oscillations part 1: comprehensive system stability analysis,” *IEEE Transactions on Power Apparatus and Systems*, vol. 95, no. 4, pp. 1446–1455, 1976.
- [136] R. D. Middlebrook, “Input filter considerations in design and application of switching regulators,” in *IEEE Industry Applications Society Annual Meeting*, pp. 336–382.
- [137] H. Nyquist, “Regeneration theory,” *Bell System Technical Journal*, vol. 11, no. 1, pp. 126–147, 1932.
- [138] J. Sun, “Impedance-based stability criterion for grid-connected inverters,” *IEEE Transactions on Power Electronics*, vol. 26, no. 11, pp. 3075–3078, 2011.
- [139] S. D. Sudhoff, S. F. Glover, P. T. Lamm, D. H. Schmucker, and D. E. Delisle, “Admittance space stability analysis of power electronic systems,” *IEEE Transactions on Aerospace and Electronic Systems*, vol. 36, no. 3, pp. 965–973, 2000.
- [140] J. Carrol, “An input impedance stability criterion allowing more flexibility for multiple loads which are independently designed,” 1992.

## Bibliography

- [141] M. Belkhat, *Stability Criteria for AC Power Systems with Regulated Loads*. Thesis, 1997.
- [142] C. M. Wildrick, F. C. Lee, B. H. Cho, and B. Choi, “A method of defining the load impedance specification for a stable distributed power system,” *IEEE Transactions on Power Electronics*, vol. 10, no. 3, pp. 280–285, 1995.
- [143] Y. Liao and X. Wang, “General rules of using bode plots for impedance-based stability analysis,” *IEEE*.
- [144] D. Yang, X. Ruan, and H. Wu, “Impedance shaping of the grid-connected inverter with lcl filter to improve its adaptability to the weak grid condition,” *IEEE Transactions on Power Electronics*, vol. 29, no. 11, pp. 5795–5805, 2014.
- [145] B. Wen, D. Boroyevich, R. Burgos, P. Mattavelli, and Z. Shen, “Inverse nyquist stability criterion for grid-tied inverters,” *IEEE Transactions on Power Electronics*, vol. 32, no. 2, pp. 1548–1556, 2017.
- [146] F. Liu, J. Liu, H. Zhang, and D. Xue, “Stability issues of  $z + z$  type cascade system in hybrid energy storage system (hess),” *IEEE Transactions on Power Electronics*, vol. 29, no. 11, pp. 5846–5859, 2014.
- [147] X. Zhang, X. Ruan, and C. K. Tse, “Impedance-based local stability criterion for dc distributed power systems,” *IEEE Transactions on Circuits and Systems I: Regular Papers*, vol. 62, no. 3, pp. 916–925, 2015.
- [148] H. Alenius and T. Roinila, “Impedance-based stability analysis of paralleled grid-connected rectifiers: Experimental case study in a data center,” *Energies*, vol. 13, no. 8, p. 2109, 2020.
- [149] Q. Xiao, P. Mattavelli, A. Khodamoradi, and F. Tang, “Analysis of transforming dq impedances of different converters to a common reference frame in complex converter networks,” *CES Transactions on Electrical Machines and Systems*, vol. 3, no. 4, pp. 342–350, 2019.

## Bibliography

- [150] A. Rygg, M. Molinas, E. Unamuno, C. Zhang, and X. Cai, “A simple method for shifting local dq impedance models to a global reference frame for stability analysis,” 2017.
- [151] C. Zhang, M. Molinas, A. Rygg, and X. Cai, “Impedance-based analysis of inter-connected power electronics systems: Impedance network modeling and comparative studies of stability criteria,” *IEEE Journal of Emerging and Selected Topics in Power Electronics*, vol. 8, no. 3, pp. 2520–2533, 2020.
- [152] B. S. Institution, “Iec tr 60909-4:2021 - short-circuit current in three-phase ac systems,” 2021.
- [153] R. Fernades, S. Achilles, and J. MacDowell, “Report to nerc erstf for composite short circuit ratio (cscr) estimation guideline,” *GE Energy Consulting*, 2015.
- [154] Y. Zhang, S.-H. F. Huang, J. Schmall, J. Conto, J. Billo, and E. Rehman, “Evaluating system strength for large-scale wind plant integration,” IEEE.
- [155] CIGRE, “Connection of wind farms to weak ac networks,” *Working Group B4.62*, 2016.
- [156] J. Jia, G. Yang, A. H. Nielsen, and V. Gevorgian, “Investigation on the combined effect of vsc-based sources and synchronous condensers under grid unbalanced faults,” *IEEE Transactions on Power Delivery*, vol. 34, no. 5, pp. 1898–1908, 2019.
- [157] N. Nimpitiwan, G. T. Heydt, R. Ayyanar, and S. Suryanarayanan, “Fault current contribution from synchronous machine and inverter based distributed generators,” *IEEE Transactions on Power Delivery*, vol. 22, no. 1, pp. 634–641, 2007.
- [158] NREL, “Understanding fault characteristics of inverter-based distributed energy resources - nrel/tp-550-46698,” report, 2010.
- [159] I. Ray and L. M. Tolbert, “The case against phase-locked loops in weak ac grids,” IEEE.

## Bibliography

- [160] X. Yue, X. Wang, and F. Blaabjerg, “Review of small-signal modeling methods including frequency-coupling dynamics of power converters,” *IEEE Transactions on Power Electronics*, vol. 34, no. 4, pp. 3313–3328, 2019.
- [161] W. Zhou, R. E. Torres-Olguin, Y. Wang, and Z. Chen, “Dq impedance-decoupled network model-based stability analysis of offshore wind power plant under weak grid conditions,” *IET Power Electronics*, vol. 13, no. 13, pp. 2715–2729, 2020.
- [162] Y. Wang, X. Wang, F. Blaabjerg, and Z. Chen, “Frequency scanning-based stability analysis method for grid-connected inverter system,” *IEEE*.
- [163] R. N. Damas, Y. Son, M. Yoon, S.-Y. Kim, and S. Choi, “Subsynchronous oscillation and advanced analysis: A review,” *IEEE Access*, vol. 8, pp. 224020–224032, 2020.
- [164] L. Harnefors, “Analysis of subsynchronous torsional interaction with power electronic converters,” *IEEE Transactions on Power Systems*, vol. 22, no. 1, pp. 305–313, 2007.
- [165] S. Ghosh, K. V. Kkuni, G. Yang, and L. Kocewiak, “Impedance scan and characterization of type 4 wind power plants through aggregated model,” *IEEE*.
- [166] A. Rygg, M. Molinas, C. Zhang, and X. Cai, “A modified sequence-domain impedance definition and its equivalence to the dq-domain impedance definition for the stability analysis of ac power electronic systems,” *IEEE Journal of Emerging and Selected Topics in Power Electronics*, vol. 4, no. 4, pp. 1383–1396, 2016.
- [167] Y. Ma, W. Cao, L. Yang, F. F. Wang, and L. M. Tolbert, “Virtual synchronous generator control of full converter wind turbines with short-term energy storage,” *IEEE Transactions on Industrial Electronics*, vol. 64, no. 11, pp. 8821–8831, 2017.
- [168] M. García-Gracia, M. P. Comech, J. Sallán, and A. Llombart, “Modelling wind farms for grid disturbance studies,” *Renewable Energy*, vol. 33, no. 9, pp. 2109–2121, 2008.

## Bibliography

- [169] L. M. Fernández, C. A. García, J. R. Saenz, and F. Jurado, “Equivalent models of wind farms by using aggregated wind turbines and equivalent winds,” *Energy Conversion and Management*, vol. 50, no. 3, pp. 691–704, 2009.
- [170] B. Liu, Z. Li, X. Zhang, X. Dong, and X. Liu, “Impedance-based analysis of control interactions in weak-grid-tied pmsg wind turbines,” *IEEE Journal on Emerging and Selected Topics in Circuits and Systems*, vol. 11, no. 1, pp. 90–98, 2021.
- [171] W. Du, J. Bi, T. Wang, and H. Wang, “Impact of grid connection of large-scale wind farms on power system small-signal angular stability,” *CSEE Journal of Power and Energy Systems*, vol. 1, no. 2, pp. 83–89, 2015.
- [172] C. Chen, W. Du, H. Wang, and T. Littler, “Sub-synchronous oscillations in power systems caused by grid-connected wind farms — a survey of mechanism studies,” *CSEE Journal of Power and Energy Systems*, vol. 4, no. 4, pp. 495–503, 2018.
- [173] L. H. Kocewiak, J. Hjerrild, and C. L. Bak, “Wind turbine converter control interaction with complex wind farm systems,” *IET Renewable Power Generation*, vol. 7, no. 4, pp. 380–389, 2013.
- [174] J. B. Glasdam, L. H. Kocewiak, J. Hjerrild, and C. L. Bak, “Control system interaction in the vsc-hvdc grid connected offshore wind power plant,” 2015.
- [175] L. Kocewiak, R. Blasco-Gimenez, C. Buchhagen, J. B. Kwon, Y. Sun, A. S. Tervisan, M. Larsson, and X. Wang, “Overview, status and outline of stability analysis in converter-based power systems,” 11th-12th November 2020 2020.



# Appendix A

## Converter Parameters

Table A.1: Common Converter Parameters

Parameter	Symbol	Value
Nominal Voltage	$V_n$	690 V
Nominal Power	$P_c$	3 MW
Nominal Frequency	$f_g$	50 Hz
Filter Resistance	$R_g$	0.198 $m\Omega$
Filter Inductance	$L_g$	0.63 $\mu H$
Measurement Filter Time Constant	$\tau_{mf}$	$1 \times 10^{-4}$ s
Pade Delay Time Constant	$\tau_{pd}$	$1 \times 10^{-4}$ s

Table A.2: PVCC Parameters

Parameter	Symbol	Value
Current Control P Gain	$k_{I,p}$	0.0505 V/A
Current Control I Gain	$k_{I,i}$	1.587 V/A
Power Control P Gain	$k_{P,p}$	$5 \times 10^{-4}$ A/W
Power Control I Gain	$k_{P,i}$	0.1 A/W
Voltage Control P Gain	$k_{V,p}$	6 A/V
Voltage Control I Gain	$k_{V,i}$	20 A/V
PLL P Gain	$k_{pll,p}$	1.557 $rad/sV$
PLL I Gain	$k_{pll,i}$	175 $rad/sV$
Reactive Droop Gain	$k_{Qd}$	$1 \times 10^{-6}$ V/VAr
Voltage Feedforward Time Constant	$\tau_{vff}$	$1 \times 10^{-4}$ s

Appendix A. Converter Parameters

Table A.3: PVCCI Parameters

Parameter	Symbol	Value
Current Control P Gain	$k_{I,p}$	0.0505 V/A
Current Control I Gain	$k_{I,i}$	1.587 V/A
Power Control P Gain	$k_{P,p}$	$5 \times 10^{-4}$ I/W
Power Control I Gain	$k_{P,i}$	0.1 A/W
Voltage Control P Gain	$k_{V,p}$	6 A/V
Voltage Control I Gain	$k_{V,i}$	20 A/V
PLL P Gain	$k_{pll,p}$	1.557 rad/sV
PLL I Gain	$k_{pll,i}$	175 rad/sV
Reactive Droop Gain	$k_{Qd}$	$1 \times 10^{-6}$ V/VAr
Voltage Feedforward Time Constant	$\tau_{vff}$	$1 \times 10^{-4}$ s
Inertia Gain	$K_{inert}$	$-2 \times 10^5$ Ws <sup>2</sup> /rad

Table A.4: PVCCD Parameters

Parameter	Symbol	Value
Current Control P Gain	$k_{I,p}$	0.0505 V/A
Current Control I Gain	$k_{I,i}$	1.587 V/A
Frequency Droop Gain	$k_{wD}$	-20000 Ws/rad
Voltage Droop Gain	$k_{vD}$	20 A/V
PLL P Gain	$k_{pll,p}$	1.557 rad/sV
PLL I Gain	$k_{pll,i}$	175 rad/sV
Voltage Feedforward Time Constant	$\tau_{vff}$	$1 \times 10^{-4}$ s

Table A.5: GFMD Parameters

Parameter	Symbol	Value
Current Control P Gain	$k_{I,p}$	0.0253 V/A
Current Control I Gain	$k_{I,i}$	0.7935 V/A
Power Droop Gain	$k_{Pd}$	$5 \times 10^{-5}$ rad/Ws
Voltage Control P Gain	$k_{V,p}$	10 A/V
Voltage Control I Gain	$k_{V,i}$	50 A/V
Reactive Droop Gain	$k_{Qd}$	$1 \times 10^{-6}$ V/VAr
Voltage Feedforward Time Constant	$\tau_{vff}$	$1 \times 10^{-4}$ s

Appendix A. Converter Parameters

Table A.6: VSMCC Parameters

Parameter	Symbol	Value
Current Control P Gain	$k_{I,p}$	0.0253 V/A
Current Control I Gain	$k_{I,i}$	0.7935 V/A
Power Control P Gain	$k_{P,p}$	$3.19 \times 10^{-6} rad/Ws$
Power Control I Gain	$k_{P,i}$	$5.24 \times 10^{-5} rad/Ws$
Voltage Control P Gain	$k_{V,p}$	40 A/V
Voltage Control I Gain	$k_{V,i}$	100 A/V
Reactive Droop Gain	$k_{Qd}$	$1 \times 10^{-6} V/VAr$
Active Power Filter Time Constant	$\tau_{apf}$	0.01 s

Table A.7: VSM Parameters

Parameter	Symbol	Value
Power Control P Gain	$k_{P,p}$	$3.19 \times 10^{-6} rad/Ws$
Power Control I Gain	$k_{P,i}$	$5.24 \times 10^{-5} rad/Ws$
Voltage Control P Gain	$k_{V,p}$	1 A/V
Voltage Control I Gain	$k_{V,i}$	100 A/V
Reactive Droop Gain	$k_{Qd}$	$1 \times 10^{-6} V/VAr$
Active Power Filter Time Constant	$\tau_{apf}$	0.01 s
PCC Voltage Filter Time Constant	$\tau_{pvf}$	0.01 s

# Appendix B

## Chapter 3 Figures

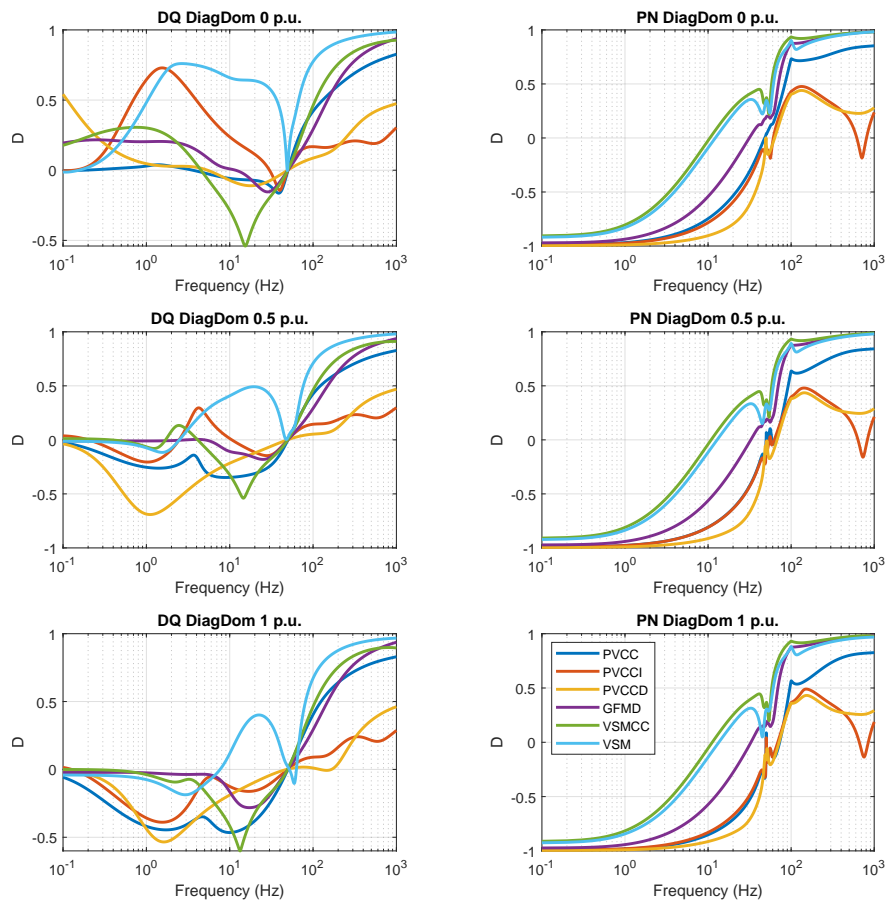


Figure B.1: Comparison of Diagonal Dominance of Controllers for Varying Operating Point at SCR = 4

Appendix B. Chapter 3 Figures

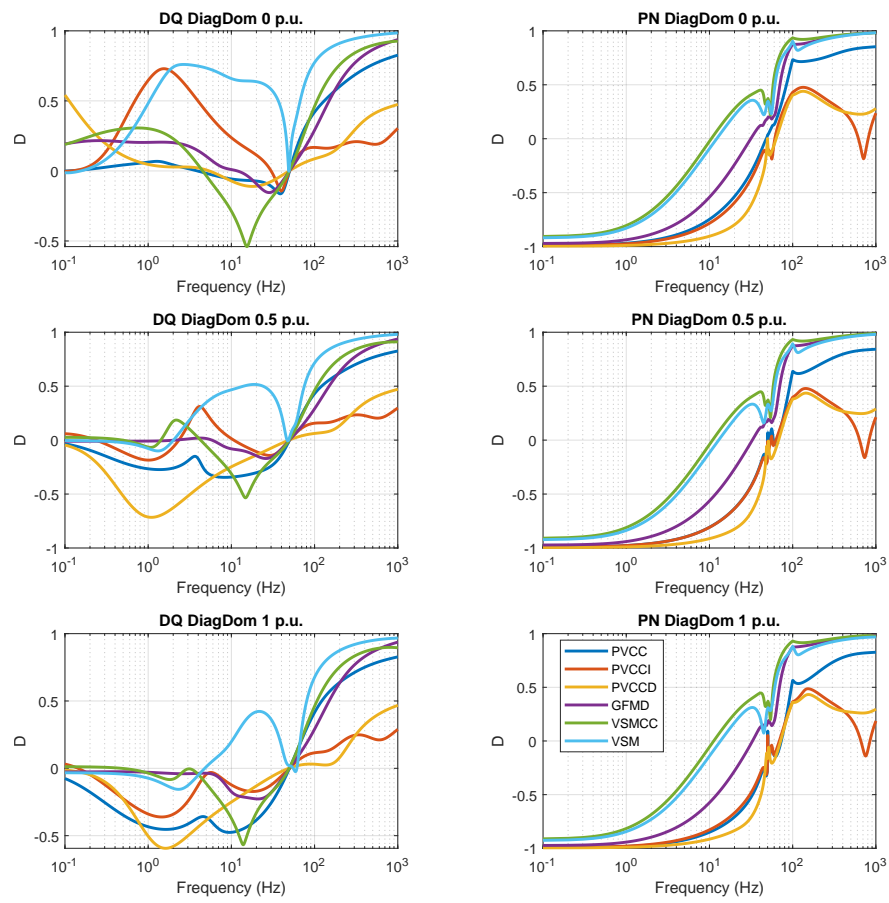


Figure B.2: Comparison of Diagonal Dominance of Controllers for Varying Operating Point at SCR = 6

# Appendix C

## Chapter 4 Figures

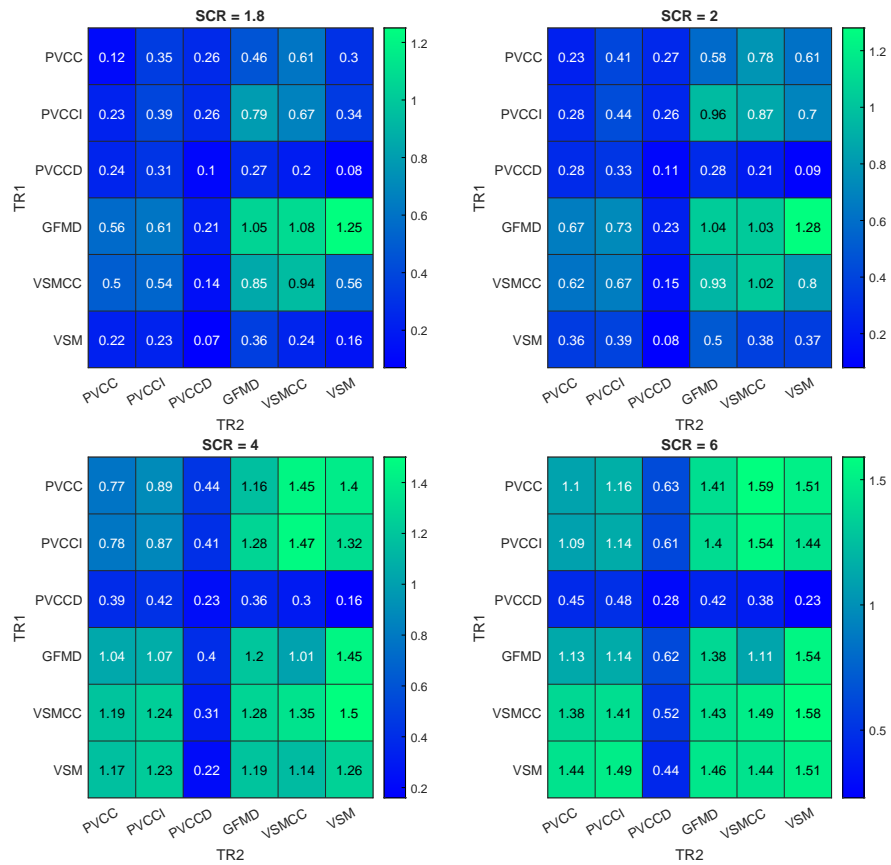


Figure C.1: Robustness Measure for Converter 1 Differential Mode at 1 p.u. active power

## Appendix C. Chapter 4 Figures

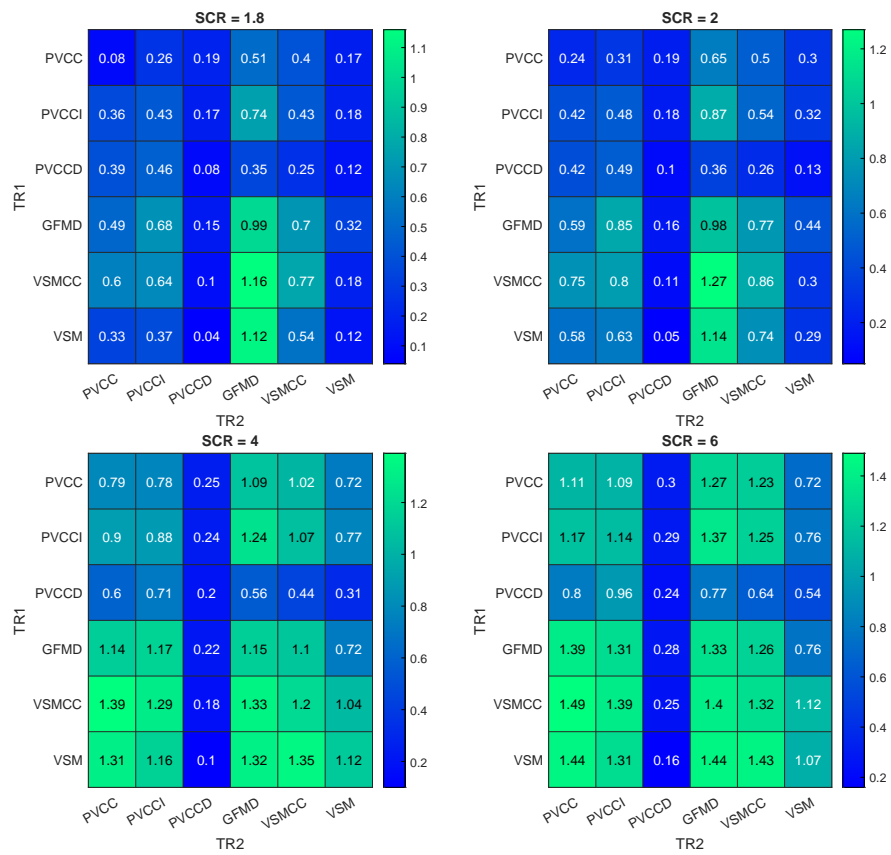


Figure C.2: Robustness Measure for Converter 2 Differential Mode at 1 p.u. active power

# Appendix D

## Chapter 5 Figures

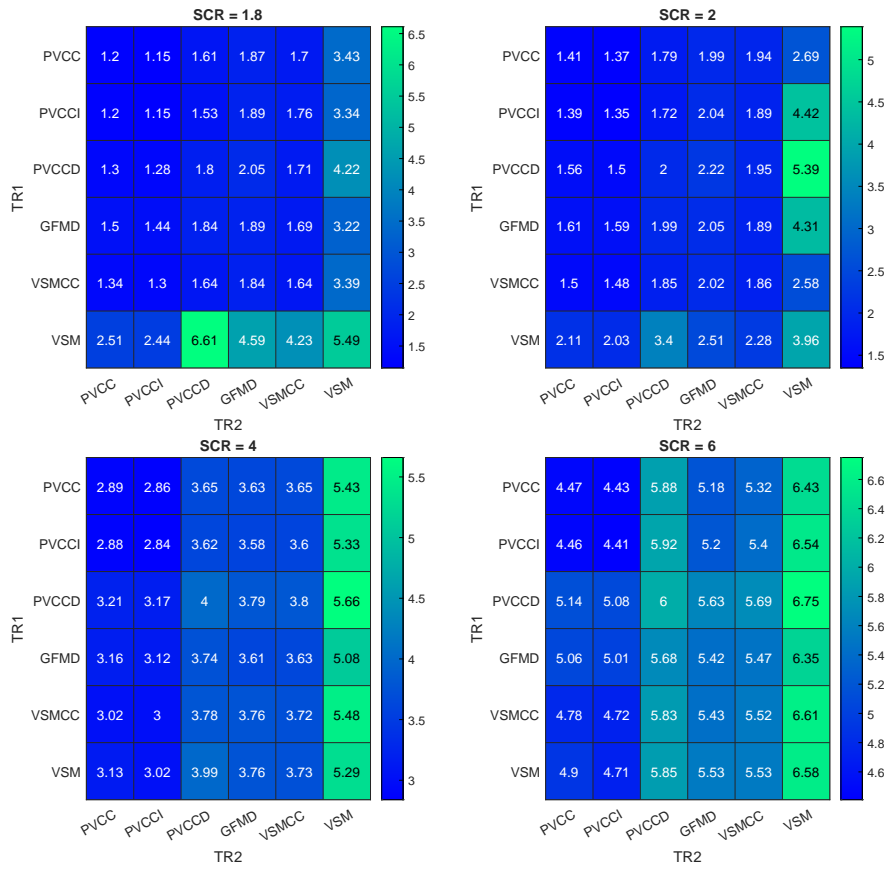


Figure D.1: GSIM for Two Converter System at 1 p.u. active power



Appendix D. Chapter 5 Figures

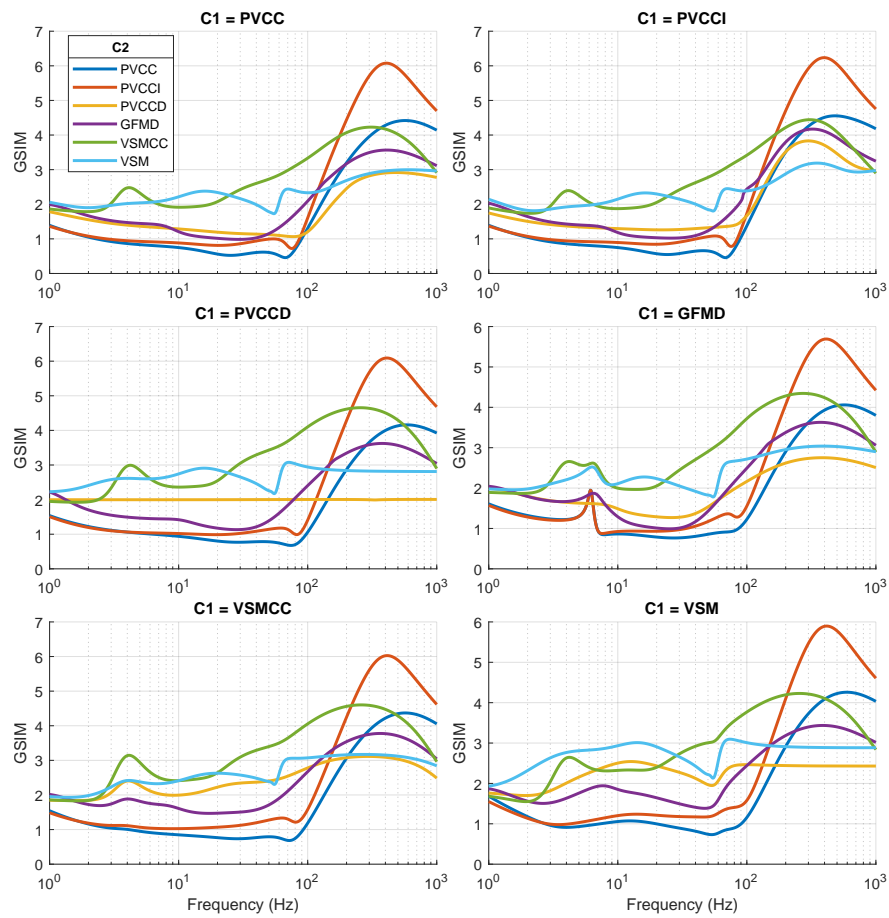


Figure D.2: Comparison of Frequency Dependent GSIM for Controller Combinations  
 1 pu SCR = 2

# Appendix E

## Wind Farm Parameters

Table E.1: Wind Farm Parameters

Parameter	Symbol	Value
Turbine Voltage Level	$V_t$	690 V
Array Voltage Level	$V_a$	66 kV
Export Voltage Level	$V_e$	220 kV
Array Line Resistance	$R_a$	0.14 $\Omega/km$
Array Line Inductance	$L_a$	0.41 mH/km
Array Line Capacitance	$C_a$	0.19 $\mu F/km$
Export Line Resistance	$R_e$	0.047 $\Omega/km$
Export Line Inductance	$L_e$	0.406 mH/km
Export Line Capacitance	$C_e$	0.208 $\mu F/km$
MVT Resistance	$R_{MVT}$	6.45 $\Omega$
MVT Inductance	$L_{MVT}$	0.247 H
Turbine Transformer Resistance	$R_{LVT}$	0.794 $m\Omega$
Turbine Transformer Inductance	$L_{LVT}$	45.5 $\mu H$